Institut de Physique et Chimie des Matériaux de Strasbourg

Thèse de doctorat de l'Université de Strasbourg

# Impact of structural defects on spin-polarized transport across magnetic tunnel junctions

par

FILIP SCHLEICHER

Soutenue publiquement le 10 Decembre 2012 devant le jury composé de :

| | |
|---|---|
| Hugues Dreysse | Directeur de thèse |
| François Montaigne | Rapporteur |
| Frédéric Petroff | Rapporteur |
| Wolfgang Weber | Examinateur interne |

# Acknowledgements

By the time I am writing these words, it has already been four days since the memorable afternoon when I officially received my PhD diploma. The defense, along with the manuscript you are holding in hands (or more probably its digital copy), summarizes more than three years of the work I've performed during my stay at the IPCMS institute. However, this place bears a special significance for me. I couldn't have expected I would get that far when, in the early morning of September 2008, I crossed the Pont de Rhin for the first time. I still recall my first journey by train to the University of Mulhouse, during which I kept gazing through the window at numerous castles of the Vosges Mountains and had a feeling that what I see is somehow different, that I'm just a passer-by and that I would never call these places 'mine'. At the University of Strasbourg, in beautiful Alsace and in France general, I've remained far from the beloved family, longtime friends, and the extensive Lower Silesian foothills, which I knew so well and where every single place was like home. For me, the new environment felt in many ways culturally and linguistically different, especially as I did not speak a single word in French upon arrival.

It is hard to say at which point did I start to call Alsace 'home' and people here 'friends'. I cannot recall when did it stop studying maps because I had already known them by heart. I don't remember when native people started to ask me about the best tariff offers to travel around and when did I start to answer them in their native language. After more than these four years spent here, I wouldn't like to leave. However, reasons for which I feel this way cannot be exclusively attributed neither to the beauty of Alsace nor to the high level of research in the IPCMS only. It is also the people I've worked with.

I would like to say a lot of "Thank you" to everyone who helped me throughout the timeframe of this thesis. Naturally, the first one goes to Martin Bowen, my *de facto* boss, who has guided me throughout the entire length of the research performed and who was my primary source of most of the knowledge that I posses now. I would like to thank people from the DMONS group with whom I had opportunity and pleasure to work, especially Jacek Arabski, Eric Beaurepaire, Samy Boukari, Hugues Dreysse, Christophe Kieber, Dong Jik Kim (now at University of Nebraska - Lincoln), Micham Majjad, Guy Schmember and Veronique Wernher.

Moreover, I could not forget about people which are not members of the DMONS

group, but without whose assistance my research could not proceed any further, especially Silviu Colis (DCMI), Matthieu Gallart (DMO) and Dominique Quince (assistant engineer).

The line which separates professional contacts and the private life of a young scientist is not easy to draw. However, it certainly runs somewhere across offices of fellow students, who share both joy and misery of their colleagues. Some of you I know better, some less. I'd like to thank all of you for the time spent together: Christian Andreas, Jean-Baptiste Beaufrand, Jean Besbas (DON), Hashim Al Daboochah, Vincent Davesne, Fatima Djeghloul (DSI), Vina Faramarazi (now Post-Doc, DMONS), Manuel Gruber, Saber Gueddida, Mohammad Haidar, Ali Hallal (now Spintec, Grenoble), Ufuk Halisdemir, Mohamad Hamieh, Changhoon Heo, Fatima Ibrahim, Marzena Materska, Reda Moubah (now Uppsala University), Nabil Najjari, Wojciech Szewc, Dimitra Xenioti, Silvia Zanettini and Łukasz Zosiak (DSI).

Most personally, I thank my future wife Gosia Kuleszo who is always close to me no matter how far, my mum, dad and grandparents for everlasting love and faith in me.

Moreover, I would like to thank prof. Jan Misiewicz from the Wrocław University of Technology for the possibility of performing a part of my studies at the University of Strasbourg thanks to the cooperation between regions of Alsace and Lower Silesia as well as between both Universities.

# Contents


**Résumé en français** 13

**Introduction** 21

**I Theoretical Basis** 27

**1 Basics of Tunnel Magnetoresistance** 29
- 1.1 From simple to epitaxial barriers . . . 29
- 1.2 Non-zero spin polarization in ferromagnets . . . 32
- 1.3 Spin-polarized tunneling in magnetic tunnel junctions . . . 33
- 1.4 Symmetry filtering in Fe/MgO/Fe . . . 34
  - 1.4.1 Electronic Bloch wavefunctions . . . 34
  - 1.4.2 Band structures impact . . . 36
    - 1.4.2.1 Magnesium Oxide . . . 36
    - 1.4.2.2 Iron . . . 38
  - 1.4.3 Transport calculations . . . 39
  - 1.4.4 Intrinsic issues . . . 42
    - 1.4.4.1 Zero bias anomaly . . . 42
    - 1.4.4.2 Interfacial resonant states . . . 43
    - 1.4.4.3 Impact of phonons . . . 44
- 1.5 Other barrier types . . . 44
  - 1.5.1 Strontium titanate . . . 44
  - 1.5.2 Titanium dioxide . . . 46
- 1.6 Different electrode materials . . . 47
  - 1.6.1 Introduction of Cobalt . . . 47
    - 1.6.1.1 Cobalt-iron alloys . . . 47
    - 1.6.1.2 Interfacial cobalt layers . . . 48
  - 1.6.2 CoFeB based textured systems . . . 50
  - 1.6.3 $La_{0.7}Sr_{0.3}MnO_3$ Half-metallic electrodes . . . 52
    - 1.6.3.1 Crystal field splitting . . . 52
    - 1.6.3.2 Double exchange mechanism . . . 54

1.6.3.3 Temperature dependence . . . 56
1.7 LSMO/STO/LSMO system . . . 57

**2 Role of defects 59**
2.1 Bulk imperfections . . . 59
2.1.1 Impact on spin-polarized transport . . . 59
2.1.2 Optical activity in crystalline systems . . . 65
2.1.2.1 Magnesium oxide . . . 65
2.1.2.2 Strontium titanate . . . 69
2.1.2.3 Titanium dioxide . . . 72
2.2 Interface Issues . . . 72
2.2.1 Oxidation . . . 73
2.2.2 Consequences of annealing . . . 75
2.2.2.1 Interfacial oxide layer formation . . . 75
2.2.2.2 Diffusion of materials among the layers . . . 75
2.2.3 Uncertain interfacial termination . . . 76
2.3 Electromigration and bias-crafting . . . 78
2.4 Defect-induced magnetism . . . 79
2.5 Conclusions . . . 80

**II Experimental realization 83**

**3 Sample growth techniques and development 85**
3.1 Ultra-high vacuum pumping systems . . . 85
3.2 Substrate preparation . . . 86
3.3 Sputtering . . . 88
3.3.1 The hybrid System sputtering . . . 88
3.3.2 Nancy Sputtering . . . 92
3.4 Evaporation . . . 93
3.5 Pulsed laser deposition . . . 93
3.5.1 Reflection high-energy electron diffraction . . . 94

**4 From samples to devices 95**
4.1 In-situ pattering . . . 95
4.2 Optical lithography . . . 97
4.2.1 Lithography mask . . . 98
4.2.2 Photoresists . . . 101
4.2.2.1 Positive photoresist - S1805 . . . 101
4.2.2.2 Negative photoresist - AZ5215 . . . 101
4.2.3 Processing . . . 102
4.2.3.1 Photoresist deposition and its detouring . . . 102
4.2.3.2 STEP I - Pillar definition . . . 102

4.2.3.3 STEP II - Lower electrode definition . . . . . . . . . . 105
4.2.3.4 STEP III - Passivation layer deposition . . . . . . . . 106
4.2.3.5 STEP IV - Metallization . . . . . . . . . . . . . . . . . 108
4.3 Resistance probing and contact modes . . . . . . . . . . . . . . . . . 109
4.3.1 Two-point measurement of the contacts . . . . . . . . . . . . . 110
4.3.2 Four-point junction study . . . . . . . . . . . . . . . . . . . . . . 110
4.3.3 Resistance-Area products . . . . . . . . . . . . . . . . . . . . . . 111
4.4 Diamond saw cut . . . . . . . . . . . . . . . . . . . . . . . . . . . . . 112
4.5 On-chip mount and wire-bonding . . . . . . . . . . . . . . . . . . . . 113

**5 Device study apparatus and techniques 115**
5.1 "FERT" setup capabilities . . . . . . . . . . . . . . . . . . . . . . . . 115
5.2 Experimental determination of the barrier potential landscape . . . . 116
5.2.1 Direct I-V characteristics analysis . . . . . . . . . . . . . . . . 116
5.2.2 $\hat{g}$ method . . . . . . . . . . . . . . . . . . . . . . . . . . . . . 116
5.2.3 $\hat{I}$ method . . . . . . . . . . . . . . . . . . . . . . . . . . . . . 117
5.2.4 Voltage-temperature dependency maps . . . . . . . . . . . . . 117
5.3 Optical studies . . . . . . . . . . . . . . . . . . . . . . . . . . . . . . 117

## III Device study 119

**6 Transition metal oxides 121**
6.1 Strontium titanate . . . . . . . . . . . . . . . . . . . . . . . . . . . . 121
6.1.1 STO optical activity . . . . . . . . . . . . . . . . . . . . . . . . 121
6.1.2 $CoFe_2/SrTiO_3/CoFe_2$ . . . . . . . . . . . . . . . . . . . . . . 124
6.2 Titanium dioxide . . . . . . . . . . . . . . . . . . . . . . . . . . . . . 129
6.2.1 $CoFe_2/TiO_2/CoFe_2$ . . . . . . . . . . . . . . . . . . . . . . . 129
6.2.2 $Co/TiO_2/Co$ . . . . . . . . . . . . . . . . . . . . . . . . . . . . 134
6.3 Conclusions and move towards LSMO . . . . . . . . . . . . . . . . . 135

**7 Magnesium oxide 139**
7.1 Barrier studies . . . . . . . . . . . . . . . . . . . . . . . . . . . . . . . 139
7.1.1 Optical activity . . . . . . . . . . . . . . . . . . . . . . . . . . . 139
7.1.2 Electrical measurements . . . . . . . . . . . . . . . . . . . . . . 140
7.2 Fe/MgO/Fe . . . . . . . . . . . . . . . . . . . . . . . . . . . . . . . . 145
7.3 CoFeB/MgO/CoFeB . . . . . . . . . . . . . . . . . . . . . . . . . . . 147
7.3.1 General properties . . . . . . . . . . . . . . . . . . . . . . . . . 147
7.3.2 Analysis of the V,T parameter space . . . . . . . . . . . . . . . 154
7.3.2.1 TMR in (V,T) space . . . . . . . . . . . . . . . . . . . . 155
7.3.2.2 The annealed system . . . . . . . . . . . . . . . . . . . 158
7.3.2.3 The non-annealed system . . . . . . . . . . . . . . . . 164

**IV Conclusions and perspectives** 169

**8 Summary** 171
8.1 Transition metal oxides . . . 171
8.2 Magnesium oxide . . . 172

**9 Roadmap** 175
9.1 Transition metal oxides . . . 175
9.2 Magnesium oxide . . . 175
9.3 Optical access . . . 176

**Bibliography** 179

# Résumé en français

L'électron fût au cœur de révolutions technologiques qui modifièrent profondément la société dans la deuxième moitié du siècle précédent, avec notamment l'avènement de l'ordinateur personnel et l'apparition de nouveaux moyens de communication. Jusque récemment, deux propriétés intrinsèques de l'électron furent utilisées dans ces différentes technologies : i) la charge de l'électron, utilisée dans tout les dispositifs d'électroniques classiques, contrôlée au moyen d'un champ électrique et ii) son spin, utilisé à travers ses manifestations macroscopiques, pour des enregistrements magnétiques par exemple. Cependant ces deux propriétés n'avaient jamais été utilisées en association pour accomplir un but précis. C'est précisément à ce croisement qu'intervient la spintronique : son objectif est de modifier le mouvement des électrons, et donc la conduction électrique, en agissant sur le spin à l'aide d'un champ magnétique extérieur.

Bien que le spin de l'électron soit connu et étudié depuis de nombreuses années, jusque très récemment son utilisation en terme d'application à été négligé. En 1988, la découverte de la magnétorésistance géante (GMR) par Albert Fert, et indépendamment par Peter Gruenberg, à rapidement attiré l'attention de la communauté scientifique sur le transport électronique dépendant du spin dans des matériaux consistant en une succession de fines couches ferromagnétique et non magnétique (F/NF/F) d'épaisseurs nanométriques. Dans de tels systèmes, il est possible de changer la résistance en modifiant la configuration de l'aimantation des électrodes ferromagnétiques (d'un état parallèle P, à un état antiparallèle AP) en appliquant un champ externe par exemple. En 1995 Moodera a observé un changement de résistance encore plus important dans des structures composées d'électrodes ferromagnétiques séparées par une fine couche de matériau non conducteur. De telles structures sont appelées des jonctions tunnels magnétiques (JTM). Le changement de résistance dans ces systèmes à été appelé la magnétorésistance tunnel (TMR), car les électrons sont transférés d'une électrode à une autre par effet tunnel. La magnétorésistance est définie comme la variation relative de la résistance entre l'état parallèle et antiparallèle : $TMR = (R_{AP} - R_P)/R_P$.

L'origine de la magnétorésistance (MR) dans les JTM provient de la différence de densité d'états (DOS) à l'énergie de fermi entre population de spin « up » et « down » dans les matériaux ferromagnétiques. Cette différence est caractérisée par la polarisation de spin définit par $P = (N_\uparrow - N_\downarrow)/(N_\uparrow + N_\downarrow)$. Si nous supposons la

conservation de spin lors du transport, un électron peut passer par effet tunnel à travers la barrière seulement si un état possédant le même spin est accessible dans la deuxième électrode. La densité d'état accessible pour un électron varie avec la configuration relative de l'aimantation des électrodes, parallèle ou antiparallèle, et conduit à une différence de résistance entre ces deux états.

Avec l'amélioration des techniques expérimentales, il est possible aujourd'hui de fabriquer des JTM totalement épitaxiées. Dans ces systèmes les atomes sont empilés de manière ordonnée et les électrons peuvent être décrits par les fonctions d'onde de Bloch. De plus la théorie des groupes permet de classer ces électrons en fonction des symétries des orbitales occupées. Les symétries des fonctions d'onde de Bloch jouent un rôle important dans le transport tunnel dans les systèmes épitaxiés, i) le fait que la barrière soit elle aussi cristalline permet de conserver la symétrie des électrons lors du transfert à travers la barrière, on parle de transport électrique cohérent ; ii) les différentes symétries des fonctions d'onde de Bloch sont atténuées de manière différente dans la barrière. Il est ainsi possible de filtrer les différentes symétries dans la barrière et de concentrer le transport sur des symétries totalement polarisées à l'énergie de Fermi. D'importantes valeurs de MR peuvent ainsi être obtenues. Les JTM avec des barrières composées de MgO et $SrTiO_3$ sont des candidats potentiels pour la prochaine génération de dispositifs spintroniques.

En 2001 des travaux théoriques ont prédit des valeurs de magnétorésistances de plus de 1000% dans les systèmes totalement épitaxiés du MgO. Bien que ces prédictions aient été validées expérimentalement, il existe encore de fortes différences entre les valeurs prédites et les résultats expérimentaux. Cette différence est principalement du au fait qu'il est extrèmement difficile de créer un système parfait expérimentalement, et plusieurs phénomènes sont responsables des relativement faibles valeurs de MR obtenues. Des phénomènes d'oxydations et de diffusions sont à l'origine de l'apparition de couches supplémentaire aux interfaces qui peuvent avoir des effets indésirables et aussi réduire la magnétorésistance. Les défauts dans la barrière cristalline peuvent également avoir un impact indésirable sur la magnétorésistance. En effet ces défauts réduisent la hauteur moyenne de la barrière et créent des canaux de conduction pour les électrons indépendamment de leurs symétries.

Comprendre la physique des défauts dans les JTM est donc très important. En effect, cela peut permettre de créer des jonctions de meilleures qualités avec des propriétés optimisées et ainsi se rapprocher des valeurs théoriques. Mais il est également possible d'utiliser ces défauts pour créer des dispositifs possédant de nouvelles fonctionnalités, comme des jonctions avec des propriétés memristives par exemple. Il existe différentes méthodes pour étudier les défauts dans les JTM. Les mesures de magnéto-transport en température permettent d'accéder aux hauteurs de barrière aux interfaces, ainsi qu'à d'autres phénomènes thermiquement activés. Des mesures optiques permettent également d'obtenir de précieuses informations sur le type de défauts. Cette thèse a pour objectif d'ouvrir la voie à la compréhension de l'impact des défauts sur le transport tunnel dans les JTM cristallines.

Des jonctions tunnels avec des barrières de MgO et $SrTiO_3$ ainsi que des échantillons contenant seulement des barrières furent fabriqués par pulvérisation cathodique et par PLD (pulsed laser deposition). Certains des échantillons ont été fabriqués en collaboration interne avec d'autres départements à l'IPCMS, notamment le DCMI pour les dépositions PLD, ou en collaboration externe, avec notamment Michel Hehn du département P2M de l'institut Jean Lamour de Nancy pour des échantillons CoFeB/MgO/CoFeB.

Des expériences effectuées sur des JTM fabriquées par pulvérisation cathodique avec des barrières de MgO montrent que certain types de défauts dans la structure cristalline de la barrière peuvent être éliminés en fabriquant les échantillons dans certaines conditions de dépôt. Des barrières MgO(001)//MgO(50nm) ont été fabriquées avec différent taux d'oxygènes du dépôt, et des expériences optiques ont été effectuées. Les résultats montrent qu'une augmentation du ratio oxygène/argon à pour effet de réduire les pics d'absorption à des énergies qui correspondent aux absorptions optiques de défauts pièces.

Les pics d'absorption à 4.2 eV correspondent à la combinaison de deux lacunes d'oxygène (centres $F_2$), les pics à 5 eV correspondent à une lacune d'oxygène neutre ou ionisée ($F$, $F^+$), tandis que les pics à 5.6 eV correspondent à une lacune d'oxygène doublement ionisée ($F_2^+$). Les pics résultant des centres $F/F^+$ disparaissent du spectre d'absorption pour un cristal de MgO déposé dans une atmosphère composée de 10% d'oxygène et 90% d'argon. Ces résultats suggèrent la disparition de ces défauts dans la structure cristalline.

Afin de confirmer cette hypothèse, des échantillons Fe(20nm)/MgO(1.2nm) furent fabriqués avec des ratios oxygène/argon de 0% et 10%. Des expériences de C-AFM montrent que la couche de MgO ultrafine possède moins de « hotspots », points plus conducteurs, lorsque l'atmosphère est enrichie en oxygène. Il a été vérifié que ces résultats ne sont pas liés à des différences de topographie.

La disparition des pics $F/F^+$ du spectre d'absorption et l'amélioration des propriétés des échantillons correspondants conforte l'idée selon laquelle les centres $F$ sont responsables de la majorité du transport électronique dans la barrière de MgO dû aux défauts. Pour confirmer ceci, des courbe courant-voltage ont été mesurées sur les deux types d'échantillons. La comparaison des données pour une tension appliquée positive (correspondant à l'interface supérieure) donne des informations pertinentes sur la présence des défauts et leur impact sur le transport tunnel. La hauteur de barrière passe de 0.9eV à 2.3eV-4.1eV dans l'arrière-plan et de 0.4eV à 1.1eV sur les « hotspots ». Si on assume que l'énergie de Fermi se trouve au milieu du gap du MgO alors la hauteur effective de la barrière serai de 1eV, à cause de centres $F$ et $F^+$ situés à 5eV dans la barrière. De plus, la disparition du pic de conductance à 0.9eV dans les courbes I(V) sur l'échantillon fabriqué avec 10% d'oxygène confirme bien que la conductance excessive du MgO provient des sites $F$ et $F^+$ qui sont éliminés dans ces conditions de dépôt.

Plusieurs échantillons ont été fabriqués en collaboration avec l'institut Jean La-

mour de Nancy. Les premiers échantillons sont des hétérostructures du type CoFeB/MgO/CoFeB, sur lesquelles des mesures de magnéto-transport ont été effectuées. Le second type d'échantillon concerne des hétérostructures ne possédant pas de contre électrode (la barrière de MgO est alors la dernière couche de la structure). Des mesures de photoluminescence ont été effectuées dans le but de déterminer l'impact du recuit sur le transport électronique à travers de telles jonctions. Pour chaque type d'hétérostructures, des échantillons recuits à 300°C ainsi que des échantillons non recuits ont été étudiés et comparés.

Les pics observés lors de mesures de photoluminescence effectuées à différentes longueurs d'onde permettent de déterminer l'énergie des défauts introduits pas des lacunes d'oxygène dans la barrière. Ces observations sont en accord avec d'autres travaux/études présentes dans la littérature. La fabrication de jonctions tunnel magnétique a été effectuée avec par un protocole de lithographie standard. Les jonctions ainsi obtenues, présentent un produit RA uniforme, ce résultat suggère que l'échantillon est globalement homogène. Les mesures magnétiques effectuées à température ambiante sont cohérentes avec les mesures de magnétisation effectuée à l'aide d'un SQUID. Dans le cas des échantillons non recuits, l'état antiparallèle n'est pas bien défini, résultant en un signal TMR faible. En revanche, sur les échantillons recuit, l'état antiparallèle est bien définit, et la MR observée est de plus de 100% (dans ce cas, il faut également prendre en compte la cristallisation de la barrière lors du recuit). De plus, nous observons sur les échantillons non recuits que la hauteur de barrière est identique dans l'état parallèle et antiparallèle, alors qu'elle est inégale dans le cas des échantillons recuits (0.7eV pour P et $>$0.8eV pour AP).

La dépendance en température de la résistance ainsi que de la magnétorésistance (MR) montrent un changement de régime à 180K dans les deux cas (recuit et non recuit), ce point sera discuter plus tard. On peut également observer un plateau à partir de 40K jusqu'aux plus faibles températures, dans les cas des échantillons recuits. La présence de ce plateau peut être attribué à l'absence de défauts. Les variations de la magnétorésistance en fonction de la tension et de la température, MR(T,V), montrent que la MR diminue plus rapidement en tension et en température dans le cas des échantillons recuits.

L'analyse des canaux de conduction thermiquement activé sur les jonctions recuites montre une diminution rapide de la MR en fonction de la température, autour de 1,1V, cette effet peut être attribué aux sites $F$ et $F^+$. Afin de comprendre les phénomènes liés à l'activation thermique de la conductance ainsi que les différences de la hauteur de barrière, une étude de la variation de conductivité en fonction de la température a été effectuée (aussi appelé I chapeau ou Î). La conductivité de l'échantillon non recuit est dominée par la transmission de porteur de charges via des centres $F$, $F^+$, et $F^{+*}$, à partir 80K sa conductivité est dominé par des sites $F^{+*}$ jusque 180K, température à partir de laquelle le transport est dominé par des centres $F_2$. Pour cette raison, une diminution significative de la résistance est observée au delà de cette température. Dans le cas des jonctions recuites, l'augmentation

de la conductivité en dessous de 40K est dominée par des effets de structure de bande dans le cas AP, alors qu'aucun effet similaire n'apparait dans le cas parallèle. Ceci est une explication à la présence du plateau observé dans les R(T) ainsi que les TMR(T). Cependant, au dessus de 40K, les centres $F$ et $F^{+}$ commencent à dominer le transport et ce régime persiste jusque 150K. Au dessus de cette température, les centres $F^{+*}$ commencent à affecter le transport, résultant en une diminution rapide de la résistance et de la MR. De plus, l'impact des centres $F^{+*}$ n'est pas la même dans l'état P et AP, d'où une différence dans la hauteur de barrière dans les deux configurations.

Nous avons également obtenu des résultats intéressants dans des dispositifs possédant des barrières de $SrTiO_3$ (STO). Des jonctions $CoFe_2/SrTiO_3/CoFe_2$ ont été fabriquées par PLD. Afin d'étudier l'impact de la température de dépôt sur l'interface $CoFe_2$/STO, la structure à été fabriquée avec une électrode inférieur déposée à 300°C, tandis que la barrière à été déposée à 80°C ou 300°C (nommé échantillon « basse-T » et « haute-T » respectivement). La couche supérieure à été déposée à 80°C. Les deux échantillons ont été caractérisés, et possèdent une bonne structure cristalline. Des mesures d'AGFM à température ambiante ont été effectuées et montrent un retournement net de l'aimantation des électrodes, on remarque également que le champ coercitif est supérieur pour l'échantillon « haute-T », ce qui suggère que le dépôt de STO à température élevée augmente le taux d'oxydation de l'interface $CoFe_2$/STO.

Cette oxydation devrait avoir un impact négatif sur le transport cohérent à travers la barrière et de ce fait devrait diminuer fortement le ratio de magnétorésistance. Ceci à été confirmé en mesurant des courbes R(H) sur les deux échantillons. La TMR observé est de 3% pour l'échantillon « low-T », et aucune TMR n'a pu être observé pour l'échantillon « high-t ». Cette différence peut s'expliquer ainsi : i) Le transport tunnel est dominé pas les symétries électronique $\Delta_2$ et $\Delta_5$ à travers le STO. Dans le cas d'électrodes composées de Fer, la structure de bande pour ces symétries coupe l'énergie de Fermi pour les spins majoritaires et minoritaires, donc le filtrage reste faible. D'autre part, dans le cobalt, les bandes $\Delta_2$ and $\Delta_5$ existent seulement pour les spins minoritaires, et sont donc totalement polarisé à l'énergie de Fermi, ce qui permet d'obtenir des ratios MR importants. Pour obtenir cette polarisation, il faut que la couche çofe soit assez riche en cobalt, ce qui peut ne pas être le cas dans nos échantillons, d'où le faible ratio MR ; ii) Un autre facteur peut être la structure de la barrière à l'interface. La barrière de STO consiste en une succession alternée de couche SrO et $TiO_2$. Bien que des expériences ont confirmé une structure de barrière correct, les « marches » atomiques à l'interface sont extrèmement difficile à éviter, et le signe de la TMR peut dépendre de la couche de terminaison de la barrière de STO. Dans le système étudié, la couche à l'interface peut consister en un mélange de SrO et de $TiO_2$, dont la polarisation combinée, positive et négative, résulte en un ratio MR assez faible.

La raison pour laquelle aucune TMR n'est observée pour l'échantillon « high-

T » pourrait été la température de déposition elle-même. Au fait, la pression dans la chambre de dépôt augmente d'un ordre de grandeur, ce qui peut contaminer la surface de çofe. Cette hypothèse est corroborée par la valeur de champ coercitif plus élevé pour ces échantillons. Pour confirmer cette hypothèse, on présente les courbes I(V) pour chaque échantillon, à partir desquelles les hauteurs de barrière à chaque interface à été extraite. Une hauteur de barrière supérieure de 0.61eV pour les deux échantillons a ainsi ont obtenue, ce qui correspond bien au fait que ces interfaces ont été déposées dans les même conditions expérimentales. D'autre part, une hauteur de barrière de 0.39eV (0.51eV) à été obtenue a l'interface inférieure pour « haute-T » (« basse-T »). Ceci montre l'impact de l'oxydation de l'électrode inférieur, qui est plus importante pour l'échantillon « haute-T ». Le fait que la TMR décroît plus rapidement lorsque les électrons sont injectés à partir de l'électrode supérieure montre que l'interface supérieure soutient ici aussi l'hypothèse d un état d'oxydation plus avancé de l'électrode inférieure.

L'analyse des résultats suggère que l'amélioration des propriétés des jonctions peut être obtenue de deux façons différentes ; i) En contrôlant la terminaison de la barrière de STO, on peut assurer la dernière couche à l'interface, et ainsi éliminer les différents filtrages de symétrie dont la contribution combinée résulte en une faible valeur de TMR. Remplacer la barrière de STO avec du $TiO_2$ peut également aboutir à des résultats intéressants ; ii) L'insertion de cobalt à l'interface peut non seulement permettre d'éviter la formation d'oxyde à l'interface mais aussi augmenter le filtrage de symétrie, car les états $\Delta_2$ and $\Delta_5$ ne sont présents que pour une population de spin à l'énergie de Fermi dans le cobalt.

En conclusion, ces travaux ont montré comment la présence de défauts dans la barrière de JTM peut influencer les propriétés magnétiques et de magnéto transport de ces dispositifs. Nous montrons notamment comment contrôler la nature et la densité de ces défauts au sein de couches de MgO, et avons discuté de l'impact de ces défauts sur les hauteurs de barrière du diélectrique. Nos études sur des JTM intégrant des barrières â base d'oxydes de métaux de transition montrent la difficulté de maîtriser le degré d'oxydation des électrodes ferromagnétiques â base de métaux de transition qui composent ces JTM.

# Introduction

## Motivation

Since discovery of the electron and subsequently its practical application in the wide scientific and engineering field of what we nowadays call electronics, the spin of the electron was for a long time neglected in context of practical devices. Electronics serves humanity very well, allowing to develop at an astonishing speed compared to prior development. Obviously, computerization overtakes the duty of performing most of calculations, allowing people to perform tasks more efficiently and, interestingly, to accelerate the technological advancement even more. The global network allows humanity to access and share information almost without any physical borders and this process is still expanding. The size of a single transistor, thus its power consumption and time interval required between consecutive numerical operations is shrinking year by year, fulfilling the hypothesis raised in 1965 by Gordon E. Moore [1] which predicted that the number of transistors that can be placed on an integrated circuit would double approximately every eighteen months. This applies to the ratio between computing speed and the price as well. This hypothesis is still valid, though it is slowly approaching a scale below which classical laws of physics may not be valid anymore and quantum effects start to occur. In other words, it is not possible to miniaturize elements endlessly. At a certain moment, one has to start looking for alternative means of achieving better performances. **Spintronics** is one of such research fields.

Spintronics, i.e. *spin-electronics* is a wide field of physics and electronics that encompasses multiple subject studies worldwide taking advantage of the fact that the electron has an internal angular momentum - **spin**. The fact that in presence of magnetic field electrons with different spins may behave differently can have a crucial impact on the behavior of prototypical or even commercial devices, thus offering desired features like shorter response time, faster speeds, more error-free data processing or higher capacity.

In 1988, a new effect was observed separately by Gruenberg and Fert [2, 3]. They discovered that when a current flows through a thin structure consisting of a non-magnetic (NM) copper sandwiched between two ferromagnetic (FM) iron layers, the resistance of the system changes by a few percents when an external magnetic field

switches the relative orientation of magnetization of the electrodes from parallel (P) to antiparallel (AP). This difference in the device resistance between the P and AP configurations is nowadays called **Giant Magnetoresistance** (GMR).

The idea of the device whose resistive state could be altered by applying an external magnetic field seemed to be very promising and the GMR effect has already been applied in hard disk read heads, increasing their storage by over one order of magnitude [4]. The same effect was also applied to many magnetic field sensors.

The electron's spin may also influence properties of a device in which the metallic layer is replaced by an ultrathin insulator. Such device is called the **magnetic tunnel junction**. Beyond initial proof-of-concept experiments in the 1970s [5, 6], Moodera *et al* reported the observation of spin-polarized tunneling across an amorphous $Al_2O_3$ barrier at room temperature [7]. Interestingly, the **tunneling magnetoresistance** (TMR) amplitude of these new devices (12% at RT) was much higher than that typical of GMR systems (less than 10% at RT), and thus drew strong applicative interest.

Those results, although promising, were still limited. The TMR ratio obtained from the structures with amorphous spacers never exceeded 70% at the room temperature [8]. Calculations performed in 1997 by MacLaren *et al* on structures with ZnSe semiconducting barrier showed that epitaxial systems would yield higher values due to their specific filtering mechanisms [9]. In 2001, the theoretical calculations by Mathon and Umerski predicted up to 1000% TMR for crystalline MgO-based structures [10], shortly followed by first results of Bowen *et al* [11], Popova *et al* [12] and Yuasa *et al* [13]. This was possible due to a coherent **symmetry-preserving tunneling** of electrons through the crystalline barrier.

However, even TMR as high as 200% obtained for the systems with the MgO spacers sandwiched between the Fe or CoFe electrodes, albeit satisfactory, would not allow those structures to be used for practical applications. This is due to the practical applications requirements for which the magnetization of one of the electrodes needs to be 'pinned', thus remain fixed in space while the magnetization of the free layer is switched between parallel and antiparallel [14]. Industry spent more than a decade to create a structure of this type without any strain fields. The solution, which incorporates CoFeB electrodes yields the TMR signal up to 604% at the room temperature [15]. These issues are all presented within both theoretical and the experimental part of this thesis.

To further the ends, the field of spintronics ideally requires a source of electrons that is fully spin-polarized. The Fe/MgO accomplishes this through the filtering of appropriate electron symmetries in the course of the solid-state tunneling process. Another path is to use ferromagnets that provide electron conduction only of one spin type. This class of materials is called half-metals. Beyond initial observations [16], integration within tunnel junctions led to the observation of over 1800% TMR ratio [17]. The problem arising from using half-metals is that their outstanding properties, when integrated into magnetic tunnel junctions, vanish above the Curie

temperature of the junction interface, which lies well below the room temperature level due to the interfacial modification of the electronic structure. This is the case for the most commonly studied half-metal, the $La_{0.7}Sr_{0.3}MnO_3$ [18].

However, all of the aforementioned magnetic tunnel junction systems face a problem shared by all crystalline structures, namely **defects**. Various dislocations and vacancies in the atomic network can strongly affect the barrier properties. Being insulators, their intrinsic band gap may be filled with defect states with energies lying between the top of the valence band and the bottom of the conduction band. Their presence effectively reduces the barrier height and affects the coherent transport of electrons by promoting a hopping regime of transport. As will be presented, interfacial oxidation, substitution of sites between sublattices, atomic diffusion and uncertain termination of both barrier or electrode layers can also strongly affect the spin-polarized transport.

An ability to control the defects during the device fabrication, and monitor their activity during the tunneling process, would shine an additional light at their role in the spin-polarized transport. Concurrently, the possibility to create specific types of these defects would allow to classify their properties and potentially make an use of them in order to further enhance properties of magnetic tunnel junctions, leading to specific applications like *memristors*. In these devices, vacancies are driven by the current flow, which results in alteration of the electronic transport properties via the defect sites and consequently change the resistance of the system [19].

Defect-related research is widely acknowledged to be crucial for understanding the performance of devices based on semiconducting materials like silicon, germanium or gallium arsenide. However, the same level of defects control does not exist for oxide dielectrics even though they are considered the base for future spintronic and memristive materials. The aim of this thesis is to establish processes that lead to the defect control in magnetic tunnel junctions based on MgO, $SrTiO_3$ and $TiO_2$ barriers. We will describe the growth, characterization, junction patterning and magnetotransport results on stacks in which we focus on the nature of defect states, and their role on spin-polarized transport.

# Manuscript Organization

The first part of the thesis, called *"Theoretical Basis"* is divided in two chapters: In the first one, basics of the spin-polarized transport are explained. Within the first three sections, starting from the simple case of the spin-independent electron transport through the potential barrier, the spin-dependent picture is consecutively introduced. The Julliere model, the majority and minority electron spin populations and the local density of states concept in electrodes are explained. In section 4, the impact of Bloch symmetries on the tunnel magnetoresistance is shown using the example of the model Fe/MgO/Fe system, as it is well-understood and is a pedagogical example. Section 5 describes differences in spin-polarized transport across MgO and $SrTiO_3/TiO_2$ crystalline barriers. The sixth section introduces junctions with iron electrodes replaced by CoFe, Co, CoFeB and $La_{0.7}Sr_{0.3}MnO_3$, with a special attention given to the last two. This is due to two facts: 1) A significant part of this thesis concerns devices incorporating CoFeB electrodes and 2) half-metallic LSMO is an interesting candidate for the electrode material in magnetic tunnel junctions so fabrication of devices based on this compound was also attempted during this thesis. Section 7 introduces the LSMO/STO/LSMO system, on which the highest TMR signal was observed up to date.

The second chapter of the theoretical part describes the impact of defects in crystalline systems on spin-polarized transport. The first section concentrates on defect sites present within dielectric crystals and how they may be optically and electrically probed, whereas the second section describes the origins and consequences of imperfections present at metal/insulator interfaces. The third section discusses issues of electromigration and presents the phenomenon as a tool with which magnetic tunnel junctions may be engineered in order to alter their transport properties. The fourth section introduces defect-induced magnetism in dielectric insulators and its promising possibilities of future technological applications.

The second part, *"Experimental realization"* describes equipment, materials and procedures used for fabrication, processing and measurements of structures studied within the timeframe of this thesis. The first chapter of this second part briefly introduces several UHV pumping systems, while the second one discusses the procedure of substrate preparation for the sputtering deposition which was performed by our group. Thin films growth techniques and procedures of sputtering, evaporation and pulsed laser deposition are presented in sections 3 to 6, respectively. Various quality control systems for both fabrication and processing are also presented. As the nature of this thesis is mostly experimental and both the fabrication of samples and their processing technique development were its essential tasks, many of experimental results as well as failed attempts are presented in this section.

The second chapter of the second part (chapter 4) describes procedures to convert entire multilayers into measurable devices. Its first section describes an *in situ* shadowmask patterning technique introduced within our sputtering system during

the timeframe of this thesis. It is followed by a long section 2 that describes principles of multi-step optical lithography. Short sections 3 to 5 discuss initial probing of the processed devices, precise cutting issues and the final on-chip mount and the wire-bonding, respectively.

The third chapter of the second part (chapter 5) introduces our techniques to measure devices. Capabilities of the custom-made "FERT" setup on which most of device-related experiments were performed are presented in section 1. The second section presents experimental techniques of the barrier height determination. The third section presents properties of optical setups with which absorption and photoluminescence spectra presented in the manuscript were obtained.

The third part, *"Device study"*, presents results obtained on dielectric crystals and magnetic tunnel junctions studied within the timeframe of this thesis. The first two sections of the first chapter (chapter 6) describe results related to $SrTiO_3$ and $TiO_2$ dielectric crystals and devices based on these materials. The third section presents attempts to improve properties of these magnetic tunnel junctions by replacing their transition metal electrodes with $La_{0.7}Sr_{0.3}MnO_3$. The second chapter (chapter 7) discusses results of experiments performed on MgO barriers (section 1) and magnetic tunnel junctions in which the MgO barrier was sandwiched between two types of electrodes, i.e. the Fe/MgO/Fe systems fabricated with the shadowmask technique (section 2) and the CoFeB/MgO/CoFeB devices, on which experiments were performed in the final months of this thesis (section 3). The latter section is particularly long due to the detailed analysis of the voltage and temperature dependence of the spin-polarized conductance.

The fourth and the final part, *"Conclusions and perspectives"* is divided in two chapters - the summary and the roadmap. The first one briefly recalls experiments and results obtained on both types of devices (transition metal oxides and MgO) during this thesis in separate sections. The second one presents potential solutions of fabrication, processing and transport issues encountered during the timeframe of this thesis. Moreover, propositions of further experiments that would shine additional light on impact of structural defects on spin-polarized transport are presented.

# Part I

# Theoretical Basis

# Chapter 1

# Basics of Tunnel Magnetoresistance

The first section of this chapter describes the way electrons tunnel across the potential barrier. The second one explains origins of the non-zero spin polarization in ferromagnets. The third one uses the information from the former two, presenting a system composed of an insulator sandwiched between two ferromagnets in which the current flow is spin-polarized. The principle of operation of this system (called a Magnetic Tunnel Junction) is presented in the fourth section based on the example of the Fe/MgO/Fe system. The influence of electronic Bloch wavefunctions arising from the band structure of the materials is discussed, and theoretical calculations of transport and intrinsic features which govern it are presented. The fifth section presents properties of two crystalline barriers different than MgO, namely $SrTiO_3$ and $TiO_2$. The sixth one introduces several different electrode materials and describes why CoFeB electrodes are of interest in terms of practical applications, as well as issues related to CoFeB-based devices and differences from the Fe/MgO/Fe in terms of a spin-polarized transport. $La_{0.7}Sr_{0.3}MnO_3$ electrodes are also presented in this section. A detailed mechanism of double exchange giving rise to the half-metallic behavior and transport principles of the LSMO electrode is presented. The last section of this chapter presents the magnetic tunnel junction on which the highest TMR up to date was observed - the LSMO/STO/LSMO system.

## 1.1 From simple to epitaxial barriers

It may seem impossible from the classical point of view that one may simply walk through a wall. However, due to the wave-particle duality of matter, these things are possible in nanoscale systems for which quantum laws of physics apply. As illustrated on fig. 1.1, if one imagines an electron with energy E and wavevector **k** approaching a simple barrier with potential V, there is a finite probability that it will penetrate through the barrier with its amplitude attenuated exponentially with the barrier thickness and its decay parameter $\kappa = (2m/\hbar)(V - E)$, where $V > E$ [20].

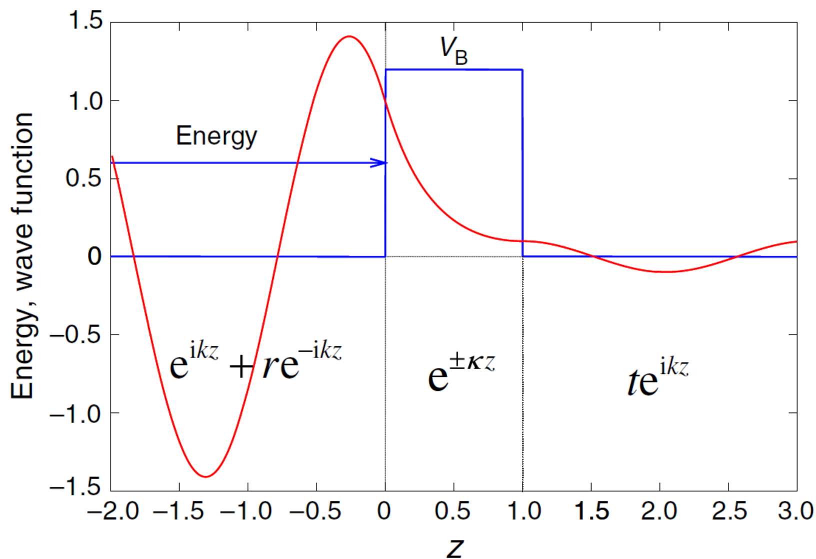


Figure 1.1: *Schematic picture of an electron tunneling through a simple barrier. The resulting conductance is related to the evanescent state of the electron and its decay parameter within the insulator. If the barrier is thin enough so its amplitude does not fall to zero, the electron may reach the other side with the probability of its wavefunction diminished. [20].*

Despite certain experiments that involve vacuum barriers (like non-contact mode of scanning electron microcopy), this thesis deals with thin-film systems in which the barrier is composed of atoms. Barriers in which these atoms are ordered are of special interest of this study. In such crystalline case, the Bloch condition for states propagating from site $\mathbf{r}$ to a neighboring site $\mathbf{r} + \mathbf{a}$ may be written as $\Psi_k(\mathbf{r} + \mathbf{a}) = c\Psi_k(\mathbf{r})$ where $c = exp(i\mathbf{k} \cdot \mathbf{a})$.

The above equation describes motion in a periodic potential with a wavevector $\mathbf{k}$, which is a real quantity for electron motion in a metal, but is imaginary when the electron traverses a semiconductor through the tunneling process. In that case, the wavefunction decays exponentially as the electron propagates through each additional layer. The electron state is then called evanescent.

When an electric bias is applied to the structure, the energy levels are driven out of the equilibrium. This is schematically shown on fig. 1.2. Simmons performed theoretical calculations on current flowing across potential barriers under different bias voltages and established well-known equations of electronic tunneling through generalized barriers [21]. His model was further extended by Brinkman, who predicted the phenomena for asymmetric barriers by adding a $\Delta\phi = \phi_{right} - \phi_{left}$ parameter [22]. As expected, the amount of current tunneling through a potential barrier increases with the applied bias, the crucial value being $V = \phi_0/e$. In order to determine parameters of an unknown barrier, one may fit its current-voltage characteristics at

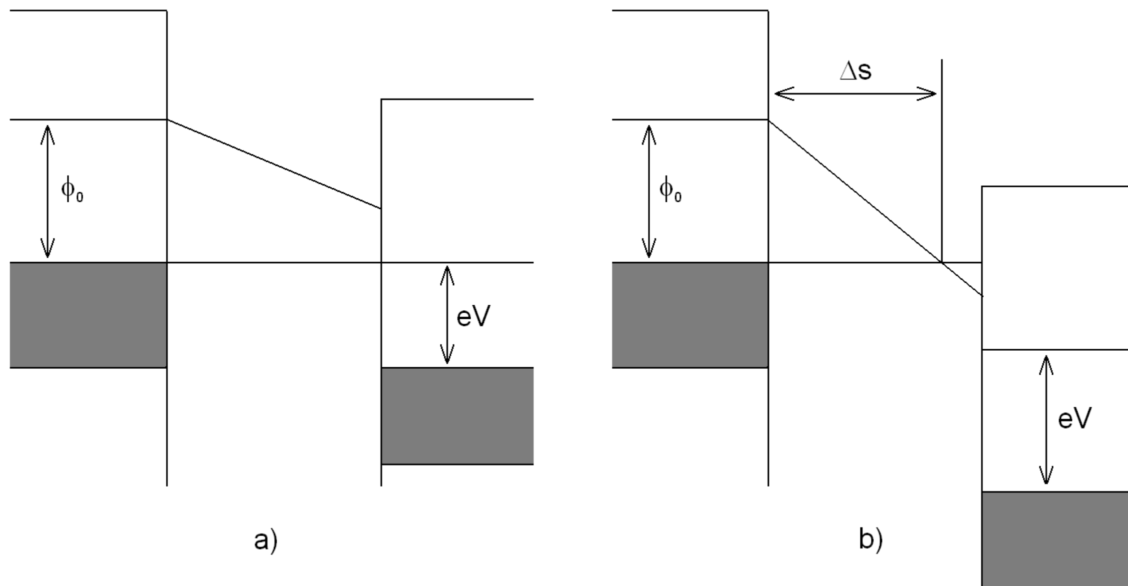


Figure 1.2: *Schematic energy diagram for a barrier under the bias $eV$ applied lower (left) and higher (right) than the barrier height $\phi_0$. Note that in the latter case, not only the barrier height is reduced, but its effective thickness $\Delta s$ as well.*

lower and higher bias according to the model of Brinkman. However, this model still suffers from disadvantages resulting from the omission of certain effects like the zero bias anomaly (section 1.4.4.1). Whenever possible, an experimental procedure called $\hat{I}$ was used in order to determine the barrier heights (see section 5.2).

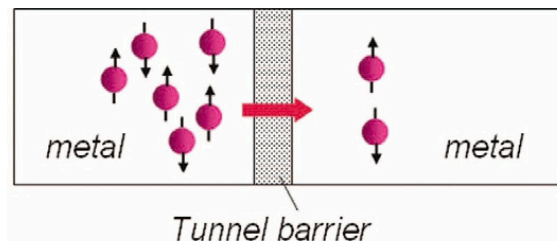


Figure 1.3: *For most tunneling systems, the electron transmission probability is independent of its spin orientation. Here, the spin polarization equals zero on both sides of the barrier. [23].*

In most of real systems, the current flow means not only one but a large number of electrons. The electron as a fermion has its spin of $1/2\ \hbar$. This value can be positive or negative, which will be called spin-up (↑) or spin-down (↓) respectively. For non-magnetic materials the amount of spin up and spin down electrons is the same and one may say the spin polarization equals zero. In such case, no transport properties depend on the spin (see fig. 1.3). The spin polarization in a material

may be described with the equation below, 'N' being number of the electrons at the Fermi level with respective ↑ or ↓ spins.

$$P = \frac{N_\uparrow - N_\downarrow}{N_\uparrow + N_\downarrow} \tag{1.1}$$

## 1.2 Non-zero spin polarization in ferromagnets

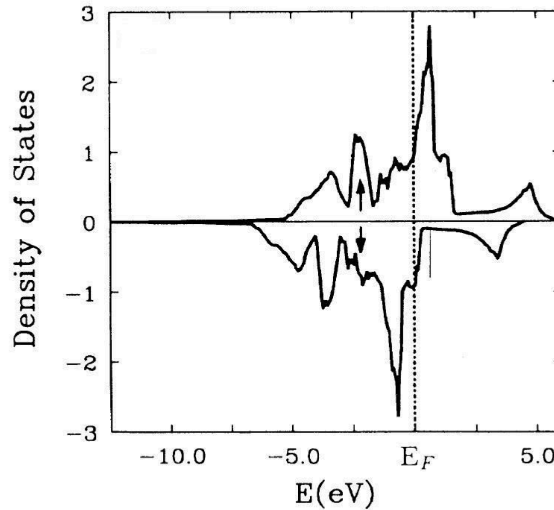


Figure 1.4: *Exchange splitting of spin density of states for Fe(bcc). Due to the exchange splitting of spin sub-bands, the DOS at the Fermi level is different for spin ↑ and spin ↓ populations (top and bottom parts respectively) [24].*

The electronic properties of materials can be represented by their band structure. When averaged over k-space, the energy dependence of the band structure yields the material's energy-dependent **Density of states** (DOS). The conductance in metals is obviously carried out by the electrons laying at the Fermi level $E_F$ or very close to it. As noted before, for non-magnetic materials the DOS distribution is equal for both spin populations so the spin polarization can be neglected. However, in materials that exhibit ferromagnetic properties, their two spin subbands are affected by the exchange splitting, as shown for the example of iron on fig. 1.4. This crucially affects the electron population at the Fermi level. The number of states available at $E_F$ for electrons with respective spins is non-equal and one may talk about a non-zero spin polarization.

At the macroscopic level, a ferromagnet is characterized by the spatial orientation of its magnetization. This magnetization reflects the fact that, due to exchange splitting, one spin subband is filled more than the other. The degree of filling depends on the ferromagnet considered. This implies that one spin population, called

the **majority** spin or spin-up population is more numerous than the other. The macroscopic magnetization of the material and the quantization axis of majority spin electrons are defined to be identical. The spin quantization axis for the **minority** or spin-down electrons, is therefore antiparallel to the magnetization axis.

## 1.3 Spin-polarized tunneling in magnetic tunnel junctions

The structure in which a few-nanometers-thick insulator is sandwiched between two ferromagnetic electrodes is called a **Magnetic tunnel junction** (MTJ). Techniques used to fabricate such systems are extensively presented in the second part of the manuscript. Here, the general information about a Ferromagnet-Insulator-Ferromagnet (FM/I/FM) system is given.

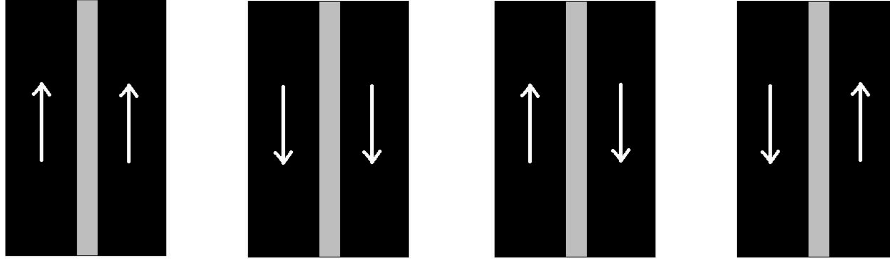

Figure 1.5: *Four different magnetization configurations of the ferromagnetic electrodes in a magnetic tunnel junction.*

If the coercive fields of the two FM layers are different, then, as an external magnetic field is ramped from a positive value through zero to a negative value, the magnetization of each FM layer will flip separately. In that case, the structure may take one of four different configurations of ferromagnets, as shown on fig. 1.5.

In absence of any symmetry breaking (e.g. induced by the exchange bias field of an antiferromagnet), the positive and negative directions of magnetization for each layer are equivalent in energy. In that case, the four presented cases of the relative magnetization of the ferromagnets can be simplified to two: **Parallel** (P) and **Antiparallel** (AP).

At the very beginning of the spintronics field timeline, Julliere proposed that electron conduction across a metallic system should be considered as occurring primarily within two spin sub-channels [25]. This means that the total conductance of the system in the P or AP configuration is the sum of the corresponding minority and majority conduction channels, i.e. $G_P = G^{\uparrow\uparrow} + G^{\downarrow\downarrow}$ and $G_{AP} = G^{\uparrow\downarrow} + G^{\downarrow\uparrow}$. Moreover, he proposed that current tunneling through each channel be proportional to its DOS at the Fermi level for both electrodes. In these terms, their spin polarization can be written as $P = (D_\uparrow - D_\downarrow)/(D_\uparrow + D_\downarrow)$. However, the two-current model

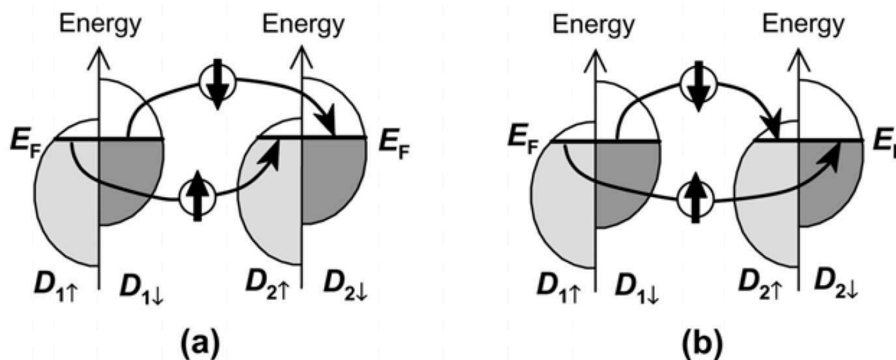


Figure 1.6: *Simple spin-conserving tunneling representation for both a) parallel and b) antiparallel FM configuration. 'D' denote densities of states of the respective electrodes; Note that in the AP configuration, the spin-up states in the magnetization referential of one electrode become spin-down states in the magnetization referential of the other, and vice versa [14].*

neglected the spin-orbit interaction, which was further extended by Slonczewski for the case of tunneling across magnetic tunnel junctions with an amorphous barrier [26]. The phenomena was later described in more detail for crystalline barriers by Butler and Mathon [27, 28]. The spin-conserving tunneling is schematically shown on fig. 1.6. It is important to note that these models apply to the perfect systems and do not take into account additional effects like population mixing due to the spin-flipping or collective excitations of spins known as magnons.

## 1.4 Symmetry filtering in Fe/MgO/Fe

A substantial part of this thesis is dedicated to the Fe/MgO/Fe system. MgO deposited atop the perfect Fe monocrystal grows crystalline, however rotated by 45° as the MgO lattice constant is roughly $\sqrt{2}$ larger than that of Fe (2.886Å) (fig. 1.7). The lattice mismatch is around a few percent, which is not enough to distort the MgO crystal [29]. It is also theoretically well-understood structure that can serve as a pedagogical model to describe the spin-polarized tunneling through the magnetic tunnel junctions. Thus, this section presents the impact of Bloch wavefunctions and band structures on the tunneling-induced filtering of electrons with a particular symmetry across the Fe/MgO/Fe magnetic tunnel junctions.

### 1.4.1 Electronic Bloch wavefunctions

In crystalline systems, which are exclusively studied within this thesis, the atom-generated periodic potential felt by the electron as it traverses the lattice depends on the direction of propagation within the lattice. Thus, both in the barrier and in

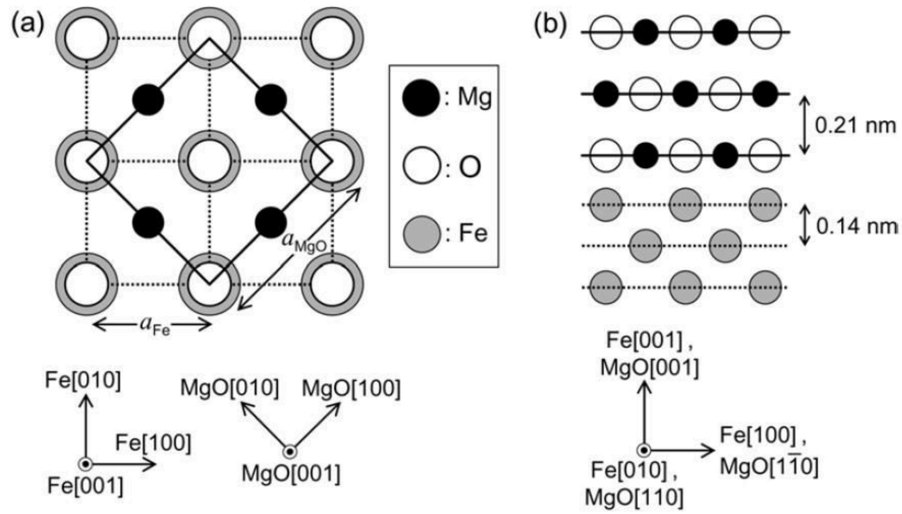


Figure 1.7: *a) Top and b) cross-sectional view of the MgO grown atop the Fe monocrystal. Vectors below denote crystalline orientations of both materials [14].*

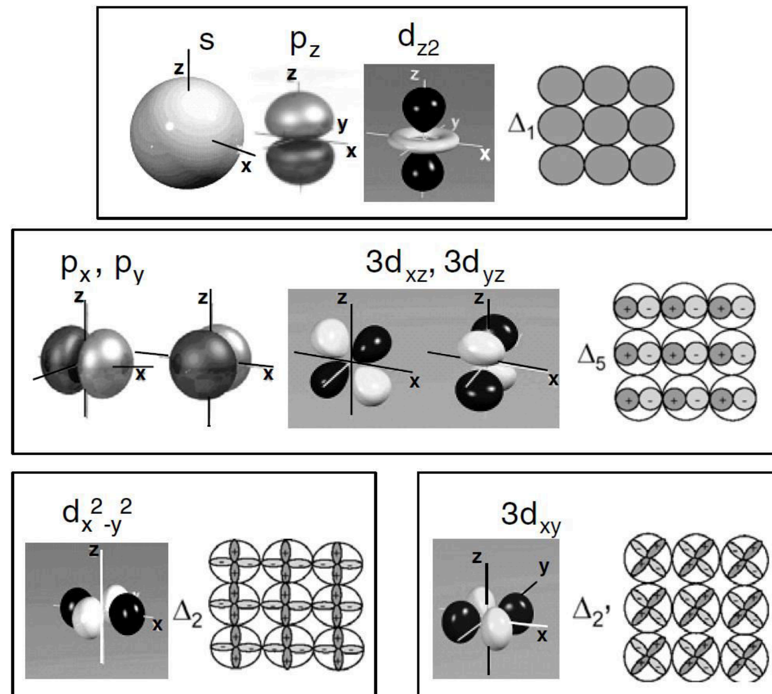


Figure 1.8: *Atomic-like orbitals grouped by symmetry properties in the direction of propagation. Their transverse nodes are schematically drawn on the right of each symmetry [30].*

the electrodes, the electrons can be described with their components of the Bloch wavevectors, parallel to the interfaces, i.e. perpendicular to the direction of propaga-

tion: *spd*- *pd*- and *d*-like, usually called $\Delta_1$, $\Delta_5$ and $\Delta_2/\Delta_{2'}$, respectively. Depending on the band structure of the material (either metal or insulator), electrons with specific transverse modes (symmetries) undergo their respective scattering rates. For this reason one may speak about specific conduction channels (fig. 1.8).

## 1.4.2 Band structures impact

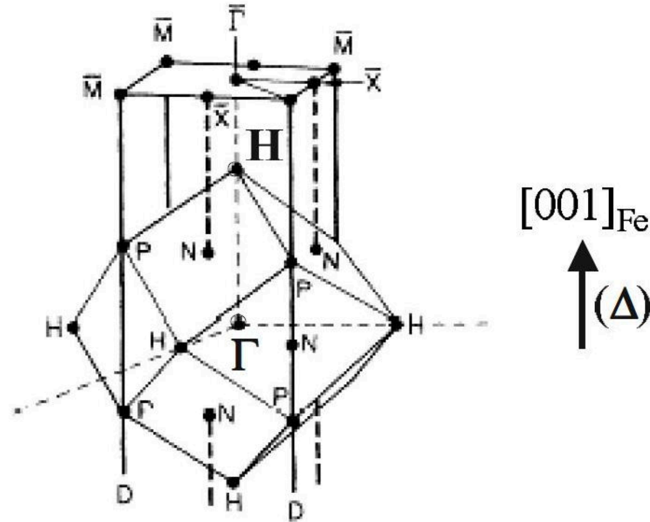


Figure 1.9: *Bcc Fe(100) bulk Brillouin zone with high symmetry points denoted. The* $\Gamma - H$ *is the direction of the propagation of electrons. The (001) surface zone is also drawn on the right with the* $\overline{\Gamma} - \overline{X}$ *direction specified [30].*

In order to understand the impact of electrode and barrier band structures on the spintronic response of the Fe/MgO/Fe system, a Brillouin zone for *bcc* (base-center-cubic) system is presented on fig. 1.9. In *bcc* systems like Fe/MgO/Fe, electrons are made to propagate along the Γ−H direction thanks to an external applied electric field.

### 1.4.2.1 Magnesium Oxide

The general reason for using crystalline barriers is their ability to preserve the symmetries of electrons during the transport. This *Coherent transport* is the main advantage over amorphous insulators like $Al_2O_3$, in which intermixing of symmetries within the barrier results in their poor filtering by the collector (fig. 1.10a). In the case of a crystalline barrier (fig. 1.10b shows the MgO case), electrons of each symmetry undergo their respective symmetry-dependent attenuation within the barrier.

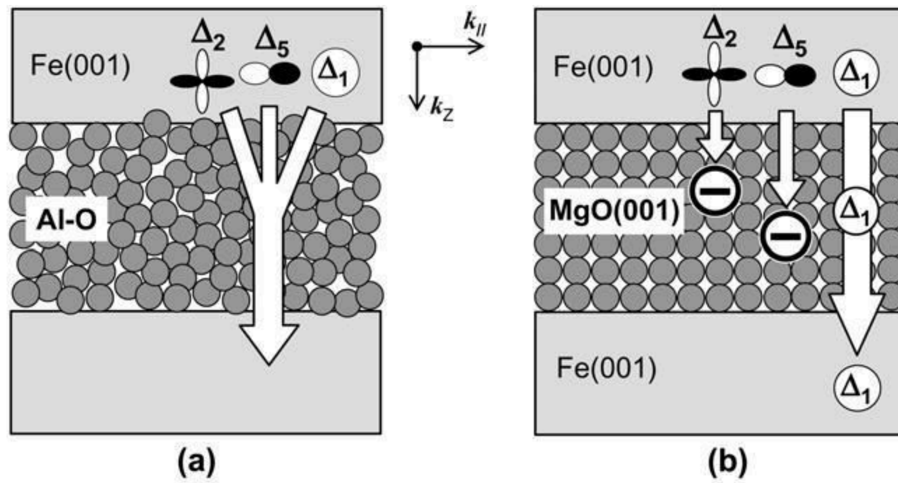


Figure 1.10: *Schematic comparison of a) an incoherent tunneling through the $Al_2O_3$ amorphous barrier and b) a coherent transport trough the crystalline MgO. [14].*

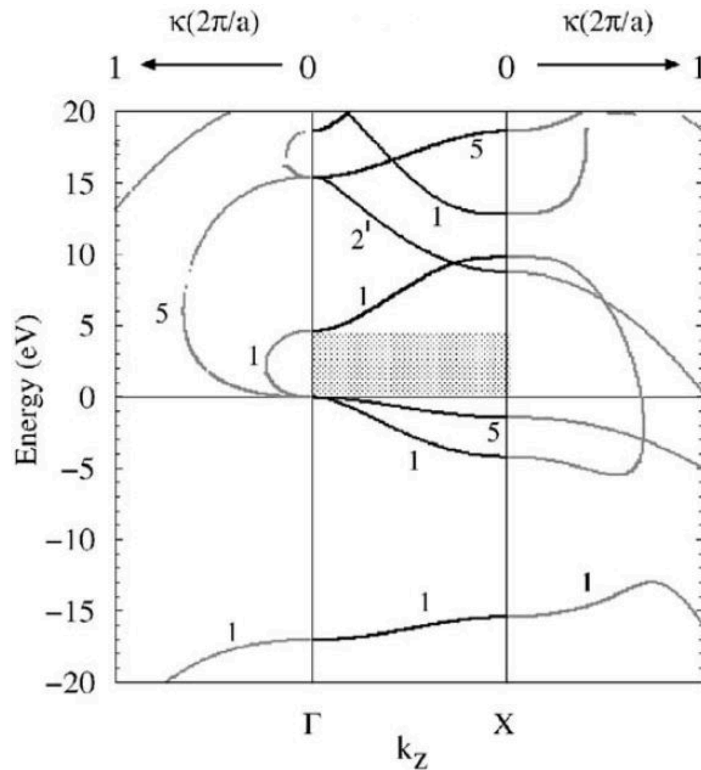


Figure 1.11: *Real (center) and complex (sides) band structure of [001] MgO. Numbers denote respective Δ electronic symmetries [31].*

As mentioned in section 1.1, wavefunctions become complex when tunneling occurs. In order to understand the mechanism of decay within the insulator, one has

to look at its complex band structure. This structure, calculated for the MgO crystal along with contributions of its respective electronic symmetries, is shown on fig. 1.11 [32, 33]. The essential concept of the complex band structure is the interfacial matching of wavefunctions at the boundary of the two crystals, which in case of the metal-insulator interface are metal-induced gap states (MIGS). These states are itinerant in the metal but decay exponentially in the insulator due to presence of the band gap, forming the complex band structure of the insulator [31] (the aforementioned evanescent states). Their key parameter is the decay parameter $\kappa$ [20], whose dispersion is plotted as as a function of energy across the band gap of the semiconductor. The complex band which connects the $\Delta_1$ valence and conduction real bands is smaller than any other and it does not extend towards the higher values of the decay parameter $\kappa$ that drives the transmission probability ($e^{-2\kappa d}$). This implies that it is the $\Delta_1$ state that has the lowest decay rate. Thus, for a current encompassing all symmetries that impinge on the MgO tunnel barrier, most of the current tunneling across the barrier is effectively of the $\Delta_1$ symmetry. For the Fermi level lying in the center of the gap, there is only one ($\Delta_1$) $\kappa$ evanescent state that connects conduction and valence bands symmetrically. $\kappa$ of the $\Delta_5$ band is second to that of $\Delta_1$, thus it decays within the barrier faster. The $\Delta_{2'}$ complex band extends further towards high $\kappa$ values so electrons of the $\Delta_{2'}$ symmetry will contribute to the tunneling current much less than these of $\Delta_1$ and $\Delta_5$ symmetries.

Note that the case presented concerns the MgO crystal. The analysis of the complex band structure needs to be performed for each type of the oxide barrier in order to determine its attenuation rates for specific symmetries, as will be shown in section 1.5 for barriers different than MgO.

#### 1.4.2.2 Iron

Let's take a look at the band structure of the bcc Fe ferromagnet for both spin populations (fig. 1.12). Along the $\Gamma-$H (i.e. (100)) electron propagation direction, one can see that states with certain wavefunction symmetries exist at the Fermi level only for one of the spin populations. This is particulary true for $\Delta_1$ and $\Delta_2$, whose bands cross Fermi level exclusively for majority or minority spin channel, respectively. The $\Delta_{2'}$ and $\Delta_5$ symmetries cross the $E_F$ for both spin populations so they do not give rise to spin polarization of the current, as they provide current flow in any relative orientation of the ferromagnets.

Electrons tunneling across a perfectly crystalline system conserve both their spin and symmetry. In each of the P and AP configurations, the total system conductance is the sum of conductances resulting from electrons tunneling via both majority and minority channels, which are in turn the sums of conductances of all symmetries available in these channels. Thus, following fig. 1.12, the total conductance in the P state is the sum of $\Delta_1$, $\Delta_{2'}$ and $\Delta_5$ in the majority channel and $\Delta_2$, $\Delta_{2'}$ and $\Delta_5$ in the minority channel, respectively. In the AP state, for which majority (minority)

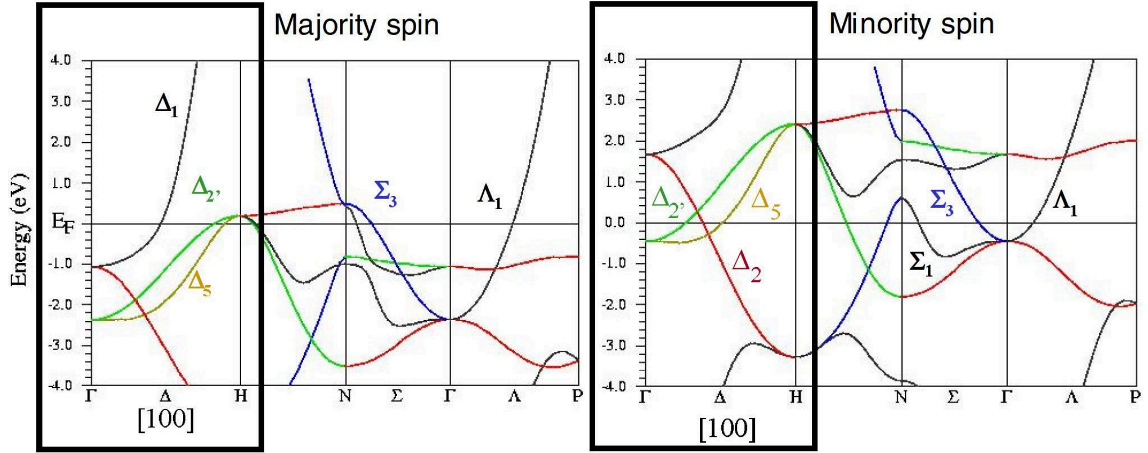


Figure 1.12: *Exchange split band structure in bcc Fe for both majority and minority spin. The $\Gamma - H$ is highlighted. $\Sigma$ and $\Lambda$ denote (110) and (111) propagation directions in the real space, respectively [30].*

electrons from the injecting electrode tunnel into available states in the minority (majority) channel within the collecting electrode, the total conductance is the sum of $\Delta_{2'}$ and $\Delta_5$ in both *majority-to-minority* and *minority-to-majority* channels. The absence of the tunneling of $\Delta_1$ and $\Delta_2$ symmetry electrons in the antiparallel case yields a significant difference between P and AP configurations of the system. Thus, the band structure of the ferromagnetic electrodes is yet another property of the magnetic tunnel junctions that is responsible for the symmetry filtering.

### 1.4.3 Transport calculations

Butler *et al* performed calculations for the Fe/MgO/Fe system and described a tunneling behavior of all the separate conduction channels. They are presented in figure 1.13. One can see that the moderately decaying $\Delta_5$ symmetry is present in all the cases. States capable of injecting (left electrode) or collecting (right electrode) electrons with $\Delta_5$ symmetry exist at Fermi level for both majority and minority populations of iron. The same applies to the $\Delta_{2'}$ channel, yet due to its high decay rate, it is not able to effectively tunnel across the barrier.

The crucial difference lies in presence or absence of the $\Delta_1$ symmetry and, to a lesser extent, the $\Delta_2$. The $\Delta_1$ is the slowest decaying channel which implies its responsibility for most of the total conductance. However, this symmetry does not have states at the Fermi level among the minority population so it cannot be injected into the barrier from the minority population of the injector. On the other hand, in the antiparallel configuration $\Delta_1$ spin-up electrons tunnel towards $\Delta_1$ spin-down states in the collecting electrode. Since there are no available $\Delta_1$ spin-down states, they continue to tunnel in absence of spin- or symmetry-scattering. Similarly,

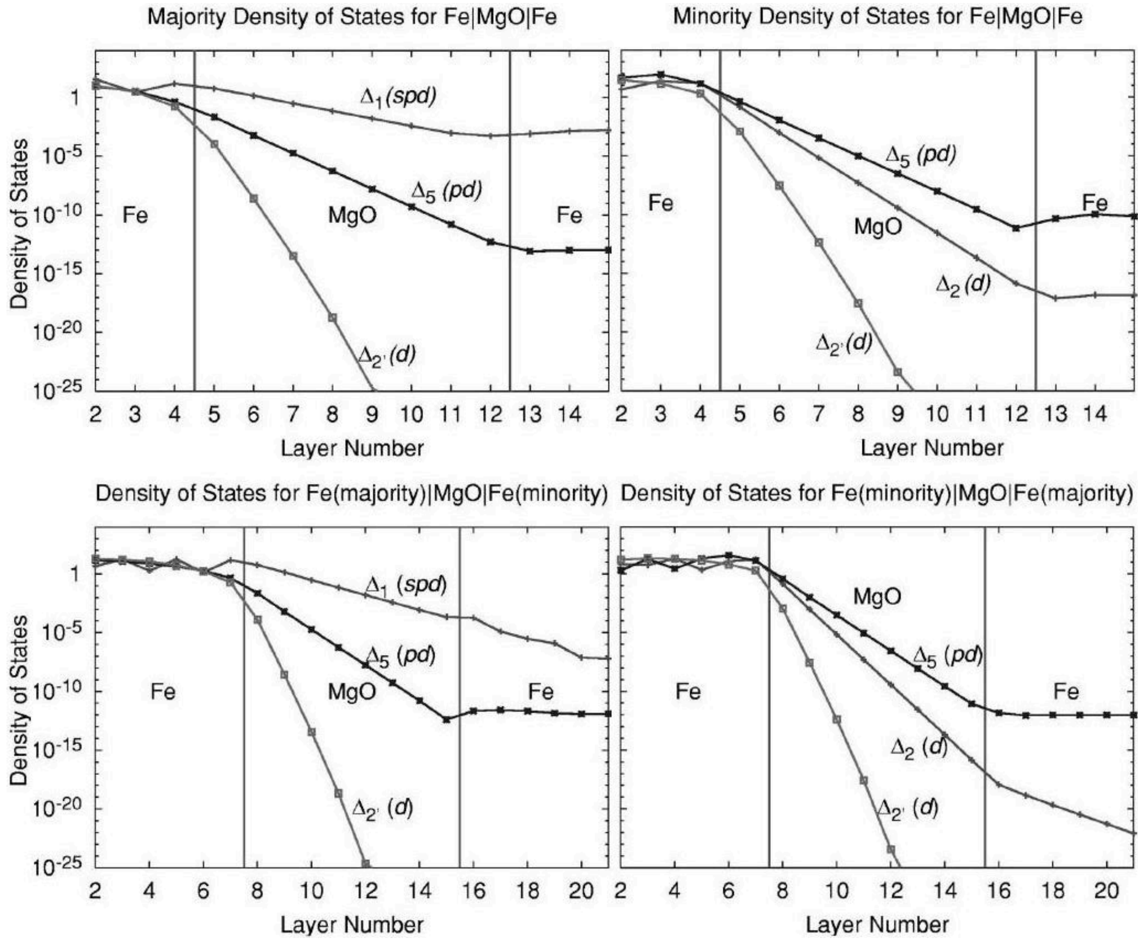


Figure 1.13: *Tunneling DOS (TDOS) for Fe(100)/MgO/Fe(100) system with the MgO barrier being 8 monolayers thick. The top two graphs show tunneling in the parallel state, the left one for majority and the right one for minority spin populations. The bottom graphs depict the antiparallel configuration consisting of tunneling from majority to minority states (left panel) and from minority to majority states (right panel). Additional outer Fe layers are drawn in the antiparallel configuration to show how, in absence of spin and symmetry decoherence, tunneling beyond the MgO barrier can occur in the collecting metal layer as well if a symmetry is absent. Each TDOS is labeled by the symmetry of the incident Bloch state at the Fermi level of the injector. Note that the density of states scales are logarithmic [27].*

minority $\Delta_2$ states injected into the barrier are accepted at the collector in the P configuration, but 'rejected' (i.e. they continue to decay) in the AP state.

By simply summing up all the symmetry channels measured at the end of the collector for both parallel and antiparallel configurations, one may clearly see the difference between conductances in both P and AP configurations. This difference, most often shown as the difference in resistances, is called the **Tunnel Magnetore-**

**sistance** (TMR) and described with the following formula:

$$TMR = \frac{G_P - G_{AP}}{G_{AP}} = \frac{R_{AP} - R_P}{R_P}[\%] \tag{1.2}$$

$G$ and $R$ are the conductance and resistance of the system in the parallel (P) and antiparallel (AP) configurations, respectively.

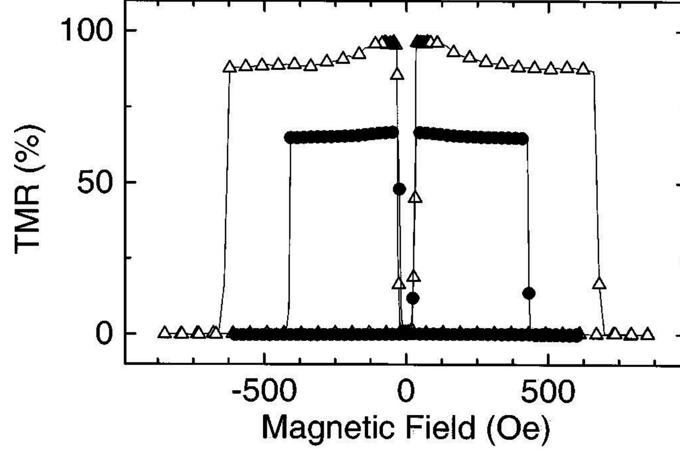


Figure 1.14: *Tunnel magnetoresistance ratio versus applied magnetic field reported on 65x95 $\mu m^2$ Fe/MgO/Fe junctions with 2.5 nm thick MgO barrier at room temperature (full circles) and 80K (empty triangles) obtained by Faure-Vincent* et al. *[34].*

Fig. 1.14 shows a typical resistance versus applied field curve (RH). The magnetic field H is applied along the easy magnetization axis of the Fe layers so as to achieve AP state. The easy axis is in plane, therefore the field is applied in plane, which is perpendicular to the direction of current flow. One may see that, starting with the high negative field, the relative magnetization of the ferromagnets is parallel (both aligned along the negative field lines) and the resistance of the system is low. A reduction of the field strength to 0 does not affect the magnetization of the system until the value reaches positive 40 Oe when one of the ferromagnets switches its magnetization and aligns along the positive field. The relative orientation of electrode magnetization becomes antiparallel and the overall system resistance increases. The magnetization of the second electrode remains unchanged at this point due to its higher coercivity. Increase of the magnetic field strength towards higher positive values causes the magnetization of the second electrode to flip as well and the configuration becomes parallel again (however this time aligned along the positive field direction) resulting in the initial low resistance again. The mirror-like behavior occurs on the return sweep of the field from positive towards negative values.

As the $\Delta_1$ symmetry electrons are very weakly attenuated within the MgO barrier, the absence of states with this symmetry within the minority spin channel

drastically reduces its total conductance and even presence of additional, strongly attenuated $\Delta_2$ symmetry states does not compensate the former 'loss'. As one may conclude from the fig. 1.13, the difference between majority and minority channel conductances (and so the TMR ratio) increases with the barrier thickness, as the $\Delta_{2,2'}$ and $\Delta_5$ symmetries decay much faster than the $\Delta_1$. The sample thickness, however, cannot be increased unlimitedly and while reaching a few nanometers the decay across layers becomes so high that transport may be realized only across defect sites which in turn disturbs its coherency. The incidence of these defects on transport across magnetic tunnel junctions will be discussed in the 2 section. However, even perfectly crystalline system contain certain intrinsic features which negatively affect its spin-polarized tunneling.

### 1.4.4 Intrinsic issues

#### 1.4.4.1 Zero bias anomaly

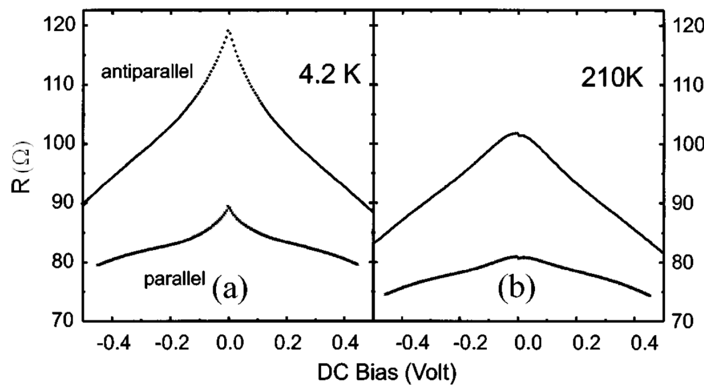


Figure 1.15: *Resistance dependence on applied bias of Co/$Al_2O_3$/CoFe magnetic tunnel junction in a) and 4.2K b) 210K for AP (top) and P (bottom) alignment. Resistance drop below 150mV is referred to the zero bias anomaly [35].*

Zhang *et al* for the first time reported an unusually high, 'anomalous' TMR decrease across $Al_2O_3$-based MTJs within small bias range up to 150mV (fig. 1.15). The effect was observed both at room temperature and at 4K, albeit much more pronounced in the latter case (especially in the AP conductance channel). As the energy scale of this *zero bias anomaly* was of the same order as that of the magnetic excitations, it was assumed that the electrons just above the Fermi level produce collective excitations of local interfacial spins which result in an additional factor in lowering the TMR signal within this bias range (the first factor being the standard barrier height lowering) [35]. The effect was for the first time observed and described for amorphous barriers, but it is commonly observed in crystalline systems as well.

#### 1.4.4.2 Interfacial resonant states

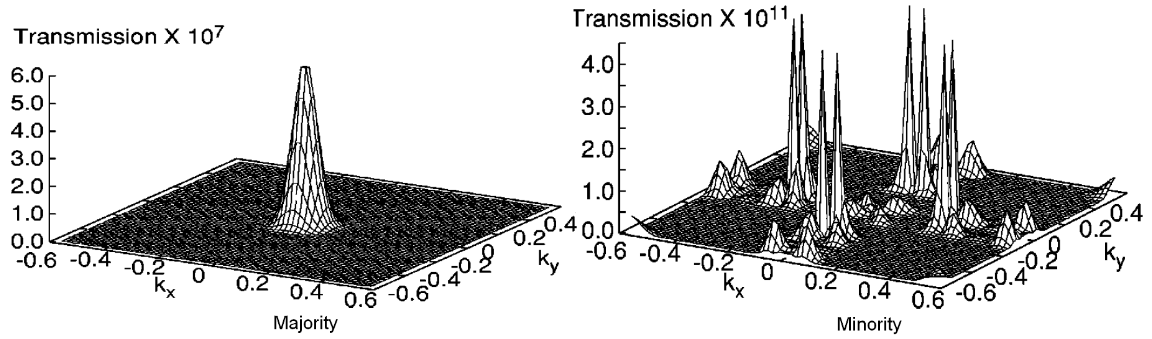


Figure 1.16: *Theoretical calculation of majority (left) and minority (right) conductance channels in Fe/MgO/Fe system with 12 monolayers thick barrier. The large peaks at* $k_{\parallel} \neq 0$ *result from interface resonant states [27].*

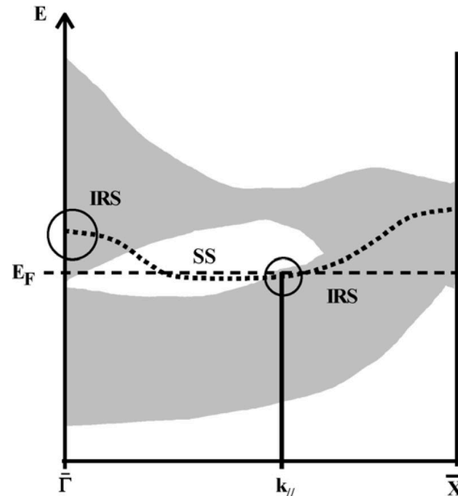


Figure 1.17: *Schematic surface energy bands dispersion for minority spin channel in Fe(001). The grey zone depicts the bulk bands, whereas the dash line is the dispersion of surface states (SS). When the two overlap, they form interfacial resonant states (IRS) and contribute to the transport towards the bulk (example circles). [36].*

Calculations performed by Butler *et al* [27] show that, even though minority channel conductance across MgO-based devices is much lower than the one of the majority, it is dominated by large peaks away from the $k$ normal to the barrier 1.16. These features are directly related to the minority spin surface states (see schematic fig. 1.17). The surface states cross $E_F$ at certain $k_{\parallel}$. Contributions from this state become significant once it hybridizes with a bulk band. As these surface states exist on both sides of the barrier, they may couple to each other, resulting in

*interfacial resonant states* that are responsible for large conductance peaks in the minority conductance channel. These intrinsic features lower the $G_{maj}/G_{min}$ ratio, which significantly affects the effective TMR value.

#### 1.4.4.3 Impact of phonons

All of magnetic tunnel junctions show decrease of the TMR ratio with increasing temperature. Apart from structural defects (described in chapter 2), this issue is often attributed to thermally- or voltage-induced excitations of the barrier atoms, i.e. phonons. Although relatively few works report their direct impact on the spin polarized transport, barrier phonons with energy of 80meV and 120meV are reported on several MTJ systems at corresponding bias in the second derivative of current voltage characteristics $d^2I/dV^2(V)$, so called inelastic electron-tunneling spectroscopy (IETS) [37, 38].

## 1.5 Other barrier types

The MgO barrier was presented in the former sections as an easy example of solid-state spin-polarized tunneling in the Fe/MgO/Fe system. However, due to interesting symmetry filtering effects and to the relative accessibility of their optical studies, devices based on $SrTiO_3$ and $TiO_2$ insulators were also studied during this thesis. This section presents properties of these materials from a spintronic standpoint. Although several more complex compounds are proposed as MTJ barriers [39, 40], they lie beyond the scope of this thesis.

### 1.5.1 Strontium titanate

$SrTiO_3$, abbreviated to STO, crystallizes in face center cubic (*fcc*) **perovskite** $ABO_3$ structure as shown in fig. 1.18, with its lattice constant being 3.905Å. It is a stack of alternating (200) SrO and $TiO_2$ planes [42].

The complex band structure for the cubic perovskite strontium titanate is presented on fig. 1.19. If compared with the respective calculation for MgO (fig. 1.11), one can easily see that the electronic transport is not governed by the same electronic symmetries. $SrTiO_3$ barrier exhibits a very different band structure profile from that of MgO, as its valence band has $\Delta_1$ and $\Delta_5$ symmetries resulting from oxygen $2p$ orbitals, while the conduction band has $\Delta_{2'}$ and $\Delta_5$ symmetries from Ti sites. As the consequence, more than one $\kappa$ loop exists in the gap and the charge neutrality level (CNL), defined as the intersection between these loops, lies closer to the the conduction band, and so shall the Fermi level in case of contact with a metal. This is because empirically the chemical potential of STO is found to lie close to the conduction band, which means that $E_F$ can be at best lowered to the CNL, not lower. For electron propagation along the (001) direction, the electron barrier

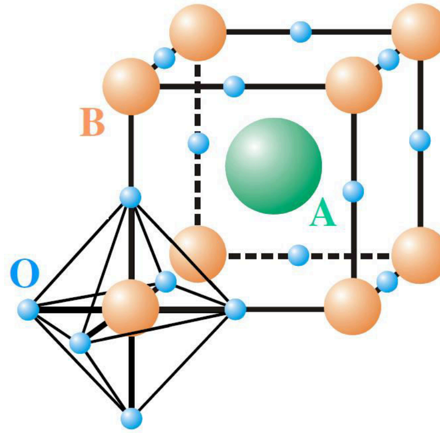


Figure 1.18: *Perovskite $ABO_3$ structure. In case of $SrTiO_3$, A stays for Sr and B for Ti site, respectively. The common octahedral $BO_6$ representation with the B site in the center is shown in the bottom-left [41].*

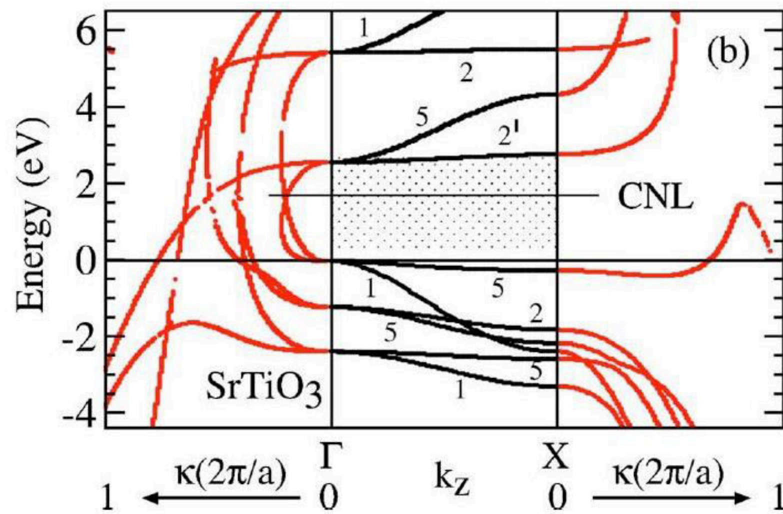


Figure 1.19: *Complex band structures of $SrTiO_3$. CNL stays for the charge neutrality level. Numbers denote the Δ electronic symmetries [43].*

height ($\Delta_{2'}$ and $\Delta_5$) is then lower than that of the holes ($\Delta_1$ and $\Delta_5$) [43]. Moreover, the extension of the $\Delta_5$ symmetry band is the one extending the least towards high $\kappa$ values, resulting in the dominant conductivity of this channel within the barrier. This in contrary to the MgO band structure profile, for which the charge neutrality level lies in the center of the gap as only one ($\Delta_1$) $\kappa$ loop connects conduction and valence bands symmetrically.

### 1.5.2 Titanium dioxide

The alternating occurrence of SrO and $TiO_2$ planes within the $SrTiO_3$ crystal can lead to an uncertain interface termination. Even though $TiO_2$ termination was observed to be more energetically favorable than SrO, the interfacial mixing may have a crucial impact on the tunnel magnetoresistance ratio, diminishing its value or even switching the sign [44]. Such uncertain interfacial termination will be described in chapter 2. In order to avoid the issue, the additional $TiO_2$ layer may be deposited from a separate pure titanium oxide source. Such interfacial layer would ensure the interfacial termination of the barrier. However, some groups have also predicted that wholly $TiO_2$ barriers would be good candidates for the spintronic applications [45]. The titanium oxide barriers might then serve as an alternative to the strontium titanate.

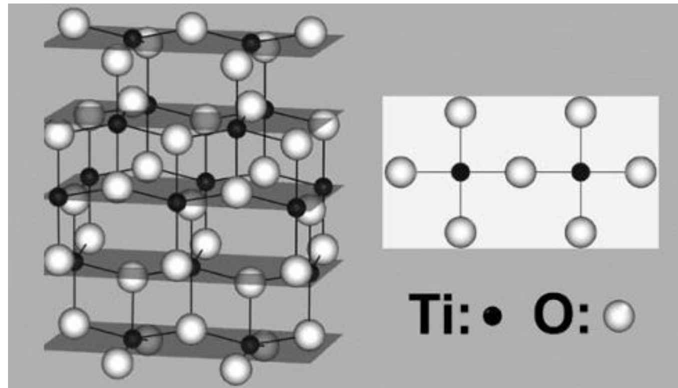


Figure 1.20: *Crystallographic three dimensional and planar structure of anatase $TiO_2$(001) [46]*

Anatase phase $TiO_2$ has a band gap of 3.2eV [47]. Bibes *et al* show that a 2.4nm epitaxially grown layer shows both high resistivity and electrical homogeneity with no conductive hotspots [45]. Its lattice parameters, 3.8Å for a=b and especially 9.5Å for the c direction (fig. 1.20) promise small lattice mismatch with perovskite materials.

The tunneling behavior of the anatase $TiO_2$ barrier is similar to that of the $SrTiO_3$, due to their corresponding band structures - symmetries of the valence band are of $\Delta_1$ and $\Delta_5$ types due to 2p orbitals, whereas the bottom of the conduction band consists of symmetries resulting from Ti atoms - $\Delta_{2'}$ and $\Delta_5$ [48].

The ease with which the anatase phase of $TiO_2$grows upon other perovskites gives an additional suggestion that it can be well used as the forced termination layer of the $SrTiO_3$ barriers or may even become its replacement. For these reasons and due to relatively scarce experimental results on $TiO_2$-based structures, their study was also approached within the timeframe of this thesis.

# 1.6 Different electrode materials

Iron was described as the model electrode material because of its well understood band structure and symmetry filtering properties in the Fe/MgO/Fe system. However, there are several disadvantages of the mentioned system due to properties of iron, i.e. its easy oxidation and simultaneous existence of certain symmetry bands for both spin populations. This section presents properties of different materials that may be used as ferromagnetic electrodes in magnetic tunnel junctions.

## 1.6.1 Introduction of Cobalt

In this subsection cobalt-iron alloys and pure cobalt electrodes are presented, as they proved to be great candidates for high TMR yielding magnetic tunnel junctions due to their good symmetry filtering properties [29] and lower enthalpy of oxidation (see table 2.6).

### 1.6.1.1 Cobalt-iron alloys

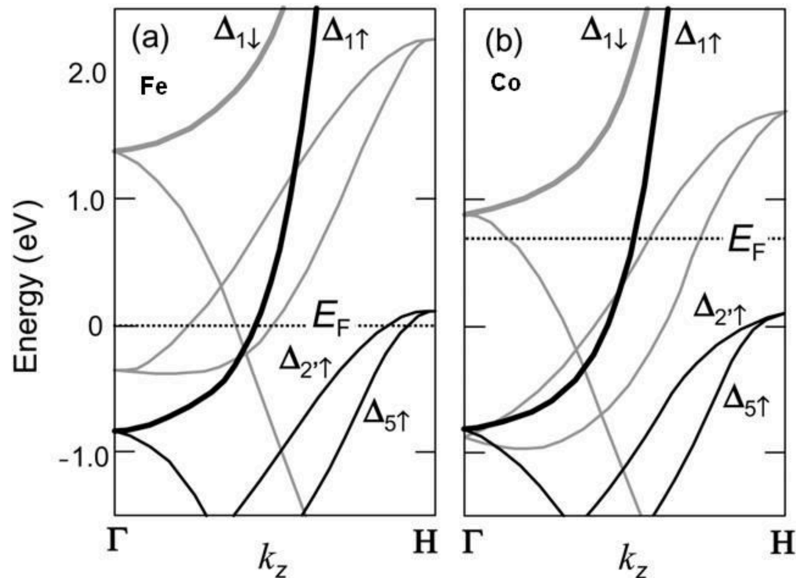


Figure 1.21: *Schematic band dispersion of bcc a) Fe and b) Co along the [001]* $\Gamma - H$ *direction. The solid and dotted lines represent majority and minority spin subbands, respectively. Bottom edges of the majority* $\Delta_1$ *subband were aligned in order to compare the* $E_F$ *position in both materials [49].*

As presented before, magnetic tunnel junctions composed of iron electrodes suffer from tunneling via certain symmetry channels (namely $\Delta_5$ and to lesser extent the

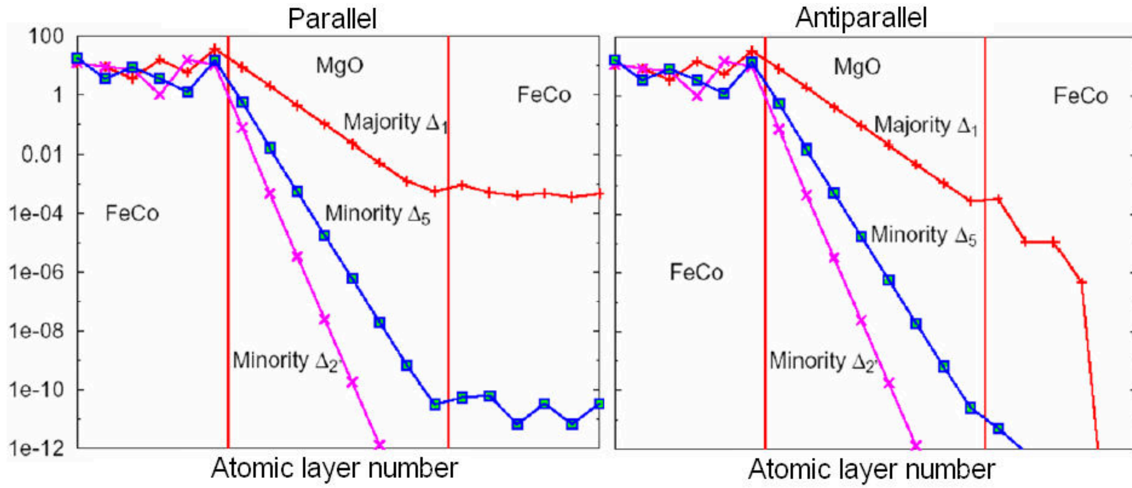


Figure 1.22: *Total tunneling DOS for bcc CoFe(100)/MgO/CoFe(100) system with the MgO barrier being 8 monolayers thick in P (left) and AP (right) relative orientation of the electrodes [50].*

$\Delta_{2'}$) that are present both in P and AP configurations, which results in a low conductance difference. Parkin *et al* presents that by replacing Fe with CoFe electrodes one may enhance the TMR ratio. This can be easily explained if one compares band dispersions of bcc Fe and Co (fig. 1.21). Contrary to the iron case, both $\Delta_5$ and $\Delta_{2'}$ subbands in cobalt lay below the Fermi level in the majority-spin band. This implies that electrons of these symmetries can contribute to the total conductance only in the parallel configuration, which results in the TMR reported on CoFe-based junctions being higher than for their iron counterparts [51]. The calculations of the tunneling DOS performed by Zhang *et al* are shown on fig. 1.22.

As previously mentioned, Fe crystallizes in the bcc structure with a lattice constant that can form a crystalline interface with MgO. Cobalt, on contrary, takes the hexagonal-close-packed (*hcp*) form, disallowing the correct lattice matching with the MgO barrier. However, it is well known that the CoFe compound retain the iron-like bcc structure up to 70/30 Co/Fe ratio, with its lattice constant being very similar to that of iron, i.e. 2.82Å [50]. Even though intermixing of Co and Fe band structures in CoFe is inevitable, reports show that it is the Co interfacial termination that is energetically more favorable, which results in the desired more cobalt-like band structure at the interface [50]. On the contrary, very recent results by Bonell *et al* show that x=0.25 within the $Co_xFe_{1-x}$formula may also lead to an enhanced TMR ratio due to specific band structure modification at this ratio [52].

#### 1.6.1.2 Interfacial cobalt layers

As it is the Co band structure that forbids $\Delta_5$ and $\Delta_{2'}$ electrons from tunneling in the AP state, even more pronounced effects are expected for the Co/MgO interface.

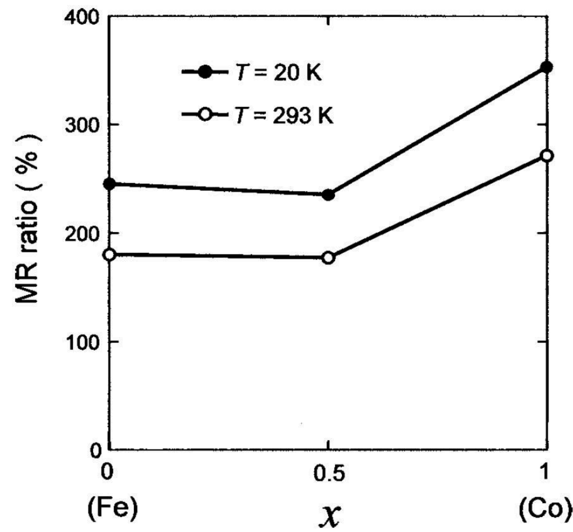


Figure 1.23: *TMR ratio for bcc Fe/Co$_x$Fe$_{1-x}$/MgO/Fe structures fabricated under same conditions and measured at room temperature as well as at 4K with 10mV bias [49].*

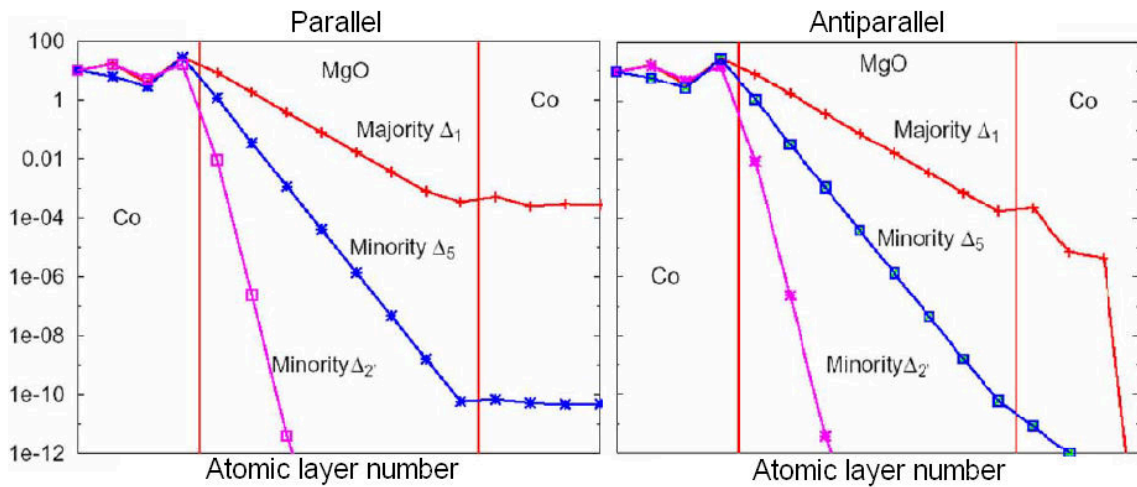


Figure 1.24: *Total tunneling DOS for bcc Co(100)/MgO/Co(100) system with the MgO barrier being 8 monolayers thick in P (left) and AP (right) relative orientation of the electrodes [50].*

The problem resulting from the aforementioned hcp crystalline structure of cobalt is not present in case of up to a few monolayers thick (0.6nm) interfacial Co layers, which follow the bcc structure of the Fe or CoFe electrode they are grown on, with the lattice constant being 2.86Å [53]. Yuasa *et al* compared the tunnel magnetoresistance ratio for several structures fabricated with comparable conditions, i.e. Fe/Co$_x$Fe$_{1-x}$/MgO/Fe systems, with the 'x' value being 0, 1/2, or 1. The re-

sults are presented on fig. 1.23. The TMR values obtained for the pure Co lower electrode are clearly better than for the others. The relatively low TMR value for the CoFe-based system is explained by the need of to perform electrode annealing at 600°C in order to obtain the lattice planes with alternating Co and Fe occupation [54]. Calculations performed by Zhang *et al* on hypothetical systems with bcc Co electrodes show similar results as these performed on the bcc CoFe-based system (fig. 1.24).

### 1.6.2 CoFeB based textured systems

As the MgO-based systems show reasonably high TMR signals at room temperature, they are promising candidates for entering the industrial stage. However, the stack structure required for potential applications requires only one of the ferromagnetic layers to be able to switch with the magnetic field applied, while the other has to remain fixed. This cannot be done with traditional iron or cobalt-based systems. The desired possibility to 'pin' one of the layers forced researchers to look for another solutions.

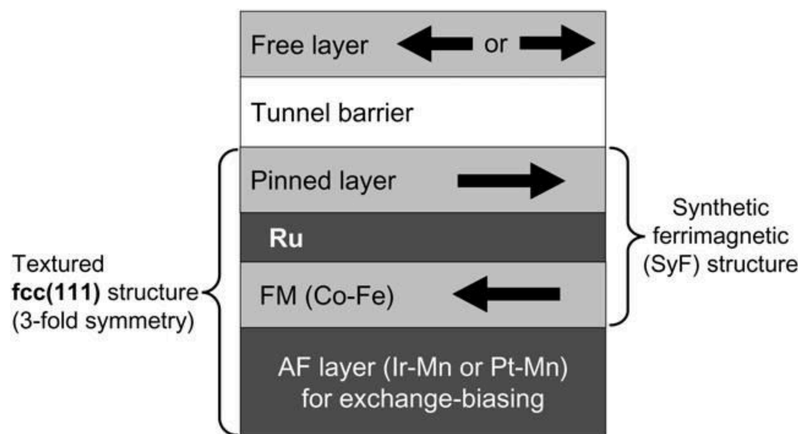


Figure 1.25: *Stack structure of a magnetic tunnel junction required by the industry. The synthetic ferrimagnet (SyF) acts as a 'pinned' layer of the structure, which ensures strong exchange-bias and small stray magnetic fields acting on the top layer. Only the top 'free' layer can switch its magnetization while the field is applied [14]*

The pinned lower electrode can be created as a synthetic ferrimagnet (SyF) composed of antiferromagnetically coupled Ferromagnet/Non-ferromagnet/Ferromagnet (F/NF/F) structure, exchange-biased by the antiferromagnetic layer. An example of such a structure is shown on fig. 1.25.

For more than 15 years material engineers were looking for an AF/SyF structure with a strong exchange-bias and minimum stray magnetic fields acting on the free layer. So far the most promising candidates are IrMn or PtMn as the antiferromagnets and CoFe/Ru/CoFeB as the synthetic ferrimagnet [14]. However, the

main obstacle in application of these materials into the magnetic tunnel junctions was that their crystalline orientation does not follow the NaCl(001) structure of the MgO barrier. Instead, the fcc(111) is formed, yielding large lattice mismatch that does not allow the MgO barrier to grow atop this AF/SyF multilayer as the desired monocrystal. A solution to this problem was found in form of the CoFeB electrodes.

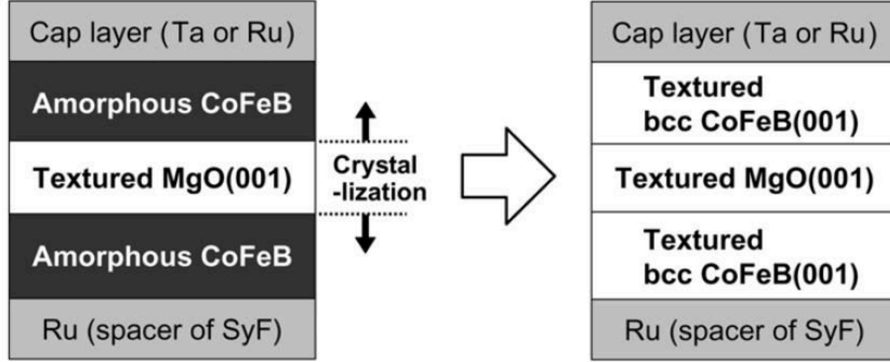


Figure 1.26: *Schematic picture of the CoFeB/MgO(001)/CoFeB structure recrystallization during the annealing [14].*

CoFeB is an amorphous material so the first few monolayers of MgO grow amorphously on top of it. However, once certain number of MgO layers is grown amorphously, the crystalline structure starts to appear [55]. This MgO is not epitaxial but rather a 'textured' crystal, composed of (001) crystalline domains separated by grain boundaries and amorphous regions. The upper CoFeB electrode again grows on such textured MgO amorphously. As presented before, the crystallinity of the magnetic tunnel junction is essential for a reasonable TMR ratio. The crystallization is therefore achieved by annealing the entire stack at temperature not lower than 300°C, which results in a spread of the crystalline structure originating from the textured areas of the MgO barrier [55, 56]. Once the crystallization reaches the insulator/ferromagnet interface, the latter starts to form the bcc structure as well, adapting to the MgO(001) NaCl structure, instead of forming its stable fcc(111) phase (fig. 1.26). Mizuguchi *et al* showed that, despite the polycrystalline nature of the barrier, there is very little or no influence on the electron transport by the grain boundaries [57]. As could be expected, the tunnel magnetoresistance value is very small on the non-annealed amorphous systems as compared to the annealed ones, because of the symmetry mixing resulting from the incoherent transport that is typical for amorphous barriers [56].

CoFeB-based magnetic tunnel junctions proved to be not only promising candidates for industrial applications, but the tunnel magnetoresistance observed in these structures is much higher than that in standard Fe- and Co-based systems [15]. This is believed to be due to the impact of the texturization process on quality of the interfaces (discussed in section 7.3). On the other hand, very recent work by

Duluard *et al* surprisingly shows that up to 140% high TMR ratio may be achieved also from the textured Fe/MgO/Fe system [58]. Moreover, Schreiber *et al* report that replacing the lower CoFeB electrode with the CoFeB/CoFe bilayer improves both crystallization and and thermal stability of the junction, which consequently leads to its better performance in comparison to the standard CoFeB-based system [59].

### 1.6.3 $La_{0.7}Sr_{0.3}MnO_3$ Half-metallic electrodes

The TMR in defect-free Magnetic Tunnel Junctions rely on three factors: a) spin polarization in the injector, possibly for a specific electron symmetry, b)difference in symmetry-dependent decay rates within the barrier and c) acceptance or rejection of symmetry-dependent states available inside the collector (analogy to the point a)). Even a slight system modification leading to a larger spin polarization may enhance the tunnel magnetoresistance value. Unfortunately, the spin polarization within the ferromagnets has certain finite value, which does not allow to enhance the TMR ratio further.

In 1983, de Groot *et al* introduced materials with band structure exchange split the way that one of their spin populations would be conducting whereas the other one would be semiconducting or insulating [60]. They were subsequently named **Half-metals**.

Within the timeframe of this thesis, a process of obtaining junctions with half-metallic lanthanum strontium manganite $La_{0.7}Sr_{0.3}MnO_3$ electrodes (abbreviated LSMO) was approached. This sections describes fundamental properties of this structure.

#### 1.6.3.1 Crystal field splitting

In order to understand the half-metallic behavior of certain materials, their physical properties need to be described. The $La_{0.7}Sr_{0.3}MnO_3$ compound is essentially the Sr-doped lanthanum manganite ($LaMnO_3$ or LMO) which crystallizes in the perovskite $ABO_3$ structure already presented for the $SrTiO_3$ barriers on fig. 1.18. In the LMO case the $A$ and $B$ spheres correspond to lanthanum and manganese, respectively. Upon doping the LMO with strontium, a specific proportion of the La sites is replaced by Sr.

Manganese, being a transition metal, has its 3d-level modified in a periodic structure. In case of the octahedral $ABO_3$ symmetry of manganites, two of its fivefold degenerate 3d levels (named $e_g$) are directed towards the negatively charged oxygen sites, while three of them (called $t_{2g}$) are facing diagonals between those sites (fig. 1.27).

Due to the Coulomb repulsion between the 3d Mn orbitals and negatively charged ligands (O sites), the energy of the $e_g$ orbitals directed towards the O sites rises as

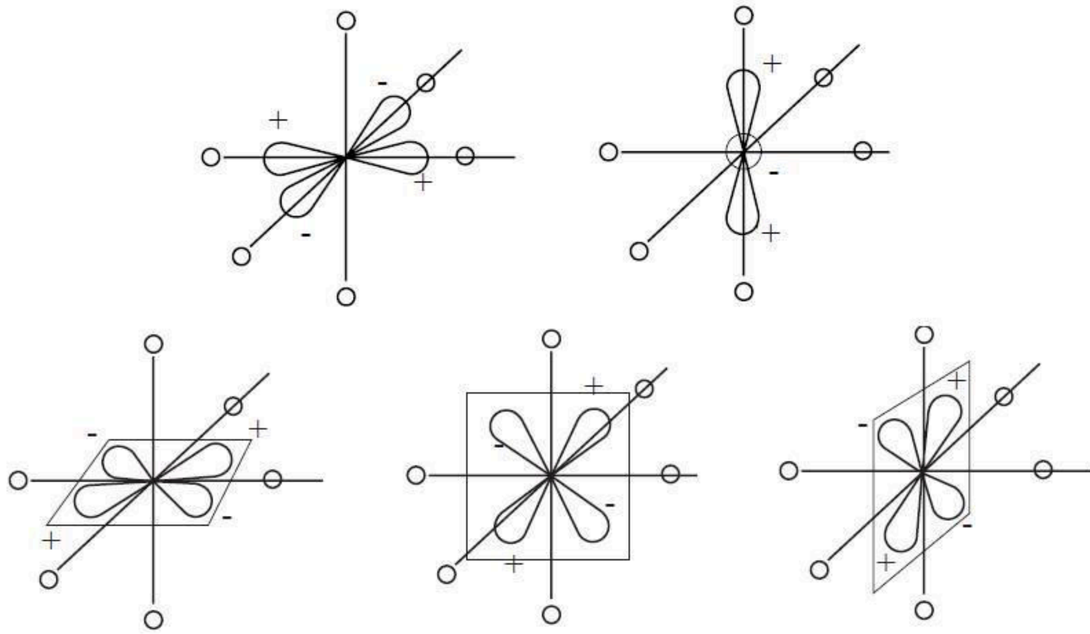

Figure 1.27: *The shape of the Mn site wave functions. (From left to right) Top: The* $e_g$ *orbitals* $d_{x^2-y^2}$, $d_{z^2}$. *Bottom: The* $t_{2g}$ *orbitals* $d_{xy}$, $d_{xz}$, $d_{yz}$. *The external circles depict oxygen sites [61].*

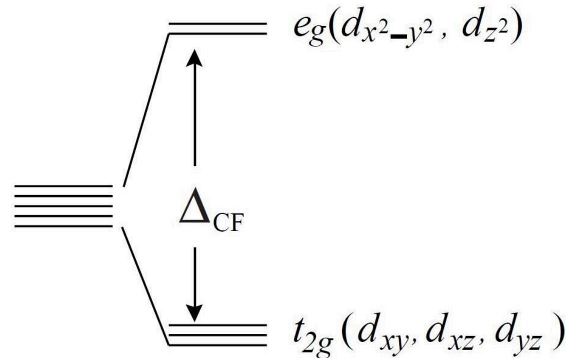


Figure 1.28: *Energy level splitting of a 5-fold degenerate d-level in octahedral crystal [61].*

compared to the energy of the $t_{2g}$. This is called $\Delta_{CF}$ - ligand field splitting of energy levels due to the crystal field (fig. 1.28).

According to Hund's rule, electrons fill orbitals so as to minimize the overall energy of the system. For an ion with four 3d electrons (which is the case for the $Mn^{3+}$) this can be done two-way. First three electrons always occupy the lowest degenerate $t_{2g}$ levels with all of their spins directed one way. But the behavior of the fourth electron is driven by the ratio between the $\Delta_{CF}$ and the Hund's rule stabilization energy $J_H$. If $\Delta_{CF} > J_H$, it is more favorable for the electron to

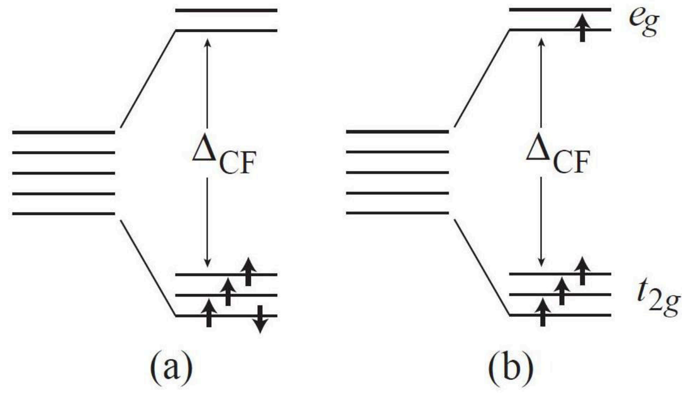


Figure 1.29: *Possible a) low-spin and b) high-spin states of $Mn^{3+}$ in octahedral crystal, the latter being favored in transition-metal oxides [61].*

switch its spin and occupy the lowest $t_{2g}$ level. However in the opposite $J_H > \Delta_{CF}$ situation, the electron chooses the $e_g$ level. These two situations are respectively called *low-spin* and *high-spin* states (fig. 1.29). In case of most of transition-metal oxides ($Mn^{3+}$ being no exception), the high-spin state configuration is energetically more favorable. The $t_{2g}$ electrons form the electrically inert core spin, while the $e_g$ electron is coupled to it by Hund's rule coupling.

#### 1.6.3.2 Double exchange mechanism

In order to explain the half-metallic nature of the LSMO, it is important to understand the impact of the LMO doping with Sr atoms. LMO is an antiferromagnetic material and its Mn ionic state is as shown on fig. 1.29b. Without dopants, the $x$ in the $La_{1-x}Sr_xMnO_3$ formula is zero and its ionic composition is $La^{3+}Mn^{3+}O_3^{2-}$. However, replacing one trivalent cation of lanthanum with bivalent strontium removes one electron from the system. As result, the $Mn^{3+}$ ion becomes quadruply charged ($Mn^{4+}$), leaving a hole in the $e_g$ subband. Because of the crystalline symmetry of the system, the Mn ions are too far apart to overlap and an electron cannot be transferred directly between two differently ionized Mn sites. An $O^{2-}$ site has to play a role. Zener showed that the electron transfer between two Mn sites is realized by hopping of one electron from the Mn site to the $O^{2-}$ site and the simultaneous jump of another electron from this $O^{2-}$ site to the other Mn site [62]. This phenomenon is called **Double exchange**. Moreover, he found that the spin of the transferred electron would couple with both Manganese ion cores. The hopping amplitude thus strongly depends on the relative spin orientation, being zero for the antiparallel case [63]. As even in the parallel alignment of spins there is only one spin-type of electrons among the the $e_g$ levels, this results in the material being conductive for the majority spin population only, giving rise to the **Half-metallic** behavior. The Zener model was further extended by Anderson and Hasegawa [64].

Millis *et al* points out that the double exchange mechanism is not the only reason for the carrier hopping [65]. They found a solution to the discrepancy between certain aspects of the data by proposing a strong electron-phonon interaction arising from the Jahn-Teller degeneracy lifting of the outer Mn $d$ levels [66]. Essentially speaking, the Jahn-Teller level splitting arises from the geometrical distortion that a crystalline system undergoes in order to lower its overall energy. It is this distortion that lifts the degeneracy.

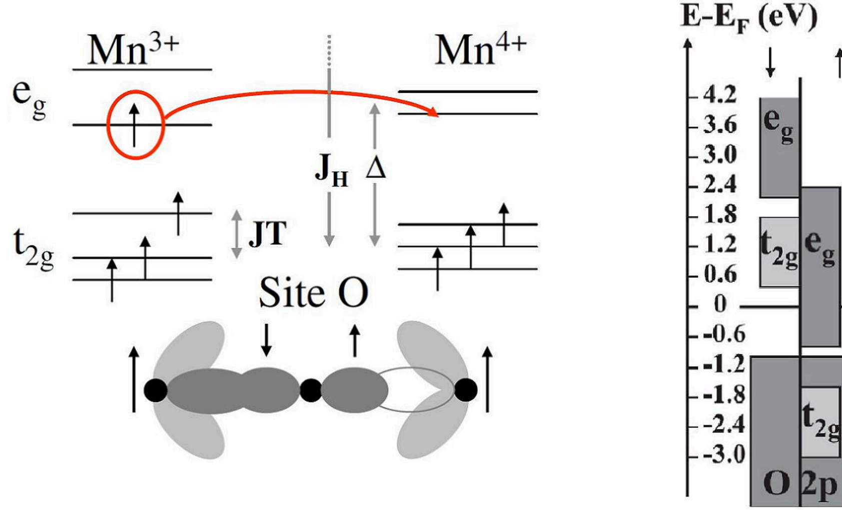


Figure 1.30: *Left: Schematic picture of the double exchange mechanism in* $La_{0.7}Sr_{0.3}MnO_3$ *between* $Mn^{3+}$ *and* $Mn^{4+}$ *sites assisted by oxygen 2p orbitals. The* $e_g$ *levels split in* $Mn^{3+}$ *is caused by the Jahn-Teller crystalline lattice distortion, labeled JT. Right: Spin-resolved band structure of the* $La_{0.7}Sr_{0.3}MnO_3$*. [41].*

The schematic picture of double exchange between $Mn^{3+}$ and $Mn^{4+}$ sites via the Oxygen 2p orbitals, depicting the Jahn-Teller degeneracy distortion of both $e_g$ and $t_{2g}$ levels of $Mn^{3+}$ is shown on fig. 1.30, along with the resulting half-metallic band structure of the LSMO material.

As $LaMnO_3$ is an antiferromagnetic material with the nearest neighbors having opposite spins, an electron cannot simply hop to the other site because the strong Hund rule coupling forces it to keep its spin parallel to the one of the site. The effective hopping of the electron is then drastically reduced for the sites with the spins antiparallel relatively to that of the electron. As shown by de Gennes, increasing the amount of free carriers within the material causes the original antiferromagnetic structure to become *canted* and ferromagnetically ordered components start to appear [67]. At certain concentration of dopants, the structure becomes fully ferromagnetic. This $x$ doping ratio was found to be between 0.2 and 0.4, so it is this Sr-to-La ratio that is commonly used in LSMO compounds. The LSMO abbreviation is usually used to describe such Sr doping of the structure and such notation

will be used within this manuscript. It may be interesting to note that overdoping the $LaMnO_3$ system with strontium yields insulating state which is unwanted for the experiment [68].

#### 1.6.3.3 Temperature dependence

The main obstacle in implementation of half-metallic materials within commercial magnetic junctions is the temperature dependence of their properties. The high TMR value of manganite-based junctions decreases rapidly with temperature and disappears below the room temperature, way below Curie temperature of the bulk LSMO, which is 360K [69]. The effect is explained in form of a premature loss of polarization at LSMO interfaces, as it is the interfacial spin polarization that determines the tunneling properties. Park *et al* show [70] that the spin polarization of a free LSMO surface decreases much faster with increasing temperature than the magnetization of the bulk material. A Curie temperature lowering, smaller magnetization and reduction of the metallic character in a few nm thick manganite layers were reported to result in their weakened ferromagnetic properties. [71, 72].

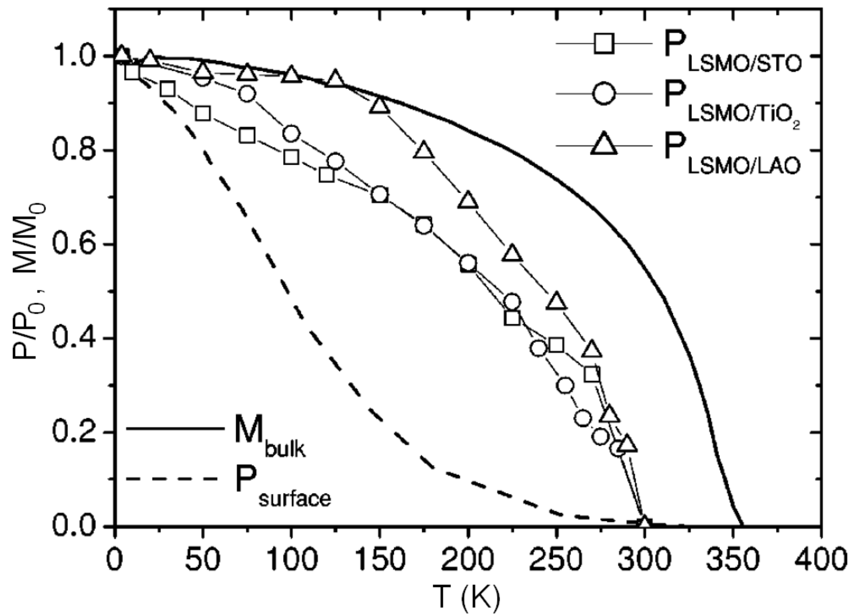


Figure 1.31: *Temperature dependence of the interfacial spin polarization for different barriers combined with LSMO compared to that of the free LSMO surface and to its bulk magnetization obtained by Park* et al *[69].*

Garcia *et al* performed measurements on the temperature dependence of polarization for different LSMO/insulator interfaces [69] and compared them with these obtained by Park for the bulk and free surface of the LSMO (fig. 1.31). The result shows that the interfacial polarization curves resemble the one of the bulk magne-

tization rather than surface polarization, indicating that the LSMO magnetism is preserved not just at the surface but in the vicinity of the interface, although the critical temperature is around 60K lower.

The difference in the spin polarization decay between the surface and the interface lies in the preservation of the $BO_6$ octahedra at the surface ($B$ sites being manganese, see fig. 1.18), where the outermost layers may be oxygen deficient, which results in large splitting of the $e_g$ levels. As a result, the double exchange mechanism is weakened and the mentioned temperature dependence shows a very different character from that of the interface [73]. On the other hand, the continuity of these octahedra is preserved at the interfaces with the mentioned STO, LAO or $TiO_2$ and, even in the presence of distortions, its impact on the electronic structure is lower than in the case of the free surface which results in more bulk-like character at the fig. 1.31. It is the decrease of the charge carrier density and the alteration of the $BO_6$ structure geometry at the interfaces that are responsible for the $T_C$ reduction [74].

## 1.7 LSMO/STO/LSMO system

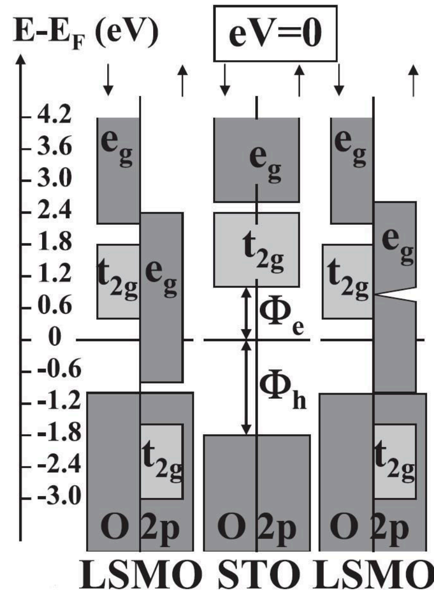


Figure 1.32: *Density of states of the LSMO/STO/LSMO system at equilibrium.* $\Phi_e$ *and* $\Phi_h$ *denote electron and hole barrier heights, respectively.* $t_{2g}$ *corresponds to the* $\Delta_{2'}$ *and* $\Delta_5$ *symmetries, while the* $e_g$ *represents* $\Delta_1$ *and* $\Delta_2$*, as previously shown on the fig. 1.19 [43].*

The schematic equilibrium alignment of the aforementioned bands for the complete, (001)-oriented LSMO/STO/LSMO system is shown on fig. 1.32. As explained

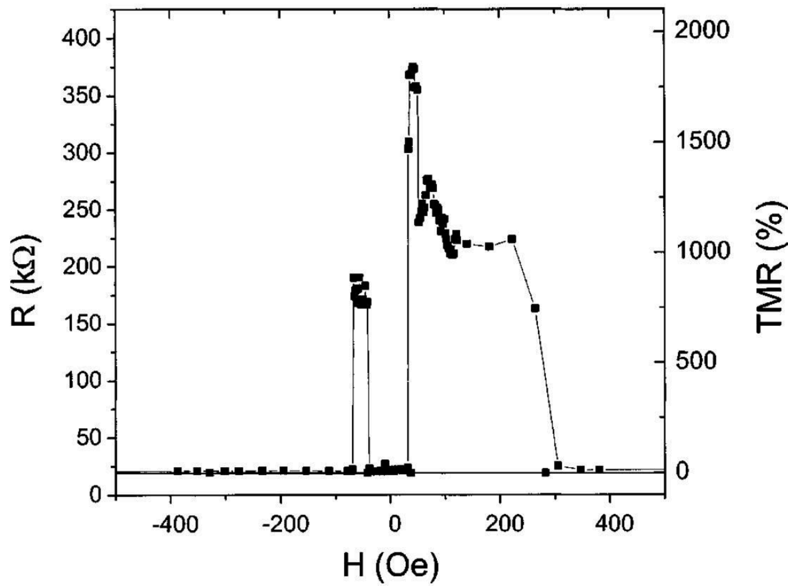


Figure 1.33: *LSMO/STO(2.6)/LSMO resistance dependence on magnetic field applied for 5.6$\mu m^2$ at 4.2K [17].*

in section 1.6.3, at sufficiently low temperature there are only majority spin states available at the Fermi level of LSMO electrodes, whereas the material is insulating for the minority spin. The spin polarization of the electrons tunneling through the structure was determined to be 95% at 4.2K, and can reach 99% [41]. The resulting nearly total spin polarization at low temperatures gives rise to large TMR values, dubbed *Colossal tunnel magnetoresistance* or shortly *Colossal magnetoresistance* (CMR). The TMR measurement yielding 1800% is shown on fig. 1.33. Such high value decays rapidly with the temperature and the TMR disappears at 280K due to the loss of the spin-polarization at the LSMO/STO interfaces [69].

# Chapter 2

# Role of defects

All crystalline systems presented in the previous chapter may suffer from imperfections resulting from the growth of succeeding layers one atop one another. This implies that the efficiency of the spintronic response predicted theoretically is often suppressed by additional effects arising from the presence of defects. As the defect control and characterization are crucial to obtain devices showing desired behavior, it is therefore essential to understand their origin and properties. This chapter focuses on several types of defect-induced situations that lead to the depressed magnetoresistive response. The first section encompasses the field of defect study within crystalline dielectrics that we use as tunnel barriers, and the incidence of these defects on the spin-polarized transport, with an emphasis on optical means to identify these defects. The second section concentrates on deviations from nominal crystal structure at interfaces. It also describes well-established methods of suppressing or diminishing the role of these structural imperfections. The third section describes phenomena of electromigration and how one can use it as a tool to influence the spintronic properties of dielectric junctions. The last section introduces a rise of research on magnetism within crystalline dielectrics due to presence of defects in undoped insulators.

## 2.1 Bulk imperfections

This section describes properties of bulk structural defects. Its first subsection concentrates on their impact on spin-polarized transport and resulting discrepancies between theoretical predictions and experimental observation, whereas the second one presents optical properties of the defect sites.

### 2.1.1 Impact on spin-polarized transport

The reason for which experimental results on magnetic tunnel junctions rarely match the theoretical expectations lies partially in presence of defects within their crys-

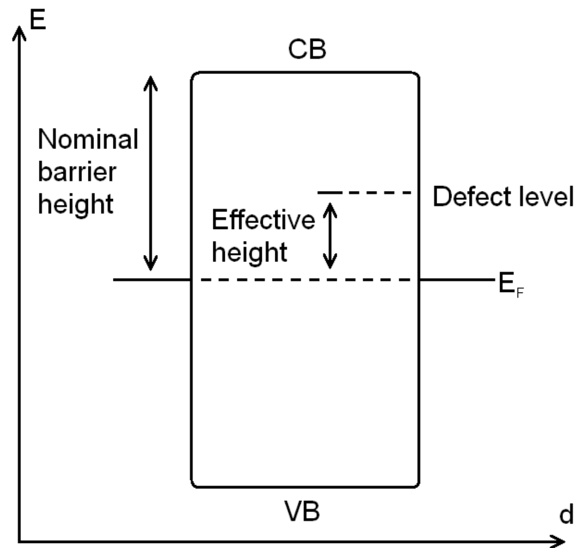


Figure 2.1: *Schematic picture of local lowering of the effective barrier height due to presence of a defect state.*

talline networks. Indeed, a defect present within a barrier creates an addition energy level in the band gap, locally reducing the effective barrier height of the material (fig. 2.1). Electrons crossing the barrier would tunnel via these states of lower energy with reduced scattering, thus diminishing the overall junction resistance. Yet apart from the higher system conductance, defects affect yet another important property of magnetic tunnel junctions - spin polarization and symmetry filtering [75].

Figures 1.11 and 1.19 presented in the first chapter of this manuscript show complex band structures of crystalline insulators which are of the interest of this thesis. It was presented beforehand how the symmetry of bands determines the symmetry-conserving coherent electronic transport across the barrier. In general, a state lying in the valence or conduction band of the insulator shall adopt the symmetry of that band. As one energetically traverses the band gap, e.g. in the case of a defect state, the symmetry character of that defect state shall evolve from that of the valence to that of the conduction band, much as would a metal-induced gap state arising from charge transfer at a metal/dielectric interface [76]. Thus, at a given energy level, a defect state will adopt the character of the valence and conduction band states. The proportion of each of these characters is, in turn, inversely related to the $\kappa$ value of the complex band loop of the character considered. Since the defect is at least partially of the incoming electron symmetry, it may accept this electron. Once the defect state is occupied, the time evolution of the defect state shall proceed as a linear combination of the two valence and conduction band symmetries. Transport away from the defect state shall then proceed as a linear combination of the two symmetries that describe the defect state, thus effectively leading to mixing between symmetry-polarized conduction channels. Depending on the density

of the defect states within the barrier, such processes may happen multiple times, resulting in significant reduction of the spin-polarized transport coherency and consequently of the TMR signal of the system. Moreover, in order to overcome the energy difference, such hopping via defect states may be accompanied by phonon emission or absorption during the transition [77]. This introduces an additional inelastic temperature-dependent conductance channel which may be responsible for spin-flipping events [30, 78].

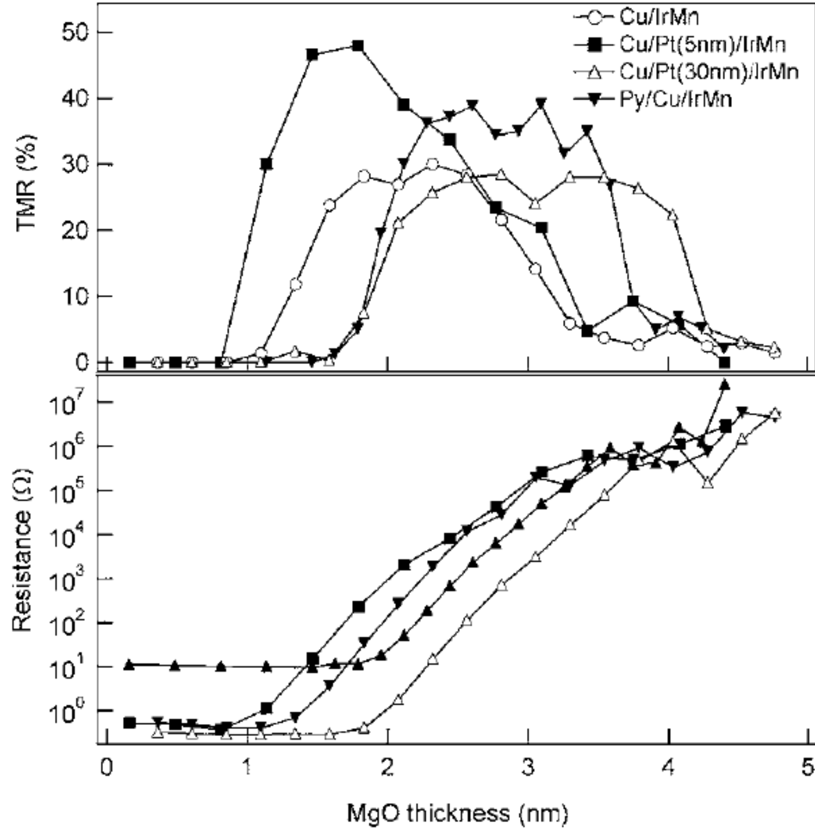


Figure 2.2: *TMR (top) and resistance (bottom) as the function of the MgO barrier thickness for CoFe/Mg(0.4)/MgO(t)/CoFe MTJs grown on different buffer layers [79].*

Even though the theoretical calculations predict that there is no limit of TMR ratio in a perfectly epitaxial junction with a very thick MgO barrier [80] and even for a few nm thick barriers the theory predicts very high signals for various systems, properties of their real counterparts are significantly less satisfactory. Figure 2.2 shows that even though resistance of the junction almost linearly increases with its thickness, the TMR ratio observed reaches certain maximum after which it starts to decrease and eventually reaches zero. It is until this maximum that the coherent tunneling described in section 1.4 dominates the conductance. Afterwards, remaining

electrons tunnel dominantly via defect sites, which gradually mixes their symmetries and eventually results in the disappearance of the TMR signal.

| Group | TMR [%] | RA product [$\Omega\mu m^2$] | barrier height [eV] | $t_{MgO}$ [nm] | $T_{anneal}$ [°C] | ref. |
|---|---|---|---|---|---|---|
| Coey | 255 | 50-100k | - | 2.5 | 350 | [81] |
| Dieny | 130 | 30 | - | 1.1 | - | [82] |
| Freitas | 165 ($223_{20K}$) | 10k ($12k_{20K}$) | 0.59 ($F^{+*}$) | 3.0 | 340 | [83] |
| Moodera | 300 | - | - | 1.5-3.0 | 500 | [84] |
| Montaigne | 150 | - | - | 3.0 | 300 | [85] |
| Petroff | 79 ($136_{3K}$) | 100k | - | 2.5 | 450 | [78] |
| Petroff | 11 ($108_{3K}$) | 1.5G | - | 4.0 | 450 | [78] |
| Ikeda | 604 ($1144_{5K}$) | 1k ($1.4k_{5K}$) | - | 2.1 | 525 | [15] |
| Ikeda | 500 ($1010_{5K}$) | 280-700 | - | 2.1 | 475 | [86] |
| Ikeda | 478 ($804_{5K}$) | 1.3k ($1.9k_{5K}$) | - | 1.5 | 450 | [87] |
| Yuasa | 230 ($294_{20K}$) | 420 ($440_{20K}$) | - | 2.2 | 360 | [88] |
| Ikeda | 124 | 18 | - | 0.9 | 300 | [89] |
| Aliev | 160 | 19 | - | 0.8 | 360 | [90] |
| Xiao | 230 | - | - | 3 | 380 | [91] |
| Thomas | 230 ($345_{13K}$) | - | - | 2.1 | 400 | [38] |

Table 2.1: *Comparison of recent highest TMR ratios reported by several groups on CoFeB-based systems along with their respective annealing temperatures.*

| Group | TMR [%] | RA product [$\Omega\mu m^2$] | $t_{MgO}$ [nm] | barrier height [eV] | ref. |
|---|---|---|---|---|---|
| Gaudin | 142 | - | 2.3 | - | [92] |
| Tiusan | 140 | 30M | 2.5 | - | [93] |
| Yuasa | 180 ($247_{20K}$) | 7k | 2.3 | - | [53] |
| Moodera | 130 ($190_{1K}$) | 200k | 2.5 | $0.38_{def}$ / $0.82_{bar}$ ($M/F$) | [94] |
| Montaigne | 150 | - | 3.0 | - | [36] |
| Yuasa | 180 ($247_{20K}$) | 1.8k ($3.2k_{20K}$) | 3.0 | $0.39_{RT}$ ($M$) | [95] |
| Tiusan | 150 | 1.6M | 3.0 | - | [58] |
| Wang | 7548 | - | 1.7 | - | [29] |

Table 2.2: *Results for Fe/MgO/Fe systems vs theoretical predictions by Wang* et al.

Many groups with outstanding experience in thin films growth and fabrication of the magnetic tunnel junctions report TMR values definitely lower than these predicted by the theory. Tables 2.1-2.4 summarize recent reports on several types of MgO-base magnetic tunnel junctions from different groups.

In the case of non-CoFeB-based devices, for which theoretical calculations were performed, one may see a large discrepancy between the experiment and the theory.

| Group | TMR [%] | RA product [$\Omega\mu m^2$] | $t_{MgO}$ [eV] | barrier height [nm] | ref. |
|---|---|---|---|---|---|
| Parkin | 220 ($300_{5K}$) | 4k | 2.0 | 1.1-1.7 ($F$-$F^*$) | [51] |
| Andrieu | 300 ($530_{20K}$) | - | 2.5 | - | [52] |
| Zhang | 33950* | - | 1.7 | - | [50] |

Table 2.3: *Results for CoFe/MgO/CoFe systems vs theoretical predictions by Zhang* et al. *The TMR value resulting from the calculations may be overestimated as the authors do not include interface resonant states in the minority channel (see section 1.4.4.2).*

| Group | TMR [%] | RA product [$\Omega\mu m^2$] | $t_{MgO}$ [eV] | barrier height [nm] | ref. |
|---|---|---|---|---|---|
| Yuasa | 410 ($507_{20K}$) | 3k ($4k_{20K}$) | 2.2 | - | [49] |
| Zhang | 12920* | - | 1.7 | - | [50] |

Table 2.4: *Results for Co/MgO/Co systems vs theoretical predictions by Zhang* et al. *The TMR value resulting from the calculations may be overestimated as the authors do not include interface resonant states in the minority channel (see section 1.4.4.2).*

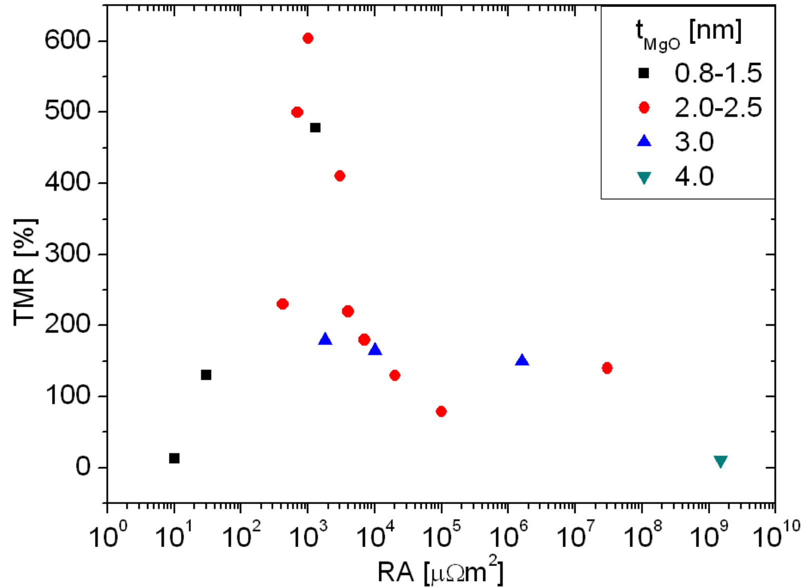


Figure 2.3: *Combined TMR dependence on the RA product for various MgO-based magnetic tunnel junctions extracted from tables 2.1 - 2.4*

.

Moreover, barrier heights (if reported) show values much lower than expected from MgO. Even though it is well-known that the bandgap of the thin film insulator can

be lower than of its bulk counterpart due to finite size effects [96], the reported values are still surprisingly low. Figure 2.3 summarizes the general TMR dependence on the resistance-area product[1]. Magnetic tunnel junctions with RA product close to $10^3 \mu\Omega\text{m}^2$ seem to show somewhat higher TMR values. Most of them incorporate CoFeB electrodes. We will refer to the graph while performing analysis of our results in section 7.3.

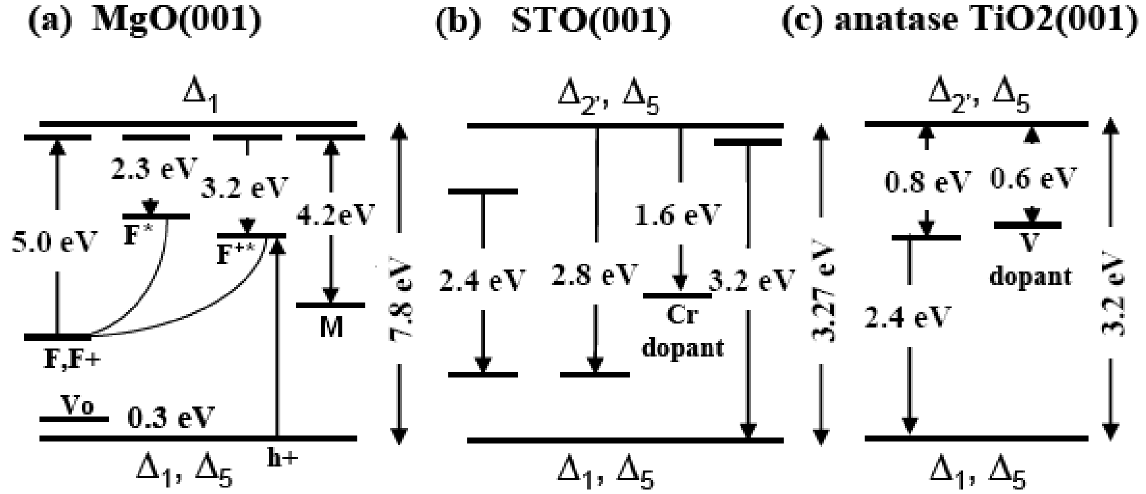


Figure 2.4: *Several calculated or experimentally-observed defect energy levels of the MgO, $TiO_2$ and $SrTiO_3$ systems studied within this thesis. Their detailed analysis is performed in the text. Energy gaps are given on the right side of each picture and the symmetries of valence and conduction bands - below and above, respectively [97, 98, 99, 100, 101, 102].*

The energy positions of certain well-known defect levels in the band gap of studied dielectrics are schematically shown for bulk crystals in fig. 2.4. As an important note, the type and density of defects can affect the pinning strength of the charge neutrality level, and thus alter the effective barrier heights, whether relative to these defect levels or to the conduction/valence band edges. Furthermore, as the presence of defects within the energy gap introduces additional channels of electronic transfer, they may be electrically probed. Moreover, if the crystalline semi-conducting system becomes exposed to the light of an appropriate wavelength, an absorption occurs on defects sites resulting in an excited state. The consecutive relaxation of the system leads to an emission of photons with corresponding energies. This suggests that both absorption and emission spectra may give essential information about the identity and density of the structural defects. The schematic figures 2.4*b, c* show that doping of these insulators may also lead to the appearance of certain energy levels.

[1] It would be elegant within this study to take into account variations in barrier thickness, but 1) this thickness is at best nominal and 2) it is analytically difficult to consider the barrier height and barrier thickness parameters, which enter into the RA product, separately.

Studies on doping of these materials in order to obtain additional functionalities are extensively performed worldwide. However, doping will not be addressed (at least explicitly) within this thesis, which rather aims to gain deeper insights into defects of the dielectric matrix rather than these resulting from explicit dopants.

Within this thesis, we will try to relate the low effective barrier heights to corresponding structural defects in the crystalline barriers. Next to reported barrier heights in the above tables, we propose possible corresponding defect types responsible for the values observed. It is indeed possible that barrier heights of 0.4eV reported by groups of Moodera [84] and Yuasa [88], as well as 1.1eV observed by the group of Parkin [51] correspond to tunneling via defect centers of $F_2$ and $F/F^+$ type, respectively. The properties of these defect sites will be explained in the following subsection.

### 2.1.2 Optical activity in crystalline systems

#### 2.1.2.1 Magnesium oxide

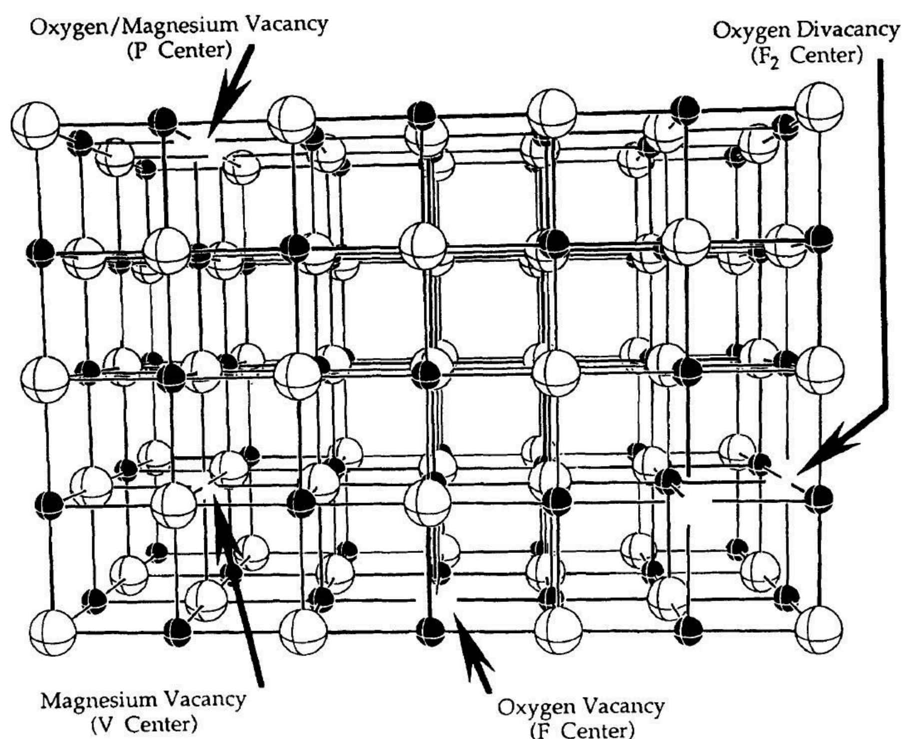


Figure 2.5: *Schematic representation of crystalline MgO lattice vacancies along with their nomenclature. White atoms are O atoms, while black ones depict Mg [100].*

The MgO monocrystal is composed of alternating Mg and O atoms as previously shown on fig. 1.7b. Vacancies within the crystalline lattice can be grouped as single

oxygen or magnesium vacancies (called $F$ and $V$ centers, respectively), oxygen di-vacancies (named $F_2$ or $M$) and neighboring oxygen/magnesium vacancies (marked as $P$) [100]. Their geometrical position within the crystal is schematically shown on fig. 2.5.

| Defect | Formation energy [eV] |
|---|---|
| $F$ | 1.82* |
| $F^+$ | 3.67* |
| $F^{2+}$ | 5.47* |
| $F_2/M$ | 3.23** |
| $V$ | 13.82 |
| $V^-$ | 14.83 |
| $V^{2-}$ | 16.35 |
| $P$ | 3.48* |

Table 2.5: *Defect formation energies in MgO crystals. The * (**) superscripts denote the energy required to remove an O atom (two O atoms) minus the cohesive energy (twice the energy) per formula unit [100].*

$F$ and $V$ centers may exist in their neutral states, as well as in the charged or doubly charged (e.g. written $F^+$, $F^{2+}$, $V^-$, $V^{2-}$ in case of the $F$ and $V$ centers). Calculated formation energies of the defects are presented in table 2.5. Thus, the creation of a $F$ defect is energetically more favorable than that of a $M$ defect. The presence of these additional states in the crystal creates additional energy levels between the minimum of the conduction band (CBM) and maximum of the valence band (VBM).

The calculations of the formation energies of the these defects, as well as their position within the energy gap, have been extensively studied. As shown by Rosenblatt *et al*, $F$ and $F^+$ centers lie close to the middle of the MgO barrier bandgap [97], which is of crucial importance, as the defects can be optically studied with light of energy approximately half that of the 7.8eV bandgap (160nm) of the MgO. This circumvents the need, at such low wavelength, for the measurement to be performed in high vacuum in order to avoid intense optical activity of the atmosphere.

Recently, Uenaka and Uchino published a detailed analysis of the time-resolved photoluminescence from the MgO system, especially regarding the $F$ and $F^+$ centers [103]. The optical absorption on both defect types occurs at 247nm (5.03eV) for $F$ and 251nm (4.96eV) for $F^+$ center, usually observed as the convoluted peak around 250nm. Given such a small difference, their excitation usually occurs simultaneously [98].

The schematic representation of the $F^+$ absorption study is schematically drawn on fig. 2.6 and is briefly described below. For the complete analysis one should refer to the article.

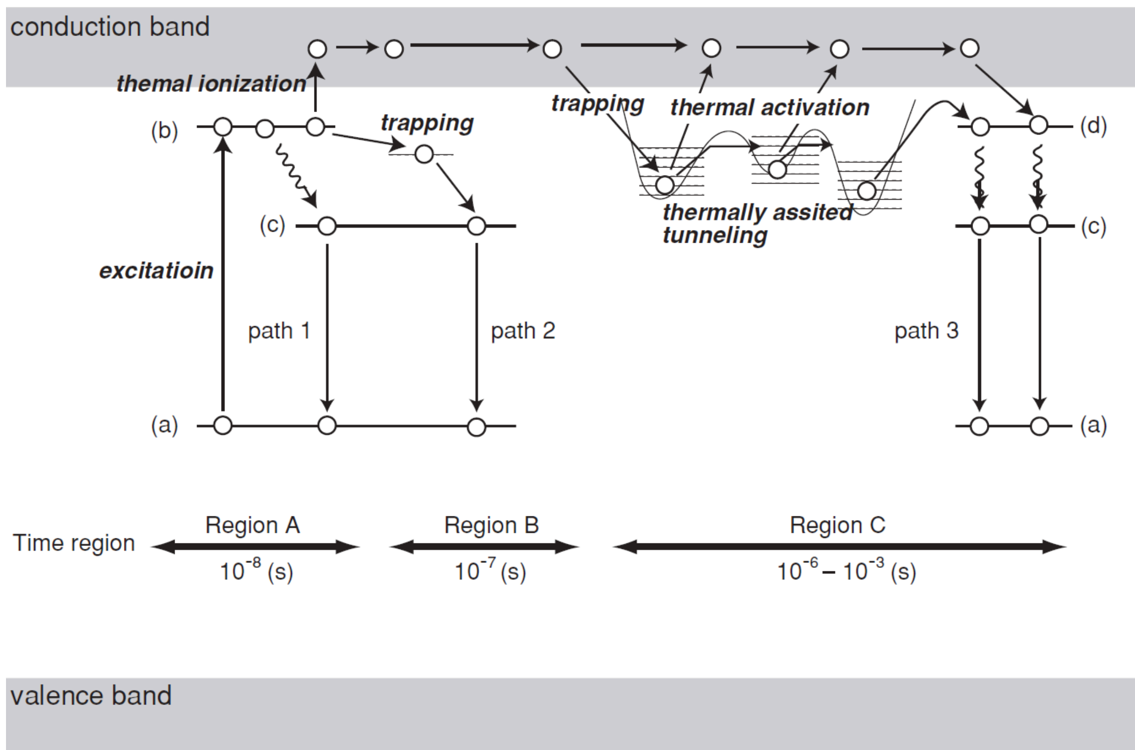


Figure 2.6: *A time-resolved model of events related to absorption of a photon at a $F^+$ center. a) The ground state level of $F^+$. b) The excited-state level. c) The emission-state level. d) the $F^+$ center excited due to recombination with a free electron from the conduction band. Note the events occur from left to right on the time-scale [103].*

The absorption process involves a 250nm photon that is absorbed at the ground-state of the $F^+$ center and promoted to the excited-state level. The center may (1) quickly thermalize directly to the emission-state level and emit the photon or (2) become shortly trapped before its relaxation, which results in a delayed emission. However, if the activation energy is much smaller than that of the two mentioned processes, it may (3) thermally ionize from its excited state and release the electron to the conduction band leaving the bare $F^{2+}$ center. The released electron can tunnel through the shallow traps by thermally-induced trapping and releasing. Eventually, the electron recombines with the $F^{2+}$ center resulting in formation of the excited $F^+$ center, which in turn relaxes to its virgin form and emits a photon. This emission would be observed in the time-resolved spectroscopy within the millisecond time scale.

The equation describing the absorption chain of events along with the resulting emitted photon energies for the $F^+$ center absorption for scenarios 1 and 2 may be written as (* being the excited state of the respective center):

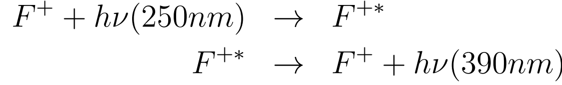

$$\begin{aligned} F^+ + h\nu(250nm) &\rightarrow F^{+*} \\ F^{+*} &\rightarrow F^+ + h\nu(390nm) \end{aligned}$$

Whereas for the 3rd scenario, when the electron is released to the conduction band:

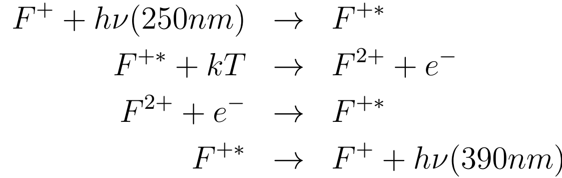

$$\begin{aligned} F^+ + h\nu(250nm) &\rightarrow F^{+*} \\ F^{+*} + kT &\rightarrow F^{2+} + e^- \\ F^{2+} + e^- &\rightarrow F^{+*} \\ F^{+*} &\rightarrow F^+ + h\nu(390nm) \end{aligned}$$

All three scenarios lead to emission of the 390nm photon.

A similar scheme applies to absorption on the $F$ center, albeit no emission within the ns-to-$\mu$s time region is observed, which suggests that most of the excited $F$ centers easily ionize by promoting an electron to the conduction band due to very small thermal activation energy, thus becoming $F^+$ centers.

The equation describing the $F$ luminescence can be written as follows:

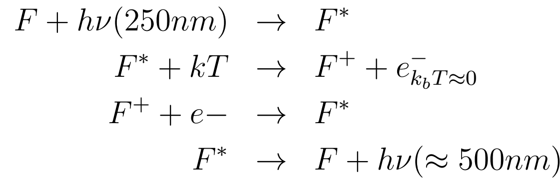

$$\begin{aligned} F + h\nu(250nm) &\rightarrow F^* \\ F^* + kT &\rightarrow F^+ + e^-_{k_bT\approx 0} \\ F^+ + e- &\rightarrow F^* \\ F^* &\rightarrow F + h\nu(\approx 500nm) \end{aligned}$$

The emission peak of the photon resulting from the absorption on the $F$ center is reported between 490nm (2.5eV) and 530nm (2.3eV) [97].

The $F^+$ centers may be considered as shallow electron traps, because even if reversed ionization of the $F^+$ center results in creation of the $F^*$ center, the excited electron may be promoted to the conduction band again due to the very small energy needed. Uenaka and Uchino conclude that weakly coupled single-vacancy $F$-type center pairs, meaning not $F_2$ or $F_2^+$ but rather a) $F$,$F^+$ ; b) $F^+$,$F$ ; c) $F^+$,$F^+$ pairs may contribute to thermally assisted tunneling via the defect sites. On the other hand, the $F_2^+$ and $F_2^{2+}$ centers are considered to behave as deep electron traps, as the energies of the aggregates of the excited vacancies tend to be lower [104].

Rosenblatt *et al* show that the excited electrons may be also trapped at shallow hydride ions $H^-$ close to the conduction band minimum. These $H^-$ centers result from the diffusing hydrogen trapped by the $F$ centers. Similarly to trapping at the sites mentioned before, the delay in the luminescence will be proportional to the concentration of those traps within the barrier. The authors also show that the

luminescence is additionally enhanced by an electron excitation from the valence band into the empty ground $F^{2+}$ or excited $F^{+}$ centers, resulting respectively in ground $F^{+}$ and excited $F$ centers, both of which eventually recombine to $F$ centers, yielding the $F$-type luminescence [97].

Multiple theoretical studies describe the energy levels of different types of defects, notably $F_2$ (or $M$) neutral and charged centers [99] or magnesium vacancies ($V$ centers) [100]. Results of these calculations are schematically shown on fig. 2.1a.

#### 2.1.2.2 Strontium titanate

Optical studies of STO crystals are easier to perform due to the lower bandgap of 3.27eV [105]. Studying a material with a photon energy lower than 5eV allows to avoid deep ultraviolet absorption by air, such that the experimental setup is greatly simplified. In this sense STO crystals are more optically accessible.

It is known that properties of $SrTiO_3$ strongly depend on its stoichiometry, especially on the oxygen species. The oxygen vacancy levels are determined to be formed at 0.5eV below the conduction band edge [106], so very little energy is needed in order to ionize such sites and promote the electron to the conduction band. Moreover, the O-vacancy can bind with other O, Sr or Ti vacancies, forming defect clusters [107]. These facts, combined with the low STO bandgap result in much more abundant photoluminescence comparing to MgO.

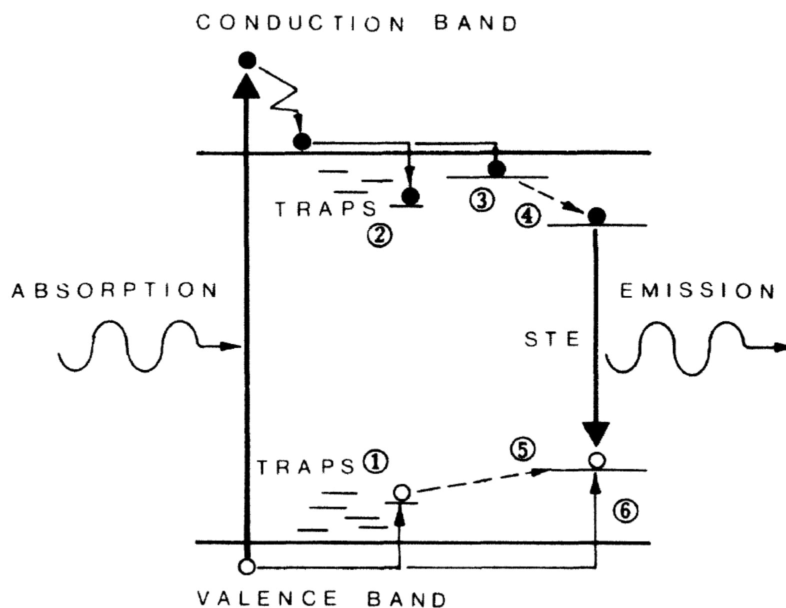


Figure 2.7: *Schematic picture of the STO luminescence after absorption of a photon: Trapping of electron/hole (1/2), polaron formation (3), delayed formation of self-trapped exciton (4/5); alternative direct STE formation (6) [101].*

The time-resolved-spectroscopy-based model describing the luminescence from STO was presented by Leonelli and Brebner (fig. 2.7). It is shown that, due to a photon absorption, an electron may be promoted from the valence band to the conduction band and form a small polaron - a local lattice polarization and deformation around the charge carrier. The polaron interacts with a hole trapped near a crystal defect or an impurity and forms a self-trapped exciton (STE), whose difficult recombination results in delayed luminescence. The STE-based photoluminescence mechanism is often observed from compounds containing titanate octahedra [101].

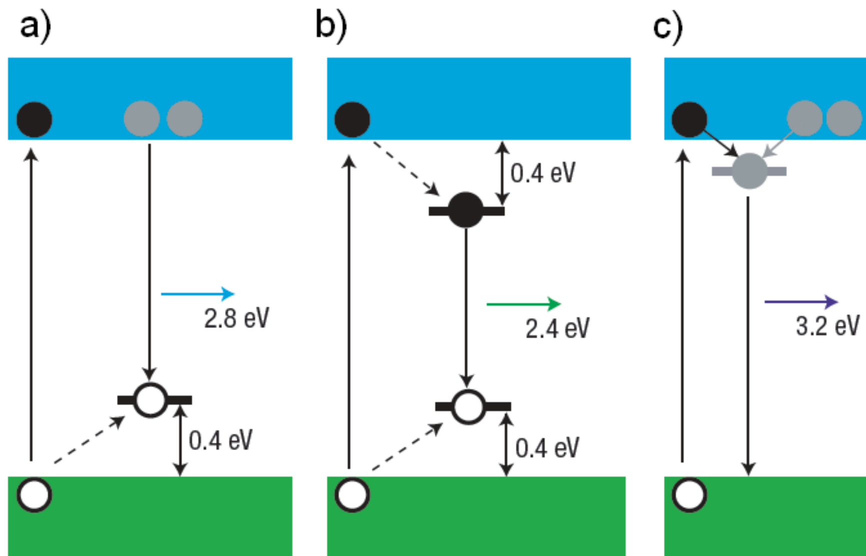


Figure 2.8: *Schematic representation of recombination processes between: a) conduction electrons and excited holes (room temperature luminescence); b) excited holes and electrons in the self-trapped excited state c) doped or excited electrons and excited holes through the shallow defect level. Green and blue bands depict the O 2p valence and Ti 3d conduction bands respectively. White, black and grey circles stand respectively for excited holes, excited electrons and doped electrons in the Ti 3d band. [108].*

One of the more prominent results was published by Kan *et al* [108], who created oxygen-deficient STO samples using the $Ar^+$ irradiation and compared their properties with the pure strontium titanate crystals. They found that the $SrTiO_3$ metallic behavior appears even after a relatively small dose of radiation, which they attribute to the creation of oxygen vacancies. The STO conductivity that appears starts to saturate as the irradiation time increases. It is accompanied by the respective appearance and saturation of the 430nm (2.9eV) blue luminescence peak observed at room temperature. The same peak is observed in originally oxygen-deficient $SrTiO_3$ layers, which relates the photoluminescence feature directly to the oxygen vacancies. This luminescence results from recombination of conduction electrons with excited

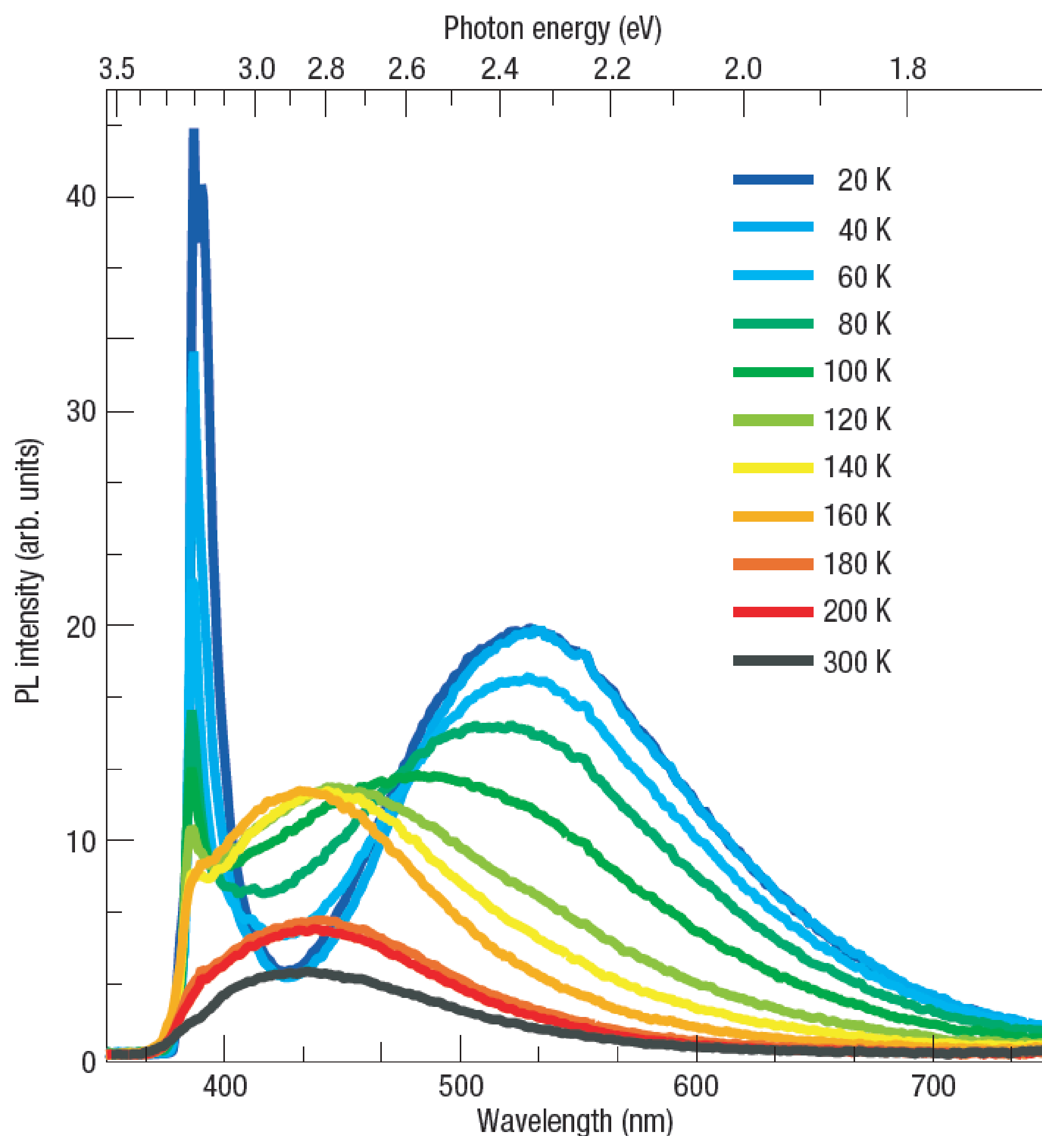


Figure 2.9: *Temperature dependence of the photoluminescence spectra obtained from $Ar^+$ irradiated $SrTiO_3$ crystals after He-Cd 325nm laser beam excitation. [108].*

holes (fig. 2.8a).

Temperature-dependent photoluminescence measurements on the $Ar^+$ irradiated $SrTiO_3$ show that while the temperature decreases, the intensity of the 430nm line gradually increases, reaching its maximum at 160K, after which it starts to disappear and two peaks at 550nm (2.4eV) and 380nm (3.2eV) begin to arise (fig. 2.9).

The green 550nm peak results from the aforementioned recombination of excited holes and electrons in self-trapped exciton states and is commonly observed even in the stoichiometric STO crystals [109] (fig. 2.8b).

The narrow but intense 380nm (3.2eV) peak is not observed in the stoichiometric $SrTiO_3$ so it is supposed to be related to the oxygen vacancy sites. As its energy is less than 0.1eV lower than the band gap of the STO, it should result from the recombination of electrons with holes through very shallow defect levels (fig. 2.8c).

#### 2.1.2.3 Titanium dioxide

Yet another set of defects are observed within the $TiO_2$ crystals. Despite extensive study of properties the material acquires upon doping, [110] research on defects in its undoped matrix remain relatively scarce. General gradient approximation calculations performed by Osorio-Guillen *et al* [102] on anatase $TiO_2$reveal that neutral vacancies of both titanium and oxygen introduces deep states in the gap (ca 0.7 to 0.8 eV below the conduction band) that cannot ionize easily (fig. 2.10).

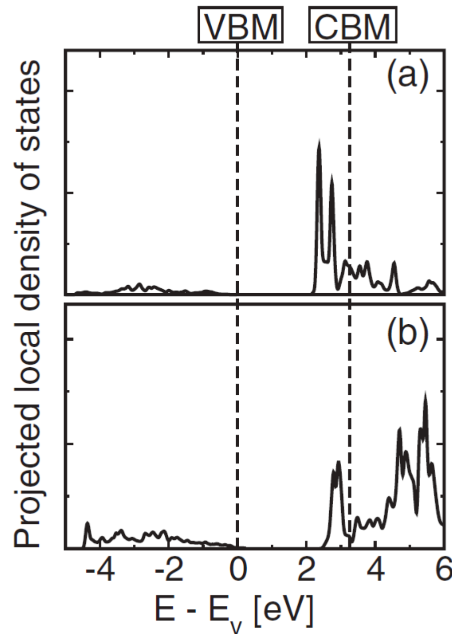


Figure 2.10: *Calculated local density of states for neutral vacancies of a) oxygen b) titanium [102].*

## 2.2 Interface Issues

Not only bulk defects have an important impact on the spin-polarized transport. As shown in the previous chapter, apart from the decay rates for specific electronic symmetries within the barrier (which are influenced by bulk defect states), the TMR signal in crystalline tunneling systems depends on one more factor: the type of symmetry states within the electrode that are injected into the insulator and

the ability of the counter-electrode to collect them. The areas within the structure that ensure the correct matching of the electron symmetries from the conduction regime within the electrode to the tunneling regime across the ultrathin dielectric are the interfaces. The former chapter described mechanics behind these processes in ideal systems. This section presents impact of interfacial imperfections on the spin-polarized transport.

### 2.2.1 Oxidation

Let's concentrate on the MgO barrier, which was well-described in section 1.4.2.1 and extensively studied in terms of its interfacial issues. Its interfacial lattice matching is crucial for the coherent electrons injection into the barrier. As will be explained within the experimental section of this thesis, the perfect Fe/MgO interface is not easy to obtain due to a risk of oxidation. This is particulary true for the lower Fe/MgO interface. Exposing the lower Fe electrode to any oxygen causes topmost Fe monolayers to oxidize and form the iron oxide layer at the interface resulting in the Fe/FeO/MgO/Fe system. Another reason for the FeO layer appearance is the oxygen interdiffusion from MgO into interfacial layers of the Fe electrode.

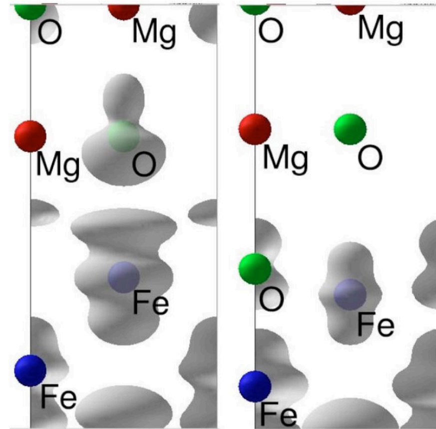


Figure 2.11: *Interfacial $\Delta_1$ symmetry DOS at the Fermi level in the majority spin channel for Fe/MgO interface without (left) and with (right) the FeO layer formation due to the Fe oxidation [28].*

As calculated by Zhang *et al* [28], at the ideal Fe/MgO interface the Fe $\Delta_1$ states effectively couple to the MgO $\Delta_1$ evanescence states in the $k_{\|} = 0$ direction, resulting in coherent tunneling of these states through the barrier (fig. 2.11a). However, in the presence of even one FeO monolayer, the density of states at the interfacial region is drastically reduced, resulting in the $\Delta_1$ Fe to MgO wavefunction hybridization that is much less effective (fig. 2.11b). Due to the O $2p$ orbital nature, oxygen sites dominate the tunneling density of states within an oxide [28]. However, as

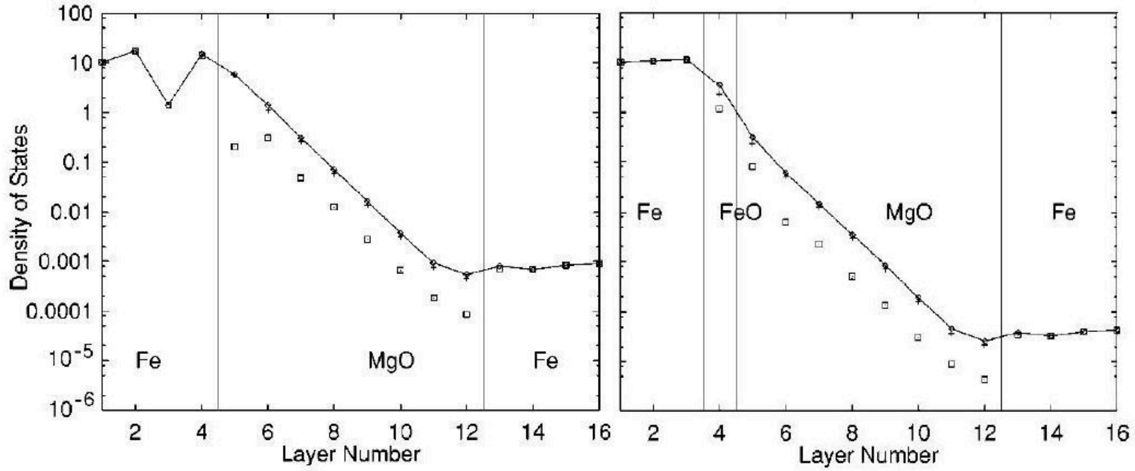


Figure 2.12: *TDOS for $k_{\parallel}$ in Fe/MgO/Fe without (left) and with (right) iron oxide layer at the lower interface. Open squares correspond to the magnesium or iron spheres in the MgO or FeO respectively. Crosses (barely visible, close to the circles connected with the line) are contributions from the O spheres. Circles (connected with the line) are summed up contributions from both. [28].*

the oxygen site wavefunction symmetry of the MgO layer is very different from that of the FeO (3*d* anti-bonding nature of conduction band in transition metal oxides [111]), coherent transport across the barrier is drastically suppressed (fig. 2.12).

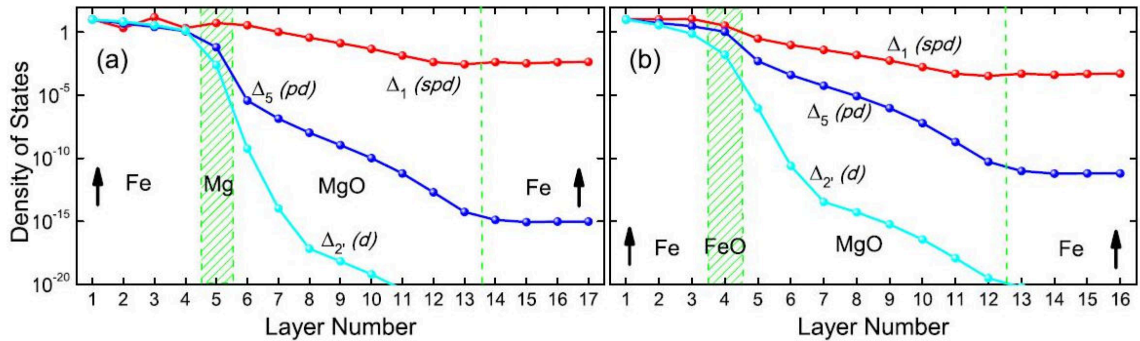


Figure 2.13: *First-principle study of tunneling density of states in parallel configuration of Fe(100)/MgO/Fe(100) system for $k_{\parallel}$ with a) Mg monolayer inserted and b) FeO formation at the Fe(100)/Mg interface. [29].*

One possibility of avoiding the appearance of the undesired FeO interfacial layer is the introduction of the Mg layer atop the lower Fe electrode [29]. The (001) in-plane Mg lattice is fixed on the bulk iron electrode lattice constant, ensuring epitaxial matching of the layers. Magnesium as a fast oxidizing element may absorb oxygen and form an additional MgO layer. This would block the oxygen diffusion into the iron and prevent the formation of the iron oxide. As shown by Wang *et*

*al*, the presence of the interfacial Mg layer (oxidized or not) does not alter the junction resistance significantly but it may enhance the transport properties as it preserves the $\Delta_1$ transmission in the P configuration, while the non-preferred $\Delta_{2'}$ and $\Delta_5$ symmetries (which exist for both P and AP configurations) decay within the magnesium layer rapidly (fig. 2.13).

## 2.2.2 Consequences of annealing

### 2.2.2.1 Interfacial oxide layer formation

It is known that appearance of the interfacial oxide barrier may be as well a consequence of annealing of the stack, as the temperature boosts the oxygen migration from the barrier towards the electrodes. Such studies were also performed within the timeframe of this thesis and the annealing impact on device properties will be presented in section 7.3. The presence of specific oxides is directly related to their formation enthalpy (see table 2.6). However, even though annealing is regarded as a trigger for the interfacial oxide formation, studies performed by Hindmarch *et al* show that in some cases (here the CoFeB/FeO/MgO) the annealing process may reduce the interfacial iron oxide layer by the Fe diffusion towards the bulk of the electrode [112].

| Oxide | Formation enthalpy (kcal/mol) |
|---|---|
| $Al_2O_3$ | -404 |
| $TiO_2$ | -228 |
| MgO | -144 |
| SrO | -142 |
| FeO | -65 |
| CoO | -57 |

Table 2.6: *Formation enthalpy of selected oxides [113].*

### 2.2.2.2 Diffusion of materials among the layers

The technologically required presence of boron in CoFeB electrodes and the need of their annealing gives rise to an additional interface-related question. There were contradicting experimental reports whether during annealing of the stack the Boron atoms diffuse towards the bulk of the electrode or in the direction of the interface [114]. Burton *et al* used *ab initio* calculations to show that it is the latter case that gives rise to the similar weakening of the wavefunction hybridization as in case of the FeO appearance (fig. 2.14, compare with fig. 2.12). On the other hand, some groups show that the boron diffusion into the barrier results in the Mg-B-O formation, which does not suppress the TMR ratio significantly [115]. For example, Han *et al*

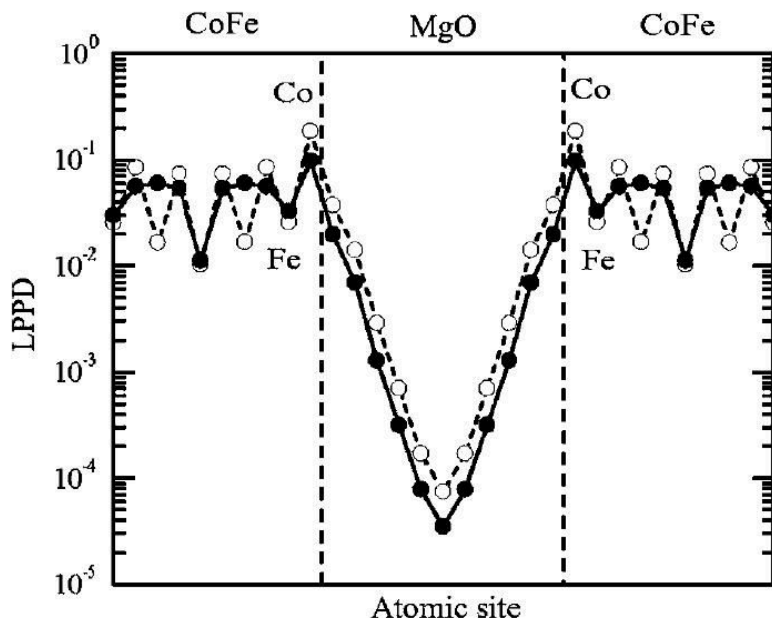


Figure 2.14: *Layer projected probability density for $\Delta_1$ symmetry in the majority-spin at $E_F$ for the Co terminated interface. White and black circles denote absence and presence of Boron, respectively. The interfacial Boron coverage used for calculations is 25%. The supercell chosen is 11 monolayers for MgO and CoFeB each [114].*

show that boron diffusion into the barrier during annealing forms the stoichiometric $B_2O_3$ which does not create any mid-gap states in the barrier, but reduces the barrier height with increasing concentration of B [116].

The annealing temperature is the key parameter to obtain correctly crystalized, high-TMR yielding junctions. As shown by Karthik *et al* [117], annealing above 500°C leads to the diffusion of atoms from outer layers into the barrier and loss of the bcc-CoFe textured structure in the bottom CoFeB electrode. Moreover, such high-temperature annealing leads to the diffusion of material from the AF layer (mostly Mn) into the barrier which results in substoichiometry of the former, yielding its reduced pinning strength. Appearance of the diffused material within the barrier also significantly affects the TMR ratio (fig. 2.15) [84]. On the other hand, recent experiments by Larson *et al* show that annealing at up to 350°C does not cause the Mn diffusion from the AF layer into the barrier, but rather its segregation at the interface, which does not alter the TMR signal greatly [118].

### 2.2.3 Uncertain interfacial termination

Materials composed of alternating planes present yet another challenge regarding the interfacial quality. In case of $SrTiO_3$, the interfacial $TiO_2$ termination was calculated to be more energetically favorable than the one of the SrO [119]. However,

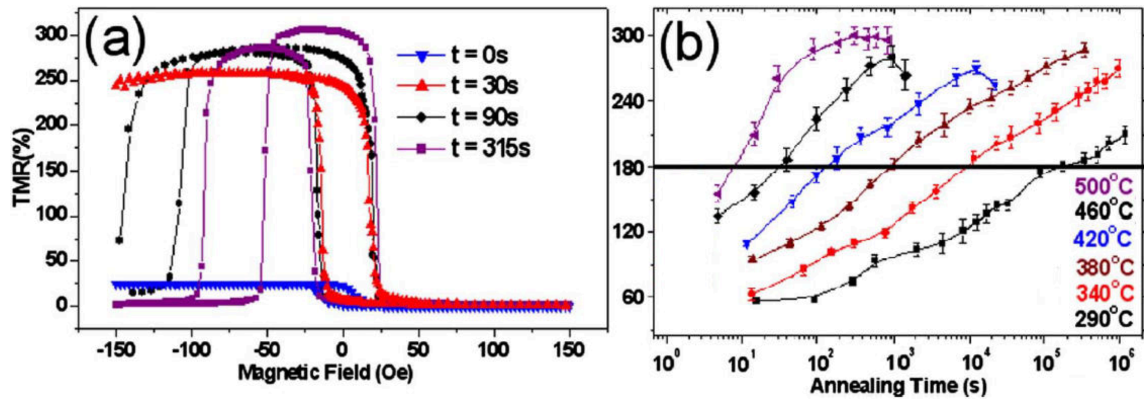


Figure 2.15: *Annealing impact on the TMR ratio of a) annealing at 500°C for different time durations and b) different temperatures and times of annealing. The structure studied was CoFe(2)/IrMn(15)/CoFe(2)/Ru(1.7)/CoFeB(3)/MgO(3)/CoFeB(3). Horizontal line on figure b) at 180% TMR value marks the ratio acceptable for practical applications [84].*

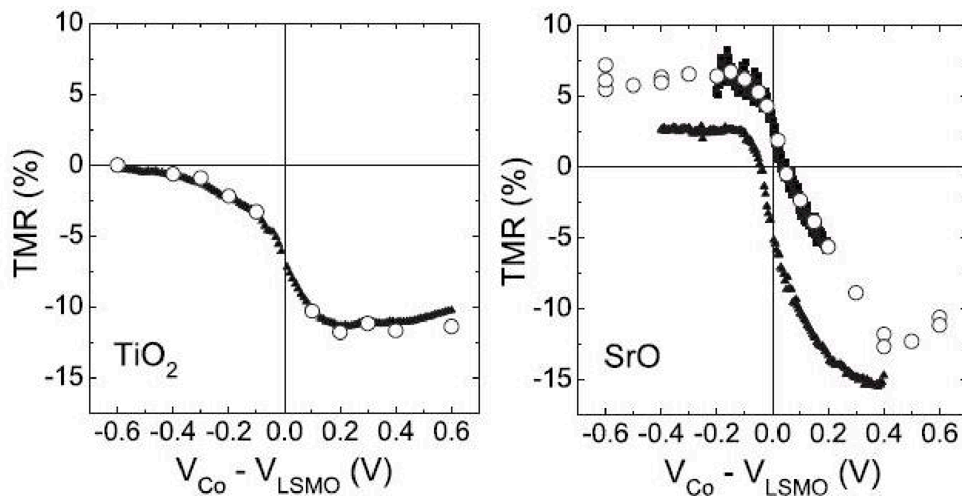


Figure 2.16: *TMR versus applied voltage at 90K for $TiO_2$ (left) and SrO (right) terminated STO/Co interface in LSMO/STO/Co junctions. Solid triangles represent data from I-V curves, open circles refer to magnetic field sweeps at given bias. The SrO graph shows data for two different junctions. [44].*

the uncertainty of this layer has a crucial impact on the behavior of the system. Studies performed on LSMO/STO/Co systems by Vera Marun *et al* show that, depending on the termination layer, the magnetoresistance value may even switch its sign (fig. 2.16), suggesting that the mixed $TiO_2$ and SrO interface would yield a total TMR being an average of both positive and negative components, obviously

much lower than expected. They also find that the effect is strongly affected by the interfacial oxygen concentration [44].

## 2.3 Electromigration and bias-crafting

In case of perfect epitaxial systems, the momentum transfer between propagating electrons and atoms forming the crystal network is negligible, such that the electron wavefunction symmetry is conserved. However, the symmetry is not conserved at grain boundaries and defects within lattices of both metal and insulator. It is at these places that the bonding energy of atoms is much lower than in the perfect crystal, which results in the transfer of momentum of a propagating electron to an ion, which in turn yields a force affecting it in the direction of electron flow. As this force rises due to the bombardment by electrons, it may become sufficient enough to overcome the bonding energy of the ion and relocate it. This drift of atoms within the material is called *electromigration*. The phenomenon is especially pronounced when high current densities flow through the material, which is true in case of micrometer-sized magnetic tunnel junctions. The transport of the material is crucial for both bulk and interfacial regions of junctions. For example, it is known that the electromigration causes a redistribution of oxygen vacancies within perovskites [120].

The term *memristor* was coined to describe a device whose resistance changes as the consequence of an applied current and persists after the current flow stops. Strukov *et al* described a Pt/$TiO_2$(10nm)/Pt device, in which half of the thick barrier is initially oxygen-deficient [121]. Oxygen vacancies act as charge carriers, meaning that the depleted layer has a much lower resistance than the stoichiometric one. When an electric field is applied, oxygen vacancies begin to drift, changing the boundary between both $TiO_2$ layers. In these terms, the *memristance* effect is defect-based.

Bowen *et al* studied LSMO/STO/$Co_{1-x}Cr_x$ junctions with x being between 0.04 and 0.2. Junctions were electrically unstable even at low temperature and successive voltage cycling led to a reversible change in amplitude and sign of the TMR. The authors find an evidence of Cr segregation to the STO/CoCr interface and its oxidation [122]. The interfacial modification is suggested to be the reason of of the TMR sign inversion (fig. 2.17), while the lower system resistance may result from the formation of O vacancies. This suggests an appearance of a conducting filament within the barrier which could result from the electrons trapping at oxygen-deficient sites [123, 124]. The observed effect is reversible, so the *bias-crafting* of junctions by applying larger currents can become a tool to engineer properties of devices. Moreover, these results were the first to demonstrate the possibility of incorporating memristance and magnetoresistance within a single device.

The research field of memristance is developing fast and gives many interesting

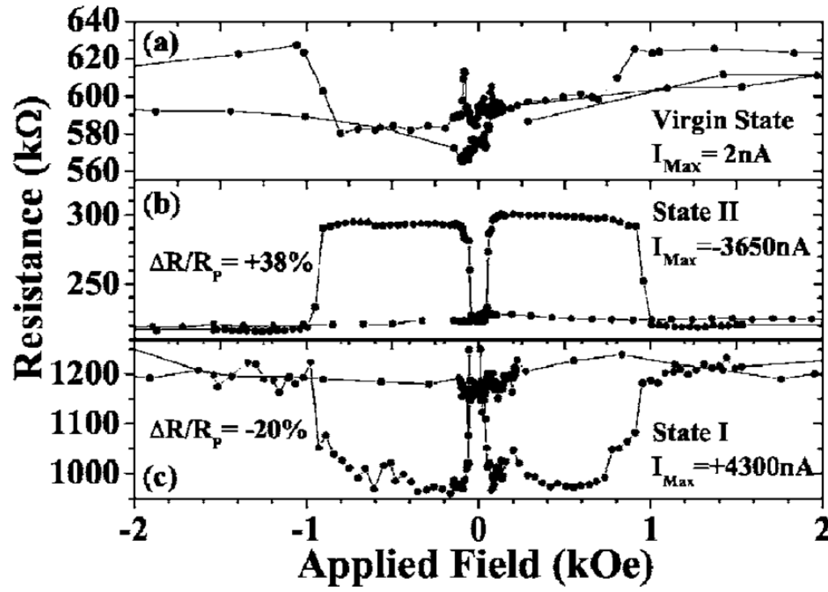


Figure 2.17: *RH measurements on LSMO/STO/$Co_{80}Cr_{20}$ in 4K (a) in its virgin state and (b) after subsequent high-bias crafting towards the negative and (c) positive currents [122].*

results [125]. A colleague of mine, Nabil Najjari, performed an extensive study on resistive switching in MgO-based devices with Cr [126, 127] and V [128] added at interfaces or in the bulk of the barrier. His group assumed an interesting hypothesis that the memristance in these systems is an effect of charging, rather than of the electromigration [129].

## 2.4 Defect-induced magnetism

Recent studies show that the presence of vacancies within crystalline insulators or semiconductors may result in the appearance of yet another phenomenon - magnetism. This was previously attributed exclusively to an explicit doping of materials and the associated research fields of diluted magnetic semiconductors and oxides abbreviated DMS and DMO, respectively [130]. The first one emerged once the low-temperature interplay between magnetization texture and dynamics with carrier population and currents were discovered in (Ga,Mn)As, p-(Cd,Mn)Te and similar structures [131]. The second field is generally acknowledged to have started when the first report of the room-temperature magnetism on Co-doped $TiO_2$ was published by Matsumoto *et al* [132].

In a recent experiment, Martinez-Boubeta *et al* observe 460nm (2.7eV) emission from Mg-deficient MgO crystals, whose delay results from trapping of holes at magnesium vacancies [133, 134]. Samples from which the emission occurs also exhibit

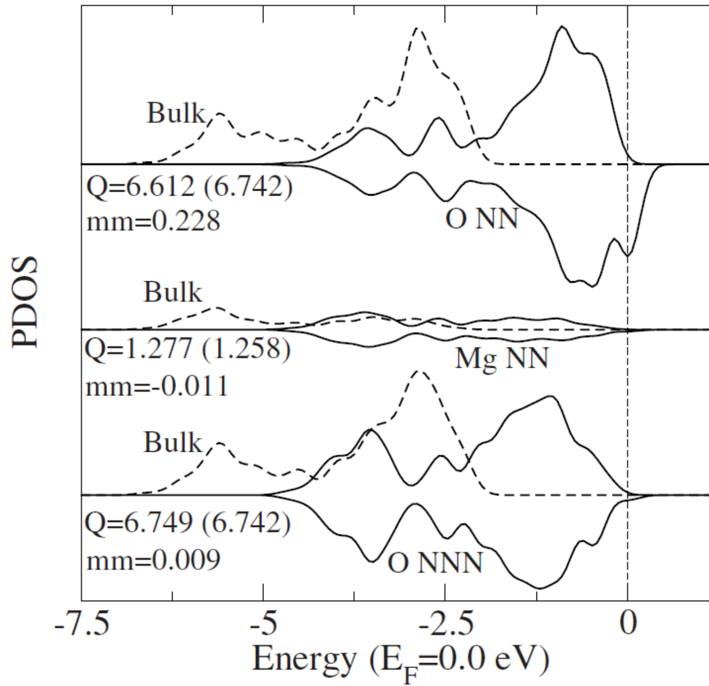


Figure 2.18: *Projection of DOS (PDOS) simulation around a Mg vacancy for its oxygen nearest neighbor (top), magnesium nearest neighbor (middle) and oxygen next nearest neighbor (bottom) shown as continuous lines, decomposed in major (positive) and minor (negative) components. Dashed lines show respective non-spin decomposed PDOS in absence of the vacancy. Magnetic moment 'mm' of respective atom is given in Bohr magnetons; Q stands for partial atomic charge (Mulliken population) given in $|e|$ and is compared to its bulk values (in parenthesis) [133].*

room-temperature ferromagnetic behavior, which in turn arises from the spin polarization of $2p$ electrons of oxygen atoms around magnesium vacancies (fig. 2.18). The ferromagnetic ordering is almost independent on the sample thickness within the 10-40nm range (fig. 2.19). Moreover, despite the magnetic properties, it remains transparent in the visible region, which makes it an intresting candidate for magneto-optical applications.

## 2.5 Conclusions

Microstructural features are of crucial importance for unconventional magnetic properties of both magnetic tunnel junctions and dielectric crystals. Despite multiple doping experiments yielding excellent results on diluted magnetic semiconductors and oxides, it becomes clear that the ability to create, control and engineer defect states within the oxide barrier is of utmost importance for further progress within the wide field of spin-filtering across inorganic oxide-based devices. This thesis aims

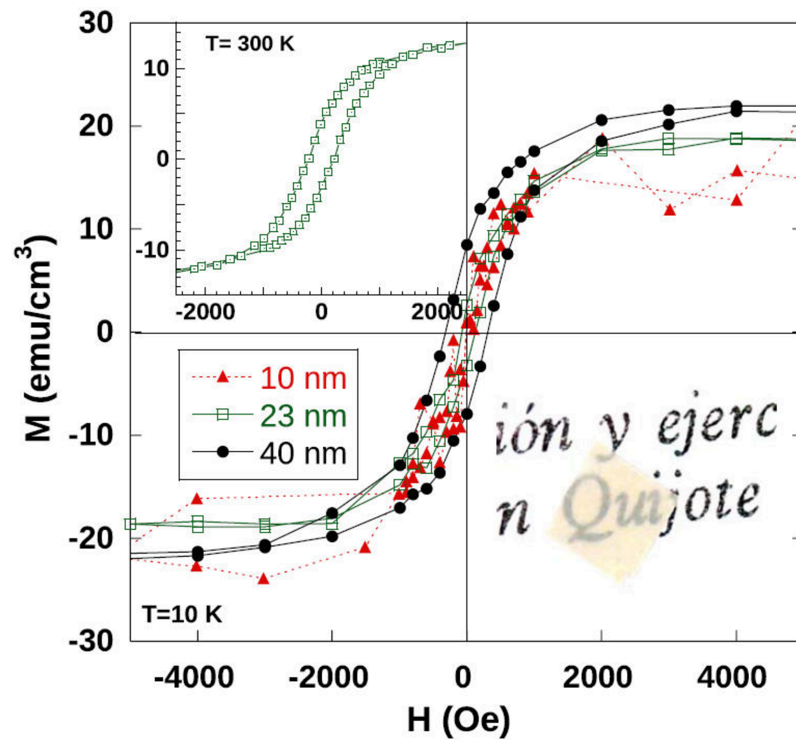


Figure 2.19: *Low (main) and room temperature (top-left inset) magnetization measurements on MgO(001) thin films of different thickness grown atop the $SrTiO_3$ substrates. Magnetic field was applied in the film plane. Data were corrected for contribution of the substrate. Bottom-right inset picture shows that the sample remains transparent in the visible region [133].*

to shine additional light on defect-related issues in magnetic tunnel junctions and materials on which they are based, with the hope that it may reveal yet elusive aspects of these structures and help the extensive worldwide studies to make a further step ahead.

# Part II

# Experimental realization

# Chapter 3

# Sample growth techniques and development

This chapter describes different growth techniques used in order to fabricate samples studied within the timeframe of this thesis. The first section briefly introduces the pumping systems used in order to create and maintain the ultra-high vacuum required for the desired growth of the structures. The second section describes the procedure and results of substrate preparation before *The Hybrid System* deposition, with which the IPCMS is equipped. This system is composed of different deposition chambers: sputtering, evaporation and OMBE (organic molecular beam epitaxy). The sputtering deposition chamber of The Hybrid System was extensively used for the fabrication and optimization of the growth conditions and defect control. The CoFeB based junctions were grown at the *Institut Jean Lamour* in Nancy as result of a collaboration with M. Hehn. Both of these sputtering protocols are presented in the third section. The evaporation chamber of the Hybrid System was to a lesser extent used for the sample capping so this thin film deposition is described in section four. During this thesis, magnetic tunnel junctions containing $SrTiO_3$ and $TiO_2$ barriers were also studied, as were structures including $La_{0.7}Sr_{0.3}MnO_3$ electrodes, all deposited by pulsed laser deposition (PLD) through an internal IPCMS collaboration with Silviu Colis from the *Departement de Chimie et des Materiaux Inorganiques* (DCMI). The PLD deposition is described in the fifth section of this chapter.

## 3.1 Ultra-high vacuum pumping systems

In order to fabricate ultra-thin structures of high quality, the deposition has to be performed in the ultra-high vacuum (UHV) range, preferably of at least $10^{-9}$ mbar order, guaranteeing minimum presence of undesired particles in the chamber during the growth. Along with the standard, mechanical rotary pumps that yield pressures down to $10^{-3}$ mbar, a number of specialized UHV dedicated pumping techniques were used within the timeframe of this thesis.

**Turbomolecular pumps** contain very rapidly (up to 90000Hz) spinning rotors, with which molecules and particles from the inlet side of the pump collide, thus are given a momentum in direction of the exhaust. These pumps are usually designed to operate below $10^{-2}$ mbar and are capable to reduce pressure in the chamber down to $10^{-9}$ mbar range.

**Ion pumps** use a high electrical potential (more than 3kV) in order to ionize gases. A strong magnetic field, induced by permanent magnets within the walls of the pump, then accelerates the ionized species and embeds them into the walls of the pump. Ionic pumps do not require neither moving parts nor oil, thus they are not only dry but vibration-free as well. Under ideal conditions, ionic pumps are capable of reaching pressures even down to $10^{-13}$ mbar range.

**Titanium sublimation pumps** contain titanium filaments from which Ti atoms sublimate once a high (up to 40A) current is applied to them. Sublimated titanium is then deposited on internal surfaces of the chamber and starts to attract and trap particles. The most common reaction is the attraction of oxygen and the formation of solid $TiO_2$, leading to the pressure reduction. Obviously, saturation is reached after a certain time, so repetitive titanium sublimations have to be performed in order to ensure presence of clean and active Ti getter on internal walls of the chamber. The drawback of the titanium sublimation is that it cannot be performed in a direct vicinity of the sample, as do to so would cause the Ti atoms to be incorporated into the sample being grown.

**Bake-out** of the entire system is performed each time the chamber is opened and exposed to external atmosphere. Normally, contamination and particles adhered to surfaces can degas for extended period of time. As outgassing is much faster in higher temperature, the chamber needs to be wrapped up with a resistance heater wire and baked out for a few of days at high temperature (100°C was used during the thesis so as to address the main contaminant, i.e. water). Additional external aluminium layer covering all the parts being baked out is recommended in order to prevent the heat from dissipation into the environment.

## 3.2 Substrate preparation

Ahead of any deposition, various organic and inorganic contaminants should be removed from the surface on which the structure is to be grown. This should be done especially because cutting the substrate to the desired size could cause the cut material to be redeposited on top. The MgO substrates were initially cleaned in subsequent acetone then ethanol baths, at least 10 minutes each, both enhanced by ultrasonic vibrations.

The extended study of MgO substrates used within The Hybrid System showed that such basic form of cleaning was not sufficient to guarantee perfect surface. After the initial cleaning and insertion into the hybrid system, the substrates were first

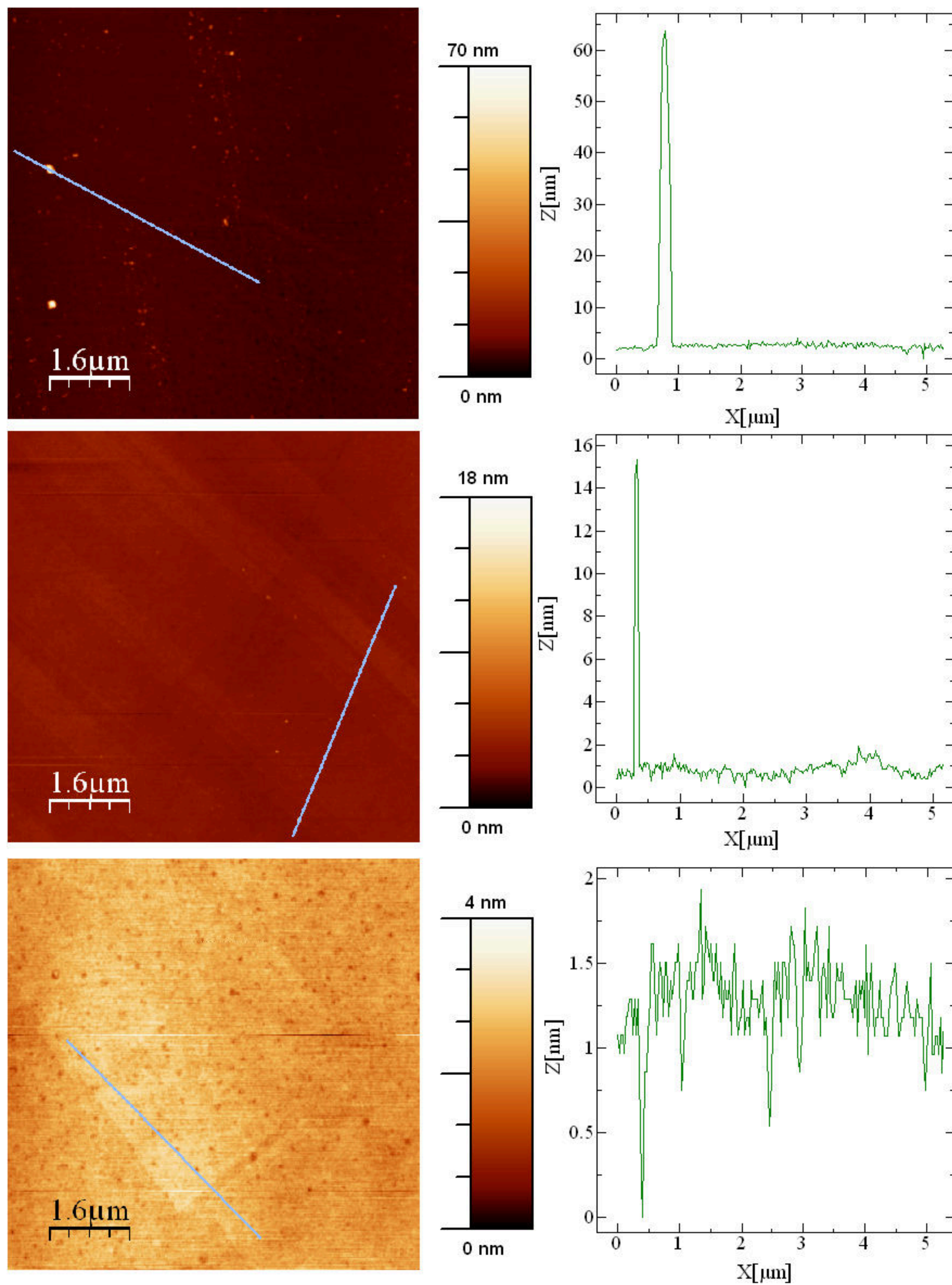


Figure 3.1: *Atomic Force Microscopy topographical maps of the raw (top), annealed (center) and etched then annealed (bottom) MgO substrate. Atomic steps are visible on the latter two.*

*in-situ* $Ar^+$ etched for 10 minutes. During this procedure, the sample is rotated in

order to ensure uniformity of the etching. This was followed by subsequent 200°C 1h pre-bake and 550°C 4h annealing, finally resulting in contamination-free surface. All of these steps were carefully studied and confirmed by Atomic Force Microscopy (AFM) measurements. As shown on the fig. 3.1, annealing alone is not sufficient to remove the surface contamination. On the other hand, the etching procedure increases concentration of up to 1nm deep holes within the MgO crystal which had to be averaged out with the buffer MgO layer, as described in section 3.3.1.

## 3.3 Sputtering

Sputtering is a thin film UHV deposition method in which argon gas arriving in the chamber becomes ionized and $Ar^+$ ions are accelerated towards the *target* - a solid disc of a pure material. Incident ions hit the target surface and cause cascades of collisions inside, exchanging momentum among the particles. If the energy that a target atom gains is larger than its binding energy, it can be ejected from the target, can propagate towards the duly placed sample holder and deposited on the sample upon arrival.

*Magnetrons* are used as the sputtering ion sources inside the system [135]. These devices consist in a magnet placed below the target. Incoming $Ar^+$ ions are trapped along helical magnetic field paths, leading to a multiplication of sputtering collisions with the target material. In case of magnetrons containing an insulating target, radio-frequency power supplies have to be used in order to avoid the charge accumulation. The high rate at which the bias between the electrodes is varied, as well as the its impedance-matching, can lead to high-quality insulating films. The advantage of the sputtering is that even materials with high melting points can be deposited with this deposition method. Moreover, a large and thick target contains an amount of material sufficient for a long period of maintenance-free usability.

### 3.3.1 The hybrid System sputtering

The custom-made sputtering setup used within the timeframe of this thesis is capable of deposition of iron, cobalt (thus CoFe as well) and magnesium among metals, as well as the MgO insulator. Due to the chamber design, only three sputtering sources may be installed in the chamber at the same time, which implies that besides the compulsory Fe and MgO targets, only one out of Mg or Co could be used as the third one within the same fabrication batch. The system is equipped with the UHV sample heater and the $Ar^+$ etching gun, both extensively used for the aforementioned *in-situ* substrate preparation before the deposition. The sputtering deposition rates were calibrated using the Sigma SQM-160 quartz balance monitor. The system is also equipped with a residual gas analyzer (RGA), allowing the precise control of partial gas pressures within the chamber. The base pressure of $2 \cdot 10^{-9}$ mbar is

achieved by simultaneous usage of rotary, turbomolecular and titanium sublimation pumps.

| Material | Deposition speed (nm/m) | Deposition pressure ($10^{-3}$ mbar) | Magnetron power (W) |
|---|---|---|---|
| Co | 1.2 | 1.3 | 20 |
| Fe | 1.2 | 1.3 | 20 |
| Mg | 2.4 | 1.3 | 20 |
| MgO | 0.18 | 1.0 | 50 |

Table 3.1: *Optimized Hybrid System deposition speeds and conditions for specific materials.*

On clean substrates, a 6nm thick MgO buffer layer was deposited. This was in order to further ensure sample flatness and crystallinity but also to trap any possible carbon impurities underneath. All of the depositions (excluding the ones requiring a *shadowmask* as explained in section 4.1) could be performed with the sample wafer rotating in order to ensure uniformity of the deposited material. Details of the optimized deposition conditions for all of the sputtered materials are presented in table 3.1.

Atop the MgO buffer layer, the iron **bottom electrode** material is deposited. Studies performed at the IPCMS showed that it is essential to anneal the lower electrode at this point [136], that is before the MgO barrier deposition. Indeed, since the lower Fe layer growth is of Volmer-Weber type (island formation instead of layer-by-layer growth), subsequent MgO deposition can lead to conductive pinholes. Annealing of the as-deposited electrode before MgO growth not only dramatically improves the quality of the subsequently deposited barrier (fig. 3.2), but also leads to better epitaxy and better-defined magnetic hysteresis loops of the entire system (fig. 3.3). The study revealed that the sufficient annealing condition for the iron electrode is 1h at 550°C.

Post-growth annealing of the lower electrode led to an interfacial quality problem. The pressure within the chamber rises during the high-temperature annealing due to outgassing of certain elements in the vicinity of the heater, which results in the contamination of the exposed interface for the duration of the annealing (see results in section 7.2). Unfortunately, due to the chamber design, the titanium filament directly faces the sample, preventing the use of this pump in presence of the sample, as to do so would incorporate Ti atoms into the sample structure. Within the timeframe of this thesis, a solution in the form of an elbow-like extension to the chamber was proposed, which would allow the titanium pump to be in constant use, without the risk of Ti atoms being incorporated into the sample. However, during the time of writing, the solution has not been fully implemented yet.

As previously mentioned (fig. 2.13), the iron oxide layer at the Fe/MgO interface can adversely affect the spintronic response of the system. Consequently, since a

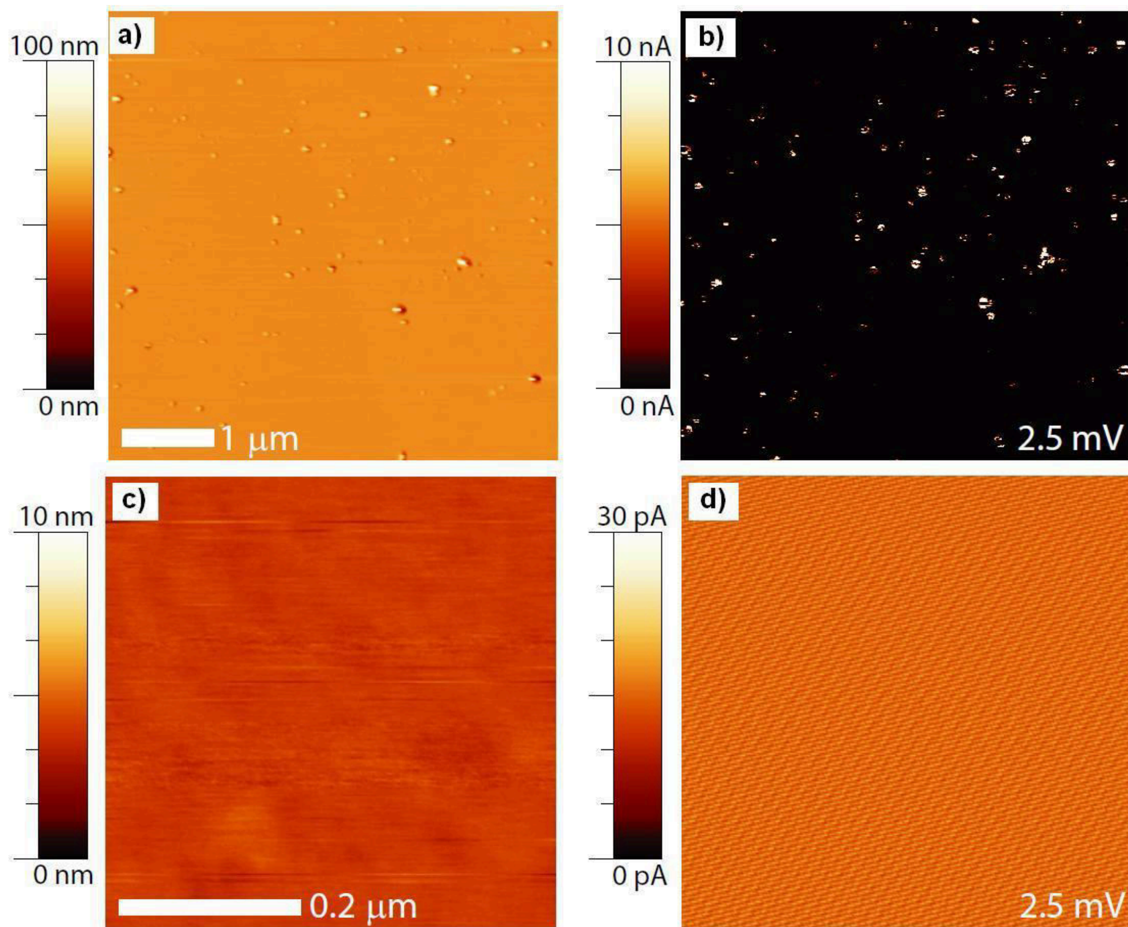


Figure 3.2: *Conductive Atomic Force Microscopy topographical (left) and local current (right) maps of non-annealed (top) and annealed (bottom) Fe(20)/MgO(2.1) grown on the MgO substrate. Note differences in scales and that the local current hotspots correspond to the topographic hills. The C-AFM measurements were done at 2.5 mV [136]*

pure Fe/MgO interface is extremely difficult to realize experimentally at the atomic scale and Wang *et al* demonstrated that Fe/Mg/MgO interface is much more favorable than the Fe/FeO/MgO [29], we also attempted to insert the Mg interfacial layer. Because the oxygen interdiffusion into a few topmost monolayers of the lower electrode would cause its oxidation during the barrier deposition, it is actually favorable that it is the interfacial Mg that oxidizes, which may even result in additional MgO monolayers creation. For these reasons, a 2 monolayers-thick (4Å) Magnesium layer was deposited atop the bottom electrode.

Once the bottom electrode is completed, the MgO **barrier** can be deposited. This is done from a single MgO target using a radio-frequency magnetron supplied with an impedance-matching box. It was noticed that the initial fast high-power

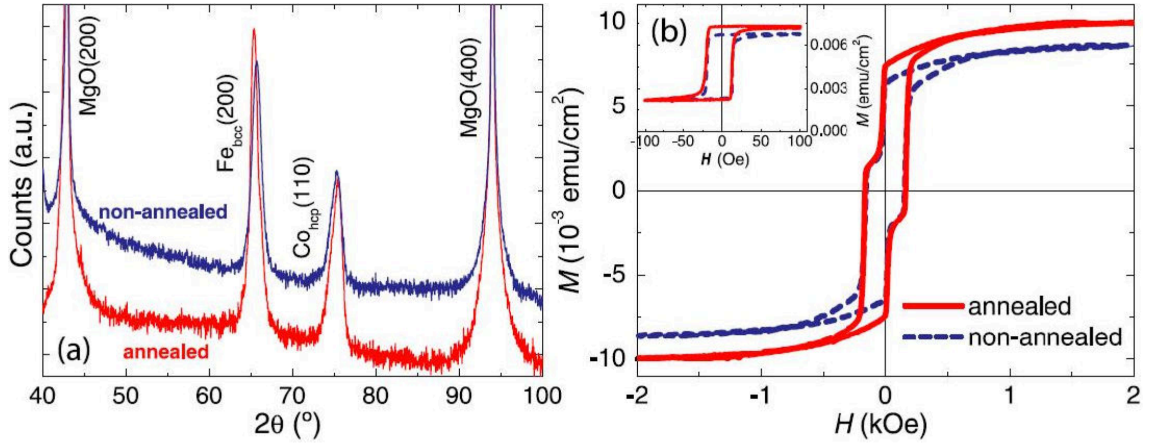


Figure 3.3: *a) Monochromatic x-ray diffractometer (XRD) and b) alternating gradient force magnetometer (AGFM) measurements along the Fe(100) easy axis for MgO/Fe/MgO/Fe/Co/Au stacks with non-annealed (blue dashed) and annealed (red solid) lower Fe electrode. The b) inset shows minor magnetization loops. [136]*

deposition causes substoichiometry of the target - it became oxygen-deficient (dark color) and cracks appeared on it as well. Twice slower, more diffusive growth rates were established. Deposition of the MgO barrier, a crucial element of the system, was studied extensively. The Ar-sputtering of the MgO barrier is performed with or without the presence of oxygen in the chamber, with an aim to control defect types within the barrier. We present these results in section 7.1.

Once the MgO barrier is deposited, the **upper electrode** can be grown atop the barrier. Depending on the sample stack, this is either iron (Fe), iron then cobalt (Fe/Co) or cobalt-iron alloy (CoFe). Despite the fact that the crystalline structure of Cobalt is hexagonal close-packed (*hcp*), CoFe can maintain the *bcc* structure up to a Cobalt/Iron ratio of 70/30 within the alloy. This two-compound material is not sputtered from a single target, but from separate Fe and Co combined sources. As mentioned before, Co and Mg targets can not be mounted in the chamber simultaneously due to the limited space of the chamber. This requires to give up either Mg spacer at the Fe/MgO interface or to grow iron only upper electrode. As the former was rather unfavorable, the latter case was chosen. However, in order to ensure ferromagnetic decoupling between the electrodes, they have to be grown with substantially different thicknesses.

The essential structure of the magnetic tunnel junction is at this point done. However the iron as a very reactive element would oxidize fast. The whole stack needs to be covered with a non-oxidizing metallic capping layer for which Au was chosen. In order to do so the samples are transferred to the *evaporation* chamber of the Hybrid System without breaking the vacuum. This is described in section 3.4.

### 3.3.2 Nancy Sputtering

Samples in which the MgO spacer is sandwiched between the CoFeB electrodes were grown as the result of a collaboration with Michel Hehn from the *Institut Jean Lamour* in Nancy, France. Only the general growth procedure is presented in the manuscript. For details, please refer to [85].

As CoFeB-based MgO systems do not need to be deposited on a crystalline substrate because they crystallize during the post-deposition annealing process (see section 1.6.2), the growth was performed on the amorphous Corning 1737 glass. In order to assure uniformity of the samples, samples were reversibly translated laterally during the growth. A tantalum (2nm-thick) layer was used as the flattening layer, followed by Co(10nm) to improve further texturization due to good adhesion of cobalt to tantalum. This was followed by an IrMn(7.5nm) antiferromagnet, whose role will be described shortly. Afterwards, the CoFeB(4nm)/MgO(2.5nm)/CoFeB(4.5nm) main tunneling structure was deposited, with each material sputtered from a single target. The CoFeB proportions are $Co_{0.4}Fe_{0.4}B_{0.2}$. The structure was capped with the Ta(5)/Pt(5) capping layer.

As already described in section 1.6.2, the CoFeB-based devices are annealed post-growth in order to obtain the textured crystalline MgO barrier and the interfacial areas of the electrodes. However, the annealing step plays yet another role. As the system was optimized for deposition of IrMn antiferromagnetic material rather than a synthetic ferrimagnet described in section 1.6.2, pinning of the lower electrode is achieved by annealing of the sample for 1h at 300°C, that is above the Neel temperature of the IrMn antiferromagnet yet below the Curie temperature of the CoFeB electrodes with the constant 200Oe magnetic field applied in plane of the sample. This enables the alignment of the IrMn antiferromagnetic and CoFeB ferromagnetic domains upon the subsequent cool-down, and thus exchange bias the lower electrode.

This growth technique has certain drawback when compared with the one proposed by Yuasa *et al*, namely the Mn diffusion during annealing. Mn-deficient antiferromagnet has its pinning strength decreased, while its appearance within the MgO barrier influences the coherent transport and reduces value of the magnetoresistance. The effect is more pronounced as the annealing temperature or time increases [84]. We will describe in detail our study on the defects generated with the recrystallized MgO due to this post-annealing process in section 7.3.

Apart from magnetic tunnel junction stacks, samples lacking the top electrode were also grown. Lower electrodes followed by MgO(2.5) or MgO(50) insulator were fabricated for optical studies of the barrier. Their respective counterparts were also subsequently annealed in order to study the annealing impact on optical properties of the barrier.

## 3.4 Evaporation

Evaporation is an UHV thin film deposition method in which a crucible with a solid source material is heated up to its melting or sublimation temperature, beyond which evaporation begins. Due to the ultra high vacuum within the chamber, the mean free path of the evaporated particle is long enough to reach the sample without or with very few collisions during its flight, then it condenses on the surface.

As mentioned before, sample transfer among chambers of The Hybrid System occurs without breaking the vacuum. Thus, the topmost upper electrode layers (Fe, CoFe or Co) were not subject to oxidation. The samples were then covered with a 3nm thick Au **capping layer**, whose evaporation was carried out at 1138°C to yield a 7.3Å/min deposition rate. The metallic nature of this layer was required in order to provide an electrical contact after the sample processing (see section 4.5 for details).

In order to further enhance the crystalline quality of the stack [51], the sample was post-annealed for one hour at 200°C. Then the capped sample is safely taken out of the ultra-high vacuum.

## 3.5 Pulsed laser deposition

The $SrTiO_3$ and $TiO_2$ based samples, as well as the ones containing LSMO electrodes, were fabricated using the Pulsed Laser Deposition (PLD) technique by Silviu Colis from the *Departement de Chimie et des Materiaux Inorganiques* as a result of an internal collaboration within the IPCMS.

While the PLD growth is relatively easy to realize, the multiple-step physics underneath is much more complex.

A laser beam is focused on a target placed under vacuum and made from the material to deposit. Depending on the laser wavelength and the optical properties (reflection and absorption) of the target material, the beam penetrates a few nm into the target. If the laser energy is above a certain threshold value, the energy transferred from the laser to material at the surface of the target is large enough to heat up the surface and the vaporization occurs. Atoms, ions, clusters etc. are therefore ejected from the target and the material expands as a plasma. The expansion parameters of the plasma are driven by deposition conditions, especially the presence of gases and working pressure within the chamber. High-speed and consequently high-energy particles can sputter material already deposited on the sample which may alter its growth rate and (more importantly) stoichiometry and formation structural defects. Especially in case of oxides, slowing down the growth rate by filling the chamber with oxygen would ensure not only uniformity of the sample but also its oxygen stoichiometry.

The laser used for the PLD deposition during this thesis was a KrF excimer laser with the wavelength of 248nm. The frequency and the energy density were 10Hz and

$1.5 J/cm^2$, respectively. The base pressure was below $5 \cdot 10^{-8}$ mbar. For all structures fabricated this way, STO(001) crystalline substrates were used. In order to desorb surface contaminants, the substrates were annealed for 15 minutes at 500°C. The base pressure prior to deposition was below $2 \cdot 10^{-7}$ mbar for high-temperature deposition and below $9 \cdot 10^{-8}$ mbar for the deposition at room-temperature. Such relatively high pressures may result from the fact that due to a lack of a separate loading chamber, the growth chamber is directly exposed to the atmosphere during the sample loading, after which it is not baked out.

In order to induce a well-defined crystalline structure, the lower magnetic electrode is usually deposited at high temperature T=320°C. As for the barrier, it is deposited at room or at high temperature (especially if the bottom electrode is an oxide). The top magnetic electrode is deposited at low temperature in order to avoid diffusion at the magnetic/non-magnetic interfaces. A 2nm Ta capping layer is grown atop the structure in order to preserve it from any further oxidation.

### 3.5.1 Reflection high-energy electron diffraction

The PLD chamber is equipped with a reflection high-energy electron diffraction (RHEED) system that allows to monitor *in-situ* the sample quality. In this growth control technique, an electron gun generates an electron beam that impinges upon the sample surface at only a few degrees angle. Once reflected, the electrons reach the detector at their specific diffraction angles where they interfere constructively or destructively, giving rise to a specific diffraction pattern at the detector screen that is directly related to the reciprocal lattice of the material. Analysis of the RHEED pattern yields information about the roughness, stoichiometry and crystallinity at the current stage of the growth. The sharpness of peaks increases with the surface crystalline quality.

# Chapter 4

# From samples to devices

Different techniques of sample growth were presented in the last chapter. Once completed, these samples were processed into working devices. This chapter presents two different ways of device pattering. The first method, called the *in-situ* type, is available exclusively for The Hybrid System sputtered devices and relies on sputter deposition through *shadow-masks*. This technique does not require the sample to undergo long and difficult *photolithography*, which is presented in the second section. The latter method, at the cost of its complexity, yields excellent spatial resolution, which allows junctions fabricated this way to be of much smaller sizes. Moreover, it results in a large number of devices per sample.

## 4.1 In-situ pattering

Within the timeframe of this thesis, the *in-situ* patterning technique was established for the Hybrid System sputtering deposition. This included mounting of an additional arm inside the UHV system with a **shadowmask** system attached to it. The shadowmask arm can be precisely moved along all three dimensions, coming in and out of the contact position. This makes it possible to deposit consecutive materials with desired patterns atop each other.

The *in-situ* patterning parameters of deposition are essentially same as for the standard full-layer deposition, except that the deposition occurs while the sample is in contact with the shadowmask, which prevents the sample rotation due to the system construction. This leads to a degree of shadow deposition along the edges of the motif. Moreover, as can be seen from the schematic figure 4.1, the thick (no less than 20nm) lower electrode edges cannot in principle be covered properly with the thin barrier material (never more than 3.5 nm). In order to avoid short-circuits between top and bottom electrodes along these edges of the bottom electrode, an additional step was introduced. A patterned, 40nm-thick **technological MgO** was deposited just after the barrier growth step, leaving only an opening in the middle of the bottom electrode through which the top electrode material could contact the

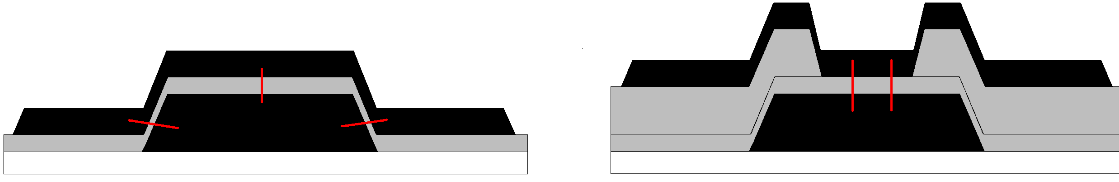

Figure 4.1: *Schematic illustration of the current leak at the electrode edges (left) and its prevention by introduction of the thick technological MgO (right). Colors depict the insulating substrate (white), conducting electrodes (black) and both barrier and technological MgO (grey). Red lines show the current flow channels for both cases. Note that the picture is not to scale.*

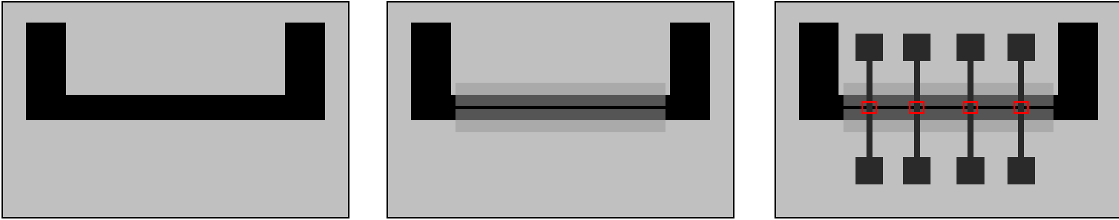

Figure 4.2: *Schematic illustration of the* in-situ *patterning during the deposition. Left: The lower electrode deposition; center: thin barrier growth (transparent) followed by the technological thick MgO introduction in order to cover the lower electrode edges; right: top contacts fabrication and the additional thin MgO capping (transparent). The red squares mark the junctions position.*

barrier directly on the barrier. The technological MgO step effectively defined the junction length and, along with the width of the bottom electrode, consequently the device area (fig. 4.2).

Since the Evaporation chamber presently lacks a shadowmask system, Au deposition in that chamber was not used. Instead, the samples were covered with the insulating 3nm thick MgO. On the other hand, the insulating nature of the MgO capping layer did not prevent accessing the conductive material below. The reason is that the shadowmask patterned sample did not have to be processed by the optical lithography but directly underwent the on-the-chip bonding. The wedge bonding used during this thesis easily bypasses the 3nm thin insulating MgO atop the contacts (see section 4.5).

Due to the limited safe thickness of the bottom electrode (technological MgO issue), its width was set to 650$\mu$m, large enough to ensure low resistivity (40$\Omega$). Such high value did not affect the MTJ properties, as their effective area was defined by 50$\mu$m or 100$\mu$m (depending on the mask pattern) opening in the technological MgO and the the 50$\mu$m width of the top contacts. Due to the fixed value of the top contacts width, their low resistance (100$\Omega$) was achieved by high flexibility of thickness augmentation.

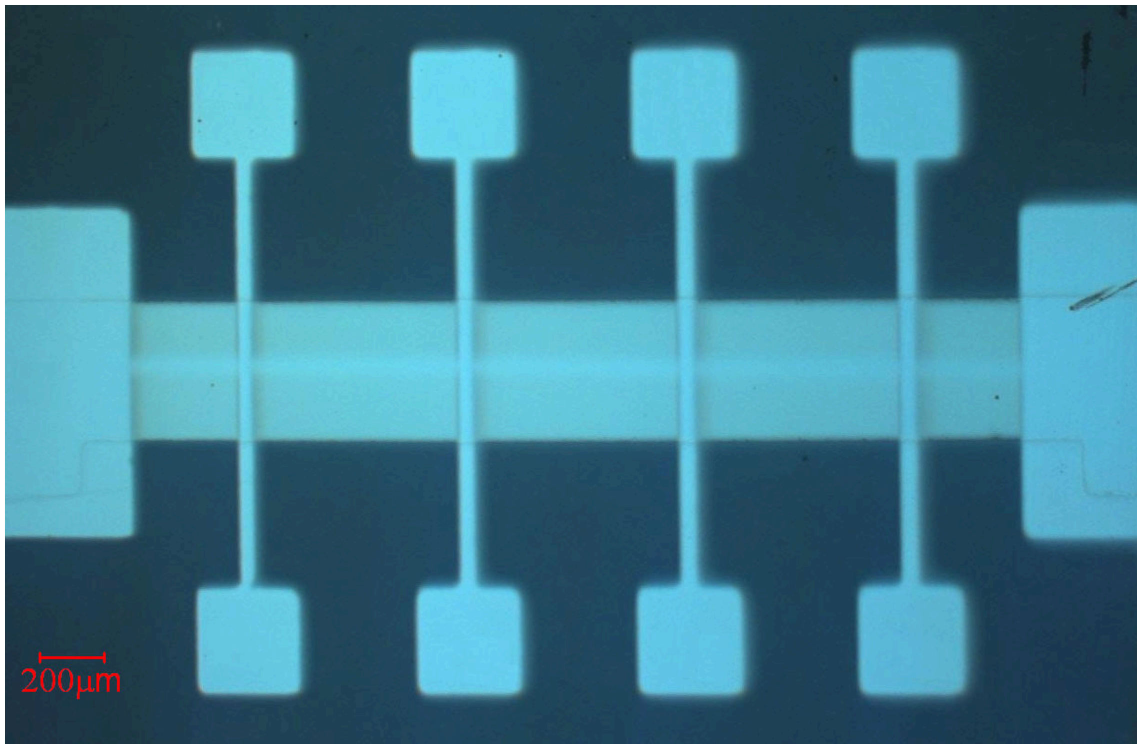


Figure 4.3: *Picture of sample patterned* in-situ *using the shadowmask technique. The opening in the technological MgO defining effective area* $2500 \mu m^2$ *per device is visible in form of the bright stripe in the middle of the bottom electrode that intersects each of the top electrodes.*

Areas of devices fabricated with the shadowmask were $2500 \mu m^2$ or $5000 \mu m^2$ - much larger than of these obtained with the optical lithography described in the next chapter. However, the *in-situ* patterning seems promising as the junctions can be fabricated within relatively short time, as compared to long and difficult multi-step lithography process. A typical sample fabricated using the shadowmask pattering is presented in figure 4.3.

## 4.2 Optical lithography

Optical lithography allows a micrometer-scale definition of patterns on the sample. It is widely used for device fabrication. Because of the high air quality and absence of ultraviolet light desired for the lithography process, these steps were carried out in a dedicated place, i.e. *the StNano cleanroom*, where most of the equipment essential for the process is installed.

### 4.2.1 Lithography mask

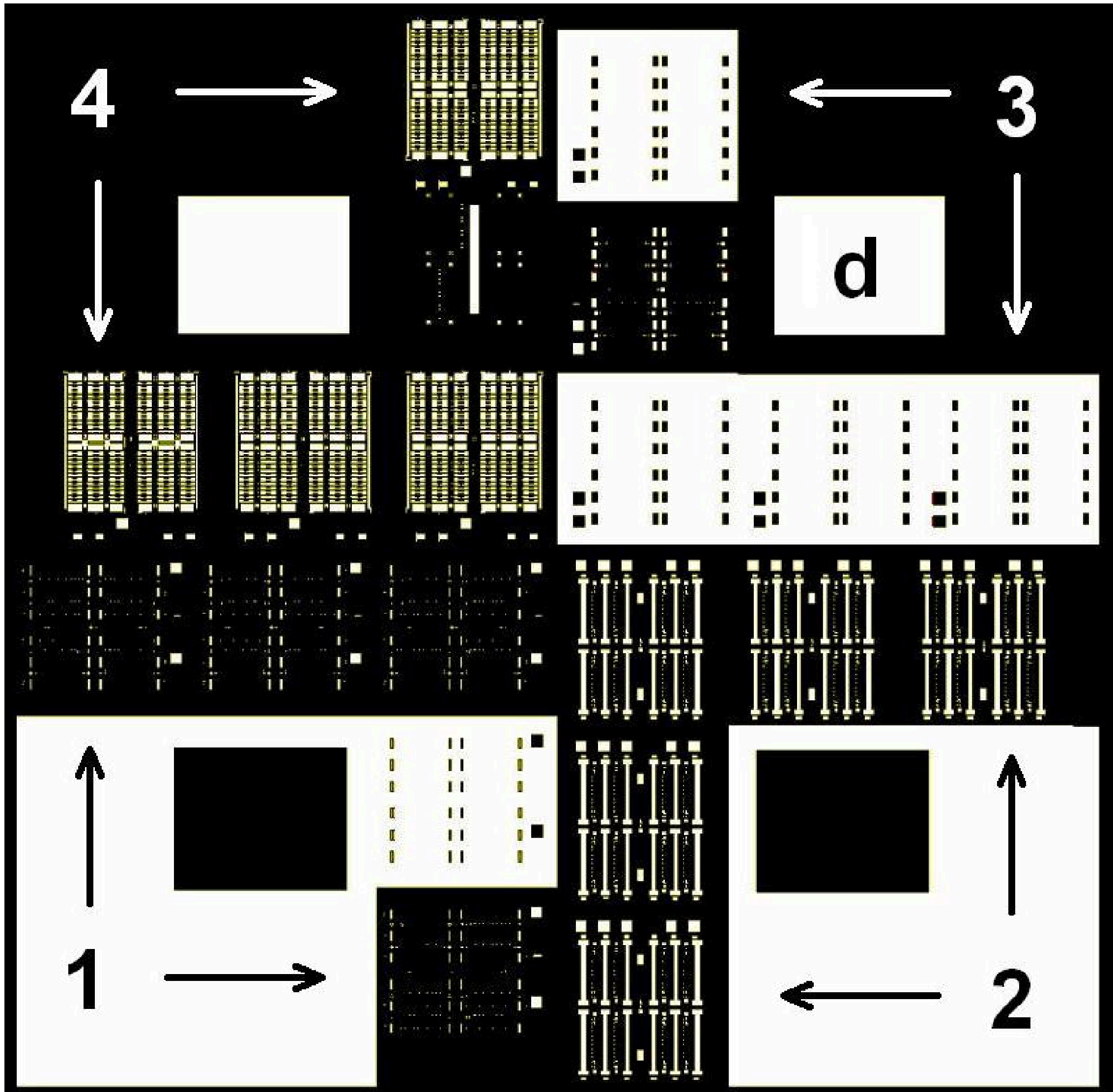


Figure 4.4: *Cadence software mask view. The areas drawn in black are transparent, the white ones mark the opaque. Arrows mark motives used during corresponding lithography steps. Large squares (marked d) are detouring squares.*

In order to selectively insulate the resist and consecutively obtain desired patterns on the sample, a lithography mask developed by A. Anane from the UMPhy CNRS/Thales group was redesigned using the Cadence software. The adaptation served purposes of the experiment and included a detouring step so as to improve resolutions for small patterns on typically small (7x10mm) samples; a two-step strategy of current injection into the bottom electrode; outer conducting connectors and

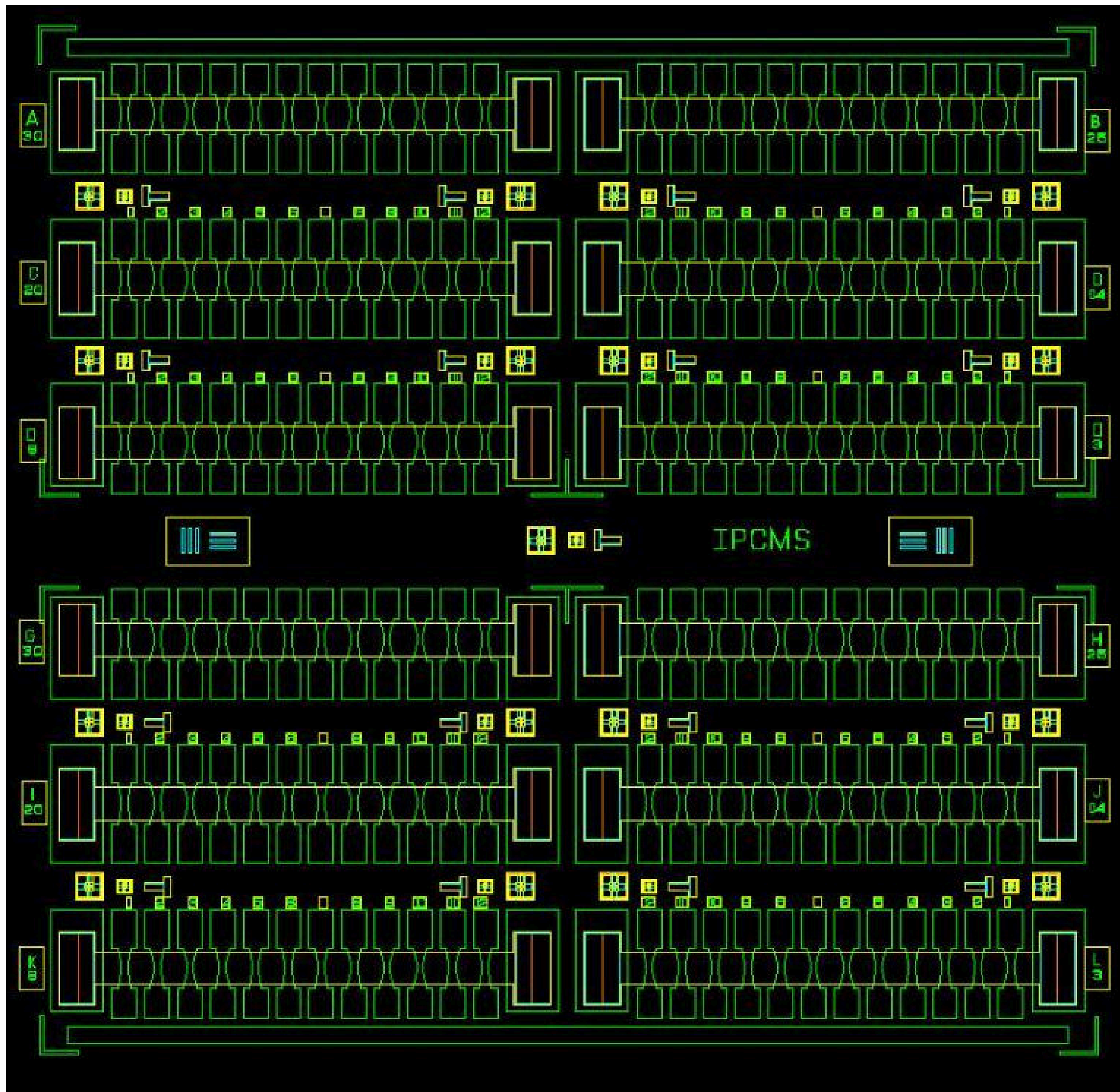


Figure 4.5: *Cadence software general visualization of the sample with all four layers overlapped. For a detailed view refer to fig. 4.6*

bars allowing possible connections among the electrodes; additional motifs so as to increase the resolution of the alignment between lithography steps; and several strategies to confer optical access to these MTJs. With these changes performed at the onset of the thesis, minor improvements were performed during the thesis so as to optimize junction sizes. The latest mask version at the time of writing the manuscript is shown on figure 4.4. Superposition of all the layers is depicted on fig. 4.5 whereas fig. 4.6 is a magnification of the latter, showing some of the aforementioned features. The mask enables the patterning of a stack into 12 rows, each containing 12 junctions of the same size. Junction sizes were 30, 25, 20, 14, 10 and

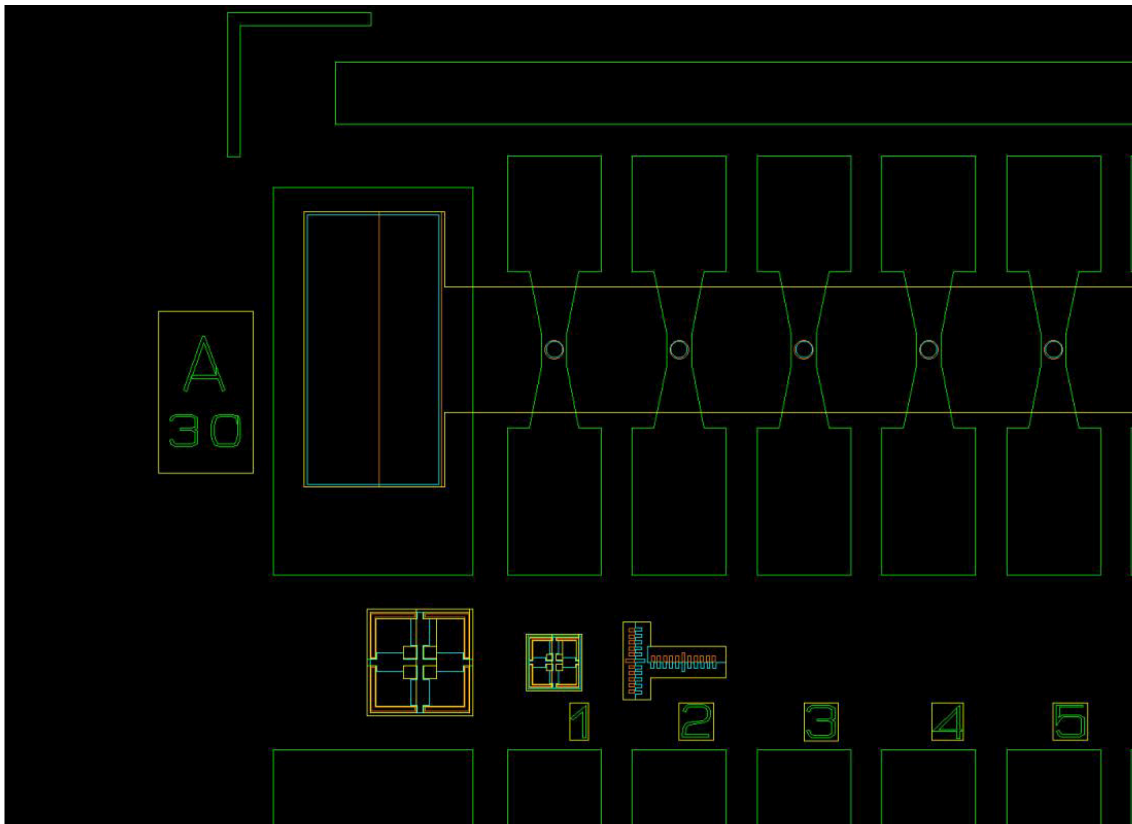


Figure 4.6: *Zoomed image by Cadence software of the sample with all four layers overlapped. Colors define the consecutive photolithography steps (fully described in the following section): I-brown, II-yellow, III-blue, IV-green. A and 30 refer to the row number and the diameter of junctions in the row in μm, respectively. Crosses and calipers in the bottom part are essential for precise alignment of steps, crucial especially for the I-III matching (note less than 3nm margin error)*

6 μm in diameter, respectively (due to resolution problems concerning the smallest junctions, modification of sizes was proposed at the time of writing). The sizes of junctions placed at 6 electrodes in lower part of the mask were the same as of these in the upper one. Thus a maximum number of junctions fabricated from one sample within a single lithography process was 144.

The mask had the lithography motifs printed on its chromium side that come into contact with the sample during the UV insulation. The sample imprint consisted of elements grouped on its quarters, each quarter containing patterns for the respective lithography step. All of the motifs were multiplied (damage-prevention) while some of them also altered. The alterations include reversal of transparency for processing of potential organic devices (steps I and III) and multifunctional access pattern (step IV) for future optical studies (within the timeframe of this thesis used only for testing purposes). A detailed use of the mask patterns in the process will be

presented in the following subsections.

### 4.2.2 Photoresists

Photoresists (PR) are light-sensitive materials, mostly polymers, the bond strength of which changes when exposed to ultraviolet light. This alters their solubility in specific developers. As there was no UV ambient light present in the StNano cleanroom, photoresists could change their properties only when exposed on purpose. Two general types of photoresists can be distinguished: **positive**, which become much more soluble in developer after the UV insulation and **negative**, which become slowly developable after being exposed to the ultraviolet light, which results from strengthening of the bonds. The 365nm UV lamp used during this thesis yielded $15mW/cm^2$ effective dose.

Figure 4.7: *Schematic cross-sectional view of positive (left) and negative (right) photoresists after their UV insulation and development. Note the* overhang *of the negative PR.*

The area insulated by the UV light is defined by covering parts of the photoresist-covered sample with the lithography mask. Depending on whether a photoresist is positive or negative, its edges acquire distinctive shape upon development (fig. 4.7). Especially, the use of the negative resist is crucial in order to obtain an *overhang* at the edge. Within the timeframe of this thesis, two specific photoresists were used: the positive S1805 and the negative AZ5215.

#### 4.2.2.1 Positive photoresist - S1805

Parameters needed for correct S1805 resist resolution were 1) selective insulation with the UV light for 2 seconds, 2) its development for 40 seconds in MF319 developer and 3) further bake-out for 90 seconds at 115°C in order to improve its stability.

#### 4.2.2.2 Negative photoresist - AZ5215

In order to obtain the desired overhang at the photoresist edge that was crucial for the *lift-off* process (described in subsection 4.2.3.4), the negative PR AZ5215 was used. This initially positive photoresist may have its polarity inverted by bake-out of its insulated parts. Its processing parameters were 1) selective insulation with the UV light for 2 seconds, 2) heating at 120°C in order to invert its polarity, 3)

flood exposure to the UV light for 40s (further selective strengthening) and 4) final 30s-long development in the AZ726 developer.

### 4.2.3 Processing

The photolithography process consisted of four steps which served to subsequently pattern the sample into more complex structure, which could finally form the device. These were subsequently: junction pillar definition (I), lower electrode pattering (II), passivation layer deposition (III) and final metallization (IV). Within the timeframe of this thesis an additional *detouring* sub-step was introduced, which allowed to remove the unwanted thick photoresist from the edges and more precise definition of motives. The detouring sub-step was optimized to be performed before each of the main steps, although due to a resulting issue (see section 4.2.3.4) it was used only if required.

#### 4.2.3.1 Photoresist deposition and its detouring

Photoresist deposited on the sample in droplets, then spin-coated for 30 seconds at 4000rpm all over its surface by spinning the sample, which yielded a flat and uniform layer. However, despite being correctly flat all over the central sample surface, it appeared to be much thicker at the sample edges. In order to further improve its uniformity in the center of the sample, it was baked for 2 minutes at 115°C.

For both photoresist types, the amount of substance in the sample edges was too high to provide further correct contact of the central part of the sample with the mask, crucial for the high-quality resolution of motives. In order to avoid this problem, the detouring sub-step was optimized so it could be performed at the beginning of each lithography step on the outer thick PR. For both PR types this was done by 40s UV insulation of the outer resist, while having the internal sample area covered with the large square imprinted on the mask. Such strongly insulated resist was then developed for 5s (S1805) or 15s (AZ5214), leaving only a flat resist in the sample center, i.e. in the device area. Additional 45s heating at 115°C was needed for the S1805 resist in order to evaporate the developer particles from it. Such heating was not performed on the AZ5214 resist, as do do so would partially invert its polarity in the early stage.

#### 4.2.3.2 STEP I - Pillar definition

While having only the flat and uniform S1805 resist left on the sample, a precise contact could be established between the sample and the lithography mask.

The junction pillar pattern was used in order to define the effective junction area. The large contact pads were defined in this step as well. They would allow the current flow towards the lower electrode which would be defined in the step II.

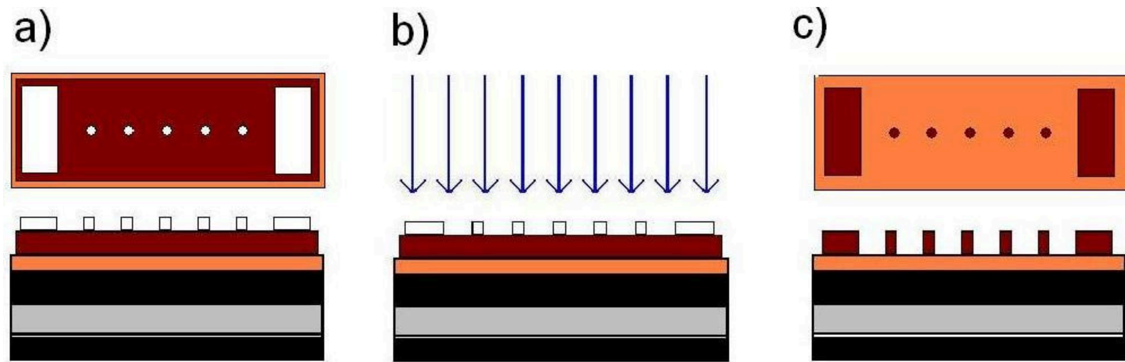


Figure 4.8: *Schematic top and cross-section view of the photoresist step I patterning. Colors depict respectively: black: electrodes, grey: barrier, yellow: metallic capping layer, red: photoresist, white: shadowmask opaque area. a) Detoured photoresist in contact with the mask just before its insulation, b) selective UV insulation process, c) patterned photoresist remaining on the sample surface. Note the picture is not to actual scale.*

The photoresist was selectively insulated and removed by its development from all the areas except pillars and pads. (fig. 4.8).

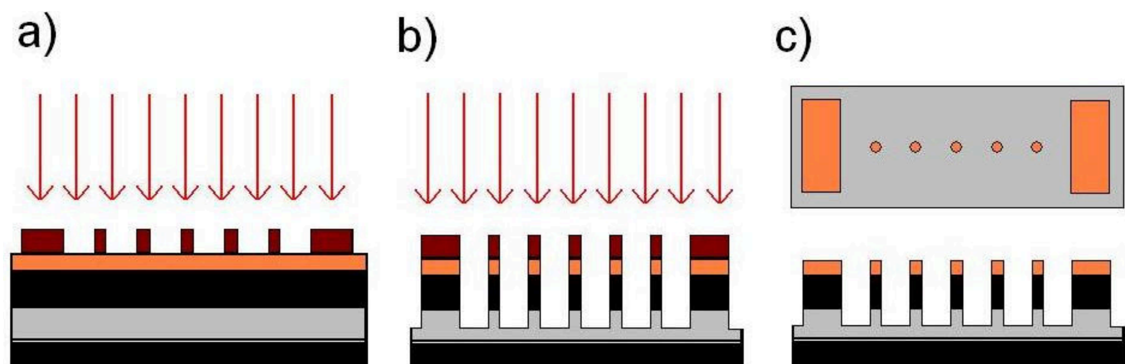


Figure 4.9: *Step I etching scheme: a) and b) selective $Ar^+$ etching down to the barrier level, c) sample schematic view after the photoresist removal.*

**$Ar^+$ etching** In order to remove material from non-covered parts of the sample, the sample underwent the $Ar^+$ etching procedure. In this UHV technique, neutral Ar atoms are injected into the chamber and stripped of their electrons to create a plasma. Then $Ar^+$ ions are accelerated towards the sample causing collisions and removing the material. One may see that this principle is similar to the sputtering deposition method with the crucial difference that there is no target from which the material is sputtered - it is the sample from which the material is removed. To protect the tunnel barrier from damage, i.e. creation of conductive filaments within

the barrier, the $Ar^+$ flux exiting the gun was neutralized thanks to the electron-emitting filament. Charge evacuation was achieved by attaching a conductive tape to the sample corners or by covering them with small amount of the silver conductive paste. In order to ensure etching uniformity, the sample was rotated during the procedure.

The etching procedure was carried out in small steps. Indeed, the crucial point of the junction pillar etching is to stop within the barrier or just at its lower interface (fig. 4.9). Etching beyond the barrier can cause the lower electrode material to be over-etched, thus effectively its thickness would be reduced. This can affect both electrical conductivity and its magnetic coercive field of the electrode. Moreover, the etched conductive material can be re-deposited on the barrier edges, causing its short-circuit. Another problem arising from the electrode over-etching, especially for $La_{0.7}Sr_{0.3}MnO_3$, is alteration of its stoichiometry. It is well-known that oxygen-deficient LSMO material becomes semiconducting or even insulating [137]. This is highly unfavorable, as the lowest possible contact resistances are needed in order to perform correct device measurements [138] (see section 4.3).

**Auger electron spectroscopy** In order to correctly determine the etching depth, the etching chamber was equipped with Auger electron spectroscopy. This form of spectroscopy is based on the *Auger Effect* in which the atom probed by the electron beam may have its core state electron removed, yielding an unstable hole. This state may be filled by an electron from an outer shell and its transition energy may be transferred to another outer shell electron which, if the energy obtained is sufficient to overcome its orbital binding, may be emitted from the atom with certain kinetic energy.

The Auger Electron Spectroscopy with which the etching chamber was equipped utilizes a 3keV incoming electron beam. The Auger electrons emitted from first few monolayers of the surface were studied in their kinetic energies up to 1300eV [139]. The system allowed to control the etching depth precisely albeit not directly during the etching process. For technical reasons the Auger gun and detector are mounted in a different position than the etching gun. In order to perform the measurement, the sample is transferred to the Auger position (without breaking the vacuum). This leads to altering small-dose etching steps, each of which is followed by the Auger measurement[1]. An example of the etching sequence for the Fe/MgO/Fe/Co system is shown on fig. 4.10. After the first etching step (black), the first few layers of the surface are purely cobalt atoms. The second one (red) yields peaks from both iron and cobalt so the Fe/Co interface was now exposed. The third etching step (blue) finished within the top iron layer, whereas after the fourth step (green), the MgO barrier started to be visible, but small quantity of Fe could be seen (Mg peaks are not visible within this energy span). In order to determine whether the iron peaks

[1]Experience shows that several small etching doses collectively lead to less etching than an aggregated, single-step etching dose.

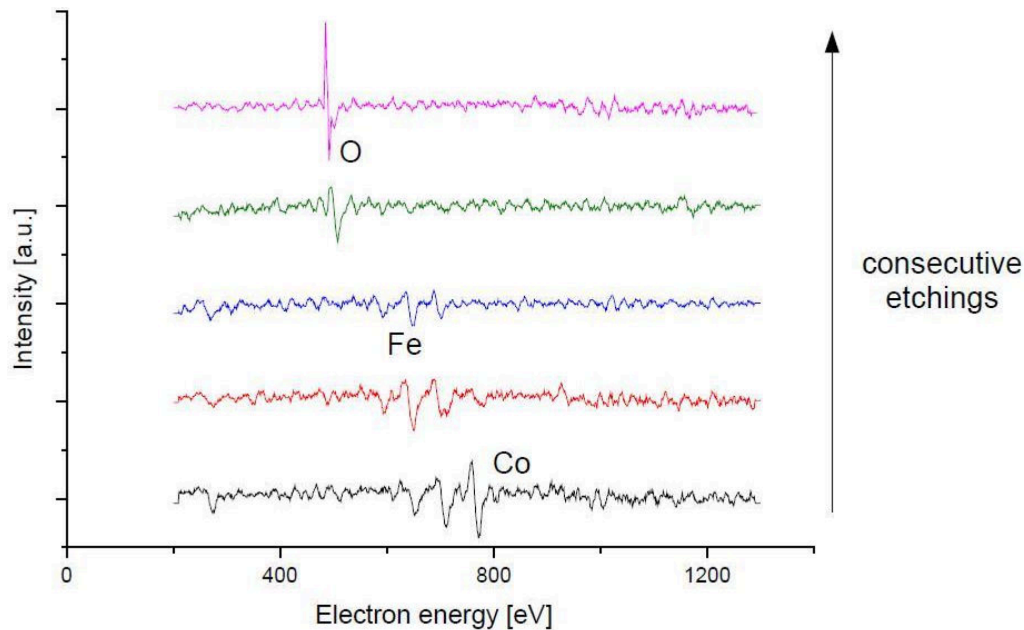


Figure 4.10: *Auger spectroscopy measurements derivatives after subsequent etchings of the Fe/MgO/Fe/Co stack. Consecutive results are shifted upwards for clarity reasons. The arrow shows the etching order, from first to last. The peak positions are (from largest to smallest, per element) Co:775,716,656,618nm. Fe:651,703,598nm. O:483nm. Mg peaks are not visible.*

come from the bottom or top Fe electrode, the sample was treated again with a small etching dose (pink), which showed an absence of the Fe peaks. This means that the former etching step had identified remnants of the upper Fe electrode and that it was the MgO that was now the sample surface layer, as desired. Note that the etching procedure does not affect the sample regions which were covered by the photoresist and if the Auger beam was focused on it, it would have yielded only the large carbon peak (slightly visible anyway at 272eV).

#### 4.2.3.3 STEP II - Lower electrode definition

After the pillar etching, the step I photoresist was removed in usual acetone and ethanol ultrasound baths. At this point the bottom electrode patterning step was performed using the S1805 photoresist. This step was experimentally realized the same way as the first one, except that the sample surface was covered with the second step (bottom electrode) photoresist pattern. It was later etched with the same $Ar^+$ beam down to the substrate (fig. 4.11). As for the first etching step, also at this point the over-etch was not desired. This was especially the case for $SrTiO_3$ substrates, whose conduction band lays close the the Fermi level (fig. 1.19) and thus any oxygen substoichiometry may cause the substrate to conduct. This is highly

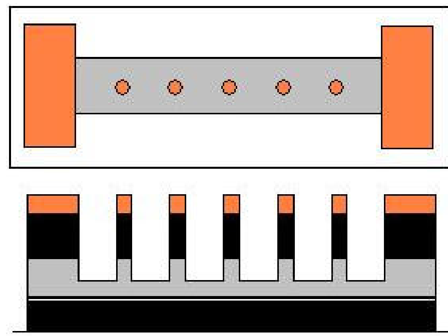

Figure 4.11: *Schematic picture of the sample after the step II etching and the photoresist removal. The white background color in the top view represents the insulating substrate*

unfavorable, as a significant amount of current would flow through the substrate in addition to the normal junction current, which increases the risk of a short-circuit between top and bottom electrodes of a given junction.

#### 4.2.3.4 STEP III - Passivation layer deposition

Once both the junction pillar and the bottom electrode were defined, a $SiO_2$ passivation layer deposition was performed. In order to do so, the AZ5214 - 1400nm thick negative photoresist was deposited atop the areas where the $SiO_2$ presence was not desired. These were especially small areas atop junction pillars which allow to create openings within the $SiO_2$ layer in order to provide further metallic contact in the following step IV. As the photoresist used in this step was negative, the *overhang* on its edges remained after the patterning. Afterwards, the 150nm thick $SiO_2$ insulation layer was radio-frequency sputtered on the sample using the *Torr International Inc.* sputtering setup at *Ecole europeenne de chimie, polymeres et materiaux ECPM* (i.e. outside the StNano cleanroom). This was done in collaboration with Silviu Colis from the DCMI group. The layer was deposited from a single $SiO_2$ 2" in diameter target placed parallel and 5cm away from the sample. The target was pre-sputtered for 10 minutes before deposition in order to remove any contaminants. The sample was rotated during the growth in order to ensure an enhanced uniformity of the layer. The pressure prior to the deposition was within the $10^{-6}$ mbar range, while during the growth it was reaching $1.1 \cdot 10^{-3}$ mbar (an argon flux of 20sccm). The deposition speed (of 1.47Å/s) and the thickness were measured in the real-time with a quartz crystal microbalance. During the sputtering process, the sample temperature increased up to 60°C.

**Lift-off** Due to the $SiO_2$ limited adhesion to some materials, ultrasounds could not in general be used to remove the photoresist and the $SiO_2$ from atop the junction

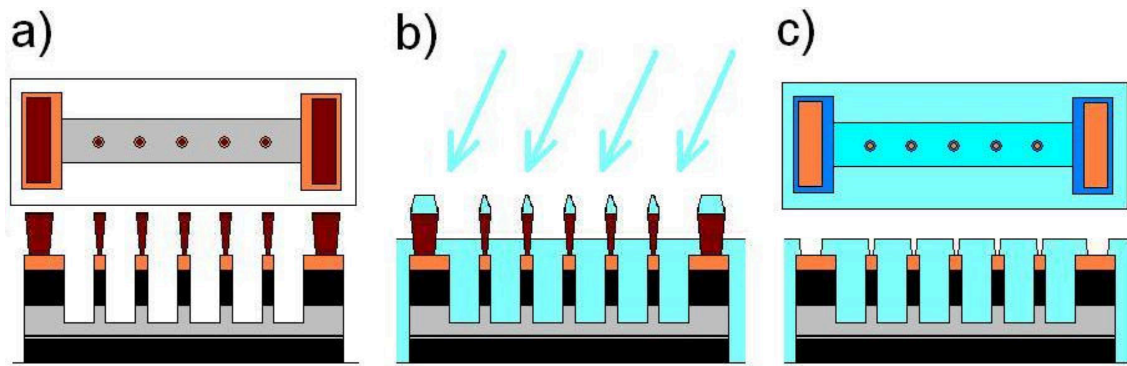


Figure 4.12: *Schematic presentation of the lithography step III. a) The negative photoresist after its selective development, b) the $SiO_2$ sputtering deposition, c) schematic view of the sample after the lift-off process. The normally semi-transparent $SiO_2$ colors on c) were altered in the top view in order to show that there are different materials underneath.*

pillars. Instead, the sample was left in the acetone bath for at least a few hours. Due to the presence of the resist overhang, the acetone attacks the exposed sides of the resist layer that have not been covered by $SiO_2$and dissolves it. The dissolved photoresist is lifted-off from the sample surface along with the $SiO_2$ atop, thus creating openings in the $SiO_2$ insulation layer (fig. 4.12).

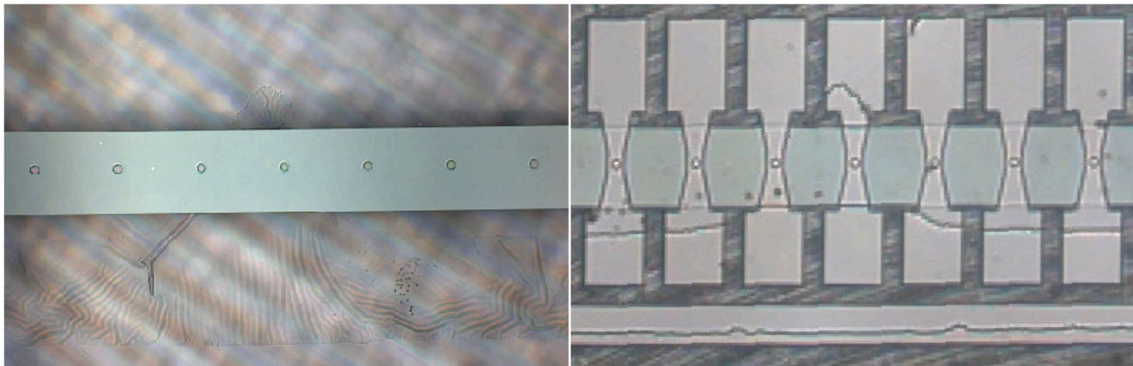

Figure 4.13: *Left: Excessive lift-off of the passivation layer originating from the detouring edge causes its unwanted removal from the electrode area. Right: Impact of the phenomena on the final state of the sample. Lack of $SiO_2$ directly atop the junction in the middle and the one directly on its left causes short-circuiting of these devices as the current flows directly between the top and the bottom electrodes.*

**Detouring edge issue** In some cases, the lift-off process was too slow or not sufficient enough to remove the photoresist with the $SiO_2$ atop. Such inefficiency of standard lift-off process was caused mostly by incorrect definition of the overhang

during the photolithography, but the problem was also noted to be related to aging of the photoresist. In such cases, up to one second short ultrasound pulses were used. The procedure drastically increased the lift-off speed, but caused an undesired $SiO_2$ lift-off from the sample surface as well. This removal was starting from the edges of the $SiO_2$ layer, which was normally far from the device area. However, if the detouring was performed during the step, the detouring edge would lie close to the active sample region. Since the edge may contain resist residues due to repeated insulation, the $SiO_2$ is particularly fragile at that point and the $SiO_2$ lift-off may thus proceed from it. This can cause the $SiO_2$ to be removed from the sensitive device area (fig. 4.13). For this reason, the detouring step was used only if high resolution of the patterned photoresist could not be obtained without it.

#### 4.2.3.5 STEP IV - Metallization

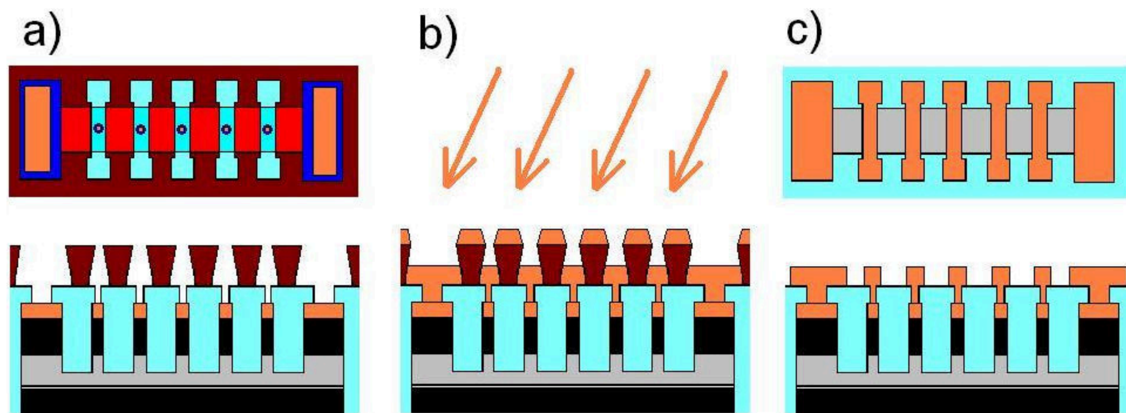


Figure 4.14: *Lithography step IV scheme. a) Negative AZ5214 photoresist after selective development, b) metallic layer deposition, c) final structure after the lift-off. On the top view a) picture the semi-transparent red color of the photoresist was slightly altered in order to show that there are different materials underneath*

With all but the contact areas covered by the $SiO_2$ insulator (bottom electrode access pads and openings atop the junctions remained exposed), a metallization was finally performed. This was done in a similar way to the former step using the same AZ5214 photoresist, only this time the remaining resist was preserved all over the sample surface except the areas, where the conductive contact pads were meant to be deposited (fig. 4.14a). The sample was then moved to the Plassys MEB 550S metallic evaporation system, where a Al(110nm)/Au(35nm) bilayer is deposited (fig. 4.14b) under base pressure less than $9 \cdot 10^{-7}$. The deposition speeds for Al and Au were 5Å/s and 2Å/s, respectively. Afterwards, the sample underwent the lift-off process, much easier at this step as large photoresist areas lift-off much more easily than the small ones. Afterwards, only the metallic contacts remain

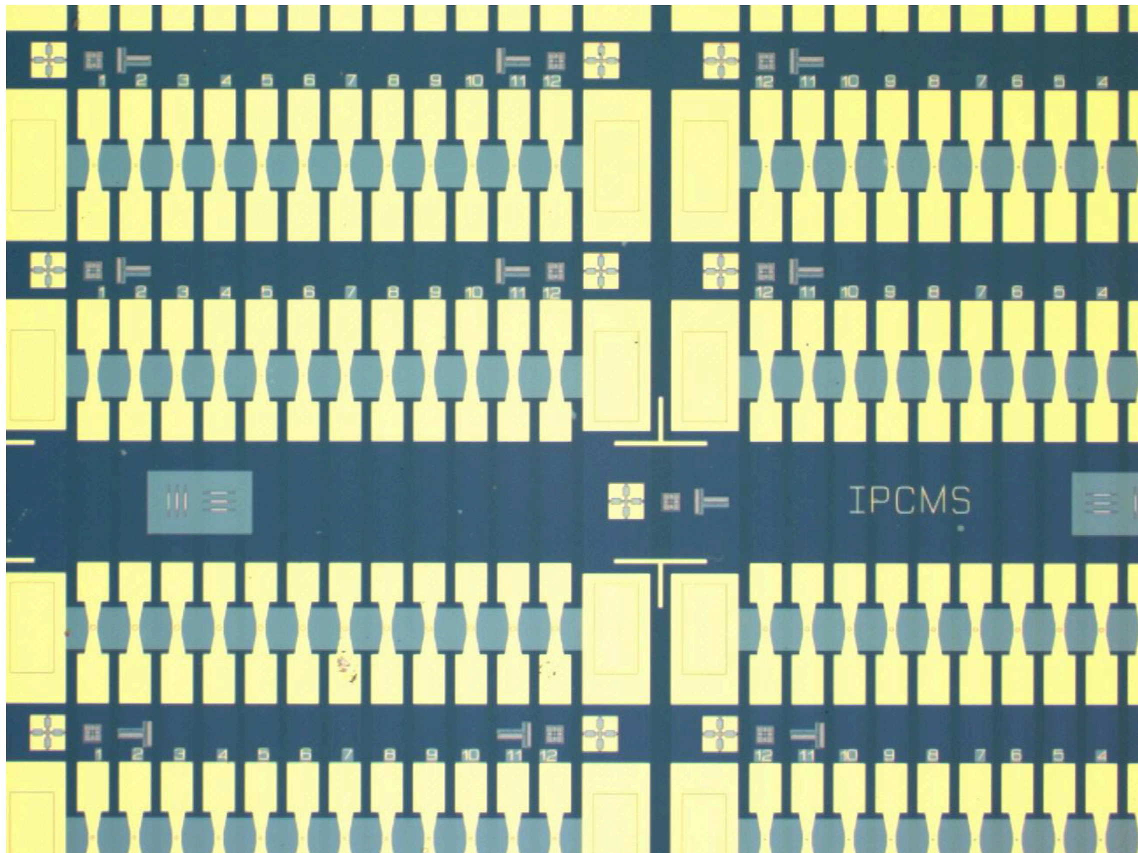


Figure 4.15: *Magnified picture of a part of a correctly processed sample. Stacked materials have respective colors: Dark blue: Substrate covered with 150nm thick $SiO_2$. Light blue: Bottom electrode covered with the $SiO_2$. Yellow: Al/Au metallic layer; Junction pillars and lower electrode access pads can be barely seen by slight contours (depressions) in the Au layer (compare with fig. 4.5 and fig. 4.6)*

.

on the sample, as presented on fig. 4.14c. Aluminium was deposited as the lower metallization layer due to its good adhesion properties to the passivation layer. The gold was chosen as the final, topmost layer as it is very hard to oxidize. A picture of the lithography final result is shown on the fig. 4.15.

## 4.3 Resistance probing and contact modes

As there are 144 junctions per each processed sample, it is essential to find out which ones would be suitable for further measurements. Thus, initial resistance studies were performed without bonding the sample or placing it in a magnetic field. This was done using a Karl Suss PM8 prober, with which one can perform quick measurements on many junctions.

### 4.3.1 Two-point measurement of the contacts

The resistances of top contacts and bottom electrodes were first checked in the standard two point configuration in order to ensure that their resistances are sufficiently small so they would not overshadow the ones of the junctions. Concerning samples processed with the optical photolithography, the top contacts fabrication conditions during the fourth step were the same for all the samples (except the deposition pressure which would alter insignificantly). As the result, they always yielded around 10Ω each. The resistance of the bottom electrode depended greatly on the sample structure and its etching depth after the first lithography step, but it usually yielded between 70Ω and 400Ω. In case of *in-situ* shadowmask-patterned Hybrid System samples, both bottom and top electrodes were custom-deposited, so their resistances varied among samples, but they rarely exceeded 100Ω each.

### 4.3.2 Four-point junction study

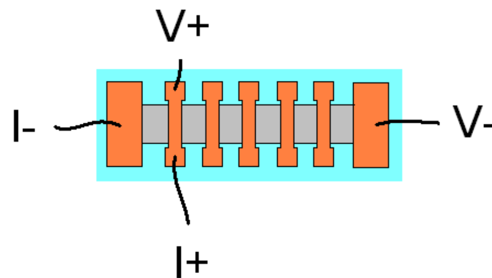


Figure 4.16: *Schematic illustration of the 4-point contact measurement. The voltage is applied between two contacts (one upper and one lower) and the current flow is measured between the other two. Effectively, the current sensed is the current flowing through the cross-point only, in this case the magnetic tunnel junction.*

Once the contact resistances are known, the junction themselves can be probed in the 4-point configuration (see fig. 4.16). This form of measurement has the advantage over the two-point mode that it measures only the current flowing through the cross-section, omitting the resistance of contacts. This allows precise junction study and is always preferred rather than the two-point mode. However, limitations of this method exist.

If the contact resistance is much larger than the resistance of the cross-section (in this case the junction), a negative resistance (an artifact) may be measured [138]. It is for this reason that the lower electrode resistance was always aimed to be as low as possible (by for instance not over-etching the lower electrode as described in section 4.2.3.2). The high contact resistances may also result from their mechanical damage. In cases of junctions for which the 3rd of 4th contacts could not be placed, they had to be measured in the standard 2-point contact or (in cases of one failed

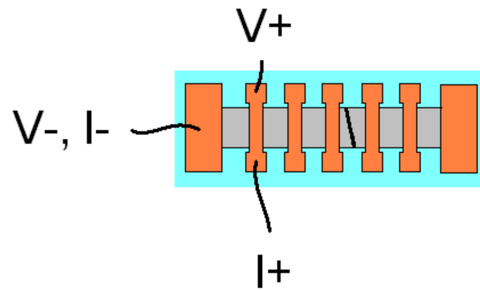


Figure 4.17: *Illustration of the 3-point or 'fake 4-point' contact measurement performed in case of the electrode excessive resistance or damage (schematically marked as the crack). The resistance of the leftmost part of the electrode along with its contact wire is added to the junction resistance.*

connector only) in the 3-point configuration sometimes referred to as the 'fake four-point contact' (fig. 4.17).

### 4.3.3 Resistance-Area products

Junctions fabricated from the same sample are expected to show similar characteristics. From a nominal growth standpoint, defect density and quantization effects aside, the only varying parameter is their area. As resistances of junctions within the same row are expected to be of the same order of magnitude due to their same size, smaller junctions should show much higher values of resistance. In order to find out whether observed resistances are statistically correct, their **Resistance-Area products** (RA) were compared, calculated as follows:

$$RA = R * A[\mu\Omega m^2] \tag{4.1}$$

Correctly patterned junctions should exhibit an uniform RA product all over the sample. However, as will be presented within the sample analysis, small junctions tend to show a RA value that is much higher than expected. This is because the smallest (7$\mu$m in diameter) junctions are hard to obtain due to the the lithography resolution and their size is usually smaller than expected. Due to the small size, even slight variation in the junction size leads to the large change in the RA product. The correctly fabricated junctions were assumed to be the ones having their RA value within the same order of magnitude. The RA study allowed to quickly set aside the devices which were either short- (RA very low), or open-circuited (the ones from which the photoresist was not removed throughout the lift-off process, causing no current flow). Since small patterns of the photoresist are difficult to remove, a large number of the smallest junctions exhibited the latter properties.

## 4.4 Diamond saw cut

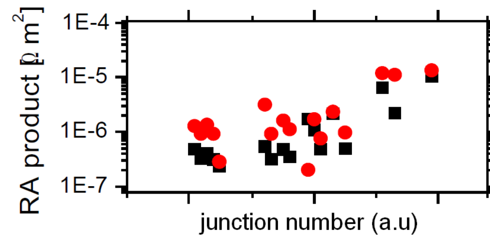


Figure 4.18: *Diamond saw cutting impact on the resistance area product of several junctions. Black squares and red circles show RA products of junctions before and after cutting the sample, respectively.*

Before any advanced measurements, the sample needs to be mounted on the dedicated *Fert Chip* (see section 5.1 for details). In order to do so, its size had to be reduced by cutting so it could fit on the 5x7mm designated chip area. To protect the sample surface from any contamination resulting from the cutting, its surface is covered with thick AZ5214 photoresist (without any further processing needed). The *Well 3242 precise diamond saw* is used in order to remove the outer parts of the sample around the device area, then the essential part is cut in two along the wide horizontal spacer between the top and bottom halves. The photoresist is then removed in the standard acetone and ethanol bath without the ultrasounds since to do so would affect the $SiO_2$ and Al/Au adhesion. We have confirmed that the cutting procedure does not affect the properties of the junctions (fig. 4.18).

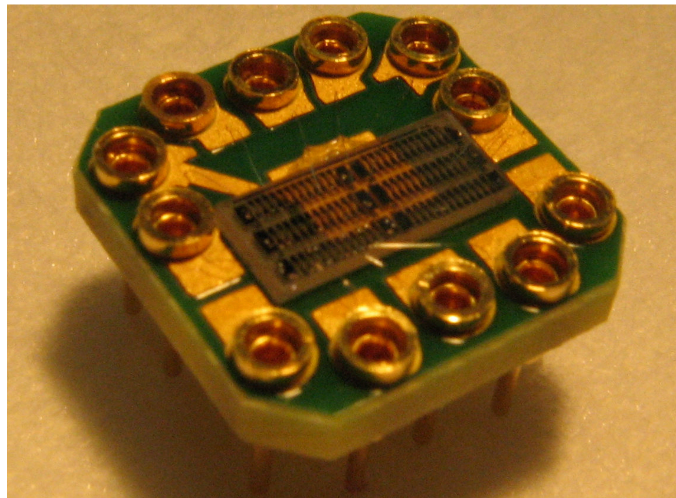

Figure 4.19: *Picture of the cut sample mounted on the "Fert" chip with five junctions on the bottom-left electrode bonded in the four-point contact mode. Bonding wires connecting the chip and device pads are visible.*

## 4.5 On-chip mount and wire-bonding

The sample, at now half of its former size, may be glued and bonded to the chip. The bonder used within the timeframe of this thesis was the Hybond 572A thermosonic **wedge bonder**. In this bonding technique, the aluminium wire is welded to both sample and chip golden pads by pressure and ultrasonic acoustic vibration. The method does not require any heat in order to create the weld, thus it is preferred to ball bonding, which is also available at the StNano cleanroom. In order to avoid any stray currents than could damage the insulating barrier, the sample is electrically grounded during the process. A sample bonded on the chip in the 4-point configuration is presented in fig. 4.19.

# Chapter 5

# Device study apparatus and techniques

This chapter describes equipment and some of the measurement techniques used within the timeframe of this thesis. It concentrates on the "Fert" setup and its dedicated chip properties (first section) and how it is used in order to obtain $\hat{I}$ characteristics and voltage-temperature dependency maps (sections 2 and 3). The fourth section presents the optical setups used in order to obtain the photoluminescence and absorption spectra.

## 5.1 "FERT" setup capabilities

Construction of the "Fert" chip (presented on pic. 4.19) makes it possible to bond and measure up to 5 junctions in 4-point mode or up to 10 junctions in 2-point configuration if all measured junctions share the lower electrode (see mask definition in section 4.2.1). The sample removal from the chip is usually not possible without damaging the device, but possibility of its multiple rebonding is a great advantage given the number of junctions per sample.

The Fert bench allows to perform multiple semi- or fully automated measurements. The equipment allows the sample to be mounted within the cryostat placed between electromagnetic coils able to yield the magnetic field of more than 2T. The cryostat can be filled with liquid helium from an external source and cooled down to less than 2K thanks to its two-chamber design. During the time of this thesis, a custom-made Labview-powered software was developed which allows to perform automated temperature-dependent measurements with fast automated switching among devices, applied bias voltage and magnetic fields. Magnetotransport measurements can be performed for multiple sample-to-field angles. Finally, current-voltage characteristics, crucial toward understanding the defect energy levels, can be obtained for different temperatures and relative magnetization orientations of the ferromagnetic electrodes. The initially semi-automated multiplexing was upgraded

within the duration of this thesis to the fully automated functionality (the work of U. Halisdemir), which allowed fast switching between junctions during the measurement, enabling a statistical comparison of the junctions behavior under conditions that might be otherwise impossible to exactly reproduce.

## 5.2 Experimental determination of the barrier potential landscape

Computational techniques to determine barrier heights based on the Brinkman's or Simmons' formulas mentioned in section 1.1 suffer from a serious drawback, i.e. their validity only for the ideal barriers. Presence of multiple types of defects (see section 2.1.1), additional interfacial oxide sites or even fitting parameters issues can give rise to a discrepancy between results of calculations and reality.

### 5.2.1 Direct I-V characteristics analysis

Since current-voltage characteristics give clear information regarding voltage at which conductance rises significantly, the $V/e$ value gives the energy of the conduction band or defect, relatively to the Fermi level ($e$ being the electron mass). This approach is used in analysis of MgO barriers in section 7.1.

### 5.2.2 $\hat{g}$ method

Rottlander *et al* proposed two experimental techniques to measure the barrier height, one based on the logarithmic derivative of I-V curves and one based on the temperature dependence of these curves [140].

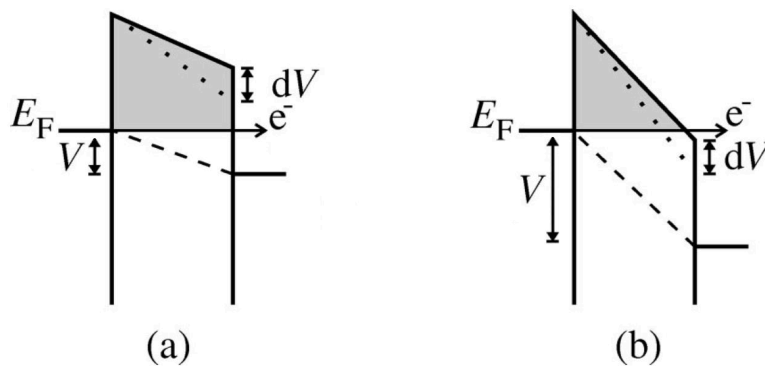


Figure 5.1: *Schematic representation of the barrier behavior upon applying bias which is a) lower and b) higher than the barrier height. Shaded areas depict the Brinkman's fitting validity [140].*

Figure 5.1 schematically shows the behavior of a potential barrier with equal heights at each interface that is voltage-biased with two different external voltage range cases. If the applied voltage $V+dV$ is lower than the barrier height, the barrier average height decreases along with the $dV$ voltage increase but its width remains constant. However, if the $V + dV$ exceeds the barrier height, the $dV$ bias voltage increment causes not only a decrease of the the average barrier height, but of its width as well, leading to an additional, more prominent rise in junction conductance.

### 5.2.3 $\hat{I}$ method

The second method proposed by Rottlander *et al* was extensively used within the timeframe of this thesis. It requires performing current-voltage characteristics at two different temperatures. As the Fermi level starts to smear out with the increasing temperature, the current tunnels most efficiently for voltages just above the barrier height of the positively biased electrode. The normalized temperature dependence yields increased values around the barrier height level of the positively biased electrode:

$$\hat{I}(V) = \frac{I(V,T_2) - I(V,T_1)}{I(V,T_1)}$$

Such measurements, once performed on a wide range of temperatures ($\hat{I}_{T_1-T_2}$, $\hat{I}_{T_2-T_3}$, $\hat{I}_{T_3-T_4}$ and so on), can yield insight into the activation temperature and voltage of certain magnetotransport features. They are called *relative* $\hat{I}$ or $\hat{I}_{rel}$ as opposed to *absolute* $\hat{I}$ or $\hat{I}_{abs}$ series, in which all the data is plotted in reference to a fixed, usually low temperature.

### 5.2.4 Voltage-temperature dependency maps

Effects that influence the magnetoresistive characteristics of the studied systems are strongly dependent on voltage and temperature variations and in order to understand these dependencies one needs to analyze them thoroughly. Thanks to the partial automation of the Fert setup measurements during the final part of the timeframe of this thesis, multiple junctions could be studied upon a single series of voltage and temperature sweep. This allowed to create two dimensional voltage-temperature dependency maps of resistance, magnetoresistance and both absolute and relative $\hat{I}$ values.

## 5.3 Optical studies

The optical studies of defects were performed in our group (thanks to Guy Schmerber), as well as by the Gilliot group within *Departement de Optique ultrarapide et*

*de Nanophotonique* (DON) group as result of an internal collaboration within the IPCMS. Both groups operate distinctive types of optical setups with different capabilities. The setup operated by G. Schmerber consisted of a 355nm excitation wavelength Nd:YAG (neodymium doped $Y_3Al_5O_{12}$) laser with 100mW power. Several of the optical studies were performed by Matthieu Gallart from the Gilliot group, using the He-Cd 325nm laser setup capable of performing temperature dependent studies by placing samples in the cryostat and filling it with the liquid helium. Moreover, MgO absorption spectra (section 7.1) were obtained with UV-Vis-NIR Perkin-Elmer Lambda 950 spectrophotometer by W.S. Choi from Seoul National University as a result of an external collaboration.

# Part III

# Device study

# Chapter 6

# Transition metal oxides

Transition metal oxides are of great interest within the field of spintronics due to their potential half-metallic properties such the ones reported in $La_{0.7}Sr_{0.3}MnO_3$. Moreover, due to low bandgap of $SrTiO_3$ and $TiO_2$ crystals (around 3.2eV), they are not as difficult to study optically as their MgO counterparts, for which deep a UV laser is needed. Using frequencies high enough to overcome the 7.8eV MgO gap causes absorption and luminescence from surrounding elements. In the case of transition metal oxide barriers study, the issue is present to much lesser extent.

In case of all experiments performed on transition metal oxide-based devices, one sample of each kind was grown, then processed with the standard lithography procedures described in section 4.2, thus yielding up to 144 devices. These devices were studied in terms of their RA products and among them a certain number was chosen for extensive studies.

## 6.1 Strontium titanate

As mentioned in section 1.7, STO barrier combined with LSMO electrodes showed the highest TMR values so far. However, the question remains whether it is possible to obtain transition metal oxide based magnetic tunnel junctions with simple electrodes, so that one may compare with theory more easily [141].

### 6.1.1 STO optical activity

In order to pave the way for future studies on the defect-mediated spin polarized transport and its properties upon illumination by a laser light, several measurements were performed. Fig. 6.1 shows the photoluminescence of non-irradiated and $Ar^+$ irradiated $SrTiO_3$ crystals illuminated with 325nm laser. 550nm peak of non-irradiated crystal is commonly observed in stoichiometric $SrTiO_3$ and reflects recombination process of excited holes and electrons at self-trapped excitons [142, 143]. On

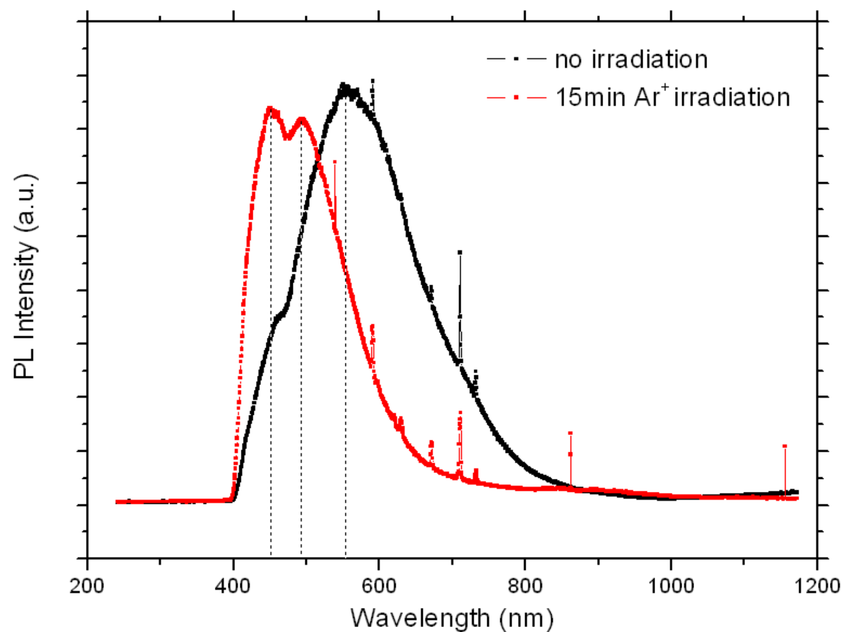


Figure 6.1: *Impact of $Ar^+$ irradiation of STO crystals on the photoluminescence spectra. The data was collected after illumination with the 325nm laser.*

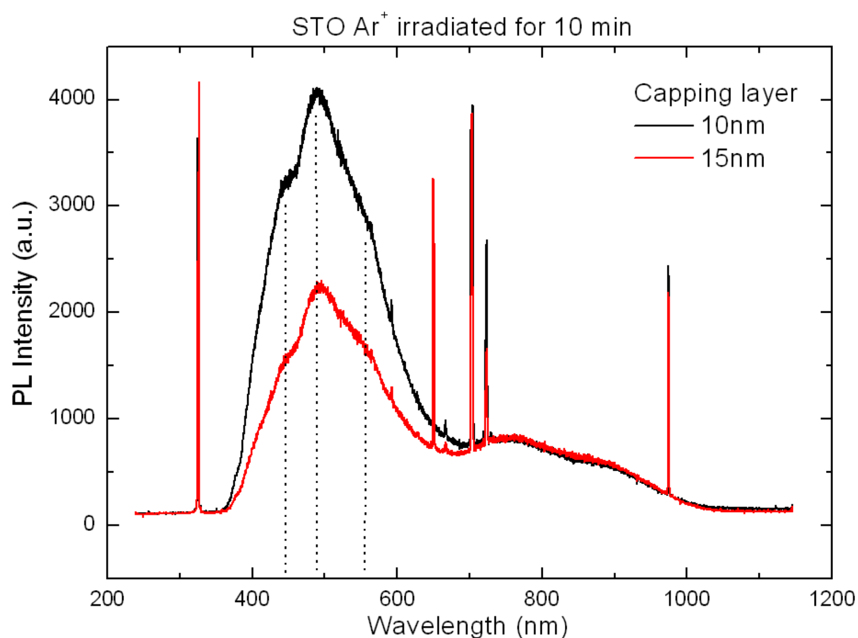


Figure 6.2: *Photoluminescence spectra collected from a STO crystal etched for 10 minutes and capped with Au(10nm) or Au(15nm). Dashed lines represent positions of peaks appearing for samples presented on fig. 6.1*

the other hand, the 450nm peak of the irradiated crystal corresponds to the recombination between conduction electrons and excited holes. The conduction electron density increases with increasing oxygen deficiency, which leads to higher 450nm luminescence intensity [108].

An additional study was performed on a sample irradiated for 10 minutes. This moderately etched sample shows partial features of both the virgin one and the one annealed for 15 minutes (fig. 6.2). One part of the sample was capped with evaporated layer of Au(10nm), whereas the other was capped with Au(15nm). As shown on the fig. 6.3, the PL signal can be reached even through the relatively thick 15nm layer of gold.

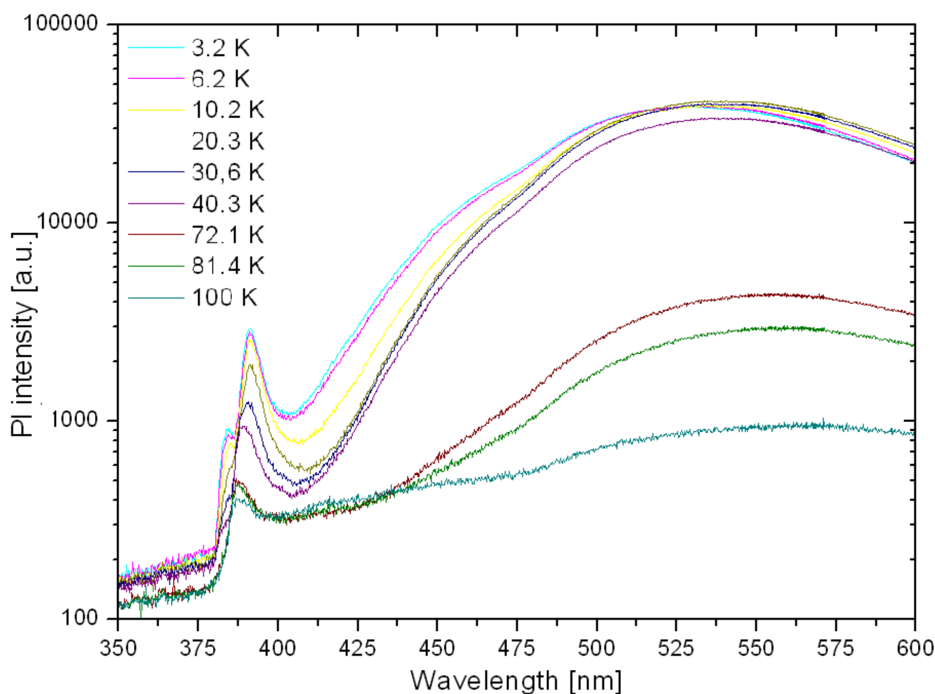


Figure 6.3: *Temperature-dependent photoluminescence spectra of STO crystal irradiated for 10 minutes and capped with Au(5nm) layer. The data was collected after the excitation with the 325nm laser.*

The experiment allowed to estimate the thickness of the top electrode which is essential for planned future experiments involving impact of the laser light illumination of junctions on their defect-driven spin-polarized transport. In order to determine whether temperature-dependent optical properties of the capped crystal would be measurable, studies at low temperature were performed on a sample irradiated for 10 minutes and capped with Au(5nm) layer (fig. 6.3). The 100K spectrum shows a peak at 387nm which, upon cooling down to 3.2K, splits into 384nm and 391nm peaks. Moreover the position of the main peak at 3.2K is 530nm. The first feature is attributed to the recombination process between doped or excited elec-

trons and exited holes through a defect level, whereas the second one corresponds to recombination of excited holes and electrons in a self-trapped exciton (see section 2.1.2.2).

### 6.1.2 $CoFe_2/SrTiO_3/CoFe_2$

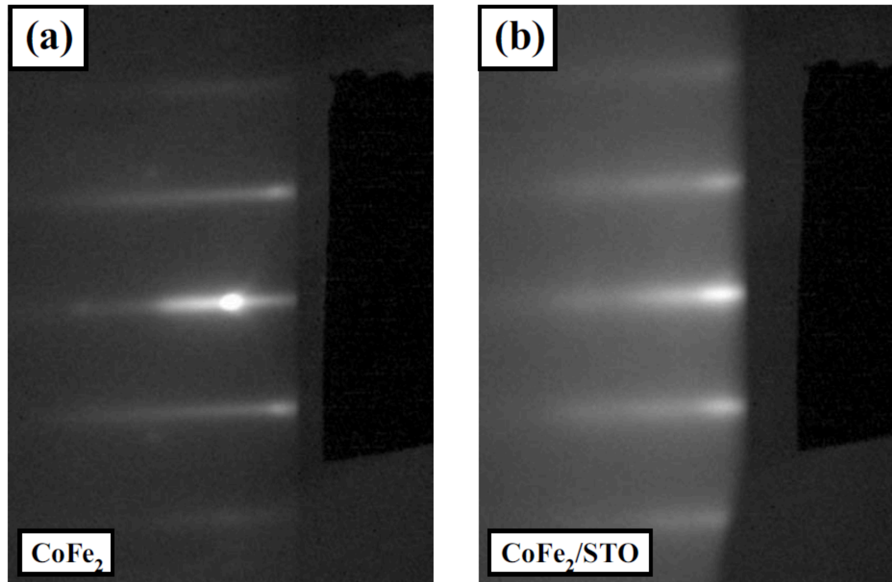


Figure 6.4: In situ *RHEED images taken on the low-T sample after the a) $CoFe_2$(7.5nm) and b) subsequent $SrTiO_3$(3nm) growth. The pictures were taken along the [100]STO(001) substrate azimuth [144].*

In order to study the temperature influence on defects formation in the bulk STO [145] as well as its incidence on the $CoFe_2/SrTiO_3$ interface, a stack with the $CoFe_2$(7.5nm)/$SrTiO_3$(3nm)/$CoFe_2$(1nm)/NiFe(8nm)/Ta(2nm) structure was grown on the STO(100) substrate by the pulsed laser deposition technique in conditions described within section 3.5. The lower $CoFe_2$ layer was grown at 300°C, whereas the $SrTiO_3$ barrier was grown at 80°C (Low-T sample) and 300°C (High-T sample). The $CoFe_2$/NiFe top magnetic layer was grown at 80°C and capped with a RT-grown tantalum layer in order to protect the sample from oxidation. The deposition pressure was maintained at $2 \cdot 10^{-7}$ mbar. RHEED measurements performed on the low-T sample both after the lower $CoFe_2$ and the $SrTiO_3$ barrier growth show correct crystalline structure of interfaces (fig. 6.4).

The microcrystallinity of layers and their respective orientation were checked through high-resolution transmission electron microscopy measurements. Fig. 6.5 reveals the formation of fairly uniform and structurally sharp interfaces below and above the $SrTiO_3$ barrier. The barrier thickness estimated from the TEM picture

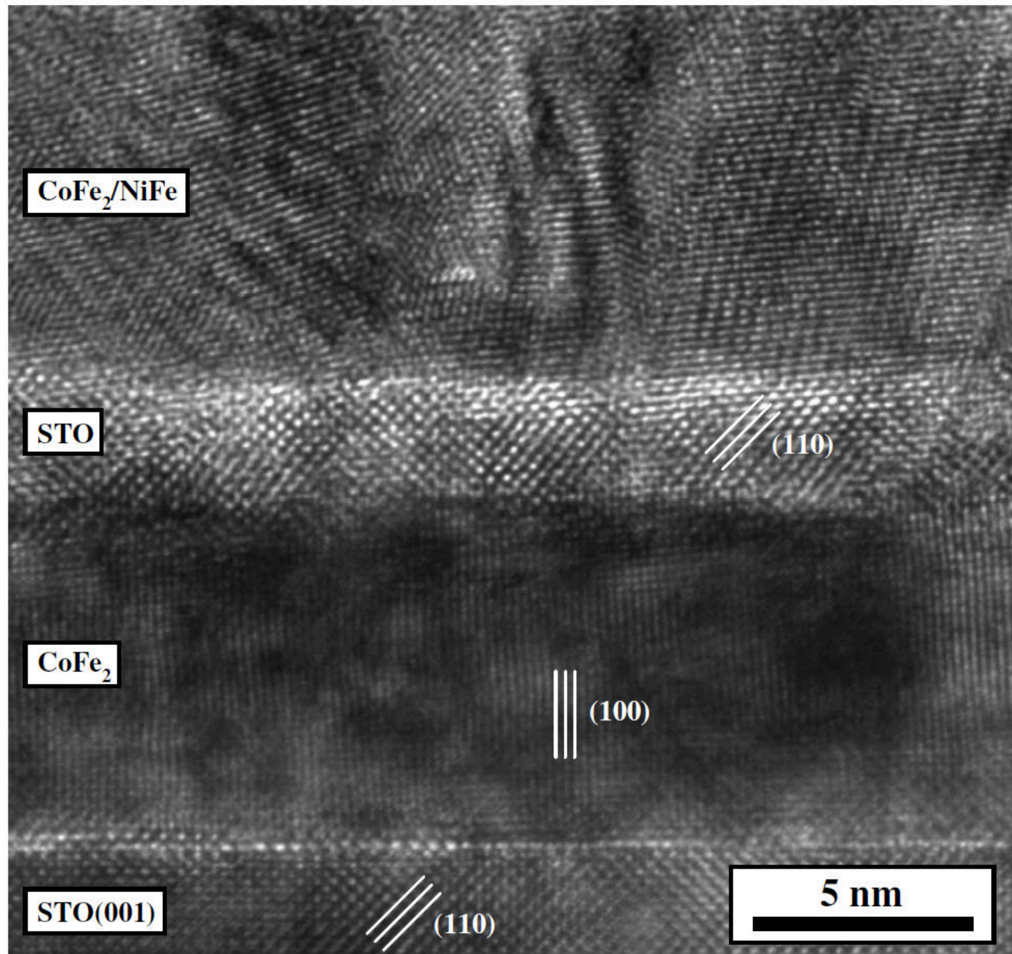


Figure 6.5: *High resolution cross-sectional TEM of the STO(100)//$CoFe_2$(7.5nm)/$SrTiO_3$(3nm)/$CoFe_2$(1)/NiFe(8nm)/Ta(2nm) low-T stack. The topmost NiFe/Ta bilayer is not shown. The picture was taken with the Jeol 2100FCs TEM with the point resolution of 2.3Å[144].*

is $3.1 \pm 0.2$nm. The atomic structure of both the bottom electrode and the barrier is monocrystalline, as observed on the RHEED spectra. On the other hand, the top $CoFe_2$ electrode is polycrystalline with the atomic planes not well defined. We attribute this to the low growth temperature of this electrode.

Room-temperature alternating gradient-field magnetometer (AGFM) measurements performed on both samples show a sharp reversal of electrodes magnetizations and coercive fields of 7Oe and 18Oe for the low-T stack and 8Oe and 22Oe for the high-T stack (fig. 6.6). The magnetic field was applied along the STO(001) substrate direction. The smaller and larger coercive field values correspond to the magnetization switching of the bottom and the top electrode, respectively. The slight rise of these values for the high-T sample may be attributed to the interfacial oxidation.

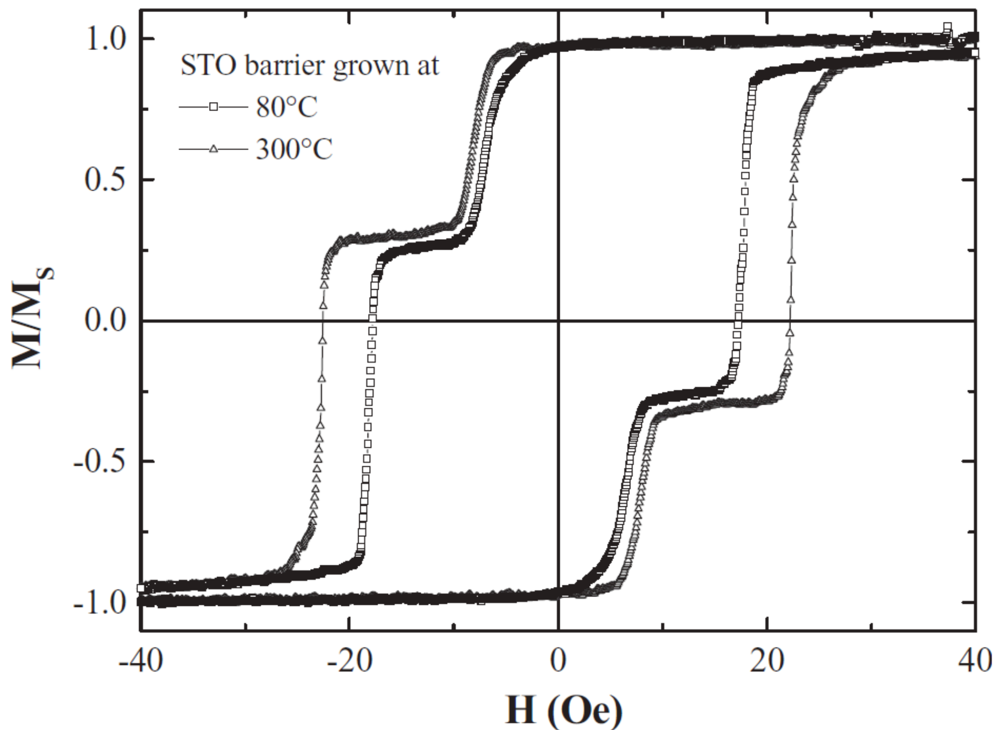


Figure 6.6: *AGFM room-temperature measurement of the STO(100)//CoFe$_2$(7.5nm)/SrTiO$_3$(3nm)/CoFe$_2$(1)/NiFe(8nm)/Ta(2nm) low-T and high-T multilayers along the [100]STO(001) axis [144].*

For the same reason, the low-T deposition results in slightly sharper AGFM curve.

The room temperature TMR was not observed for the high-T sample, while the low-T one yielded a positive 3% value (fig. 6.7). The resistance area product of these junctions was of $10^5 \mu\Omega m^2$ range. The switching fields are in agreement with the hysteresis curves obtained from AGFM measurements.

There are several reasons attributed to the low value of the tunnel magnetoresistance ratio for the sample in which the $SrTiO_3$ barrier was grown at the lower temperature. If one analyzes the STO barrier band structure, it is easy to see that electrons that dominantly tunnel across the barrier are mostly of the $\Delta_{2'}$ and $\Delta_5$ symmetry (fig. 1.19). In the case of iron electrodes, bands of these symmetries cross the Fermi level for both minority and majority electrons populations, resulting in poor filtering. On the other hand in cobalt, bands of the $\Delta_{2'}$ and $\Delta_5$ symmetry exist only in the minority spin channel (fig. 1.21). The Co-like band structure occurs in sufficiently cobalt-rich CoFe [49], which may not be the case in our $CoFe_2$ structures ($Co_xFe_{1-x}$, $x = 0.5$).

Another factor that may have a crucial impact on the low TMR ratio is the barrier structure at the interface. As described in the theoretical part, the $SrTiO_3$ monocrystalline barrier consist of alternating SrO and $TiO_2$ planes (see section

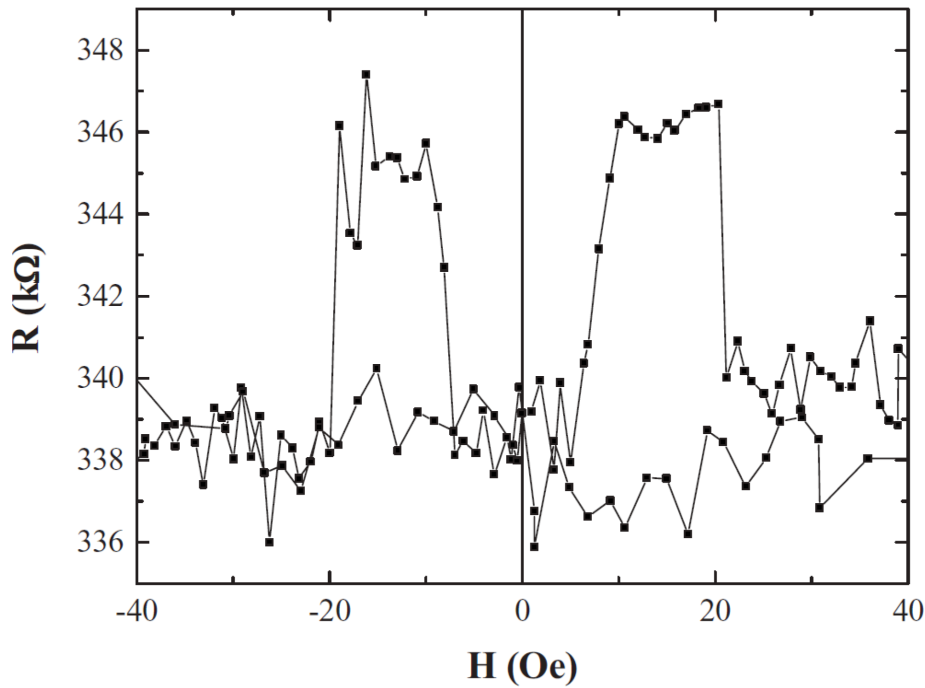


Figure 6.7: *Room temperature RH curve measured on the* 20$\mu m$ *in diameter junction processed from the low-T STO(100)//CoFe*$_2$*(7.5nm)/SrTiO*$_3$*(3nm)/CoFe*$_2$*(1)/NiFe(8nm)/Ta(2nm) stack [144].*

1.5.1). Although TEM and RHEED experiments confirmed the epitaxial structure of the barrier, the interfacial atomic steps are extremely hard to avoid. Even the high-resolution TEM microscopy image cannot give a definite answer as whether there is only one type of the interfacial termination layer or not. As shown by Vera Marun *et al*, the TMR sign may depend on the STO termination layer [44]. This may be the case in the studied system, in which the interface may consist of the SrO and $TiO_2$ mixture, whose positive and negative spin polarizations average out and result in relatively low TMR value.

The reason for which the tunnel magnetoresistance is not observed in the high-T sample could be the barrier deposition temperature itself, for which the higher energy of atoms during the growth favors the oxide formation at the bottom interface, notably the iron oxide. This hypothesis is supported by somewhat larger coercive fields observed on the high-T sample. On the other hand, the low TMR signal observed in the low-T sample may result from the same oxidation issue as the base pressure in the PLD chamber prior to the deposition is within the $10^{-8}$ mbar range (see section 3.5).

In order to further confirm the oxidation hypothesis, the current-voltage characteristic is presented. Barrier heights at both interfaces were calculated using the

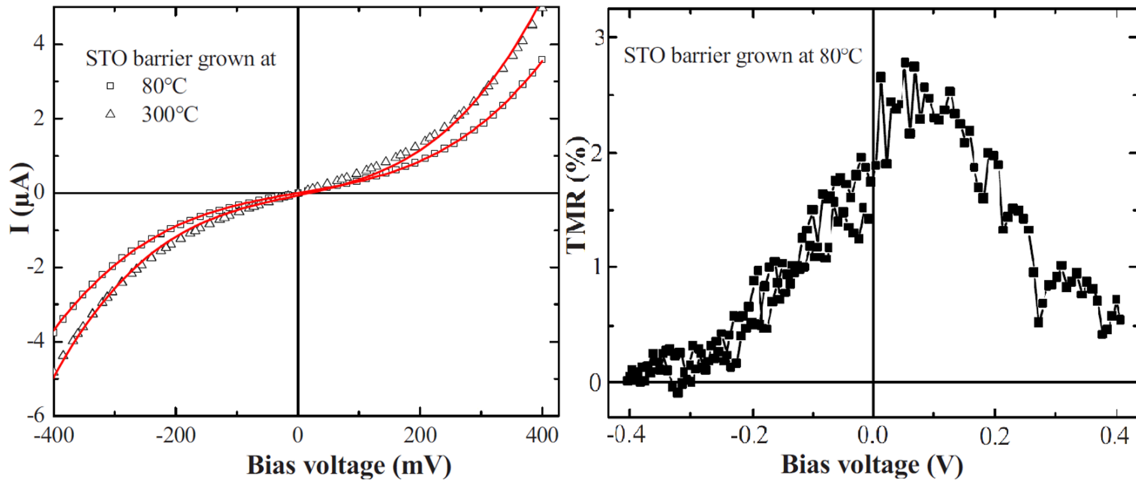


Figure 6.8: *Room temperature IV measurements on identical 20$\mu m$ in diameter junctions from the low-T and high-T stacks (left) and corresponding TMR on voltage dependence for the low-T junction (right). No magnetoresistance was present on the high-T junction (not shown) [144].*

Brinkman model [22], as temperature-dependent $\hat{I}$ measurements were not available at the time (fig. 6.8). A Brinkman fit of the top interface barrier height for both high-T and low-T samples showed 0.61eV. The identical value is expected for both samples as their upper interfaces were fabricated in the same deposition conditions. On the other hand, barrier heights of lower interfaces were 0.39eV and 0.51eV for the high-T and low-T junctions, respectively. This shows the impact of oxidation on the lower interface, which is further enhanced for the high-temperature barrier deposition. The effective thickness determined by the Brinkman fit for both samples fit was 2.7nm, close to the one observed by the TEM (3.1nm).

Despite the relatively low TMR signal observed, we conclude that it is the first time that the TMR signal is reported across $SrTiO_3$ based junctions with simple transition metal electrodes. Analysis of the results suggests that significant improvement in properties of junctions could be achieved in two ways. 1: By controlling the composition of interfacial $SrTiO_3$ layers one may ensure the atomic termination of the barrier and eliminate the simultaneous presence of different symmetry filtering channels which result in averaging of positive and negative magnetoresistance ratios. Substitution of $SrTiO_3$ with $TiO_2$ can accomplish this. 2: The interfacial iron oxide formation may be avoided by moving fast-oxidizing elements away. Introduction of thin cobalt at both interfaces may also improve the symmetry filtering as it would remove bands of the $\Delta_{2'}$ and $\Delta_5$ symmetry from the Fermi level of electrodes (fig. 1.21). Both of these scenarios were attempted.

## 6.2 Titanium dioxide

This section presents results obtained on devices based on the titanium oxide barrier. The use of $TiO_2$ instead of strontium titanate is mainly motivated by the need to limit possibilities of having many different chemical environments at magnetic/non-magnetic interfaces due to perovskite termination issues. Two types of devices based on the $TiO_2$ barrier were grown and prepared with optical lithography: with $CoFe_2$ and Co interfacial layers, respectively.

### 6.2.1 $CoFe_2/TiO_2/CoFe_2$

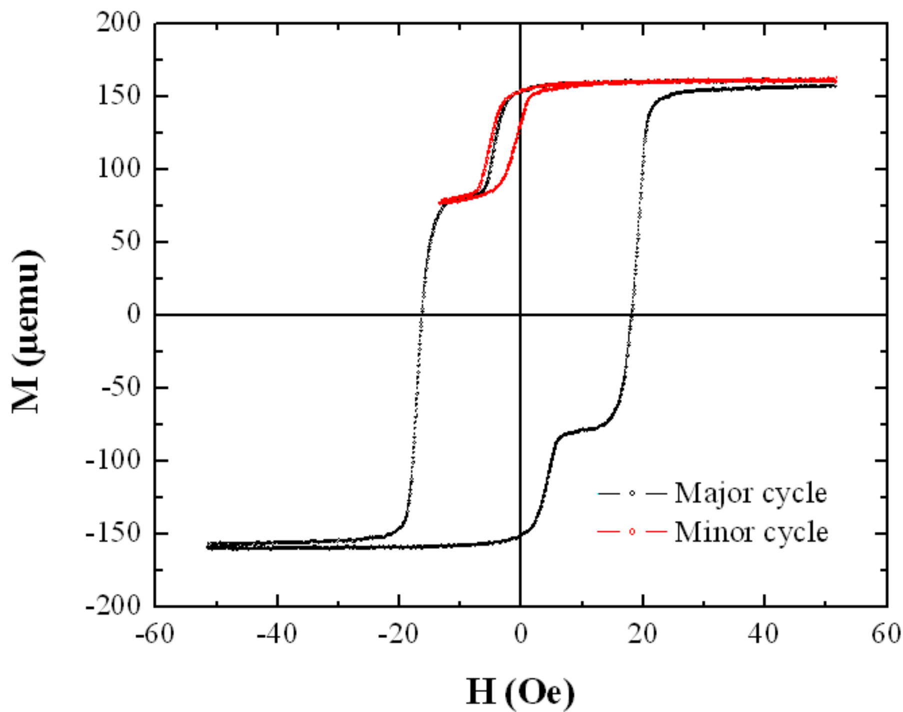


Figure 6.9: *Room temperature AGFM measurements performed on the $CoFe_2$(7.5nm)/$TiO_2$(3nm)/$CoFe_2$(0.75nm)/NiFe(6nm)/Ta(2nm) sample along its easy axis.*

The structure $CoFe_2$(7.5nm)/$TiO_2$(3nm)/$CoFe_2$(0.75nm)/NiFe(6nm) was grown in the PLD chamber on STO(001) substrate and capped with a Ta(2nm) using deposition conditions described in section 3.5. The $TiO_2$ deposition temperature was kept at 50°C. Subsequent room-temperature AGFM measurements showed that the stack exhibits a reasonably defined antiparallel magnetization state (fig. 6.9). The reason for which the plateau is not perfectly defined is tentatively attributed to high ($2 \cdot 10^{-7}$ mbar) pressure during the lower $CoFe_2$ deposition at the elevated

temperature 320°C, similarly to the case of STO-based devices described in the former section.

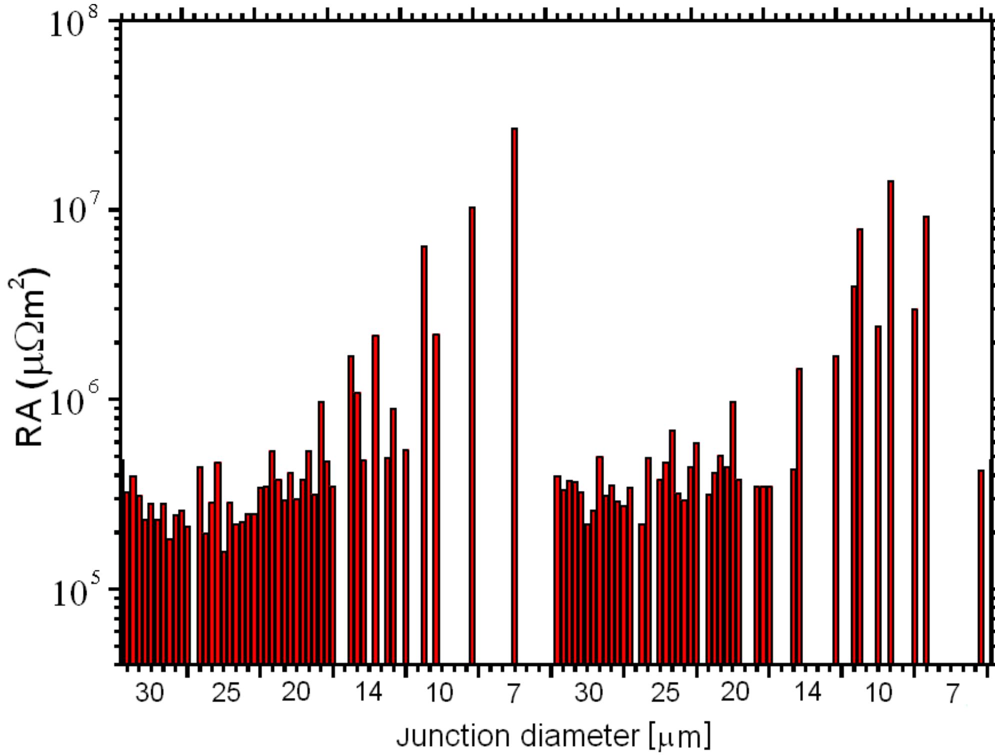


Figure 6.10: *RA map of $CoFe_2$(7.5nm)/$TiO_2$(3nm)/$CoFe_2$(0.75nm)/NiFe(6nm) system junctions. Only working junctions out of 144 are shown. Left and right sides correspond to the top and bottom parts of the sample, respectively, of which the latter was later annealed.*

The stack underwent the standard lithography and cutting procedure, after which resistance-area products were measured using the KarlSuss PM8 prober using 5mV bias in the 4-point contact mode. The RA product values were within the same order of magnitude ($10^5 - 106\mu\Omega m^2$), underscoring the electrical homogeneity of the devices (fig. 6.10). A relatively low number of working junctions was obtained among the smallest ones (7 to 10 $\mu$m in diameter) due to the difficult lift-off process. On the other hand, small working junctions show unusually high RA product that results from the limited lithography resolution, yielding diminished effective area (both issues described in section 4.3.3).

The sample was then cut and one of the identical halves was subsequently annealed at 200°C in air for 2h in order to determine the annealing impact on system properties. As shown on fig. 6.11, the post-annealing increased their resistances by 2 orders of magnitude, which in turn increased by up to one order more while cooling down to 4K. the resistance of the junctions increases fast upon cooldown to 100-

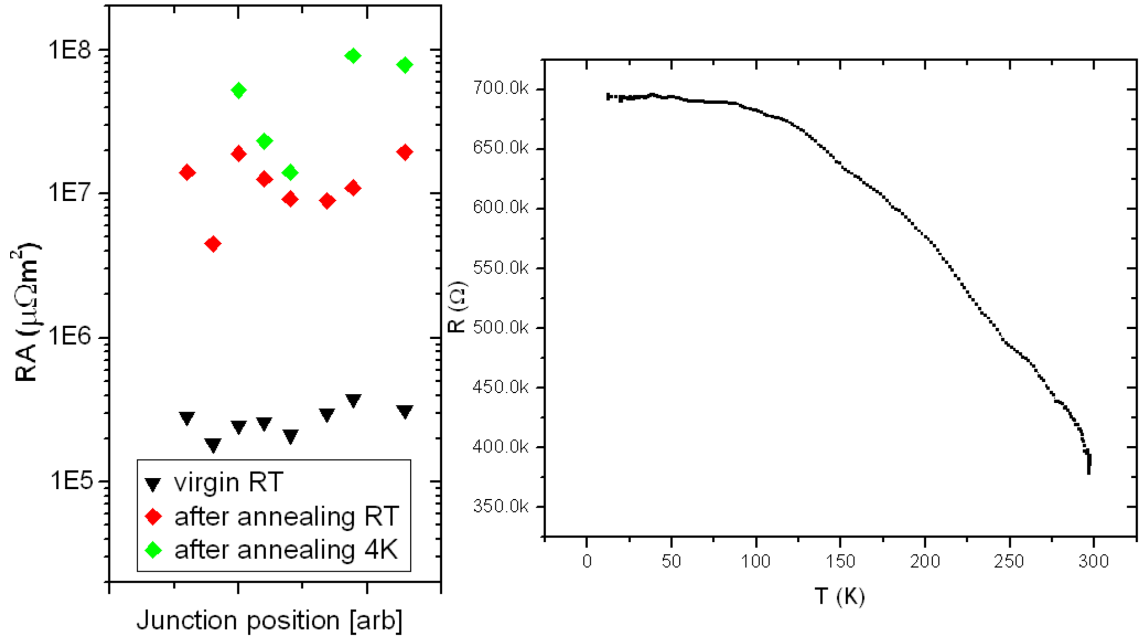


Figure 6.11: *Left: Annealing and subsequent cool-down impact on the RA product of several $CoFe_2$(7.5nm)/$TiO_2$(3nm)/$CoFe_2$(0.75nm)/NiFe(6nm) junctions. RA product in the virgin state of junctions (black) and after annealing at 200°C measured at room temperature (red) and at 4K (green). Right: Temperature dependence of a typical annealed junction with* 10$\mu m$ *diameter measured at 5mV.*

150K, after which it stabilizes, which suggests thermal deactivation of conducting shallow defect levels described in section 2.1.2.2.

Barrier heights of devices were determined by studying their current-voltage characteristics at room and liquid helium temperatures and applying the $\hat{I}$ method. However, results varied among junctions, yielding poorly-pronounced cusps corresponding to effective interfacial barrier heights ranging between 100 and 200meV (fig. 6.12) irrespective to whether the device had been annealed or not (only annealed junctions shown on the figure). $\hat{I}$ cusps at such low energies are not reported in defect-free $TiO_2$-based junctions where the electron barrier height is rather estimated to be 1eV [43]. On the other hand, theoretical calculations predict the presence of both oxygen and titanium vacancies in defective crystals between 0.7 and 0.8eV below the conductance band minimum. Assuming that the barrier height of a thin film may be reduced [96], the cusps we observe may result from these vacancies. It has to be noted that the lack of clearly pronounced features in results of the $\hat{I}$ method is typical for junctions yielding a low TMR signal [140].

Junctions from the $CoFe_2$/$TiO_2$/$CoFe_2$ structure showed no TMR at room temperature and even at 5K no TMR signal in the virgin state was observed. However the subsequent bias-crafting (see section 2.3) at the low temperature yielded changes

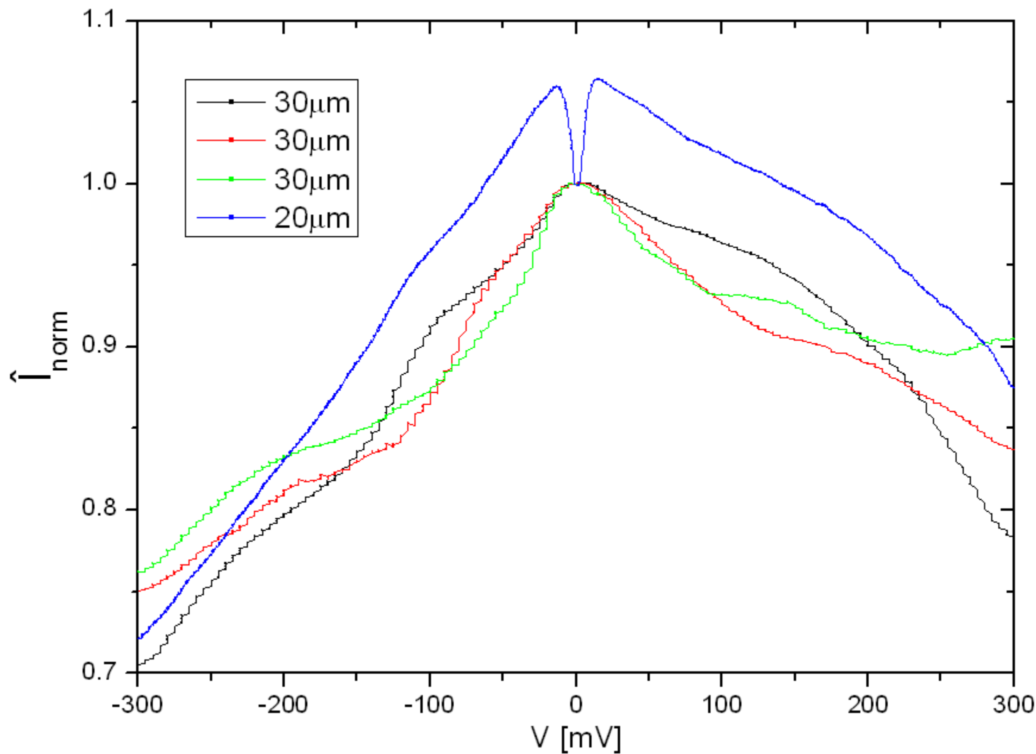


Figure 6.12: *Normalized absolute $\hat{I}$ measurements between 293K and 5K on several annealed $CoFe_2$(7.5nm)/$TiO_2$(3nm)/$CoFe_2$(0.75nm)/NiFe(6nm) junctions with diameters of 20μm and 30μm.*

in resistances accompanied by appearance of the TMR signal. This result was not reproducible and both the resistive state and the TMR sign seem to be independent of the applied bias. Fig. 6.13 shows an example of a MTJ that, after a few seconds long biasing at -300mV showed a resistance increase accompanied by the appearance of a negative TMR=-16.3%, whereas after subsequent crafting with the same value and sign of bias its resistance dropped down and the TMR became positive +25%. Further crafting with the same, higher, then positive biases (in this order), resulted in random resistance switching and no TMR (the signal was barely distinguishable from the noise). The behavior was observed on all devices processed from the sample. However the highest magnetoresistance signal measured on the annealed junctions was significantly lower (up to -0.5%, not shown) than the one observed from their non-annealed counterparts.

Similarly to the case of $SrTiO_3$-based devices, to the best of our knowledge, this preliminary result constitutes the only available evidence of reasonably large TMR across $TiO_2$-based junctions with transition metal electrodes.

In case of both non-annealed and annealed samples, low effective barrier heights (from 0.1eV) and low voltages at which electromigration can be triggered (from

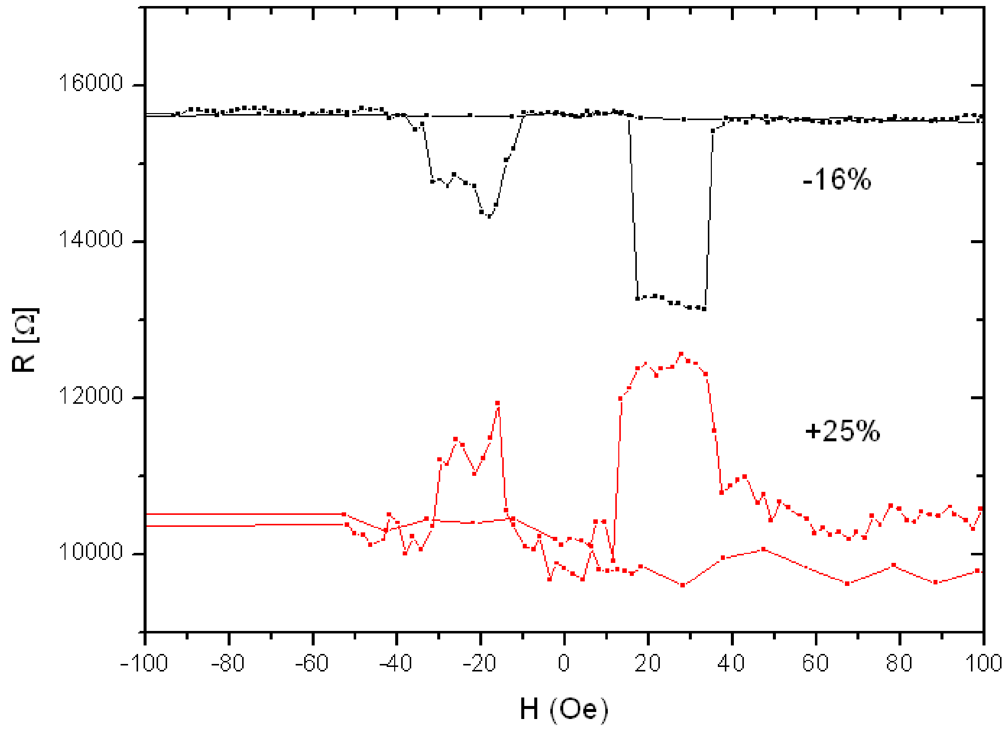


Figure 6.13: *TMR measured on a single non-annealed $CoFe_2/TiO_2/CoFe_2$ junction with 20$\mu$m in diameter. The virgin MTJ showed R = 14.7k$\Omega$ and noisy R(H) characteristics with no MR signal (not shown). Bias-crafting with consecutively rising bias in the bottom-to-top direction of the electrons flow resulted in random resistance changes with no MR signal until -300mV crafting when the negative -16.3% TMR was observed (black curve). Subsequent crafting with the same -300mV voltage once again yielded random resistance jumps and noisy R(H) characteristics (not shown) until unexpected positive TMR +25% (red curve). Further bias-crafting did not result in any clear TMR signal.*

200mV) suggest that these $TiO_2$ barriers exhibit defects, i.e. are structurally disordered, which may be attributed to the $TiO_2$ deposition temperature (50°C). In such systems, the disorder plays a crucial role in the spin-polarized transport, as it is not distributed homogeneously but rather flows through local defective configurations that serve as conducting channels. Tsymbal *et al* shows that these channels are characterized by low effective potential barriers[146], which is the case in our experiment. The same authors also describe the dependence of the TMR sign on the energetical position of conductive impurities relatively to the Fermi level. Once such a localized state appears within the $E_F$ and $E_F$+$eV$ range, the contribution of electrons tunneling through it may invert the tunnel magnetoresistance [147]. This is a possible hypothesis in the performed experiment, where the bias-crafting alters the occupation of defect states, though in an uncontrolled way.

### 6.2.2 Co/$TiO_2$/Co

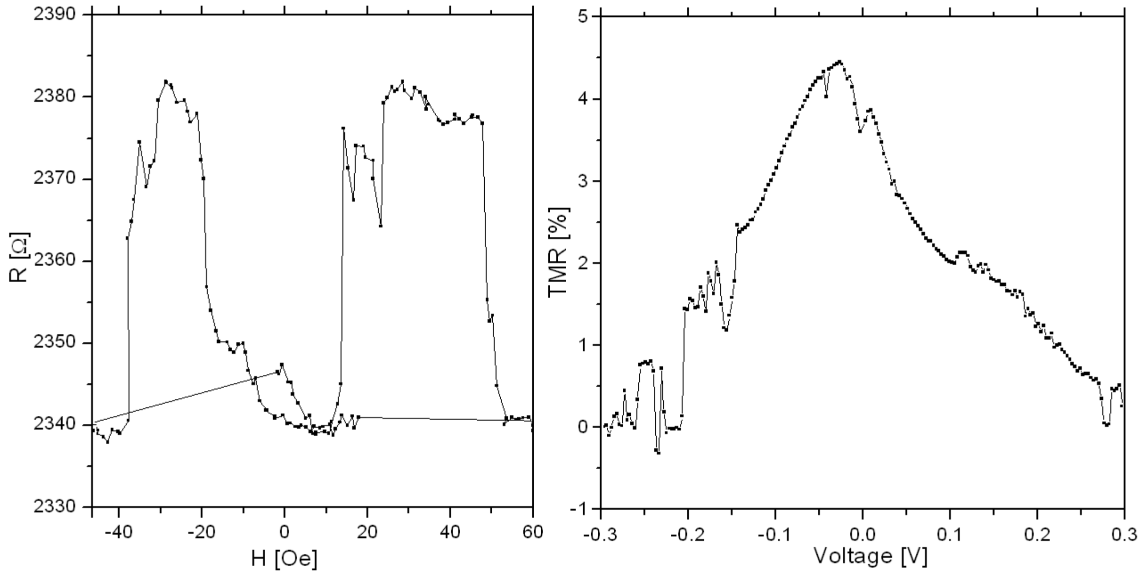


Figure 6.14: *4K field (left) and voltage (right) dependencies of the TMR ratio in the studied Co/$TiO_2$/Co structure.*

An additional attempt to improve the spin-polarized transport across transition metal oxides was to introduce thin cobalt layers at $TiO_2$ interfaces in order to reduce the interfacial oxidation (see section 1.6.1.2). Such change would also make the interface easier to understand in terms of its band structure. In the PLD chamber the STO//$CoFe_2$(6)/Co(1.6)/$TiO_2$(3)/Co(1.6)/NiFe(6)/Ta(2) structure was grown. Magnetization characteristics were found to be similar to these of the previously studied $CoFe_2$/$TiO_2$/$CoFe_2$ sample (fig. 6.9). However, despite the correct lithography processing and relatively large number of junctions showing correct values of the RA products varying between $10^5 \Omega \mu m^2$ and $10^6 \Omega \mu m^2$, devices performed poorly from a spintronic standpoint. Their temperature dependence was also similar to that of the $CoFe_2$/$TiO_2$/$CoFe_2$ junctions. Again, none of junctions showed the TMR signal in their virgin state, while bias-crafting at 4K temperature resulted in random TMR signal reversals, the highest observed being an unambiguous +4% on a non-annealed MTJ of diameter $10 \mu m^2$ (fig. 6.14). Once again, TMR was obtained neither at room temperature nor from annealed devices (even at 4K). These poor performances are attributed to the same barrier distortions as in the $CoFe_2$/$TiO_2$/$CoFe_2$ case.

## 6.3 Conclusions and move towards LSMO

In the consecutive studies of $SrTiO_3$- and $TiO_2$-based devices, we attempted to resolve several issues: 1) interface termination of $SrTiO_3$, i.e. SrO and $TiO_2$ mixing, which affects wavefunction hybridization at the interface and 2) interfacial oxidation due to high oxidation enthalpy of the material (Co vs $CoFe_2$ issue) or because of contaminants in the chamber at the given pressure. The latter one reflects either the high base pressure in the chamber or the additional compounding fact that the lower electrode is annealed before the barrier deposition, leading to even higher pressure resulting from excessive outgassing due to the direct exposition of the PLD chamber during the loading of samples after which it is not baked out. Despite the incremental improvements in the structure of samples presented, it is suggested that the design of the chamber precludes the study of MTJs with a lower electrode consisting of a transition metal, even cobalt. As the consequence, research was directed towards $La_{0.7}Sr_{0.3}MnO_3$. Usage of LSMO as the bottom electrode would result in no oxidation of the lower interface. Moreover, the LSMO/$TiO_2$/Co structure would present no issues connected to the uncertainty of the barrier termination.

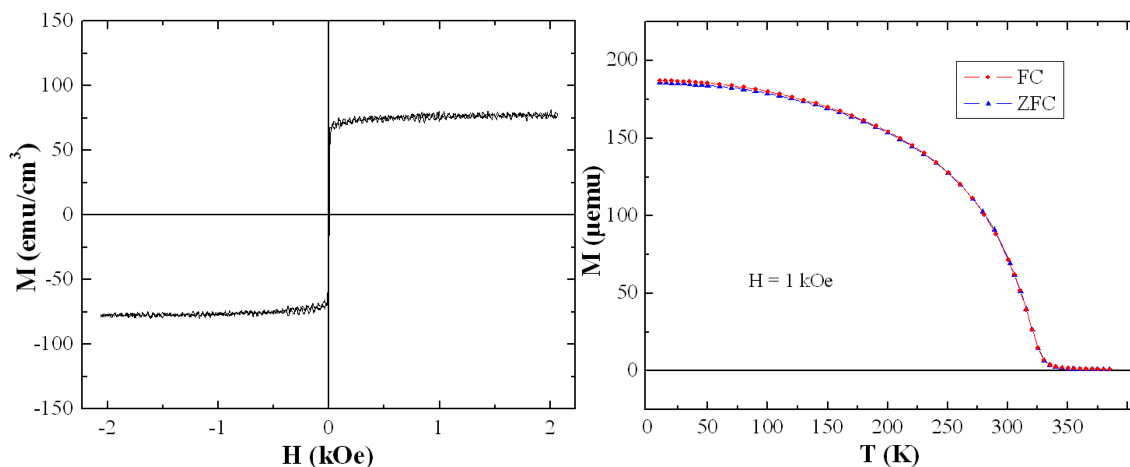


Figure 6.15: *Room temperature AGFM (left) and SQUID (right) measurements on STO//LSMO(50nm) structure fabricated with the PLD setup. FC and ZFC denote field-cooled and zero field-cooled SQUID measurements, respectively.*

LSMO films grown by the DCMI group using the PLD setup were satisfactory from the magnetic standpoint. They exhibited a low coercive field reversal and a Curie temperature of about 330 K (fig. 6.15). Moreover, the field-cooled and zero field-cooled superconducting quantum interference device (SQUID) measurements did not show any difference, which means that the LSMO crystal was free of impurities.

However, devices containing working LSMO electrode were very difficult to obtain, essentially due to oxygen content issues within the nominally grown material.

Indeed, the oxygen-deficiency of LSMO films disturbs the double-exchange electronic transfer mechanism, which results in drastically reduced conductance of the material and gives rise to its insulating nature [137]. This therefore implies that it is crucial that these films be sufficiently oxygenated during the growth, and remain sufficiently oxygenated from the growth stage to the device measurement stage. Filling the PLD chamber with 0.5mbar of oxygen during the LSMO growth proved to be not enough in order to achieve its full stoichiometry.

As the result, a typical resistance of the 25nm thick bottom LSMO electrode resulting from the standard lithography processing was of 100MΩ order. Vestigial conductance disappears upon cooldown, reaching more than 30GΩ already at 250K, below which the value was unmeasurable due to sensing capabilities of the setup. Obviously, such high resistances did not allow any study of devices.

Several experiments were performed in order to determine whether the substoichiometry of the material could be prevented. At the first step, increasing the oxygen content during the LSMO deposition was attempted [41]. However, the resistive heating system used in order to maintain the substrate temperature at 778°C during the growth got oxidized, which eventually led to its breakdown upon numerous attempts.

| | Electrode type | |
|---|---|---|
| Annealing time | Correctly etched | Slightly overetched |
| 0 | 250kΩ | 3MΩ |
| 24h | 10kΩ | 70kΩ |
| 48h | 10kΩ | 40kΩ |

Table 6.1: *Incidence of in-atmosphere annealing time of substoichiometric* $La_{0.7}Sr_{0.3}MnO_3$ *lower electrodes at 200°C.*

Another way to handle the problem was to perform an additional annealing of the lower electrode following the second lithography step. Such annealing was done at 200°C in air in order to reoxygenate the LSMO. The study was performed on two types of samples - etched correctly (stopped in the barrier) or slightly overetched. Referring to table 6.1, after 24h and 48h annealing, we obtain resistance values for the LSMO lower electrode of thickness and shape that are similar to devices which are reported to yield correct results [145]. However, the lower electrode resistance dramatically increased once the $SiO_2$ encapsulation was performed. This could either reflect 1) exposure of the LSMO layer to the vacuum or 2) oxygen pumping of LSMO by the substoichiometric $SiO_2$. The first case would imply that LSMO is not maintaining its oxygen stoichiometry, whether nominally obtained through the deposition or through the subsequent annealing in air. The growth conditions of LSMO could be then responsible for this technological shortcoming. If the poor

performance results from the second case, a more stable $SiO_2$ or even the silicon nitride ($Si_3N_4$) passivation layer may be needed for LSMO-based devices.

# Chapter 7

# Magnesium oxide

This chapter describes studies performed on MgO-based structures. Such studies can be divided into two sections: 1) studies on magnesium oxide films, which were grown using the Hybrid System, then studied electrically and optically from their defective standpoint; 2) study of MgO-based magnetic tunnel junctions. As the latter section describes two different approaches to tunneling devices, it is also split in two: preliminary results of the *in-situ* processing of devices grown with the Hybrid System, which includes a discussion on issues relating to the sputter chamber pressure; and a study of CoFeB-based structures grown by M. Hehn at the *Institut Jean Lamour* in Nancy.

## 7.1 Barrier studies

As it is widely accepted, the barrier quality has a crucial impact on the device properties. Within the timeframe of this thesis, extensive studies were performed on the magnesium oxide growth conditions that strongly affect the quality of this dielectric.

### 7.1.1 Optical activity

As mentioned in section 2, oxygen defects play an important role in the barrier behavior. In order to alter the density of the defects during the MgO layer Hybrid System deposition, oxygen was introduced in addition to the argon flow required by magnetrons to maintain the plasma. The working pressure remained unchanged ($1 \cdot 10^{-3}$ mbar), while the oxygen-to-argon ratio was varied from 0% to 10% for specific deposition runs.

Several MgO(001)//MgO(50nm) samples with different $O_2/Ar$ ratios were grown. They underwent optical transmission spectra measurements using the UV-Vis-NIR Perkin-Elmer Lambda 950 spectrophotometer, after which their optical absorption was calculated. The results are shown on fig. 7.1.

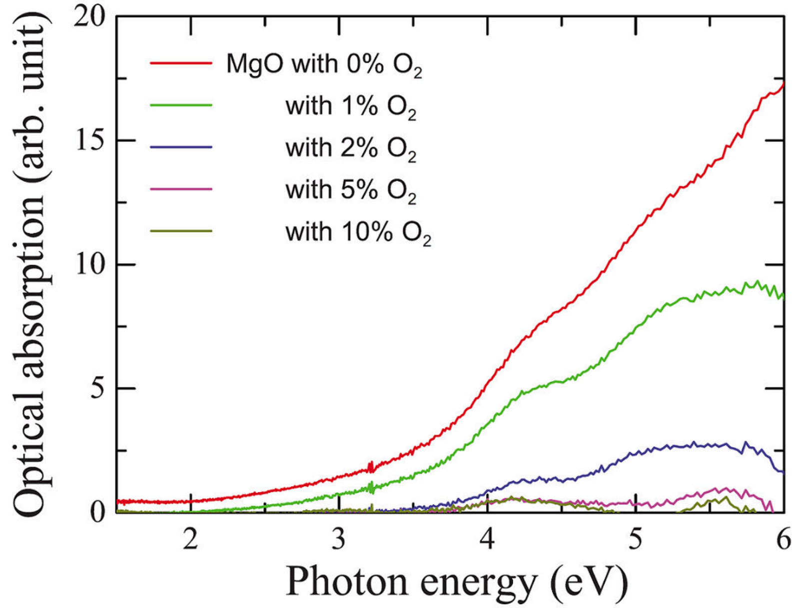


Figure 7.1: *Optical absorption spectra of MgO(000)//MgO(50nm) samples fabricated under the same pressure but with different $O_2/Ar$ ratios. Substrate-related features are subtracted [148].*

There are three significant absorption peaks for the sample grown in the pure argon conditions. The peak positions were assumed to represent absorptions on the double oxygen vacancy ($F_2$ or M center) at 4.2eV [99] and the oxygen neutral and singly charged vacancy ($F$ and $F^+$ centers, respectively) at 5eV [149, 150, 103, 97, 98]. The position of these defects in the MgO energy gap is schematically shown on fig. 7.2 and we will return to this picture several times throughout the analysis. Moreover, a peak that we can associate with a doubly charged oxygen vacancy ($F^{2+}$ center) is visible at 5.6eV [100, 151], but it will not play a significant role in the interpretation of results. It is evident that, by increasing the oxygen content during the growth, the spectral weight of peaks decreases, especially that of the one attributed to the $F$ and $F^+$ centers (at 5.0eV) which disappears nearly entirely.

### 7.1.2 Electrical measurements

In order to determine the impact of defects on the tunneling transport, conductive atomic force microscopy was performed using the N-Tracer Nanofocus Inc. C-AFM (collaboration with W. S. Choi at Seoul National University) on 1.2nm-thick MgO layers grown atop MgO(001)//MgO(10nm)/Fe(20nm) stacks. The layers were grown in 0% and 10% $O_2/Ar$ ratio using standard Hybrid System conditions. In the latter case, the first MgO monolayer was sputtered without oxygen introduced in the

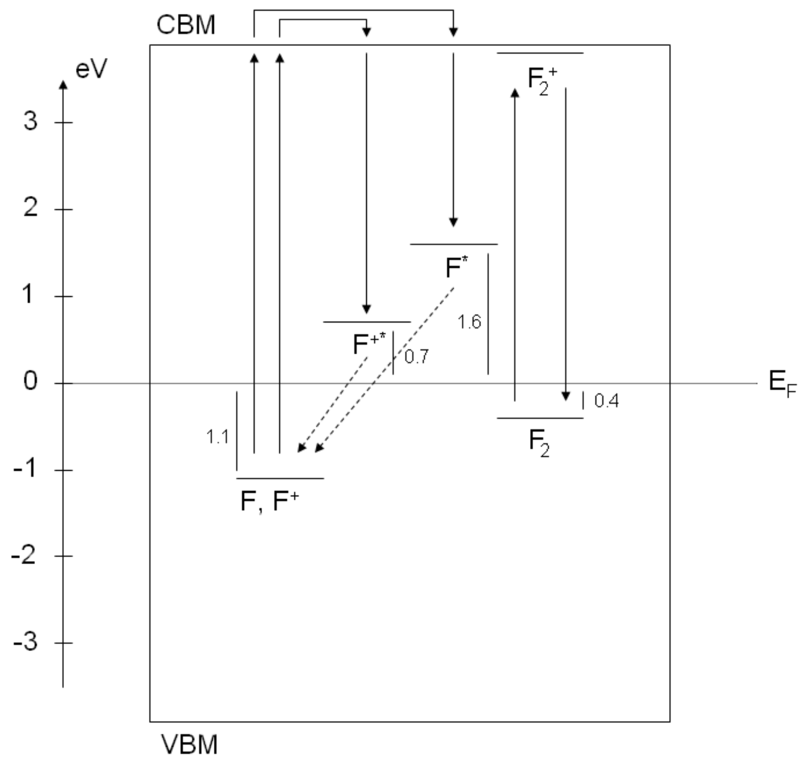


Figure 7.2: *Schematic representation of oxygen defect levels in the MgO barrier height. The band gap is assumed to 7.8eV and $E_F$ to lie in the center of the barrier. Numbers denote absolute energy differences (in eV) between the $E_F$ and the level of the corresponding defect site. Solid arrows depict optical absorption and emission processes associated with corresponding defect sites, while their dashed counterparts mark a phonon-assisted relaxation from excited state to ground state. Mg defect levels are not represented for clarity.*

chamber in order to avoid the iron oxide formation at the Fe/MgO interface.

Despite the fact that the root mean square roughness remains mostly unchanged throughout the study, the density and intensity of the local current hotspots is clearly evolving (fig. 7.3). As this local current inhomogeneity is not topography-related, it has to result from the insulator barrier thickness or its effective height. Considering the photoluminescence-inferred decrease in the oxygen vacancy density with increasing oxygen content in the Ar plasma, we assume that these local current modifications are associated with oxygen vacancies [152]. The fitting of the fig. 7.3e data reveals the averaged currents of 6.1pA and 0.3pA for the 0% and 10% $O_2$ barriers, respectively, which implies at the qualitative level a significant improvement in the barrier height.

As conductive hotspots on the local tunneling maps originate from defects in the barrier, current-voltage measurements were performed at and away from the

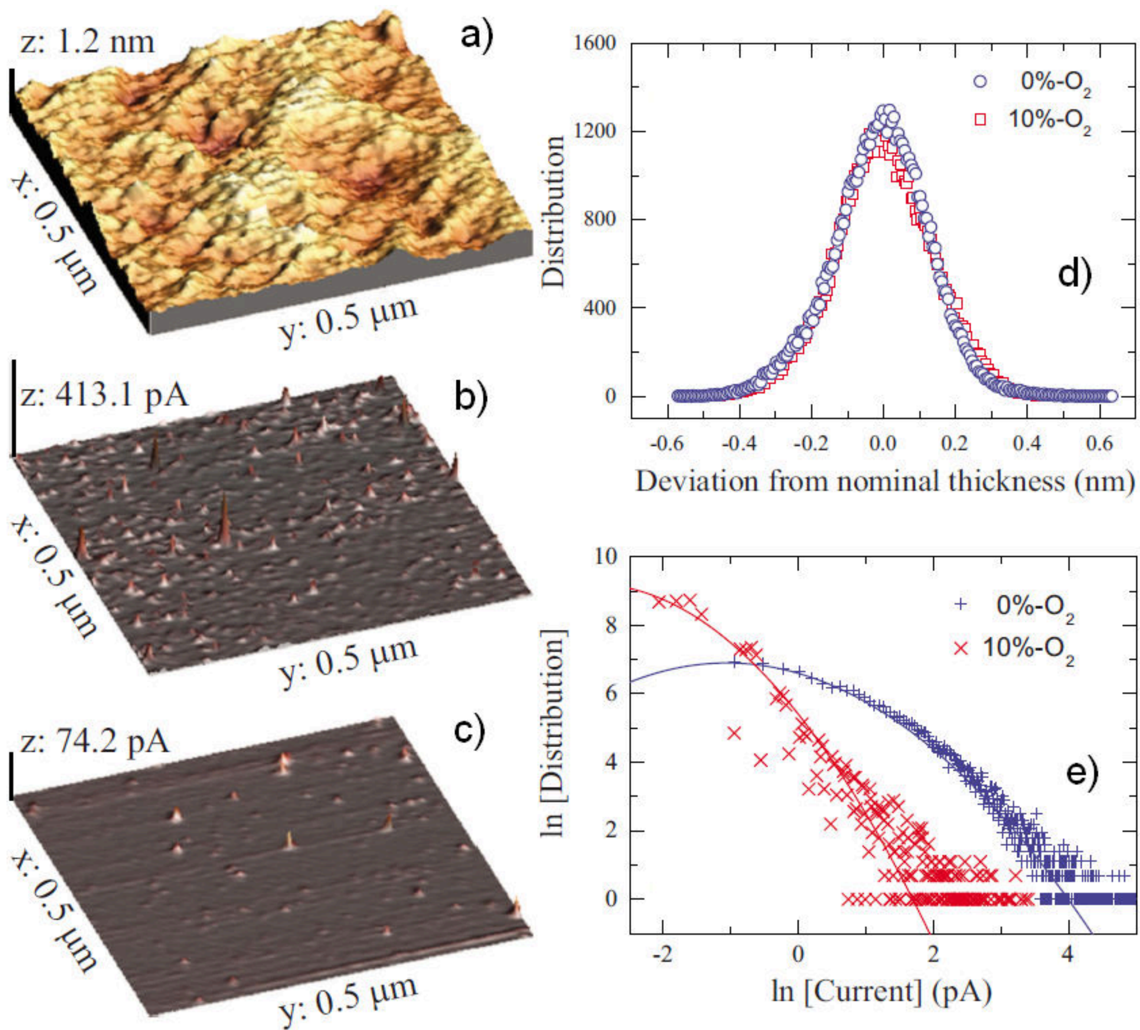


Figure 7.3: *a) Topographic map of the MgO barrier deposited without oxygen present in the chamber during the growth. The result is similar to that for the 10% $O_2$ layer. b) Local tunneling map with 1V bias of the 0% $O_2$ layer. c) Same for the 10% $O_2$ MgO layer. d) Comparison of topographic distribution deviation from the nominal thickness for both samples. e) Local current distribution comparison from figures b) and c) [148].*

hotspots in order to study their impact on the barrier height. This was done on both samples using the aforementioned conducting AFM. Typical and reproducible I-V curves are shown on fig. 7.4. We assume here that the turn-on of the IV curve represents a qualitative estimate of the effective barrier height [153]. In order to facilitate an understanding of the I-V curve, the schematic is drawn in fig. 7.5. As the first half-monolayer of the MgO barrier was deposited without any oxygen within the chamber, the lower interface of the 10% $O_2$ sample may resemble the one of the

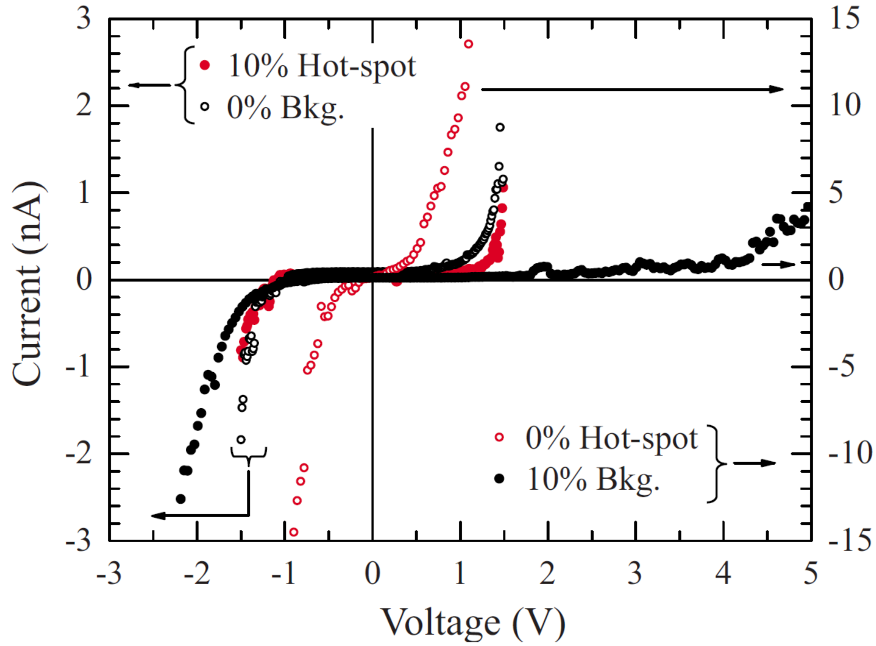


Figure 7.4: *IV characteristics measured at 300K by conductive AFM tip on 0% and 10% $O_2$ samples both at and away from the local tunneling hotspots [148].*

sample grown in the pure argon. As it is the lower interface which is probed with the negative bias, left-hand curves measured in the background look alike for both samples. Within the positive voltage range, while going from 0% to 10% $O_2$, the barrier height rises from 0.9eV up to 4.1eV in the background and from 0.4eV to 1.1eV on hotspots. The 0% $O_2$ background and 10% $O_2$ hotspot characteristics are similar, which suggests that the increase in oxygen content during the growth results in the disappearance of the defects leading to the 0.4eV barrier height. Moreover, the defect-induced 0.9eV-high barrier present in the background of the 0% $O_2$ sample exist only locally (i.e. on hotspots) within the 10% one due to the improvement of the barrier structure. If we assume that the Fermi level lies in the middle of the MgO band gap [97] (fig. 1.11), we may attribute the barrier height of 0.4eV to result from the presence of defect sites of the $F_2$ type (figure 7.2). The barrier height of around 1eV corresponds to $F$ and $F^+$centers. The turn-on at around 4eV in the background of the 10% sample is assumed to be the intrinsic barrier height of the MgO insulator.

Combining results of I-V characteristics with these of the absorption spectra, one may see that $F$ and $F^+$ centers which lie 5eV below the conduction band and are responsible for the optical absorption at 5eV define the effective MgO barrier height at around 1eV (fig. 2.4a). Their almost total disappearance from the absorption spectra of the 10% $O_2$ sample is followed by the significant increase of the barrier height in the background from around 1eV to up to 4eV. This suggests that $F$ and

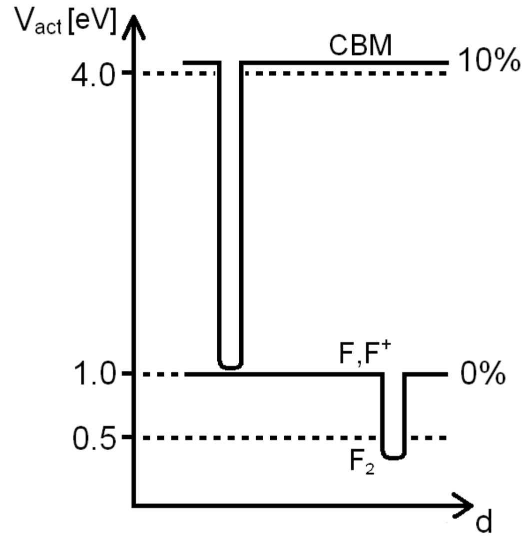


Figure 7.5: *Schematic representation of the right-hand part of the fig. 7.4. The horizontal scale corresponds to a hypothetical lateral C-AFM measurement encountering a single hotspot. The vertical scale shows typical voltage of the conductance activation. Highly conductive hotspots of the 0% sample are eliminated in the 10% sample. Value of background conductance of the 0% sample is reported on the 10% sample hotspots. Background conductance of the 10% is significantly lower than in the 0% case.*

$F^+$ centers, if present, determine the effective barrier height around 1eV and greatly reduce the dielectric quality of a MgO barrier.

Combining results of I-V characteristics with those of the absorption spectra, one may see that $F$ and $F^+$ centers, which lie 5eV below the conduction band and are responsible for the optical absorption at 5eV, define the effective MgO barrier height at around 1eV (fig. 2.4a). Their almost total disappearance from the absorption spectra of the 10% $O_2$ sample is followed by the significant increase of the barrier height in the background from around 1eV to up to 4eV. This suggests that $F$ and $F^+$ centers, if present, determine the effective barrier height around 1eV and greatly reduce the dielectric quality of a MgO barrier.

In conclusion, our experiments show that the density of oxygen vacancies can be controlled during the growth by altering the oxygen content during the MgO deposition and that the presence of certain types of these defects can be be to a certain extent suppressed. This results in a significant improvement of the barrier height and reduction of possible undesired hotspot-driven filamentary current channels.

## 7.2 Fe/MgO/Fe

This section described results obtained on devices fabricated with the shadowmask technique. Results concerning the spin-polarized transport are rather preliminary, as most of the related work concentrated on the growth optimization.

A significant part of this thesis concentrated on fabrication of MgO-based devices using the Hybrid Systems' sputtering chamber with the shadowmask deposition (section 3.3.1). Due to technical aspects, it is not possible to rotate the sample during the MgO deposition while maintaining a precise positioning so as to perform the correct alignment of the technological MgO step. Profilometer and AFM tests performed on samples grown in the absence of the rotation showed topographic uniformity of samples. Yet the device resistance is not uniform across a given sample. In case of the sample presented on fig.4.3 (area $2500\mu m^2$) resistances of junctions were 6Ω, 560Ω, 2kΩ and 4.8kΩ, in that order. These values correspond to RA products (in $\mu\Omega m^2$) 15k, 1.4M, 5M and 12M, respectively. Figure 7.6 shows the observed resistances on a logarithmic scale as a function of the evenly spaced junction position. Three junctions show exponential dependence of resistance on the junction position, which suggests linear thickness decrease among them. One of the signatures of a tunneling regime, in the form of non-linear current-voltage characteristics [22], was observed on all four junctions (see fig. 7.7). Interfacial barrier heights calculated using Brinkman's formula were 1.47eV and 1.58eV for the bottom and the top interface, respectively. The difference could reflect oxidation issues at the lower interface.

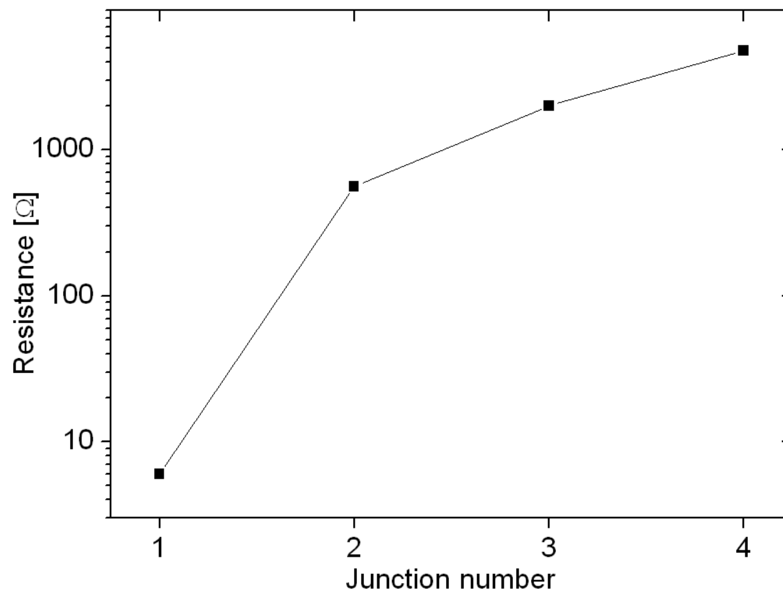


Figure 7.6: *4-point resistances of $2500\mu m^2$ Fe/Mg(0.4nm)/MgO(3nm)/Fe junctions grown in a single batch using the shadowmask technique.*

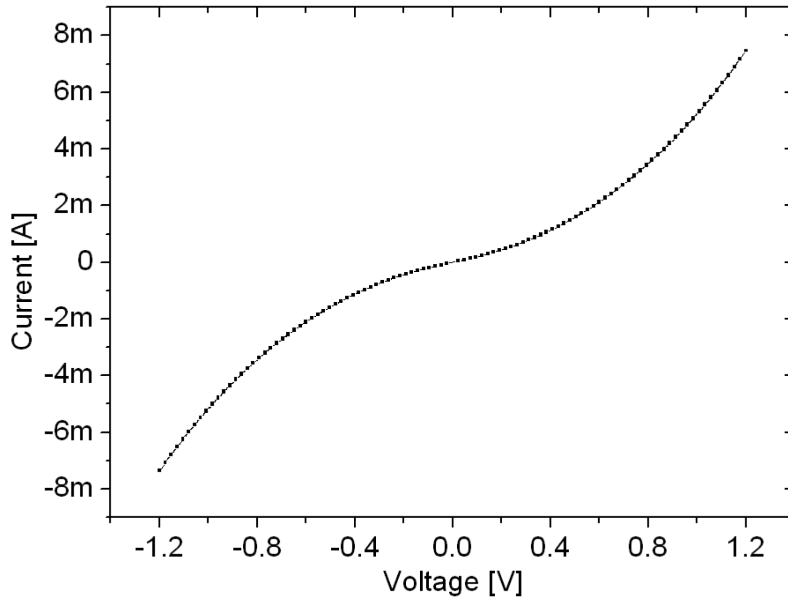


Figure 7.7: *RT current-voltage measurement performed on 2500$\mu m^2$ Fe/Mg(0.4)/MgO(3)/Fe junction grown in a single batch using the shadowmask technique. The 4-point junction resistance at 5mV was 560Ω.*

If we compare RA products of our junctions with the ones reported on MgO samples in the literature (fig. 2.3), we may see that within this RA range the TMR signal of more than 60% is observed. However, no TMR signal was observed on magnetic tunnel junctions grown with our Hybrid sputtering system, even at low temperatures.

Although significant results concerning the defect incidence on properties of the MgO crystal were obtained, devices grown with the Hybrid System's sputtering were not satisfactory from the spintronic standpoint. As mentioned within the section 3.3.1, the crucial issue related to the poor spintronic performance of the devices fabricated with the hybrid system was assumed to be the excessive pressure during annealing of the lower electrode.

The heater mounted originally within the sputtering chamber was a Thermocoax Kanthal with heating elements covered in $Al_2O_3$, which allowed to reach 800°C if the annealing was performed in oxygen. However, due to excessive outgassing of Cr and Ni elements it was replaced with a platinum rod heater. However, even in this case the stainless steel cover caused outgassing of chromium, which resulted in pressures of $10^{-6}$ mbar range at 550°C. During the time of writing, the current solution for the annealing pressure is the Ta heater, which improved the annealing pressure down to $10^{-7}$ mbar at 550°C, albeit it can be used only below 0.4mbar. Unfortunately, analysis of the results suggests that this pressure remains incompatible with oxidation-free Fe/MgO interfaces.

This thesis is taking place while the hybrid system is being constantly developed and improved. Within the timeframe of this manuscript publication, a recent upgrade of the setup in the form of a titanium sublimation modification is underway, promising significantly lowered pressure during the sample annealing. However, if the solution proves unsuccessful as well, omitting the lower electrode annealing step is considered. Since such a move would result in Volmer-Weber island-like growth, it is possible that moving to CoFeB electrodes may be required.

## 7.3 CoFeB/MgO/CoFeB

This section encompasses results obtained on CoFeB-based structures grown by Michel Hehn from the *Institut Jean Lamour* in Nancy which were later processed in the IPCMS. Studies related to these devices devices were performed towards the end of the thesis. We describe our present understanding of our results and indicate future directions implied by these results.

Ta(5nm)/Co(10nm)/IrMn(7.5nm)/CoFeB(4nm)/MgO(2.5nm)/CoFeB(4.5nm) structures were grown on amorphous Corning 1737 glass using growth conditions described in section 3.3.2. This means that one of their electrodes is magnetically pinned in the direction following the magnetization direction of the antiferromagnet. The structures were capped with a Ta(5nm)/Pt(5nm) bilayer. Similar structures, albeit without the top CoFeB/Ta/Pt trilayer were also grown in order to study the MgO(2.5nm) layer optically. The goal of the study was to determine the impact of annealing at 300°C on their magnetoresistive and optical properties. However, as both sample types were not deposited in the same batch but separately, it is possible that observations of our experiment may not be unambiguously explained as due to annealing. Magnetic tunnel junctions were patterned using the standard optical lithography and were the first to be studied with the Fert setup after the automatization of measurements.

### 7.3.1 General properties

Photoluminescence experiments performed with 325nm and 355nm wavelength laser on structure terminated with the MgO(2.5nm) layer (i.e. encompassing the lower electrode and tunnel barrier but not the top electrode stack) show peaks at 440nm (2.8eV), 495nm (2.5eV) and 730nm (1.7eV) after deconvolution (fig. 7.8). Although the photon energy used in our experiment is not sufficient to excite $F$ and $F^+$ centers so the luminescence resulting from these sites cannot be observed directly, we attribute the peak at 440nm to the reverse ionization of $F$ and $F^+$ centers and recombination of electrons to the top of the valence band. The other two peaks (495nm and 730nm) we attribute to photon emission associated with relaxation of $F^*$ and $F^{+*}$ centers to their respective ground states. Similar results (not shown)

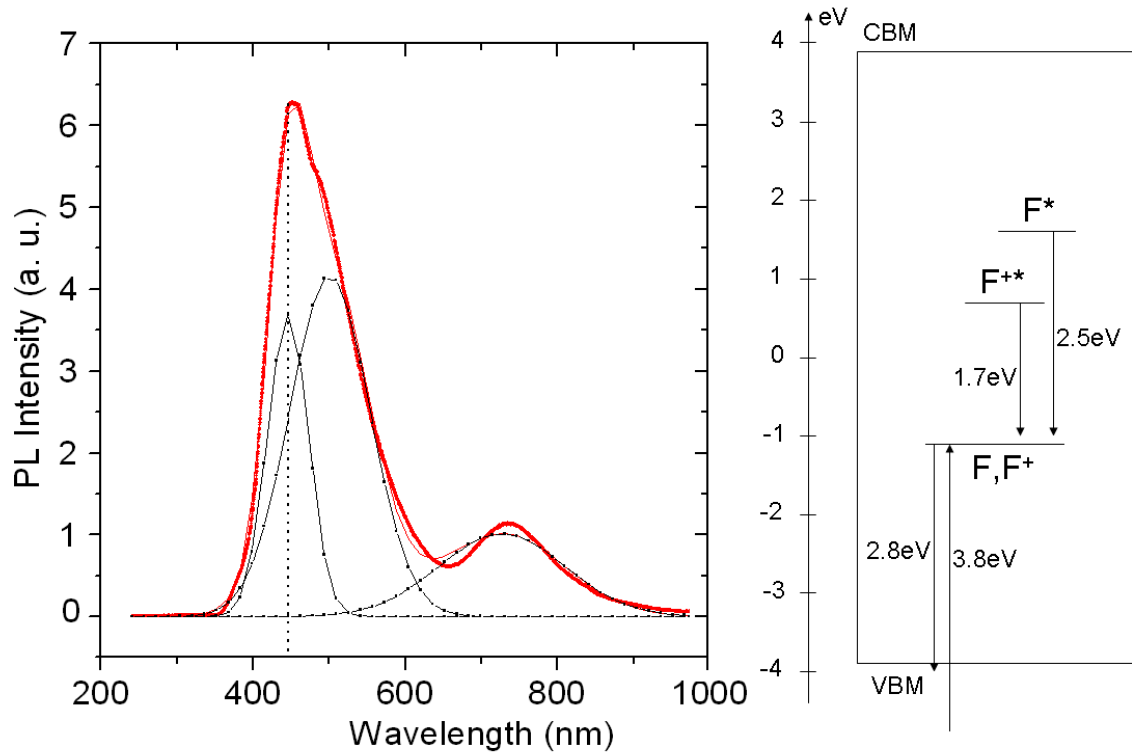


Figure 7.8: *Left: Typical room-temperature photoluminescence spectra from an annealed Ta(5)/Co(10)/IrMn(7.5)/CoFeB(4)/MgO(2.5) stack grown on Corning glass 1737 and annealed for 1h at 300C (red) collected after the 325nm laser excitation. Position of the main peak after deconvolution is 440nm. Positions of the minor peaks are 495nm and 730eV. Similar results were obtained from non-annealed devices and after 355nm light excitation (not shown). Right: Schematic representation of the observed luminescence.*

were obtained for the annealed devices, as well as upon 355nm light excitation. Therefore, we confirm presence of the mentioned defect sites in the barriers studied.

When taking into account processing issues of the full stacks (see section 4.3), magnetic tunnel junctions were characterized by very uniform RA products per sample (fig. 7.9). In the particular case presented, RA products of annealed devices are significantly lower than their non-annealed counterparts. However, studies performed on a number of samples show that the difference in RA products does not result from the annealing process, but rather from a slight variation in the sample growth conditions or processing issues, especially from the barrier over-etching during the step I of the photolithography (see section 4.2.3.2 for details).

Several junctions of each type were selected in order to perform detailed measurements and showed reproducible characteristics. On figure 7.10 we plot a typical $\hat{I}_{abs}$ graph for both an annealed and an non-annealed device. This method, among

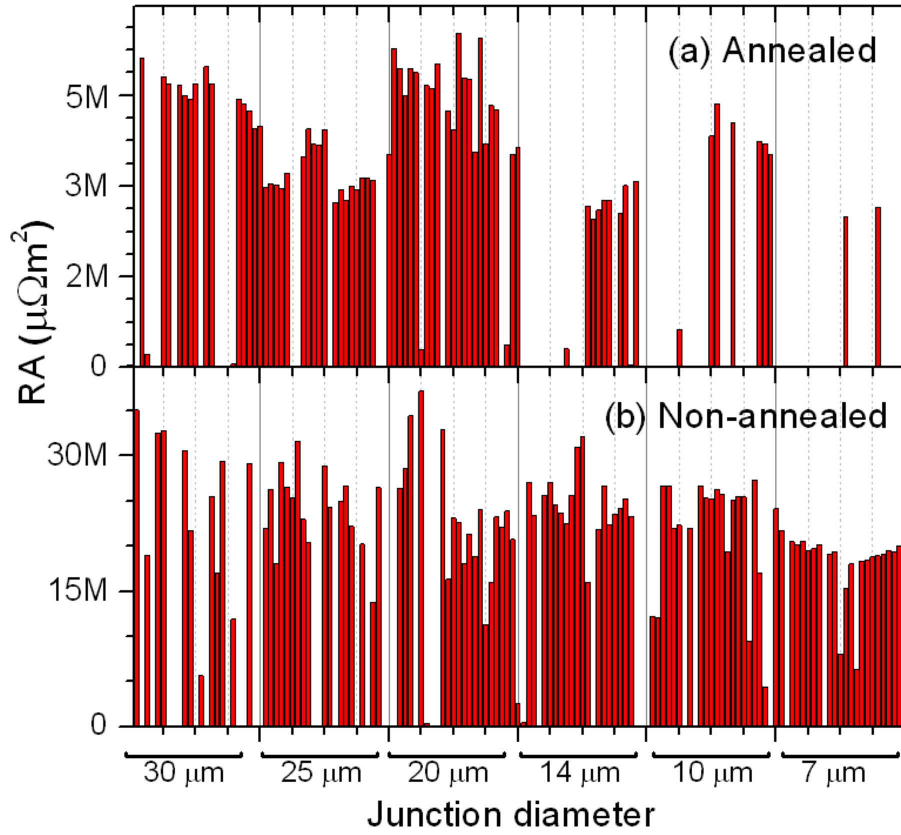


Figure 7.9: *Resistance-area products of a) annealed and b) non-annealed CoFeB(4)/MgO(2.5)/CoFeB(4.5) samples. Data for shorted and open-circuited devices are shown as zero.*

others mentioned in section 5.2 is well established as a tool to extract the effective barrier height of a magnetic tunnel junction. In case of the non-annealed device, the effective barrier height is 0.7eV for both P and AP configurations. We note that finding the same value for both P and AP configurations is in fact expected for a paramagnetic barrier [43]. However, the barrier height of the annealed device shows 0.7eV in the AP case, and more than 0.8eV in the P case[1]. Furthermore, this barrier height is obviously lower than that expected (≈4eV) if it reflected a valence or conduction band edge. It is therefore attributed to defects. In turn, this suggests that these defects have an impact on the spin- and/or symmetry-polarized transport in the system as we will see hereafter.

Magnetization curves of both samples measured at room temperature with the

[1]Room temperature measurements in voltage higher than 0.8V were not performed due to the experimental protocol that was implemented in order to mitigate the risk of the electrical breakdown. However, in the 250K-4K range the $\hat{I}_{abs}$ peak occurred at 0.88eV. As the following analysis will show, the peak is expected to lie within 0.80V-0.88V range.

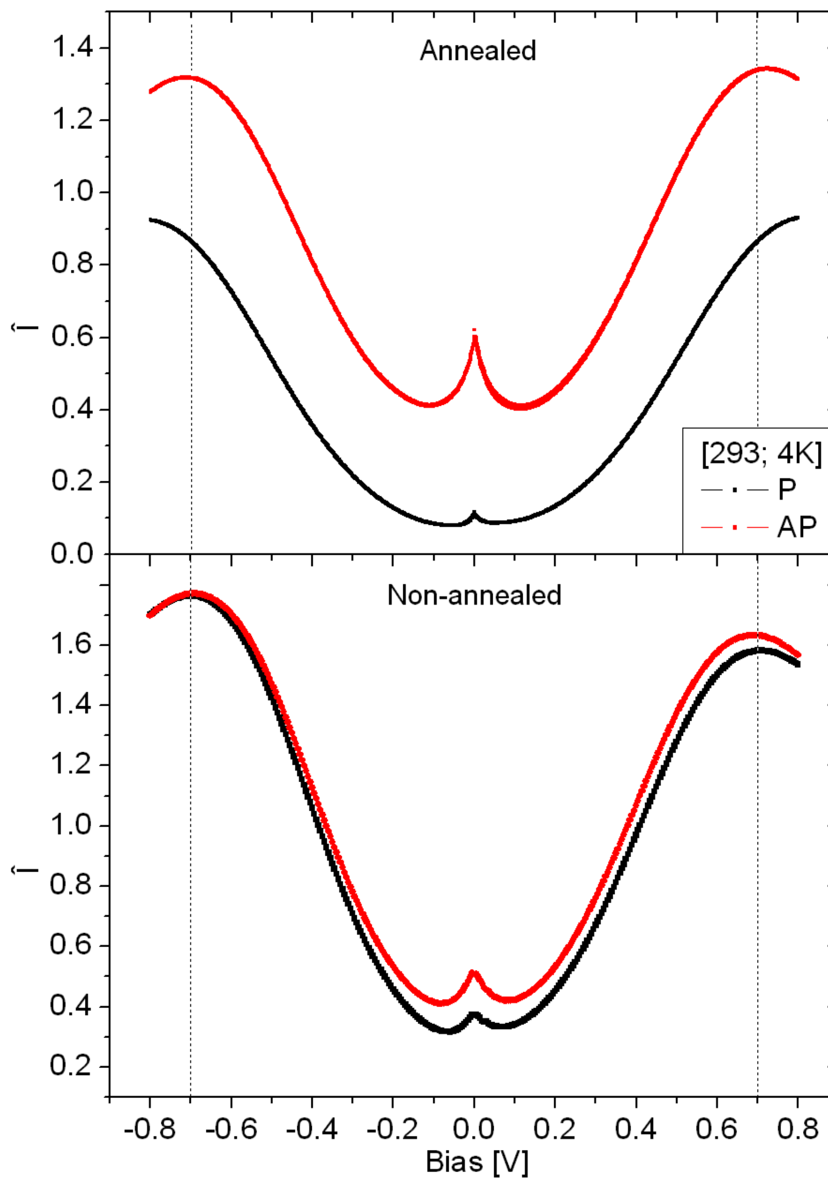


Figure 7.10: *$\hat{I}_{absolute}$ curves for an annealed (top) and non-annealed (bottom) device in the P (black) and AP (red) relative magnetization state measured between 293K and 4K. The diameter of junctions is 30μm and 25μm, respectively.*

SQUID setup are shown on figures 7.11a and 7.12a). The non-annealed sample shows a noticeable, albeit not perfectly defined flip of the magnetization with the applied field. Its annealed counterpart exhibits an improved AP alignment thanks to the pinning provided by the IrMn/CoFeB lower electrode exchange bias induced by annealing. Magnetization flipping of specific layers of the annealed sample is marked on the graph for clarification.

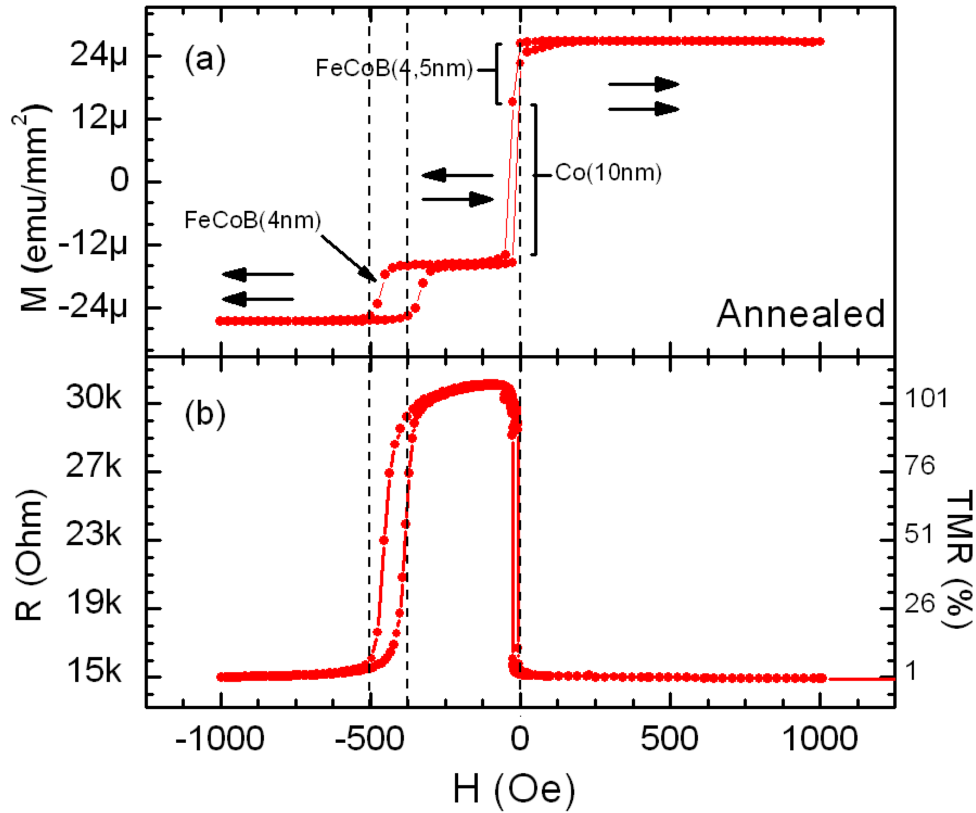


Figure 7.11: *Room temperature a) SQUID magnetization and b) resistance/TMR vs applied field measurements on the annealed Co(10)/IrMn(7.5)/CoFeB(4)/MgO(2.5)/CoFeB(4.5) sample. Arrows denote relative magnetization of electrodes. Flipping of specific layers is shown.*

We now present magnetotransport results. We emphasize that these results are statistically relevant as they are representative of 5 devices measured on the annealed stack and 4 devices measured on the non-annealed stack.

At room temperature, non-annealed and annealed devices show 12% and 110% TMR signal, respectively. Figures 7.11b and 7.12b show the TMR curves of both device types plotted with respect to their magnetization characteristics. It is not sure whether the low TMR value of the non-annealed devices is due to the AP state being not fully achieved or not. In order to check it, annealing of non-annealed junctions at consecutively 120°C, 200°C and 300°C is proposed in order to separate the recrystallization and the AP state formation explanations for the low TMR observed from the non-annealed sample. The large difference may also result from the texturization process that takes place during the annealing, when the crystallinity of the barrier is improved and the lattice imprinting of MgO onto CoFeB takes place, resulting in significant enhancement of the symmetry filtering. From a spintronic standpoint, such improvement has much more important consequences than

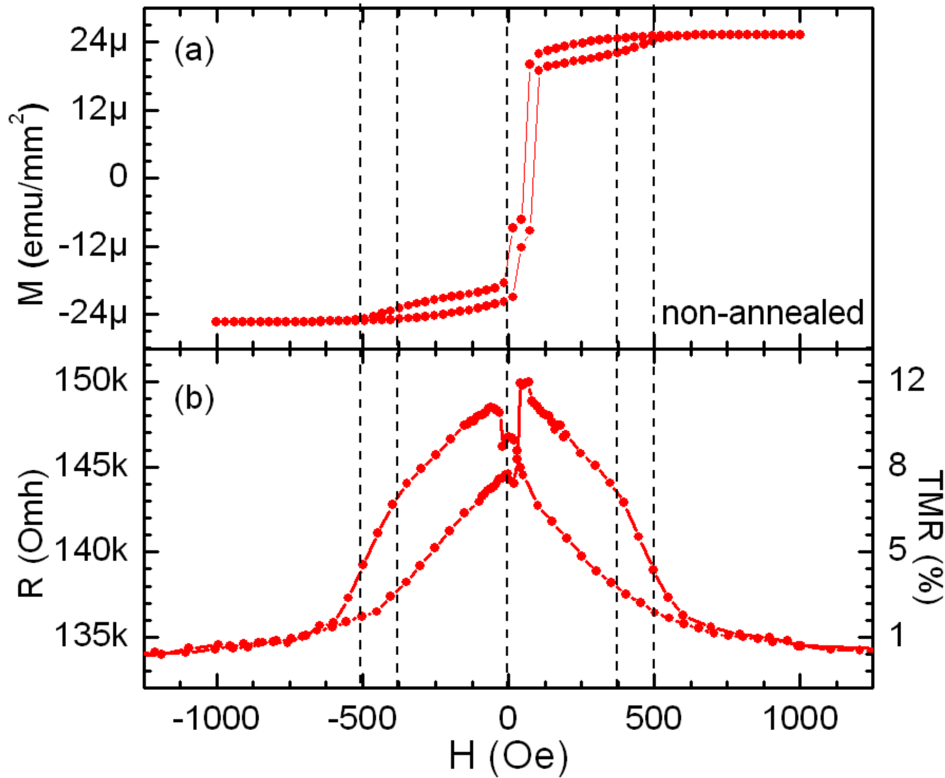


Figure 7.12: *Room temperature a) SQUID magnetization and b) resistance/TMR vs applied field curves of the non-annealed Co(10)/IrMn(7.5)/CoFeB(4)/MgO(2.5)/CoFeB(4.5) sample.*

the material diffusion or defect formation during the annealing.

In order to further understand the impact of annealing-induced defects on magnetotransport, we have varied the parameter of temperature. Referring to fig. 7.13a, the resistance dependence on temperature of an annealed device, measured at 5mV, shows a slight increase from 18kΩ to 20kΩ in the parallel state and relatively fast saturation at 150K. On the other hand, the resistance in the antiparallel case keeps increasing upon cooldown from 37kΩ to 52kΩ, until the temperature reaches around 50K. The behavior can be qualitatively understood if one looks at the band structure of CoFeB electrodes (fig. 7.14) [2]. The AP case behavior could reflect a gradual cancelation of defect-mediated mixing of symmetry-polarized transport channels, which allow electrons of the initially $\Delta_{1\uparrow}$ symmetry to tunnel into $\Delta_{2',5\downarrow}$ states in the counterelectrode. The scenario is prohibited in absence of the mixing (see fig. 1.21). On the other hand, the P case tunneling of electrons with the $\Delta_1$ symmetry is always

[2] As up to our best knowledge calculations of the CoFeB band structure have not been performed, we have averaged energy levels of respective bands of Fe and Co ($Co_{0.4}Fe_{0.4}B_{0.2}$ composition), with the incidence of boron neglected. As our analysis will show, this rigid shift assumption yields coherent results.

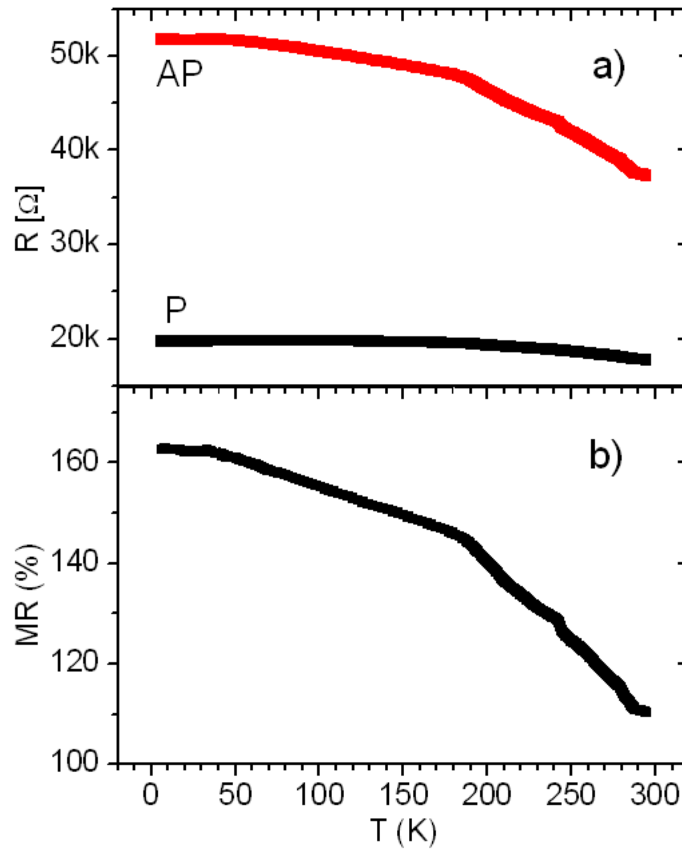


Figure 7.13: *a) Temperature dependence of resistances in parallel and antiparallel state of the annealed device (red and black data, respectively). b) TMR of the device as a function of temperature. Vertical lines mark temperatures at which the temperature dependence of the TMR ratio changes its behavior. The measurement was performed at 5mV.*

allowed, which results in the relatively quick saturation of the resistance in the parallel configuration. Such broadening of P and AP resistances obviously leads to a significant increase in the TMR value (fig. 7.13b).

The temperature dependence of a non-annealed device is presented in figure 7.15. The specific measurement shown was performed in the 2-point contact mode, but it shows same properties as these of the 4-point type due to much lower resistance of contacts than the one of the junction (100Ω and 10Ω for bottom and top electrodes, respectively - see section 4.3). Notably, compared to annealed MTJs, there is no resistance saturation within the measured temperature range. We argue that this reflects how the transport across the non-annealed barrier occurs across defect sites even at low values of temperature.

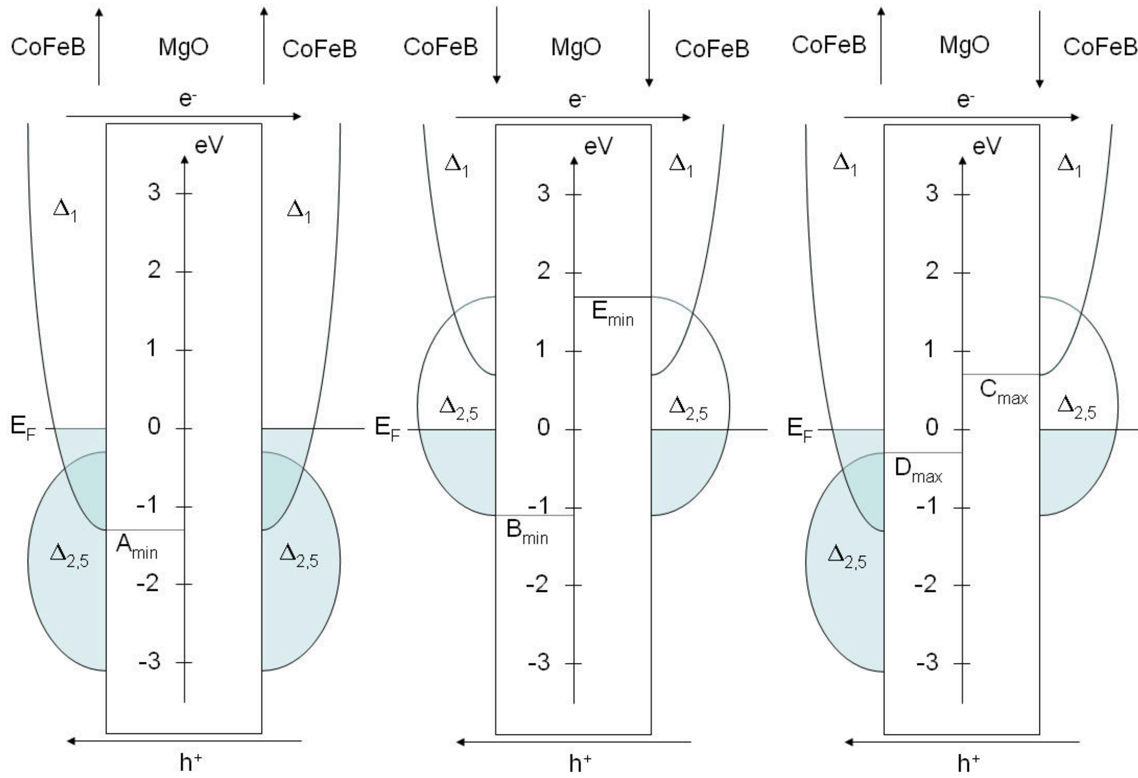


Figure 7.14: *Band alignment and schematic DOS of electrodes in CoFeB/MgO/CoFeB system in $P_{\uparrow-\uparrow}$ (left), $P_{\downarrow-\downarrow}$ (center) and $AP_{\uparrow-\downarrow}$ (right) conductance channels. The schematics are drawn for electrons flowing from left to right, i.e. for holes flowing the opposite way. Letters A-E are quick references to respective features discussed in the text, along with indications whether they account for maxima or minima at the $\hat{I}$ spectra. The $AP_{\downarrow-\uparrow}$ channel (not shown) is the mirror image of the $AP_{\uparrow-\downarrow}$ one, although it does not provide any current flow, except if defect-mediated (see text).*

### 7.3.2 Analysis of the V,T parameter space

Toward understanding these differing transport between annealed and non-annealed samples, we have explored spin-polarized transport within the (V,T) parameter space. In general terms, temperature-dependent I-V characteristics showed very good reproducibility among junctions and the TMR signal allowed to determine barrier heights using the $\hat{I}$ method. The electrical breakdown occurred around 2V at 4K and the breakdown bias threshold decreased with increasing temperature. This implied a precautionary measurement protocol. Thus, most of the full temperature-scale measurements were performed between 1.2V to 1.6V, depending on the specific junction. For each junction type (annealed and non-annealed) several devices were studied, all showing reproducible $\hat{I}_{rel}$ characteristics.

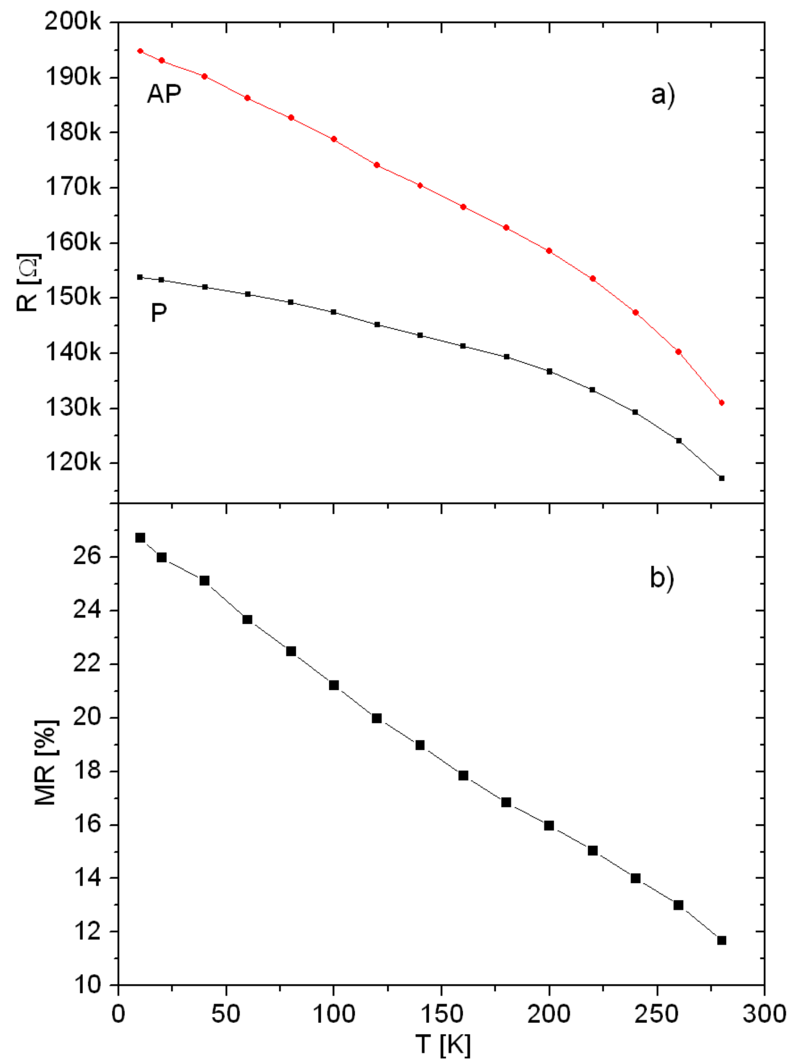


Figure 7.15: *a) Temperature dependence of resistances in the parallel and antiparallel magnetization state of the non-annealed device (red and black data, respectively). b) TMR of the device as a function of temperature. The measurement was performed at 5mV in the 2-point contact mode.*

#### 7.3.2.1 TMR in (V,T) space

In figure 7.16, we plot TMR dependence vs. temperature and applied bias for both annealed and non-annealed device. Yellow and light blue colors roughly correspond to 30% and 70% drop from the initial value, respectively. It is clearly visible that the TMR ratio decreases much faster in the case of the non-annealed sample compared to its annealed counterpart as a function of both temperature and the applied bias. This difference is expected as the transport across the barrier is more incoherent in the non-annealed sample. Moreover, the result suggests that tunneling via defect

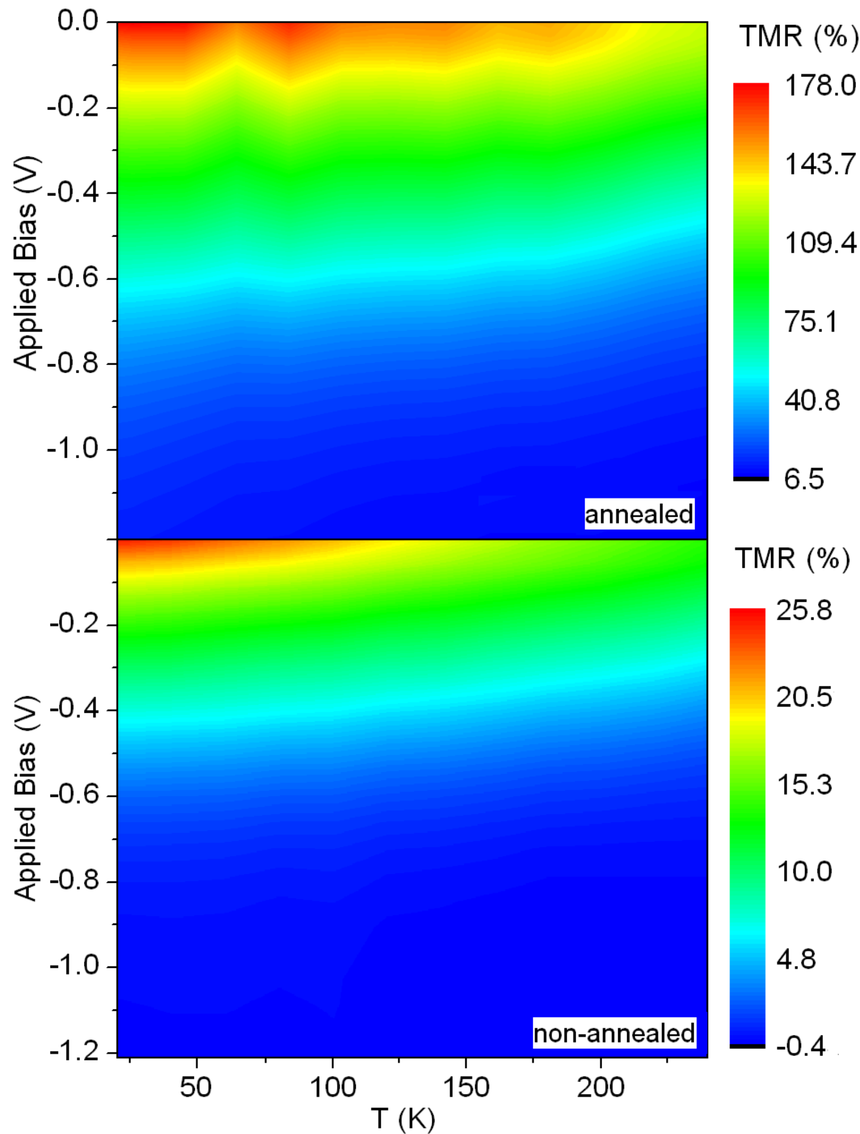


Figure 7.16: *TMR(V,T) of the annealed (top) and non-annealed (bottom) CoFeB/MgO/CoFeB device. Temperature and voltage spacing is 20K and 3mV, respectively.*

sites is activated at much higher values of V and T, which is in agreement with our studies of the temperature dependence of resistances, presented on figures 7.13 and 7.15.

In figure 7.17, we present the temperature-dependent evolution of TMR in the annealed device as a function of the voltage applied, normalized with respect to the value measured at 5mV bias for that temperature. The overall trend is that, regardless of temperature, the TMR decreases with applied bias. This suggests that

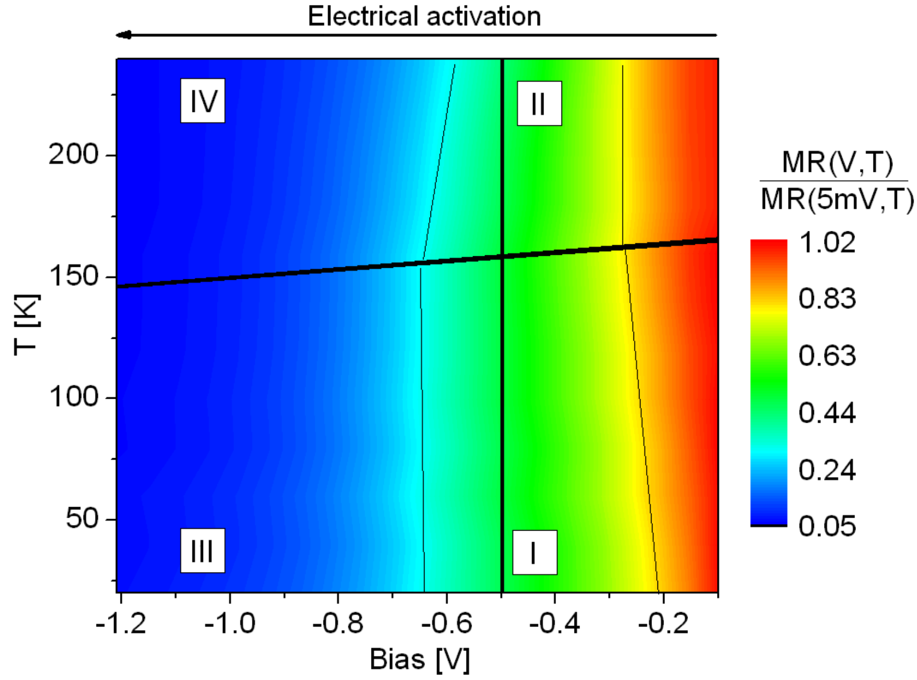


Figure 7.17: *TMR(V,T) of the annealed CoFeB/MgO/CoFeB device normalized to TMR($V_0$,T) with $V_0$=5mV. Temperature and voltage spacing is 20K and 3mV, respectively. The thin lines are guides to the eye. The thick ones separate quadrants described in the text.*

electrical activation dominates thermal activation, which is not surprising given the relative energies involved. Upon closer inspection (see guides to the eye), we may split (V,T) parameter space into four quadrants delineated by T=160K and within a $-0.5<V<-0.3$ V bias range. In quadrants I and IV, a bias dependence of the temperature evolution of relative TMR is noted, while in quadrants II and III it is essentially bias-independent. We are still working on understanding these second-order aspects at the time of this writing.

We now consider electrical activation explicitly by plotting a similar graph in (V,T) parameter space, but this time with TMR normalized at a given value of applied bias to that found at low temperature (see figure 7.18). We witness three features. At very low bias (±50mV), the data reveals a fast TMR decrease due to the zero bias anomaly. Aside from this feature, we witness within ≈ ±500mV a rather flat TMR temperature dependence up to about 40K. At higher temperature, TMR begins to drop significantly. We attribute this second feature to the onset of thermally assisted tunneling. As a third feature, we see that, starting at about 20K, there is a large relative TMR drop that is spectrally centered around ±1V.

The TMR(V,T) study presented in the case of annealed MTJs could not be obtained in a satisfactory way for non-annealed MTJs due to small differences between

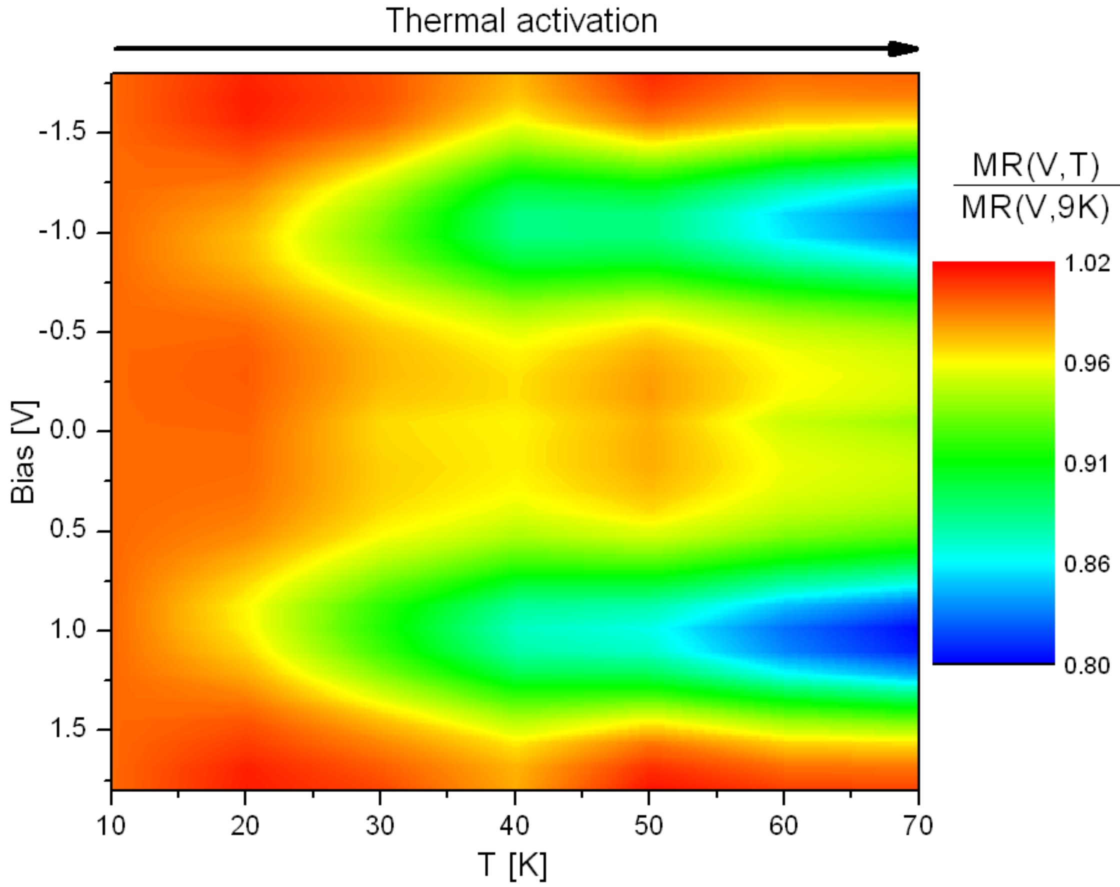


Figure 7.18: *TMR of the annealed CoFeB/MgO/CoFeB device normalized to the TMR at 9K as a function of temperature and the applied bias. Temperature and voltage spacing is 10K and 5mV, respectively.*

small MR values which caused large distortion in TMR(V,T) datasets. However, in what follows, we look beyond TMR and investigate (V,T) parameter space for the transport channels in each of the P and AP configurations. Specifically, we shall use the $\hat{I}$ methodology to uncover electrical and thermal activations of current, within (V,T) space, for P and AP junction states.

#### 7.3.2.2 The annealed system

One of the clearest and most complete $\hat{I}_{rel}$ results obtained on an annealed 25$\mu$m in diameter device is presented for P and AP configurations on figure 7.19. Consecutive measurements are shifted upwards for clarity reasons, however all of them remain in scale. A significant difference between the behavior of $\hat{I}$ curves for both magnetization configurations and specific voltages and temperatures may be seen. All curves exhibit a large peak within the 50mV range. This feature is attributed

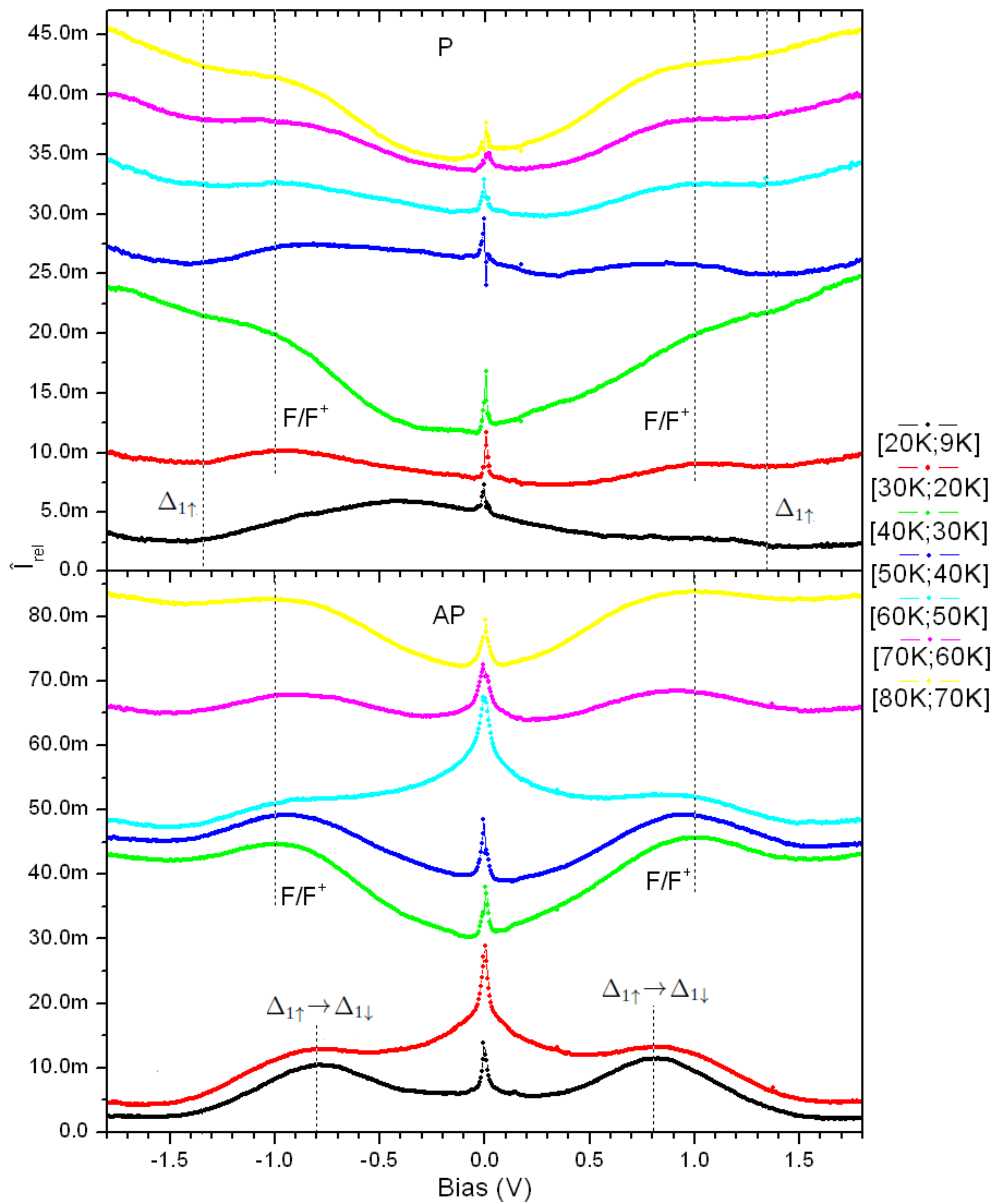


Figure 7.19: $\hat{I}_{rel}$ *curves for the annealed device in the P (top) and AP (bottom) relative magnetization state taken at different temperatures between 9K and 80K and plotted in respect to the data obtained from the preceding measurement at the lower temperature.*

to the zero bias anomaly (ZBA) that is commonly observed in this voltage range and that results from magnon excitations (section 1.4.4.1). However, according to recent experiments [85] it may also result from electron-electron interactions, which in turn originate from the CoFeB electronic structure modification due to the metal-insulator transition of electrodes. The peak is definitely more pronounced in the AP configuration than in the P one, as the ZBA contribution to the overall conductance within the mentioned voltage range (relatively to the standard tunneling) is higher in the AP state than in the P one due to much higher total conductance of the latter.

In general terms, an extremum in an $\hat{I}$, present at a given bias value V, can reflect the following possible phenomena: 1) An extrinsic phenomenon due to spin flip that can be generated by magnons due to the relaxation of electrons with energy eV above $E_F$ to $E_F$. This event occurs over the entire T parameter space considered here, but is confined to V=±50mV. 2) An extrinsic phenomenon due to hopping upon defects of electrons (holes) that are conducting at the energy $E_d$=$E_F$+(-)eV at which the defect is located. Assuming that there is an accessible temperature range for which this event can be frozen out, then this event in principle sets in with the onset of thermally assisted hopping, usually around T>40K. 3) An intrinsic phenomenon due to changes in the density of states of the electrode that is collecting the electron or hole. a) If the crystal structure (i.e. the reduced density and type of defects) of the junction permits symmetry-conserving transport, then, in the absence of thermally assisted hopping, once can consider symmetry-conserved channels of conduction. b) Once T>40K, one should take into account the possible mixing of symmetry channels in the interpretation of experimental results. In either case, unless stated, due to the complex band structure of MgO, we will mostly consider the initial tunneling of $\Delta_1$ states from the emitting electrode. This implies for a) a $\Delta_1 \rightarrow \Delta_1$ symmetry channel, augmented in the case of b) by an additional $\Delta_1 \rightarrow \Delta_5$ channel.

To explore the V,T parameter space, we begin by restricting ourselves to the 4K-40K temperature range for which thermally assisted hopping transport is absent. Using this restriction, we will therefore investigate the impact of bias-induced electrical activation on conductance in the two states of magnetization and, consequently, on TMR.

We first focus on the AP case at low temperatures (9K-20K range - the black curve), i.e. in the intrinsic regime of transport. Referring to fig. 7.19, a large peak is observed at 0.8V in the AP configuration but not in the P configuration. Since we are at low temperature, we may reasonably exclude extrinsic phenomena, as well as the phenomenon of symmetry-channel mixing. We therefore attribute this conductance rise to an intrinsic system property, namely reaching the bottom of the $\Delta_{1\downarrow}$ band, which triggers the tunneling of spin-up electrons of the $\Delta_1$ symmetry to their respective spin-down states in the counterelectrode [154] (feature $C$ at fig. 7.14). Consistently with this interpretation, we indeed do not observe the peak in the P case.

We now turn to the P case. Although the dataset shown in fig. 7.19 includes a peak at V=-0.4V, this feature is neither reproducible at positive V nor in other junctions so we won't discuss it further. We observe a minimum or plateau at 1.3V. Here again, we tentatively attribute this peak to reaching the bottom of the $\Delta_1$ band in the spin-up channel thanks to reaching the bottom of the $\Delta_{1\uparrow}$ band. Indeed, above this voltage, the tunneling rate across the junction is expected to decrease (the $A$ feature)[3]. We note that a similar feature occurs in the AP case within 0.2eV of that in the P case. The feature in the AP case cannot be explained using an intrinsic phenomenon, but could reflect the fact that this local AP $\hat{I}$ minimum is trivially the result of being spectrally located between two maxima including one beyond $\pm$1.8V[4].

To conclude this part on intrinsic phenomena, i.e. that are certain to occur within the low temperature range considered, we witness features in the AP case that we may confidently ascribe to band structure effects, while those in the P case are more difficult to unambiguously attribute.

We now consider the 40K-100K temperature range for which extrinsic phenomena may take place, notably involving defects. To better follow the analysis, we reproduce once again an in-scale landscape of energetical position of specific defects in the barrier (see fig. 7.20) based on information provided in section 2.1.2.1. The following analysis of results proceeds on the important hypothesis that, as shown in fig. 7.20, the Fermi level lies at the center of the MgO optical band gap due to charge neutrality considerations. However, the pinning strength of the charge neutrality level depends on the defect type, density, of defects within the barrier, as well as their spatial location (close to one interface, or the other, or in the middle). Thus, the actual position of $E_F$ may be different even between non-annealed and annealed junctions, let alone when compared with studies performed by other groups, whether fundamental (e.g. x-ray photoelectron spectroscopy) or device-based. In what follows, we provide a defect-based interpretation of our results that is consistent with this reasonable energetical positioning of the Fermi level in our MTJs.

Whereas the 20K-30K relative $\hat{I}$ AP data (the red curve) remains similar to the one at lower temperature (9K-20K), the conductance in the P channel becomes dominated by a 1.0eV feature that, with increasing temperature, will dominate the conductance rise at all temperature intervals. This feature also appears starting from 40K in the AP configuration (the green curve). Since the appearance of these features is only thermally related, we associate the peak with the hole tunneling via $F$ and $F^+$ centers that lie 5eV below the bottom of the conduction band, meaning

[3]In principle, the effect also concerns spin-down electrons of the $\Delta_{2',5}$ symmetry, as the bottom (top) of this band is reached in the P configuration at 1.1eV (1.6eV). This corresponds to the $B$ ($E$) feature at fig. 7.14. However, we do not observe these features within the temperature range corresponding to intrinsic transport. We suppose that, due to high decay rate of electrons of these symmetries, their corresponding peaks are not visible in the data.

[4]Electrical breakdown of junctions at higher voltages prevented a verification of this point.

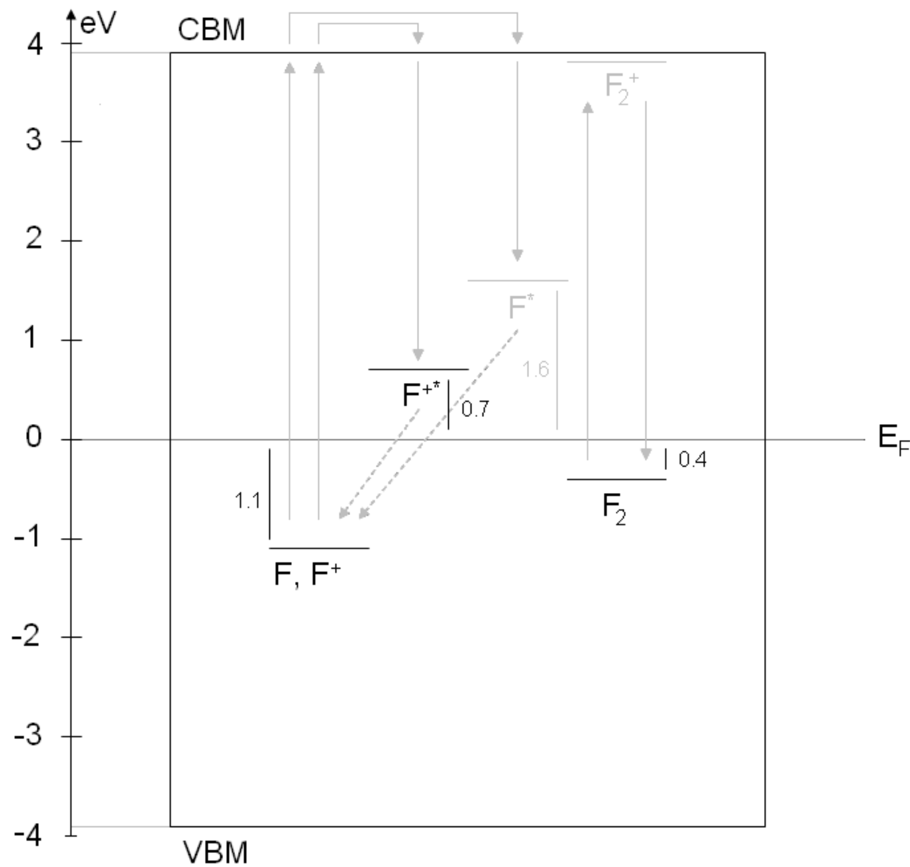


Figure 7.20: *To-scale energy landscape of defects in the MgO barrier, similar to that presented on figures 2.4a and 7.2. Features not observed in the experiment are greyed out for clarity reasons. The band gap of the Mgo barrier was assumed to be 7.8eV and the Fermi level to lie in its middle.*

1.1eV below the Fermi level[5] as seen in fig. 7.20.

We think that the reason for which the 1.0eV feature is not visible at 30K in the AP channel is attributed to its overshadowing by the aforementioned intrinsic feature that is spectrally close. At temperatures 40K and higher it is the intrinsic effect that becomes overshadowed by the defect-mediated tunneling. This is further suggested by the exceptional height of 1eV peaks in the 30K-40K temperature range compared to heights at other temperatures. This significant incidence of $F$ and $F^+$ defect sites on conductance across crystalline MgO barriers is in agreement with our studies performed on MgO crystals presented in section 7.1.

The $\hat{I}_{rel}$ study of annealed junctions at temperatures higher than 100K shows

[5]Nominally, due to the flatness of the complex band structure of MgO around mid-gap, the hole and electron tunneling should be undistinguishable, as long as the defect does not lie very close to the top of the valence band, where it could have a higher probability of being of the $\Delta_5$ symmetry (see fig. 1.11).

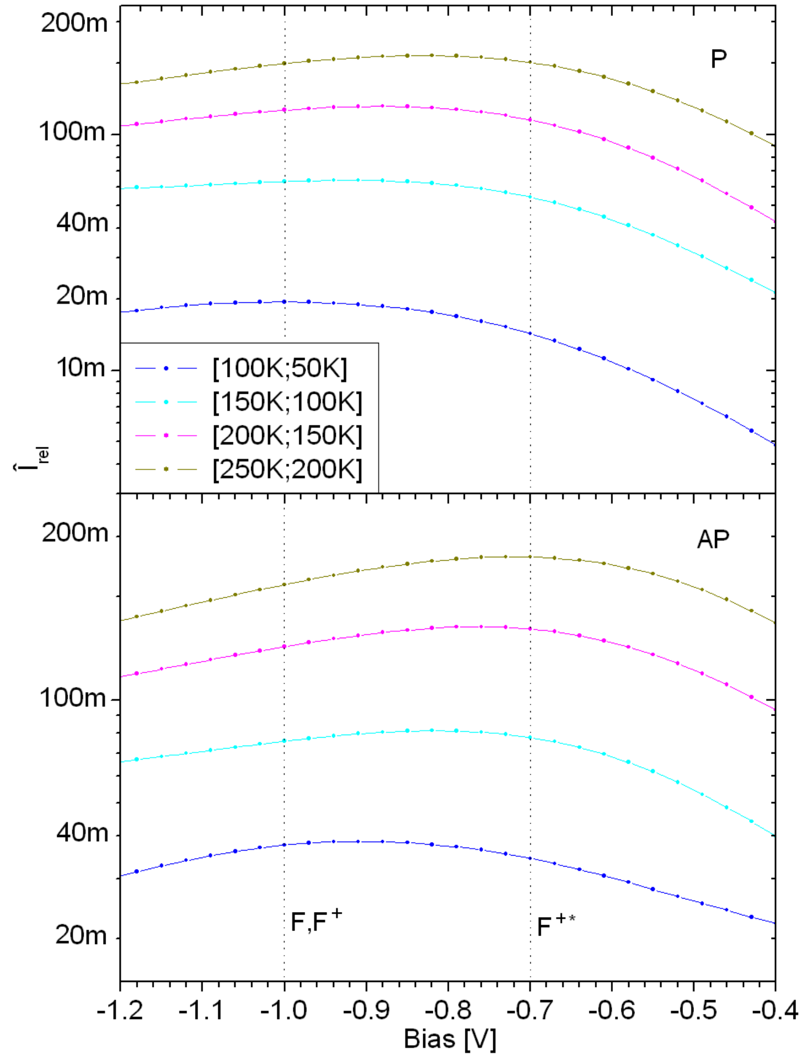


Figure 7.21: $\hat{I}_{rel}$ *curves for an annealed device in the P (top) and AP (bottom) relative magnetization state taken at different temperatures between 50K and 250K and plotted in respect to the data obtained from the preceding measurement at the lower temperature. Curves are plotted in the logarithmic scale for clarity reasons.*

that the maximum observed at 100K for P and AP configuration at 1.0V moves towards lower voltages along with the temperature rise (fig. 7.21). Within the 200K-250K range it reaches 0.82V in the P configuration and 0.72V in the AP configuration. This shift may be explained as the result of the growing dominance, with increasing temperature within the 100K-250K range and especially within 150K-200K, of transport that is assisted by the excited state $F^{+*}$ at 0.7V above $E_F$ (see fig. 7.20) to the detriment of its ground state counterpart $F^{+}$. In turn, this could explain the change in the electrical activation trend, observed at 160K in fig. 7.17 at

the same bias value. More generally, this temperature-induced change in the type of defect that mediates hopping transport may explain the additional decrease in AP junction resistance and associated TMR at low bias (fig. 7.13 past 180K. At the time of this writing, we are interpreting these results, which potentially constitute, alongside the electrical identification of defect states described above, a corroborating thermal identification, within the context of temperature dependent defect activation processes as discussed in ref. [103]. We note, however, that the peak in the P channel at 250K occurs at 0.82eV, ie it is different from that in the AP case. Consistent with our interpretation, this would imply that the relative weights of the $F/F^{+}$ and $F^{+*}$ activations within (V,T) space are not the same for P and AP. At present, we are investigating this difference in terms of symmetry-polarized transport channels in each configuration.

#### 7.3.2.3 The non-annealed system

We now consider a representative dataset for a MTJ from the non-annealed sample. $\hat{I}_{rel}$ curves obtained on a non-annealed device of 25$\mu$m diameter are shown on fig. 7.22. P and AP measurements show very similar characteristics, the only significant difference being the height of the zero bias anomaly peak, which is obviously more pronounced in the AP configuration. This similar behavior for P and AP $\hat{I}$ dataset, observed for non-annealed junctions, is in contrast to that for their annealed counterparts. Furthermore, annealed devices do not exhibit distinct 'intrinsic' and 'extrinsic' transport regimes within the parameter space of temperature. We therefore suppose that, within the MgO barrier of non-annealed junctions, transport is defect-dominated at all temperatures. This is consistent with the monotonic TMR decrease with increasing temperature observed at low bias (see fig. 7.15).

Due to the small (only 5K) difference of the first measurement (15K-20K - the black curve), its resolution is relatively poor, but a broad peak is observed, which we assume to result from a convolution of two peaks, one at 1.0V and one at 0.7V. This interpretation is supported by the temperature evolution of the relative $\hat{I}$ data, which indicate the presence of these two features more clearly. The first peak (at 1.0eV) may correspond to the thermally activated tunneling across $F/F^{+}$ defect sites, already presented in the case of the annealed sample. Its incidence on the conductance seems to persist up to 60K (the green curve), after which it becomes fully overshadowed by the feature at 0.7V, which becomes pronounced more with the temperature increase. We attribute this peak to the excited ionized oxygen vacancy, i.e. the $F^{+*}$ center (see fig. 7.20).

Figure 7.23 shows the full-temperature-scale $\hat{I}_{rel}$ dataset obtained from a non-annealed junctions with the same properties as the one for which the low temperature study was presented. The measurement was also performed using the 2-point contact mode. It is evident that above 120K the conduction rise via the $F^{+*}$ center becomes dominant up to 220K for both magnetic configurations. Afterwards, the maximum

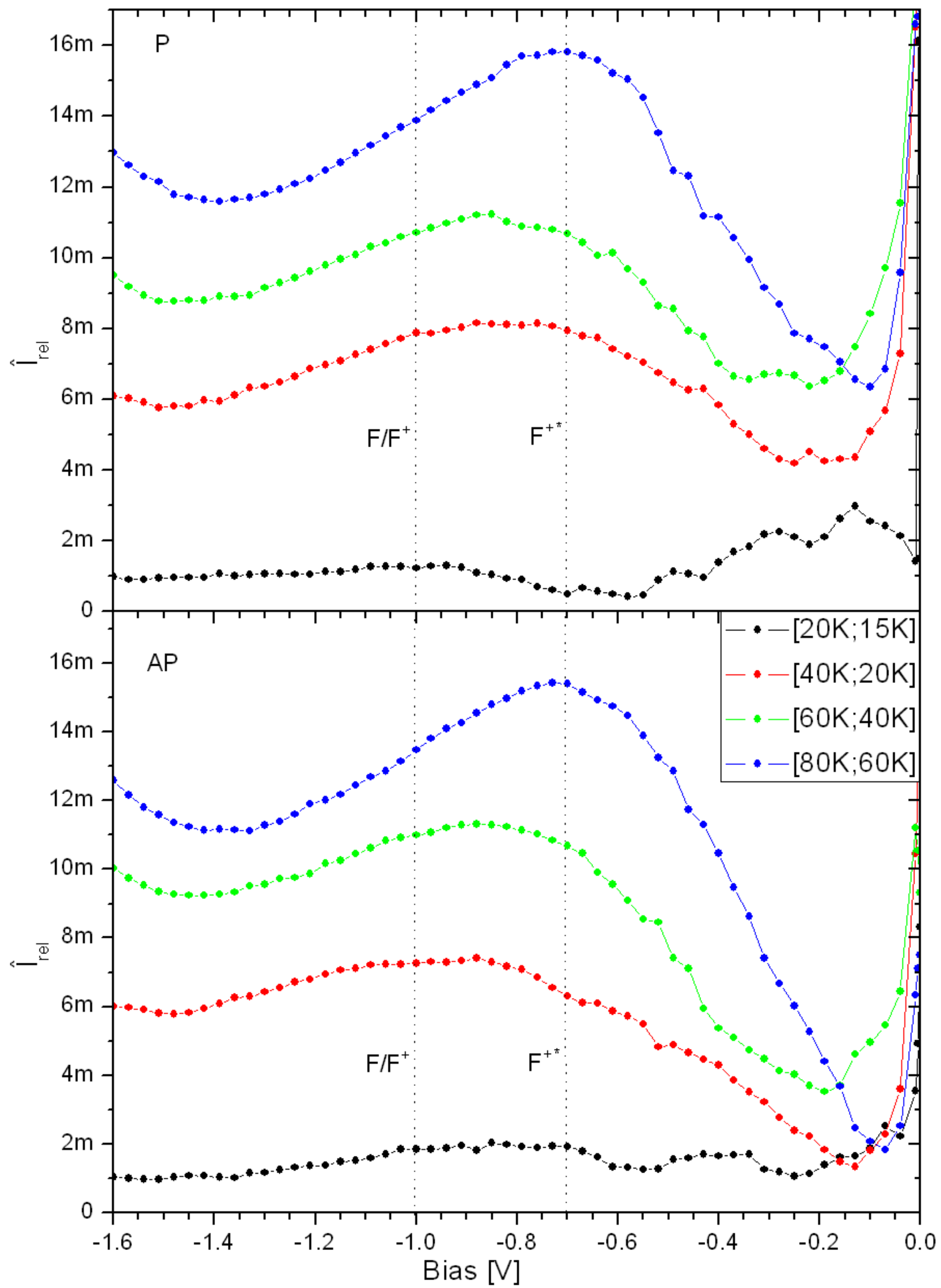


Figure 7.22: *$\hat{I}_{rel}$ curves for a non-annealed device in the P (top) and AP (bottom) relative magnetization state taken at different temperatures between 15K and 80K and plotted in respect to the data obtained from the preceding measurement at the lower temperature. Measurements were performed using the 2-point contact mode.*

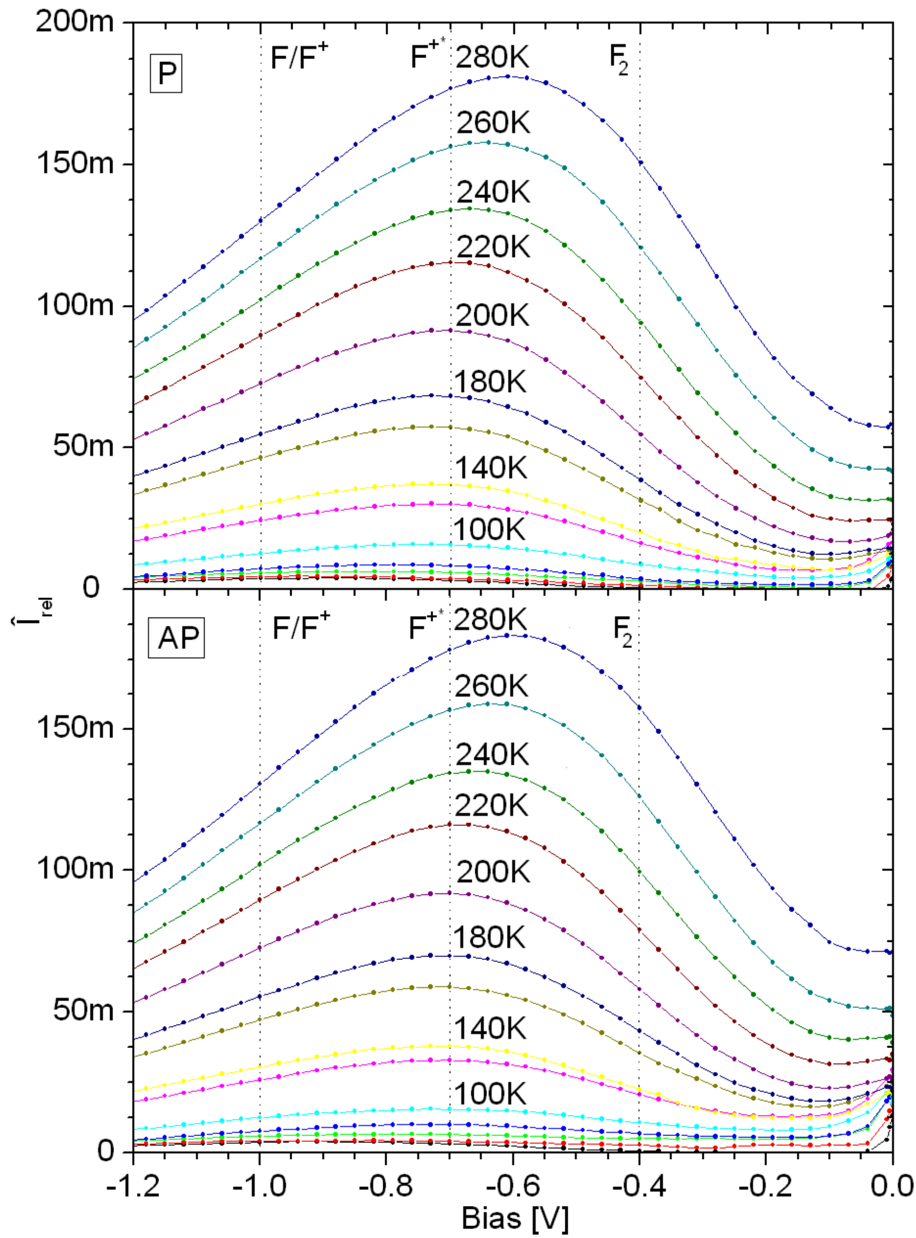


Figure 7.23: *$\hat{I}_{rel}$ curves obtained on the same non-annealed device as on fig. 7.22 in the P (top) and AP (bottom) relative magnetization state taken at different temperatures up to 280K and plotted in respect to the data obtained from the preceding measurement at the lower temperature. The Measurements were performed using the 2-point contact mode.*

starts to shift towards lower voltages reaching 0.61V at 280K. This is notably lower than what was observed regarding annealed MTJs. In principle, a $F_2$ state may provide spectral weight to the $\hat{I}$ at 0.4V (see fig. 7.20), thereby explaining the shift,

but we have not uncovered firm, statistically relevant evidence of this defect state in our magnetotransport experiments.

More generally, our magnetotransport experiments show how annealed samples can exhibit, at low temperature, a magnetotransport regime that is 'intrinsic', i.e. in which defect-mediated transport is essentially frozen out, in contrast to non-annealed samples. Upcoming PL experiments at a wavelength capable of probing not simply $F_2$ but $F$,$F^+$, $F^*$ and $F^{+*}$ centers may shine an additional light upon the physics underneath.

To conclude this section, our magnetotransport results on CoFeB-MgO based MTJs and their accompanying self-consistent analysis show that, through suitable electrical and/or thermal activation, specific, reasonably well-identified defect states present within the MgO tunnel barrier may participate in spin-polarized transport. These defect states appear to be responsible, at low bias, for the TMR decrease with increasing temperature through two separate temperature regimes. We are presently working to ascribe an additional thermal signature to the electrical signature of these defect states.

# Part IV

# Conclusions and perspectives

# Chapter 8

# Summary

This chapter summarizes the work performed within the timeframe of this thesis on magnetic tunnel junctions consisting of transition metal oxide and on magnesium oxide dielectrics. This thesis represents a compendium of work accomplished along the research chain consisting of 1) sample growth and characterization; 2) technological processing into devices; and 3) measurement of these devices.

1) At the onset of this Thesis, some preliminary work had taken place toward synthesizing devices based on stacks deposited by PLD at the IPCMS. The hybrid multichamber system had been only recently assembled and, in particular, only recently had the sputter chamber begun to operate daily. This Thesis involved exploring the growth capabilities of both these deposition systems, in particular the hybrid sputtering system, toward making inorganic spintronic stacks.

2) At the onset of this Thesis, the art of processing sample stacks into tunnel junctions had just appeared at the IPCMS yet a consistent protocol hadn't yet been achieved, notably toward processing small samples such as those from the PLD. A series of iterations to both the UV and shadow masks led to improved device structures.

3) Magnetotransport measurements became a routine part of the research workflow downstream in this research chain midway through this Thesis thanks to the assembly of the open-access Fert bench.

As such, the summary of scientific results for this thesis that are presented hereafter encompasses both a maturation of infrastructural research capabilities alongside a scientific program to be accomplished along this research chain. The overarching goal was to understand the impact of defects on magnetotransport across inorganic tunnel barriers.

## 8.1 Transition metal oxides

This thesis investigated magnetic tunnel junctions based on transition metal oxide barriers, with an emphasis on pairing these barriers with transition metal electrodes.

Devices based on $SrTiO_3$ and $TiO_2$ barriers were studied. $CoFe_2/SrTiO_3/CoFe_2$ structures fabricated with the PLD system showed low-level spintronic behavior and reasons for their moderate performance were identified in terms of interfacial and symmetry filtering issues. Moreover, the high-temperature STO deposition resulted in the likely oxidation of interfaces so as to explain an apparent tunneling behavior paired with the absence of TMR. In an attempt to solve these issues, the $SrTiO_3$ barrier was replaced with $TiO_2$ (to ensure a homogeneous barrier perovksite termination) and additional cobalt layers were inserted at interfaces. Devices on which the studies were performed consisted of $CoFe_2/TiO_2/CoFe_2$ and $Co/TiO_2/Co$ stacks, respectively. Unfortunately, these systems yielded sizeable TMR signal only at low temperature and after bias-crafting. Annealing of the devices increased their resistances by up to one order of magnitude, but caused the magnetoresistance to vanish entirely. $\hat{I}$ measurements performed on both types of devices showed very non-uniform and low (down to 0.1eV) barrier heights. Overall, the study yielded, in certain cases, samples with reproducible TMR up to 3% at room temperature, and in a few instances TMR values that reached $\approx \pm 20\%$ at low temperature thanks to bias-crafting. To the best of our knowledge, these results constitute the state-of-the-art regarding transition metal oxide barriers paired with transition metal electrodes.

Excessive ($2 \cdot 10^{-7}$mbar) pressure during lower electrode deposition was identified as the main reason for the poor performance of $CoFe_2$- and Co-based devices. This issue would not be present if $La_{0.7}Sr_{0.3}MnO_3$ was used as the lower electrode which led to the study of such devices. The films within this study exhibit a bulk Curie temperature of 330K that is reasonable for this system. However, our study has concluded that, unfortunately, the present PLD heater design and pumping stage is not compatible with the high oxygen partial pressures required to obtain LSMO films with a high oxygen content that remains stable upon lithographical processing, and this despite several attempted changes in the growth conditions.

## 8.2 Magnesium oxide

Using the sputter chamber of the IPCMS hybrid system, MgO films were grown while varying the oxygen content within the argon plasma. Optical studies revealed that, upon increasing the oxygen-to-argon ratio, optical absorption due to specific defect types diminishes significantly. The near-disappearance of conductive $F$ and $F^+$ centers was confirmed by local C-AFM measurements. Indeed, introducing oxygen led to a dramatic improvement in the MgO tunneling quality without altering its topography. The change was attributed to reduction of the defect sites concentration and further confirmed through current-voltage characteristics. The spectroscopic signatures present in both the optical and local tunneling studies unambiguously ascribe the impact of introducing oxygen during MgO growth to the population reduction of specific, well-identified defects. As such, we thus show how defects

within the MgO barrier can be controlled.

Fabrication of MgO-based devices patterned *in situ* during the growth, without the need for further processing (e.g. by optical lithography) was attempted. Even though initial batches resulted mostly in shorted devices, several technical improvements were added to the growth procedure and devices with the tunneling regime and satisfactory barrier heights were finally obtained, although the junctions did not yield any TMR signal. The main reason for this lackluster spintronic performance was attributed to excessive oxidation of the lower electrode due to high ($10^{-7}$ mbar range) pressure during the annealing.

CoFeB-based samples were grown by Michel Hehn at the Institut Jean Lamour in Nancy. Several of them were annealed in order to compare the impact of defects on electrical/magnetoresistive properties. Annealed devices showed significantly higher TMR ratio, owing to the texturization of both the MgO barrier and interfacial CoFeB layers, which gives rise to improved symmetry filtering and coherent transport across the crystalline structure. By exploring how electrical and thermal activation affects charge and spin-polarized transport, we show how it is possible to electrically address defect states. Our results tentatively show that these defect states play an important role in limiting TMR. In the process, we shed much needed light toward reconciling the disparate measurements of barrier heights reported in what is otherwise considered the most well-mastered tunneling spintronic system.

# Chapter 9

# Roadmap

Within this chapter, perspectives of further development of studies performed during this thesis are proposed. They encompass both proposed extensions and modifications to growth setups, as well as propose directions in which the related research may proceed.

## 9.1 Transition metal oxides

Perspectives of studies on transition metal oxides within IPCMS remain mostly an issue of the material science. Experiments performed within the timeframe of this thesis show that alteration of certain aspects of the PLD growth are essential in order to obtain devices with properties desired from the spintronic standpoint.

$2 \cdot 10^{-7}$ mbar pressure during the deposition of lower electrode materials needs to be reduced in order to grow high-quality $CoFe_2$ electrodes without interfacial oxidation. If this cannot be done, the alternative in form of $La_{0.7}Sr_{0.3}MnO_3$ based devices is anticipated. However, issues of oxygen stoichiometry and oxygen retention within the film during lithography will need to be addressed. We have proposed a set of options to investigate. More generally, due to the lower band gap of transition metal oxides, and by virtue of their more exotic complex band structure, transition metal oxide-based magnetic tunnel junctions constitute a promising test system for multifunctional spintronics that combine magnetic, electrical and optical functionalities (see hereafter).

## 9.2 Magnesium oxide

In terms of defects study within dielectric crystals, several further steps are proposed: reducing the impact of sample exposure between the growth and characterization, determining the evolution of the band gap across atomic planes and additional study of the surface/interface nature of defects in thin films, whose transition energies and

positions within the band gap are different from those of the bulk and remain largely unstudied. These studies are well suited for the variable temperature AFM that will be connected to the Hybrid system in the near future.

Similarly to the PLD growth technique, the rather poor spintronic performance of the shadowmask-based MgO devices is believed to be improved by decreasing pressure in the Hybrid System's chamber during the annealing of the lower electrode. One may improve the vacuum, potentially by outfitting the sputter chamber's main gasket with differential pumping. One may also potentially consider replacing Fe and CoFe electrodes with CoFeB compounds so as to circumvent oxidation issues at the junction interface.

Experiments performed on CoFeB-based devices appear to be very promising. Issues related to the data analysis remain similar to these related to of bulk crystals, i.e. the adaptation of our model of the defect landscape in MgO crystal for the thin films and taking interfacial nature of defects into the account. The correlation between separately conducted optical experiments and (magneto)transport experiments led us to tentatively position the Fermi level of the electrodes relative to the valence and conduction band edges of MgO. Performing these experiments jointly could greatly help solve this important point (see hereafter). In terms of the future device study, several additional systems are planned to be tested in cooperation with Institut Jean Lamour in Nancy. These include junctions with several excessive MgO thicknesses (i.e. the strategy initially developed by M. Bowen during his Thesis regarding STO MTJs and recently reapplied within the UMPhy group in the case of MgO MTJs) in order to study systems in which the conductance is realized via defect sites only. More generally, these results, and the scientific methodology that underscores them, may be reapplied to other oxides, notably those with nominally expected ferroelectricity or multiferroicity, so as to understand to what extent these intrinsic materials properties are governed in devices by defects.

## 9.3 Optical access

During the time of the writing of this manuscript, a brand, new custom-made setup, *The Multifunctional Bench* (Banc MultiFonctionnel in French, or BMF) was assembled and is, at the time of this writing, operational with nominal magnetotransport and rudimentary optical capabilities. It is designed to enable combined optical and electrical multiplexing studies on devices such as magnetic tunnel junctions. The BMF setup benefits from a greatly modernized design compared to the Fert setup, so it utilizes the same chip design, however it allows two chips to be mounted and measured simultaneously. Throughout this Thesis, the focus has been to utilize this bench, once operational, to explore the interplay afforded by defect states within the tunnel barrier between the magnetic, electric and optical functionalities in a magnetic tunnel junction. Toward this end, UV lithography masks were designed

starting in early 2009 so as to enable optical access and were improved as expertise was attained on how to best achieve this optical access. As you read these lines, we should be performing the first combined optomagnetoresistive measurements on the model inorganic magnetic tunnel junction system CoFeB/MgO/CoFeB. Stay tuned...

# Bibliography

[1] G. E. Moore, "Cramming more components onto integrated circuits, reprinted from electronics, volume 38, number 8, april 19, 1965, pp.114 ff.," *Solid-State Circuits Newsletter, IEEE*, vol. 11, pp. 33 –35, sept. 2006.

[2] M. N. Baibich, J. M. Broto, A. Fert, F. N. Van Dau, F. Petroff, P. Etienne, G. Creuzet, A. Friederich, and J. Chazelas, "Giant magnetoresistance of (001)fe/(001)cr magnetic superlattices," *Phys. Rev. Lett.*, vol. 61, pp. 2472–2475, Nov 1988.

[3] G. Binasch, P. Grünberg, F. Saurenbach, and W. Zinn, "Enhanced magnetoresistance in layered magnetic structures with antiferromagnetic interlayer exchange," *Phys. Rev. B*, vol. 39, pp. 4828–4830, Mar 1989.

[4] S. Parkin, X. Jiang, C. Kaiser, A. Panchula, K. Roche, and M. Samant, "Magnetically engineered spintronic sensors and memory," *Proceedings of the IEEE*, vol. 91, pp. 661 – 680, may 2003.

[5] P. M. Tedrow and R. Meservey, "Spin polarization of electrons tunneling from films of fe, co, ni, and gd," *Phys. Rev. B*, vol. 7, pp. 318–326, Jan 1973.

[6] P. Fulde, "High field superconductivity in thin films," *Advances in Physics*, vol. 22, no. 6, pp. 667–719, 1973.

[7] J. S. Moodera, L. R. Kinder, T. M. Wong, and R. Meservey, "Large magnetoresistance at room temperature in ferromagnetic thin film tunnel junctions," *Phys. Rev. Lett.*, vol. 74, pp. 3273–3276, Apr 1995.

[8] D. Wang, C. Nordman, J. Daughton, Z. Qian, and J. Fink, "70temperature for sdt sandwich junctions with cofeb as free and reference layers," *Magnetics, IEEE Transactions on*, vol. 40, pp. 2269 – 2271, july 2004.

[9] J. M. MacLaren, W. H. Butler, and X.-G. Zhang, "Spin-dependent tunneling in epitaxial systems: Band dependence of conductance," *Journal of Applied Physics*, vol. 83, no. 11, pp. 6521–6523, 1998.

[10] J. Mathon and A. Umerski, "Theory of tunneling magnetoresistance of an epitaxial fe/mgo/fe(001) junction," *Phys. Rev. B*, vol. 63, p. 220403, May 2001.

[11] M. Bowen, V. Cros, F. Petroff, A. Fert, C. M. Boubeta, J. L. Costa-Kramer, J. V. Anguita, A. Cebollada, F. Briones, J. M. de Teresa, L. Morellon, M. R. Ibarra, F. Guell, F. Peiro, and A. Cornet, "Large magnetoresistance in fe/mgo/feco(001) epitaxial tunnel junctions on gaas(001)," *Applied Physics Letters*, vol. 79, no. 11, pp. 1655–1657, 2001.

[12] E. Popova, J. Faure-Vincent, C. Tiusan, C. Bellouard, H. Fischer, M. Hehn, F. Montaigne, M. Alnot, S. Andrieu, A. Schuhl, E. Snoeck, and V. da Costa, "Epitaxial mgo layer for low-resistance and coupling-free magnetic tunnel junctions," *Applied Physics Letters*, vol. 81, no. 6, pp. 1035–1037, 2002.

[13] S. Yuasa, A. Fukushima, T. Nagahama, K. Ando, and Y. Suzuki, "High tunnel magnetoresistance at room temperature in fully epitaxial fe/mgo/fe tunnel junctions due to coherent spin-polarized tunneling," *Japanese Journal of Applied Physics*, vol. 43, no. 4B, pp. L588–L590, 2004.

[14] S. Yuasa and D. D. Djayaprawira, "Giant tunnel magnetoresistance in magnetic tunnel junctions with a crystalline mgo(0 0 1) barrier," *Journal of Physics D: Applied Physics*, vol. 40, no. 21, p. R337, 2007.

[15] S. Ikeda, J. Hayakawa, Y. Ashizawa, Y. M. Lee, K. Miura, H. Hasegawa, M. Tsunoda, F. Matsukura, and H. Ohno, "Tunnel magnetoresistance of 604300 k by suppression of ta diffusion in cofeb/mgo/cofeb pseudo-spin-valves annealed at high temperature," *Applied Physics Letters*, vol. 93, no. 8, p. 082508, 2008.

[16] J.-H. Park, E. Vescovo, H.-J. Kim, C. Kwon, R. Ramesh, and T. Venkatesan, "Direct evidence for a half-metallic ferromagnet," *Nature (London)*, vol. 392, p. 794, 1998.

[17] M. Bowen, M. Bibes, A. Barthelemy, J.-P. Contour, A. Anane, Y. Lemaitre, and A. Fert, "Nearly total spin polarization in la[sub 2/3]sr[sub 1/3]mno[sub 3] from tunneling experiments," *Applied Physics Letters*, vol. 82, no. 2, pp. 233–235, 2003.

[18] H. Itoh, T. Ohsawa, and J. Inoue, "Magnetoresistance of ferromagnetic tunnel junctions in the double-exchange model," *Phys. Rev. Lett.*, vol. 84, pp. 2501–2504, Mar 2000.

[19] J. M. Tour and T. He, "Electronics: The fourth element," *Nature*, vol. 453, pp. 42–43, May 2008.

[20] W. H. Butler, "Tunneling magnetoresistance from a symmetry filtering effect," *Science and Technology of Advanced Materials*, vol. 9, no. 1, p. 014106, 2008.

[21] J. G. Simmons, "Generalized formula for the electric tunnel effect between similar electrodes separated by a thin insulating film," *Journal of Applied Physics*, vol. 34, no. 6, pp. 1793–1803, 1963.

[22] W. F. Brinkman, R. C. Dynes, and J. M. Rowell, "Tunneling conductance of asymmetrical barriers," *Journal of Applied Physics*, vol. 41, no. 5, pp. 1915–1921, 1970.

[23] J.-G. J. Zhu and C. Park, "Magnetic tunnel junctions," *Materials Today*, vol. 9, no. 11, pp. 36 – 45, 2006.

[24] W. Zhong, G. Overney, and D. Toma, "Structural properties of fe crystals," *Phys. Rev. B*, vol. 47, pp. 95–99, Jan 1993.

[25] M. Julliere, "Tunneling between ferromagnetic films," *Physics Letters A*, vol. 54, no. 3, pp. 225 – 226, 1975.

[26] J. C. Slonczewski, "Conductance and exchange coupling of two ferromagnets separated by a tunneling barrier," *Phys. Rev. B*, vol. 39, pp. 6995–7002, Apr 1989.

[27] W. H. Butler, X.-G. Zhang, T. C. Schulthess, and J. M. MacLaren, "Spin-dependent tunneling conductance of Fe|MgO|Fe sandwiches," *Phys. Rev. B*, vol. 63, p. 054416, Jan 2001.

[28] X.-G. Zhang, W. H. Butler, and A. Bandyopadhyay, "Effects of the iron-oxide layer in fe-feo-mgo-fe tunneling junctions," *Phys. Rev. B*, vol. 68, p. 092402, Sep 2003.

[29] Y. Wang, J. Zhang, X.-G. Zhang, H.-P. Cheng, and X. F. Han, "First-principles study of fe/mgo based magnetic tunnel junctions with mg interlayers," *Phys. Rev. B*, vol. 82, p. 054405, Aug 2010.

[30] C. Tiusan, F. Greullet, M. Hehn, F. Montaigne, S. Andrieu, and A. Schuhl, "Spin tunnelling phenomena in single-crystal magnetic tunnel junction systems," *Journal of Physics: Condensed Matter*, vol. 19, no. 16, p. 165201, 2007.

[31] P. Dederichs, P. Mavropoulos, O. Wunnicke, N. Papanikolaou, V. Bellini, R. Zeller, V. Drchal, and J. KudrnovskÃ¡, "Importance of complex band structure and resonant states for tunneling," *Journal of Magnetism and Magnetic Materials*, vol. 240, no. 1âĂŞ3, pp. 108 – 113, 2002. <ce:title>4th International Symposium on Metallic Multilayers</ce:title>.

[32] V. Heine, “Theory of surface states,” *Phys. Rev.*, vol. 138, pp. A1689–A1696, Jun 1965.

[33] P. Mavropoulos, N. Papanikolaou, and P. H. Dederichs, “Complex band structure and tunneling through ferromagnet /insulator /ferromagnet junctions,” *Phys. Rev. Lett.*, vol. 85, pp. 1088–1091, Jul 2000.

[34] J. Faure-Vincent, C. Tiusan, E. Jouguelet, F. Canet, M. Sajieddine, C. Bellouard, E. Popova, M. Hehn, F. Montaigne, and A. Schuhl, “High tunnel magnetoresistance in epitaxial fe/mgo/fe tunnel junctions,” *Applied Physics Letters*, vol. 82, no. 25, pp. 4507–4509, 2003.

[35] S. Zhang, P. M. Levy, A. C. Marley, and S. S. P. Parkin, “Quenching of magnetoresistance by hot electrons in magnetic tunnel junctions,” *Phys. Rev. Lett.*, vol. 79, pp. 3744–3747, Nov 1997.

[36] C. Tiusan, J. Faure-Vincent, M. Sicot, M. Hehn, C. Bellouard, F. Montaigne, S. Andrieu, and A. Schuhl, “Spin filtering effects in monocristalline fe/mgo/fe magnetic tunnel junctions,” *Materials Science and Engineering: B*, vol. 126, no. 2âĂŞ3, pp. 112 – 119, 2006. <ce:title>EMRS 2005, Symposium B, Spintronics</ce:title>.

[37] P. A. Thiry, M. Liehr, J. J. Pireaux, and R. Caudano, “Infrared optical constants of insulators determined by high-resolution electron-energy-loss spectroscopy,” *Phys. Rev. B*, vol. 29, pp. 4824–4826, Apr 1984.

[38] V. Drewello, M. Schäfers, O. Schebaum, A. A. Khan, J. Münchenberger, J. Schmalhorst, G. Reiss, and A. Thomas, “Inelastic electron tunneling spectra of mgo-based magnetic tunnel junctions with different electrode designs,” *Phys. Rev. B*, vol. 79, p. 174417, May 2009.

[39] J. Zhang, X.-G. Zhang, and X. F. Han, “Spinel oxides: Delta[sub 1] spin-filter barrier for a class of magnetic tunnel junctions,” *Applied Physics Letters*, vol. 100, no. 22, p. 222401, 2012.

[40] D. A. Stewart, “New type of magnetic tunnel junction based on spin filtering through a reduced symmetry oxide: Feco|mg3b2o6|feco,” *Nano Letters*, vol. 10, no. 1, pp. 263–267, 2010. PMID: 20017563.

[41] M. Bowen, J.-L. Maurice, A. BarthÃľlÃľmy, M. Bibes, D. Imhoff, V. Bellini, R. Bertacco, D. Wortmann, P. Seneor, E. Jacquet, A. VaurÃĺs, J. Humbert, J.-P. Contour, C. Colliex, S. BlÃijgel, and P. H. Dederichs, “Using half-metallic manganite interfaces to reveal insights into spintronics,” *Journal of Physics: Condensed Matter*, vol. 19, no. 31, p. 315208, 2007.

[42] J.-L. Maurice, D. Imhoff, J.-P. Contour, and C. Colliex, "Interfaces in 100 epitaxial heterostructures of perovskite oxides," *Philosophical Magazine*, vol. 86, no. 15, pp. 2127–2146, 2006.

[43] M. Bowen, A. Barthélémy, V. Bellini, M. Bibes, P. Seneor, E. Jacquet, J.-P. Contour, and P. H. Dederichs, "Observation of fowler–nordheim hole tunneling across an electron tunnel junction due to total symmetry filtering," *Phys. Rev. B*, vol. 73, p. 140408, Apr 2006.

[44] I. J. Vera Marún, F. M. Postma, J. C. Lodder, and R. Jansen, "Tunneling magnetoresistance with positive and negative sign in $la_{0.67}sr_{0.33}mno_3$/$srtio_3$/Co junctions," *Phys. Rev. B*, vol. 76, p. 064426, Aug 2007.

[45] M. Bibes, M. Bowen, A. Barthelemy, A. Anane, K. Bouzehouane, C. Carretero, E. Jacquet, J.-P. Contour, and O. Durand, "Growth and characterization of tio[sub 2] as a barrier for spin-polarized tunneling," *Applied Physics Letters*, vol. 82, no. 19, pp. 3269–3271, 2003.

[46] C. C. Hsieh, K. H. Wu, J. Y. Juang, T. M. Uen, J.-Y. Lin, and Y. S. Gou, "Monophasic tio[sub 2] films deposited on srtio[sub 3](100) by pulsed laser ablation," *Journal of Applied Physics*, vol. 92, no. 5, pp. 2518–2523, 2002.

[47] L. Kavan, M. GrÃď'tzel, S. E. Gilbert, C. Klemenz, and H. J. Scheel, "Electrochemical and photoelectrochemical investigation of single-crystal anatase," *Journal of the American Chemical Society*, vol. 118, no. 28, pp. 6716–6723, 1996.

[48] R. Asahi, Y. Taga, W. Mannstadt, and A. J. Freeman, "Electronic and optical properties of anatase $tio_2$," *Phys. Rev. B*, vol. 61, pp. 7459–7465, Mar 2000.

[49] S. Yuasa, A. Fukushima, H. Kubota, Y. Suzuki, and K. Ando, "Giant tunneling magnetoresistance up to 410 percents at room temperature in fully epitaxial co/mgo/co magnetic tunnel junctions with bcc co(001) electrodes," *Applied Physics Letters*, vol. 89, no. 4, p. 042505, 2006.

[50] X.-G. Zhang and W. H. Butler, "Large magnetoresistance in bcc Co/MgO/Co and FeCo/MgO/FeCo tunnel junctions," *Phys. Rev. B*, vol. 70, p. 172407, Nov 2004.

[51] S. Parkin, C. Kaiser, A. Panchula, P. Rice, B. Hughes, M. Samant, and S.-H. Yang, "Giant tunnelling magnetoresistance at room temperature with mgo (100) tunnel barriers," *Nature Materials*, vol. 3, no. 12, pp. 862–867, 2004. cited By (since 1996) 990.

[52] F. Bonell, T. Hauet, S. Andrieu, F. Bertran, P. Le Fèvre, L. Calmels, A. Tejeda, F. Montaigne, B. Warot-Fonrose, B. Belhadji, A. Nicolaou, and A. Taleb-Ibrahimi, "Spin-polarized electron tunneling in bcc FeCo/MgO/FeCo(001) magnetic tunnel junctions," *Phys. Rev. Lett.*, vol. 108, p. 176602, Apr 2012.

[53] S. Yuasa, T. Katayama, T. Nagahama, A. Fukushima, H. Kubota, Y. Suzuki, and K. Ando, "Giant tunneling magnetoresistance in fully epitaxial body-centered-cubic co/mgo/fe magnetic tunnel junctions," *Applied Physics Letters*, vol. 87, no. 22, p. 222508, 2005.

[54] B. Nickel, W. Donner, H. Dosch, C. Detlefs, and G. Grübel, "Critical adsorption and dimensional crossover in epitaxial feco films," *Phys. Rev. Lett.*, vol. 85, pp. 134–137, Jul 2000.

[55] S. Yuasa, Y. Suzuki, T. Katayama, and K. Ando, "Characterization of growth and crystallization processes in cofeb/mgo/cofeb magnetic tunnel junction structure by reflective high-energy electron diffraction," *Applied Physics Letters*, vol. 87, no. 24, p. 242503, 2005.

[56] Y. S. Choi, K. Tsunekawa, Y. Nagamine, and D. Djayaprawira, "Transmission electron microscopy study on the polycrystalline cofeb/mgo/cofeb based magnetic tunnel junction showing a high tunneling magnetoresistance, predicted in single crystal magnetic tunnel junction," *Journal of Applied Physics*, vol. 101, no. 1, p. 013907, 2007.

[57] M. Mizuguchi, Y. Suzuki, T. Nagahama, and S. Yuasa, "In situ scanning tunneling microscopy observations of polycrystalline mgo(001) tunneling barriers grown on amorphous cofeb electrode," *Applied Physics Letters*, vol. 91, no. 1, p. 012507, 2007.

[58] A. Duluard, B. Negulescu, C. Bellouard, M. Hehn, D. Lacour, Y. Lu, G. Lengaigne, F. Montaigne, S. Robert, S. Suire, and C. Tiusan, "Fe/mgo/fe (100) textured tunnel junctions exhibiting spin polarization features of single crystal junctions," *Applied Physics Letters*, vol. 100, no. 7, p. 072408, 2012.

[59] D. K. Schreiber, Y.-S. Choi, Y. Liu, A. N. Chiaramonti, D. N. Seidman, and A. K. Petford-Long, "Enhanced magnetoresistance in naturally oxidized mgo-based magnetic tunnel junctions with ferromagnetic cofe/cofeb bilayers," *Applied Physics Letters*, vol. 98, no. 23, p. 232506, 2011.

[60] R. A. de Groot, F. M. Mueller, P. G. v. Engen, and K. H. J. Buschow, "New class of materials: Half-metallic ferromagnets," *Phys. Rev. Lett.*, vol. 50, pp. 2024–2027, Jun 1983.

[61] D. Khomskii, "Electronic structure, exchange and magnetism in oxides," in *Spin Electronics* (M. Ziese and M. Thornton, eds.), vol. 569 of *Lecture Notes in Physics*, pp. 89–116, Springer Berlin / Heidelberg, 2001. 10.1007/3-540-45258-35.

[62] C. Zener, "Interaction between the $d$-shells in the transition metals. ii. ferromagnetic compounds of manganese with perovskite structure," *Phys. Rev.*, vol. 82, pp. 403–405, May 1951.

[63] A. J. Millis, R. Mueller, and B. I. Shraiman, "Fermi-liquid-to-polaron crossover. ii. double exchange and the physics of colossal magnetoresistance," *Phys. Rev. B*, vol. 54, pp. 5405–5417, Aug 1996.

[64] P. W. Anderson and H. Hasegawa, "Considerations on double exchange," *Phys. Rev.*, vol. 100, pp. 675–681, Oct 1955.

[65] A. J. Millis, P. B. Littlewood, and B. I. Shraiman, "Double exchange alone does not explain the resistivity of $\mathrm{La}_{1-x}\mathrm{sr}_x\mathrm{mno}_3$," *Phys. Rev. Lett.*, vol. 74, pp. 5144–5147, Jun 1995.

[66] H. A. Jahn and E. Teller, "Stability of polyatomic molecules in degenerate electronic states. i. orbital degeneracy," *Proceedings of the Royal Society of London. Series A - Mathematical and Physical Sciences*, vol. 161, no. 905, pp. 220–235, 1937.

[67] P. G. de Gennes, "Effects of double exchange in magnetic crystals," *Phys. Rev.*, vol. 118, pp. 141–154, Apr 1960.

[68] J. van den Brink and D. Khomskii, "Double exchange via degenerate orbitals," *Phys. Rev. Lett.*, vol. 82, pp. 1016–1019, Feb 1999.

[69] V. Garcia, M. Bibes, A. Barthélémy, M. Bowen, E. Jacquet, J.-P. Contour, and A. Fert, "Temperature dependence of the interfacial spin polarization of $\mathrm{la}_{2/3}\mathrm{sr}_{1/3}\mathrm{mno}_3$," *Phys. Rev. B*, vol. 69, p. 052403, Feb 2004.

[70] J.-H. Park, E. Vescovo, H.-J. Kim, C. Kwon, R. Ramesh, and T. Venkatesan, "Magnetic properties at surface boundary of a half-metallic ferromagnet $\mathrm{la}_{0.7}\mathrm{sr}_{0.3}\mathrm{mno}_3$," *Phys. Rev. Lett.*, vol. 81, pp. 1953–1956, Aug 1998.

[71] M. Bibes, L. Balcells, S. Valencia, J. Fontcuberta, M. Wojcik, E. Jedryka, and S. Nadolski, "Nanoscale multiphase separation at $\mathrm{la}_{2/3}\mathrm{ca}_{1/3}\mathrm{mno}_3/\mathrm{srtio}_3$ interfaces," *Phys. Rev. Lett.*, vol. 87, p. 067210, Jul 2001.

[72] M. Bibes, S. Valencia, L. Balcells, B. Martinez, J. Fontcuberta, M. Wojcik, S. Nadolski, and E. Jedryka, "Charge trapping in optimally doped epitaxial manganite thin films," *Phys. Rev. B*, vol. 66, p. 134416, Oct 2002.

[73] M. J. Calderón, L. Brey, and F. Guinea, "Surface electronic structure and magnetic properties of doped manganites," *Phys. Rev. B*, vol. 60, pp. 6698–6704, Sep 1999.

[74] M. Imada, A. Fujimori, and Y. Tokura, "Metal-insulator transitions," *Rev. Mod. Phys.*, vol. 70, pp. 1039–1263, Oct 1998.

[75] Y. Ke, K. Xia, and H. Guo, "Oxygen-vacancy-induced diffusive scattering in Fe/MgO/Fe magnetic tunnel junctions," *Phys. Rev. Lett.*, vol. 105, p. 236801, Nov 2010.

[76] J. Tersoff, "Schottky barrier heights and the continuum of gap states," *Phys. Rev. Lett.*, vol. 52, pp. 465–468, Feb 1984.

[77] C. H. Shang, J. Nowak, R. Jansen, and J. S. Moodera, "Temperature dependence of magnetoresistance and surface magnetization in ferromagnetic tunnel junctions," *Phys. Rev. B*, vol. 58, pp. R2917–R2920, Aug 1998.

[78] Y. Lu, M. Tran, H. Jaffrès, P. Seneor, C. Deranlot, F. Petroff, J.-M. George, B. Lépine, S. Ababou, and G. Jézéquel, "Spin-polarized inelastic tunneling through insulating barriers," *Phys. Rev. Lett.*, vol. 102, p. 176801, Apr 2009.

[79] T. Moriyama, C. Ni, W. G. Wang, X. Zhang, and J. Q. Xiao, "Tunneling magnetoresistance in (001)-oriented feco/mgo/feco magnetic tunneling junctions grown by sputtering deposition," *Applied Physics Letters*, vol. 88, no. 22, p. 222503, 2006.

[80] J. Mathon and A. Umerski, "Theory of tunneling magnetoresistance in a disordered Fe/MgO/Fe(001) junction," *Phys. Rev. B*, vol. 74, p. 140404, Oct 2006.

[81] J. Y. Chen, J. F. Feng, and J. M. D. Coey, "Tunable linear magnetoresistance in mgo magnetic tunnel junction sensors using two pinned cofeb electrodes," *Applied Physics Letters*, vol. 100, no. 14, p. 142407, 2012.

[82] S. Amara-Dababi, R. C. Sousa, M. Chshiev, H. Bea, J. Alvarez-Herault, L. Lombard, I. L. Prejbeanu, K. Mackay, and B. Dieny, "Charge trapping-detrapping mechanism of barrier breakdown in mgo magnetic tunnel junctions," *Applied Physics Letters*, vol. 99, no. 8, p. 083501, 2011.

[83] J. M. Teixeira, J. Ventura, J. P. Araujo, J. B. Sousa, M. P. Fernandez-Garcia, P. Wisniowski, and P. P. Freitas, "Evidence of spin-polarized direct elastic tunneling and onset of superparamagnetism in mgo magnetic tunnel junctions," *Phys. Rev. B*, vol. 81, p. 134423, Apr 2010.

[84] W. G. Wang, C. Ni, G. X. Miao, C. Weiland, L. R. Shah, X. Fan, P. Parson, J. Jordan-sweet, X. M. Kou, Y. P. Zhang, R. Stearrett, E. R. Nowak, R. Opila, J. S. Moodera, and J. Q. Xiao, "Understanding tunneling magnetoresistance during thermal annealing in mgo-based junctions with cofeb electrodes," *Phys. Rev. B*, vol. 81, p. 144406, Apr 2010.

[85] J. Bernos, M. Hehn, F. Montaigne, C. Tiusan, D. Lacour, M. Alnot, B. Negulescu, G. Lengaigne, E. Snoeck, and F. G. Aliev, "Impact of electron-electron interactions induced by disorder at interfaces on spin-dependent tunneling in co-fe-b/mgo/co-fe-b magnetic tunnel junctions," *Phys. Rev. B*, vol. 82, p. 060405, Aug 2010.

[86] J. Hayakawa, S. Ikeda, Y. M. Lee, F. Matsukura, and H. Ohno, "Effect of high annealing temperature on giant tunnel magnetoresistance ratio of cofeb/mgo/cofeb magnetic tunnel junctions," *Applied Physics Letters*, vol. 89, no. 23, p. 232510, 2006.

[87] S. Ikeda, J. Hayakawa, Y. M. Lee, T. Tanikawa, F. Matsukura, and H. Ohno, "Tunnel magnetoresistance in mgo-barrier magnetic tunnel junctions with bcc-cofe(b) and fcc-cofe free layers," *Journal of Applied Physics*, vol. 99, no. 8, p. 08A907, 2006.

[88] D. D. Djayaprawira, K. Tsunekawa, M. Nagai, H. Maehara, S. Yamagata, N. Watanabe, S. Yuasa, Y. Suzuki, and K. Ando, "230magnetoresistance in cofeb/mgo/cofeb magnetic tunnel junctions," *Applied Physics Letters*, vol. 86, no. 9, p. 092502, 2005.

[89] S. Ikeda, K. Miura, H. Yamamoto, K. Mizunuma, H. D. Gan, M. Endo, S. Kanai, J. Hayakawa, F. Matsukura, and H. Ohno, "A perpendicular-anisotropy cofeb-mgo magnetic tunnel junction," *Nat Mater*, vol. 9, p. 721, Sep 2010.

[90] D. Herranz, A. Gomez-Ibarlucea, M. Schafers, A. Lara, G. Reiss, and F. G. Aliev, "Low frequency noise due to magnetic inhomogeneities in submicron fecob/mgo/fecob magnetic tunnel junctions," *Applied Physics Letters*, vol. 99, no. 6, p. 062511, 2011.

[91] W. G. Wang, C. Ni, A. Rumaiz, Y. Wang, X. Fan, T. Moriyama, R. Cao, Q. Y. Wen, H. W. Zhang, and J. Q. Xiao, "Real-time evolution of tunneling magnetoresistance during annealing in cofeb/mgo/cofeb magnetic tunnel junctions," *Applied Physics Letters*, vol. 92, no. 15, p. 152501, 2008.

[92] P.-J. Zermatten, F. Bonell, S. Andrieu, M. Chshiev, C. Tiusan, A. Schuhl, and G. Gaudin, "Influence of oxygen monolayer at fe/mgo interface on trans-

port properties in fe/mgo/fe(001) magnetic tunnel junctions," *Applied Physics Express*, vol. 5, no. 2, p. 023001, 2012.

[93] F. Bonell, S. Andrieu, A. M. Bataille, C. Tiusan, and G. Lengaigne, "Consequences of interfacial fe-o bonding and disorder in epitaxial fe/mgo/fe(001) magnetic tunnel junctions," *Phys. Rev. B*, vol. 79, p. 224405, Jun 2009.

[94] G. X. Miao, Y. J. Park, J. S. Moodera, M. Seibt, G. Eilers, and M. Münzenberg, "Disturbance of tunneling coherence by oxygen vacancy in epitaxial Fe/MgO/Fe magnetic tunnel junctions," *Phys. Rev. Lett.*, vol. 100, p. 246803, Jun 2008.

[95] S. Yuasa, T. Nagahama, A. Fukushima, Y. Suzuki, and K. Ando, "Giant room-temperature magnetoresistance in single-crystal fe/mgo/fe magnetic tunnel junctions," *Nat Mater*, vol. 3, p. 868, Dec 2004.

[96] A. Ohtomo, D. A. Muller, J. L. Grazul, and H. Y. Hwang, "Artificial charge-modulationin atomic-scale perovskite titanate superlattices," *Nature*, vol. 419, p. 378, Sep 2002.

[97] G. H. Rosenblatt, M. W. Rowe, G. P. Williams, R. T. Williams, and Y. Chen, "Luminescence of $F$ and $F^+$ centers in magnesium oxide," *Phys. Rev. B*, vol. 39, pp. 10309–10318, May 1989.

[98] L. A. Kappers, R. L. Kroes, and E. B. Hensley, "$F^+$ and $F'$ centers in magnesium oxide," *Phys. Rev. B*, vol. 1, pp. 4151–4157, May 1970.

[99] D. Dominguez-Ariza, C. Sousa, F. Illas, D. Ricci, and G. Pacchioni, "Ground- and excited-state properties of $M$ -center oxygen vacancy aggregates in the bulk and surface of mgo," *Phys. Rev. B*, vol. 68, p. 054101, Aug 2003.

[100] A. Gibson, R. Haydock, and J. P. LaFemina, "Stability of vacancy defects in mgo: The role of charge neutrality," *Phys. Rev. B*, vol. 50, pp. 2582–2592, Jul 1994.

[101] R. Leonelli and J. L. Brebner, "Time-resolved spectroscopy of the visible emission band in strontium titanate," *Phys. Rev. B*, vol. 33, pp. 8649–8656, Jun 1986.

[102] J. Osorio-Guillén, S. Lany, and A. Zunger, "Atomic control of conductivity versus ferromagnetism in wide-gap oxides via selective doping: V, nb, ta in anatase $tio_2$," *Phys. Rev. Lett.*, vol. 100, p. 036601, Jan 2008.

[103] Y. Uenaka and T. Uchino, "Photoexcitation, trapping, and recombination processes of the $f$-type centers in lasing mgo microcrystals," *Phys. Rev. B*, vol. 83, p. 195108, May 2011.

[104] B. D. Evans, G. J. Pogatshnik, and Y. Chen, "Optical properties of lattice defects in Îś-al2o3," *Nuclear Instruments and Methods in Physics Research Section B: Beam Interactions with Materials and Atoms*, vol. 91, no. 1âĂŞ4, pp. 258 – 262, 1994.

[105] M. Capizzi and A. Frova, "Optical gap of strontium titanate (deviation from urbach tail behavior)," *Phys. Rev. Lett.*, vol. 25, pp. 1298–1302, Nov 1970.

[106] J. Rho, S. Jang, Y. D. Ko, S. Kang, D.-W. Kim, J.-S. Chung, M. Kim, M. Han, and E. Choi, "Photoluminescence induced by thermal annealing in srtio[sub 3] thin film," *Applied Physics Letters*, vol. 95, no. 24, p. 241906, 2009.

[107] D. D. Cuong, B. Lee, K. M. Choi, H.-S. Ahn, S. Han, and J. Lee, "Oxygen vacancy clustering and electron localization in oxygen-deficient $srtio_3$: LDA+$u$ study," *Phys. Rev. Lett.*, vol. 98, p. 115503, Mar 2007.

[108] D. Kan, T. Terashima, R. Kanda, A. Masuno, K. Tanaka, S. Chu, H. Kan, A. Ishizumi, Y. Kanemitsu, Y. Shimakawa, and M. Takano, "Blue-light emission at room temperature from ar+-irradiated srtio3," *Nat Mater*, vol. 4, p. 816, Nov 2005.

[109] L. Grabner, "Photoluminescence in $srtio_3$," *Phys. Rev.*, vol. 177, pp. 1315–1323, Jan 1969.

[110] A. Zaleska, "Doped-tio2: A review," *Recent Patents on Engineering*, vol. 2, no. 3, pp. 157–164, 2008.

[111] H. H. Tippins, "Charge-transfer spectra of transition-metal ions in corundum," *Phys. Rev. B*, vol. 1, pp. 126–135, Jan 1970.

[112] A. T. Hindmarch, K. J. Dempsey, D. Ciudad, E. Negusse, D. A. Arena, and C. H. Marrows, "Fe diffusion, oxidation, and reduction at the cofeb/mgo interface studied by soft x-ray absorption spectroscopy and magnetic circular dichroism," *Applied Physics Letters*, vol. 96, no. 9, p. 092501, 2010.

[113] R. C. Weast and M. Astle, *CRC Handbook of Chemistry and Physics, 59th ed.* CRC Preess, Boca Raton, 1978.

[114] J. D. Burton, S. S. Jaswal, E. Y. Tsymbal, O. N. Mryasov, and O. G. Heinonen, "Atomic and electronic structure of the cofeb/mgo interface from first principles," *Applied Physics Letters*, vol. 89, no. 14, p. 142507, 2006.

[115] J. J. Cha, J. C. Read, J. W. F. Egelhoff, P. Y. Huang, H. W. Tseng, Y. Li, R. A. Buhrman, and D. A. Muller, "Atomic-scale spectroscopic imaging of cofeb/mg–b–o/cofeb magnetic tunnel junctions," *Applied Physics Letters*, vol. 95, no. 3, p. 032506, 2009.

[116] Y. Han, J. Han, H. J. Choi, H.-J. Shin, and J. Hong, "Effect of diffused b during annealing on the electronic structure of the mgo barrier in cofeb/mgo/cofeb magnetic tunnel junctions," *Applied Physics Express*, vol. 5, no. 3, p. 033001, 2012.

[117] S. V. Karthik, Y. K. Takahashi, T. Ohkubo, K. Hono, S. Ikeda, and H. Ohno, "Transmission electron microscopy investigation of cofeb/mgo/cofeb pseudospin valves annealed at different temperatures," *Journal of Applied Physics*, vol. 106, no. 2, p. 023920, 2009.

[118] D. Larson, E. Marquis, P. Rice, T. Prosa, B. Geiser, S.-H. Yang, and S. Parkin, "Manganese diffusion in annealed magnetic tunnel junctions with mgo tunnel barriers," *Scripta Materialia*, vol. 64, no. 7, pp. 673 – 676, 2011.

[119] I. I. Oleinik, E. Y. Tsymbal, and D. G. Pettifor, "Atomic and electronic structure of Co/srtio$_3$/Co magnetic tunnel junctions," *Phys. Rev. B*, vol. 65, p. 020401, Dec 2001.

[120] M. Brazier, S. Mansour, and M. McElfresh, "Ferroelectric fatigue of pb(zr,ti)o[sub 3] thin films measured in atmospheres of varying oxygen concentration," *Applied Physics Letters*, vol. 74, no. 26, pp. 4032–4033, 1999.

[121] D. B. Strukov, G. S. Snider, D. R. Stewart, and R. S. vWilliams, "The missing memristor found," *Nature*, vol. 453, p. 80, May 2008.

[122] M. Bowen, J.-L. Maurice, A. Barthelemy, P. Prod'homme, E. Jacquet, J.-P. Contour, D. Imhoff, and C. Colliex, "Bias-crafted magnetic tunnel junctions with bistable spin-dependent states," *Applied Physics Letters*, vol. 89, no. 10, p. 103517, 2006.

[123] N. Shanthi and D. D. Sarma, "Electronic structure of electron doped srtio$_3$: srtio$_{3-\delta}$ and sr$_{1-x}$la$_x$tio$_3$," *Phys. Rev. B*, vol. 57, pp. 2153–2158, Jan 1998.

[124] Y. Watanabe, J. G. Bednorz, A. Bietsch, C. Gerber, D. Widmer, A. Beck, and S. J. Wind, "Current-driven insulator–conductor transition and nonvolatile memory in chromium-doped srtio[sub 3] single crystals," *Applied Physics Letters*, vol. 78, no. 23, pp. 3738–3740, 2001.

[125] A. Sawa, "Resistive switching in transition metal oxides," *Materials Today*, vol. 11, no. 6, pp. 28 – 36, 2008.

[126] E. Bertin, D. Halley, Y. Henry, N. Najjari, H. Majjad, M. Bowen, V. Da-Costa, J. Arabski, and B. Doudin, "Random barrier double-well model for resistive switching in tunnel barriers," *Journal of Applied Physics*, vol. 109, no. 8, p. 083712, 2011.

[127] D. Halley, H. Majjad, M. Bowen, N. Najjari, Y. Henry, C. Ulhaq-Bouillet, W. Weber, G. Bertoni, J. Verbeeck, and G. V. Tendeloo, "Electrical switching in fe/cr/mgo/fe magnetic tunnel junctions," *Applied Physics Letters*, vol. 92, no. 21, p. 212115, 2008.

[128] N. Najjari, D. Halley, M. Bowen, H. Majjad, Y. Henry, and B. Doudin, "Electrical switching in fe/v/mgo/fe tunnel junctions," *Phys. Rev. B*, vol. 81, p. 174425, May 2010.

[129] N. Najjarri, "Switching effect in magnetic tunnel junctions based on mgo," *PhD thesis*, 2011.

[130] T. Fukumura, Y. Yamada, H. Toyosaki, T. Hasegawa, H. Koinuma, and M. Kawasaki, "Exploration of oxide-based diluted magnetic semiconductors toward transparent spintronics," *Applied Surface Science*, vol. 223, no. 1âĂŞ3, pp. 62 – 67, 2004. <ce:title>Proceedings of the Second Japan-US Workshop on Combinatorial Materials Science and Technology</ce:title>.

[131] T. Dietl, "A ten-year perspective on dilute magnetic semiconductors and oxides," *Nat Mater*, vol. 9, pp. 965–974, Dec 2010.

[132] Y. Matsumoto, M. Murakami, T. Shono, T. Hasegawa, T. Fukumura, M. Kawasaki, P. Ahmet, T. Chikyow, S.-y. Koshihara, and H. Koinuma, "Room-temperature ferromagnetism in transparent transition metal-doped titanium dioxide," *Science*, vol. 291, no. 5505, pp. 854–856, 2001.

[133] C. Martinez-Boubeta, A. Martinez, S. Hernandez, P. Pellegrino, A. Antony, J. Bertomeu, L. Balcells, Z. Konstantinovic, and B. Martinez, "Blue luminescence at room temperature in defective mgo films," *Solid State Communications*, vol. 151, no. 10, pp. 751 – 753, 2011.

[134] C. Martinez-Boubeta, J. I. Beltran, L. Balcells, Z. Konstantinovic, S. Valencia, D. Schmitz, J. Arbiol, S. Estrade, J. Cornil, and B. Martinez, "Ferromagnetism in transparent thin films of mgo," *Phys. Rev. B*, vol. 82, p. 024405, Jul 2010.

[135] H. R. Kaufman, J. J. Cuomo, and J. M. E. Harper, "Technology and applications of broad-beam ion sources used in sputtering. part i. ion source technology," *Journal of Vacuum Science and Technology*, vol. 21, no. 3, pp. 725–736, 1982.

[136] D. J. Kim, J. Arabski, V. D. Costa, G. Schmerber, M. Bowen, S. Boukari, and E. Beaurepaire, "Incidence of in situ annealing on the nanoscale topographical/electrical properties of the tunnel barrier in sputtered epitaxial fe/mgo/fe multilayers," *Journal of Physics D: Applied Physics*, vol. 43, no. 21, p. 215003, 2010.

[137] D. C. Worledge and T. H. Geballe, "Spin-polarized tunneling in la[sub 0.67]sr[sub 0.33]mno[sub 3]," *Applied Physics Letters*, vol. 76, no. 7, pp. 900–902, 2000.

[138] R. J. Pedersen and J. F. L. Vernon, "Effect of film resistance on low-impedance tunneling measurements," *Applied Physics Letters*, vol. 10, no. 1, pp. 29–31, 1967.

[139] M. Chung and L. Jenkins, "Auger electron energies of the outer shell electrons," *Surface Science*, vol. 22, no. 2, pp. 479 – 485, 1970.

[140] P. Rottländer, M. Hehn, and A. Schuhl, "Determining the interfacial barrier height and its relation to tunnel magnetoresistance," *Phys. Rev. B*, vol. 65, p. 054422, Jan 2002.

[141] J. P. Velev, K. D. Belashchenko, D. A. Stewart, M. van Schilfgaarde, S. S. Jaswal, and E. Y. Tsymbal, "Negative spin polarization and large tunneling magnetoresistance in epitaxial Co|$srtio_3$|Co magnetic tunnel junctions," *Phys. Rev. Lett.*, vol. 95, p. 216601, Nov 2005.

[142] L. F. Mattheiss, "Effect of the 110°k phase transition on the $srtio_3$ conduction bands," *Phys. Rev. B*, vol. 6, pp. 4740–4753, Dec 1972.

[143] S. Mochizuki, F. Fujishiro, and S. Minami, "Photoluminescence and reversible photo-induced spectral change of srtio 3," *Journal of Physics: Condensed Matter*, vol. 17, no. 6, p. 923, 2005.

[144] R. Moubah, S. Colis, F. Schleicher, N. Najjari, H. Majjad, G. Versini, S. Barre, C. Ulhaq-Bouillet, G. Schmerber, M. Bowen, and A. Dinia, "Effect of interface bonding on the transport properties in $cofe_2/srtio_3/cofe_2$/NiFe magnetic tunnel junctions," *Phys. Rev. B*, vol. 82, p. 024415, Jul 2010.

[145] M. Bowen, "Experimental insights into spin-polarized solid state tunneling," *PhD thesis*, 2003.

[146] E. Y. Tsymbal and D. G. Pettifor, "Spin-polarized electron tunneling across a disordered insulator," *Phys. Rev. B*, vol. 58, pp. 432–437, Jul 1998.

[147] E. Y. Tsymbal, A. Sokolov, I. F. Sabirianov, and B. Doudin, "Resonant inversion of tunneling magnetoresistance," *Phys. Rev. Lett.*, vol. 90, p. 186602, May 2003.

[148] D. J. Kim, W. S. Choi, F. Schleicher, R. H. Shin, S. Boukari, V. Davesne, C. Kieber, J. Arabski, G. Schmerber, E. Beaurepaire, W. Jo, and M. Bowen, "Control of defect-mediated tunneling barrier heights in ultrathin mgo films," *Applied Physics Letters*, vol. 97, no. 26, p. 263502, 2010.

[149] F. Illas and G. Pacchioni, "Optical properties of surface and bulk f centers in mgo from ab initio cluster model calculations," *The Journal of Chemical Physics*, vol. 108, no. 18, pp. 7835–7841, 1998.

[150] Y. Chen, R. T. Williams, and W. A. Sibley, "Defect cluster centers in mgo," *Phys. Rev.*, vol. 182, pp. 960–964, Jun 1969.

[151] J. P. Molnar and C. D. Hartman, "Induced absorption bands in mgo crystals," *Phys. Rev.*, vol. 79, pp. 1015–1016, Sep 1950.

[152] F. Bardou, "Rare events in quantum tunneling," *EPL (Europhysics Letters)*, vol. 39, no. 3, p. 239, 1997.

[153] J. M. Teixeira, J. Ventura, J. P. Araujo, J. B. Sousa, P. Wisniowski, S. Cardoso, and P. P. Freitas, "Resonant tunneling through electronic trapping states in thin mgo magnetic junctions," *Phys. Rev. Lett.*, vol. 106, p. 196601, May 2011.

[154] F. Greullet, C. Tiusan, F. Montaigne, M. Hehn, D. Halley, O. Bengone, M. Bowen, and W. Weber, "Evidence of a symmetry-dependent metallic barrier in fully epitaxial mgo based magnetic tunnel junctions," *Phys. Rev. Lett.*, vol. 99, p. 187202, Nov 2007.